2019

Ligand Effect on Gold Nanomolecules Demonstrated Using Aliphatic, Aromatic and Bulky Thiolate Ligands

Milan Rambukwella
University of Mississippi

LIGAND EFFECT ON GOLD NANOMOLECULES DEMONSTRATED USING ALIPHATIC, AROMATIC AND BULKY THIOLATE LIGANDS

A Dissertation
submitted in partial fulfillment of requirements
for the degree of Doctor of Philosophy
in the Department of Chemistry and Biochemistry
The University of Mississippi

by

MILAN RAMBUKWELLA

December 2018

ABSTRACT

Atomically precise thiolate protected gold nanoparticles (AuNPs) known as gold nanomolecules (AuNMs) are intensely pursued owing to their feasibility to elucidate their structure by single crystal X-ray crystallography. They have distinct number of Au atoms (n) and thiolate (-SR, R-hydrocarbon chain) ligands (m) with molecular formula of the form [$Au_n(SR)_m$]. AuNMs are made of a gold core protected by a thiolate-monolayer and possess size-dependent properties conferred by quantum confinement. Atomic precision has been achieved in the 1-3 nm range and crystal structures of several AuNMs ranging from 18 to 279 gold atoms have been studied. They provide significant insights into the structural assembly of AuNMs and surface protection motifs. Also, AuNMs in the range of 1-3 nm are the *most ideal form of AuNPs* and they can be *predictably manipulated at the atomic level*. Therefore, this dissertation will focus on addressing the factors governing the formation of unique atomic structure, composition, metal-ligand interface and their properties have been addressed in detail.

In this dissertation, the thiolate ligands are categorized into three main classes, namely; *aliphatic, aromatic and bulky* thiolate ligands. These distinct classes of thiolate ligands exclusively form a unique series of AuNMs and unique size-dependent properties. *Thiolate monolayer protecting the gold core of AuNMs have been shown to greatly influence the atomic structure, surface chemistry, composition and physicochemical properties of AuNMs*. Therefore, investigation of ligand effect on atomic structure of AuNMs would provide insights into designing

the atomic structure and surface assembly architecture of AuNMs and atomically precise nanomaterials beyond 3 nm as well. Numerous synthesis, molecular conversions and interconversions, crystal structures and various applications of AuNMs have been reported over the past 5-10 years. *The idea of ligand effect to tune the atomic structure and properties of materials* which has not been reviewed comprehensively and critically to date, would be highly beneficial and relevant to this field as well as other fields of metal cluster research. Tailoring chemical structure of metal nanoparticles is of paramount importance to utilize them effectively in related applications.

This dissertation comprehensively and critically describes, *a fundamental criterion, namely, the ligand effect on nanoparticles' atomic structure, metal-ligand interface and properties of thiolate-protected AuNPs*, which must be focused to enable nanoengineering at atomic level. Overall, the work presented in this dissertation discuss; 1. The influence of thiolate-ligands on atomic structure and formation of AuNMs, and their physicochemical properties will be established based on experimental and computational studies. 2. The ligand effect on atomic structure of AuNMs to reveal that ligand engineering is a promising means to enable us to achieve atomically precise next generation nanomaterials and impart novel properties. 3. The influence of ligand-ligand interactions of the three classes of thiolate ligands on thermodynamic stability of AuNMs. 4. Understandings of ligand effect on atomic structure and properties of AuNMs will

improve the predictability of the designed synthetic protocols and can be extended to metal nanoparticles, quantum dots, magnetic nanoparticles and self-assembled monolayers.

DEDICATION

I would like to dedicate this dissertation to all my family members, teachers and friends. A special feeling of gratitude to my loving parents for their endless support and putting me through the best education possible. Finally, I dedicate this work and give special thanks to my research advisor Dr. Amala Dass for his continue support and inspiration throughout the doctoral program. I will always appreciate all the people who help me in anyway.

LIST OF ABBREVIATIONS AND SYMBOLS

AL	Aliphatic
Au	Gold
Ag	Silver
AgCl	Sliver chloride
AIMD	Ab-initio molecular dynamics
AR	Aromatic
BHT	Butylated hydroxytoluene
BU	Bulky
COOH	Carboxylate
Da	Dalton
DCM	Dichloromethane
DCTB	Trans-2-[3[(4-tertbutyl-phenyl)-2-methyl-2-propenylidene] malononitrile
DFT	Density functional theory
DPV	Differential pulse voltammetry
EA	Electron affinity
ESI-MS	Electrospray ionization mass spectrometry
$HAuCl_4 \bullet 3H_2O$	Chloroauric acid
HOMO	Highest-occupied molecular orbital
IP	Ionization potential

K	Kelvin
KOH	Potassium hydroxide
LUMO	Lowest unoccupied molecular orbital
MALDI	Matrix assisted laser desorption ionization
MBT	Methylbenzene thiols
MPC	Monolayer-protected cluster
m-MBT	Meta- methylbenzene thiols
MS	Mass spectrometer
$NaBH_4$	Sodium borohydride
nm	Nanometer
NM	Nanomolecule
o-MBT	Ortho- methylbenzene thiols
Pd	Palladium
PDOS	Projected density of states
p-MBA	Para-mercapto benzoic acid
p-MBT	Para- methylbenzene thiols
Pt	Platinum
RDE	Rotating disk electrochemistry
SAdm	Adamantane thiol
SAMs	Self-assembled monolayers

SCH_3	Methane thiol
SCH_2CH_2Ph	Phenyl ethane thiol
SCy	Cyclohexane thiol
SEC	Size exclusion chromatography
SG	Glutathiolate
STO	Slater type orbitals
SPh	Thiophenol
SPhCOOH	Para-mercapto benzoic acid
SPh-tBu	Tert-butyl benzene thiol
S-tBu	Tert-butyl thiol
TBBT	Tert-butylbenzene thiol
THF	Tetrahydrofuran
TDDFT	Time dependent density functional theory
TOABr	Tetraoctylammonium bromide
TOF	Time of flight
TZP	Triple zeta plus polarization
UV-Vis	Ultra violet-visible
XRD	x-ray diffraction
ZORA	Zero order relativistic approximation

ACKNOWLEDGEMENTS

First, I would like to record my sincere gratitude to my research supervisor Prof. Amala Dass for his supervision, advice, and guidance throughout my PhD candidature. I also gratefully acknowledge my advisory committee Dr. Jerad H. Delcamp, Dr. Jonah Jurss, Dr. James Cizdziel and Dr. Dhammika Nanayakkara for their advices and support during the PhD program. A special thank you to research collaborators: Dr. Alessandro Fortunelli and his group at the Italian National Research Council, and Dr. Jared H. Delcamp at the University of Mississippi (UM).

I acknowledge the UM, Department of Chemistry and Biochemistry for the tuition fee scholarship and other financial support, which enabled me to undertake this research project. The assistance from the UM academic and technical staff in the Department of Chemistry and Biochemistry is greatly acknowledged and appreciated. Special thanks to Dr. Walter Cleland for the given support as the graduate advisor.

I would like to extend my thanks to the former alumni students Dr. Vijay Jupally, Dr. Praneeth Nimmala, Dr. Nuwan Kothalavala, Dr. Chanka Kumara, Asantha Dhramaratne, Dave Crasto and Shevanuja Theivendran for their advice and support. Lastly, I acknowledge the collegial support from my fellow doctoral students, Tanya Jones, Naga Arjun Sakthivel, Vignesh Raja Ganesh, and Senthil Kumar Eswaramoorthy.

A very special gratitude goes out to Dr. Buddhika Dassanayake for his kind guidance and support by steering me in the right direction whenever he thought I needed it. Nevertheless, I would

like to express my thanks to a dear friend, Sampath Bandara, who supported me throughout this venture.

Finally, yet importantly, I would like to express my heartfelt gratitude to my loving parents, and Asoka Sanjeewani for being there with me in every step of the way. This work would not have been completed without their immense support and encouragement. I would also like to record my sincere gratitude to my two brothers for their love, support and encouragement.

TABLE OF CONTENTS

LIST OF FIGURES

LIST OF SCHEMES AND TABLES

SCHEMES

TABLES

CHAPTER 1

INTRODUCTION TO GOLDNANOMOLECULES

1. Introduction

1.1 Nanoparticles and Nanomolecules

Metal nanoparticles (NPs) less than 100 nm length scale show properties that are significantly different to that of bulk metal. In the 18th century, gold colloids were first recognized by Michael Faraday and Thomas Graham.[1-3] Many colloid gold nanoparticles are not stable and usually decompose, therefore research since then and up to now has looked at focusing reducing the size of the colloids into nanoparticles. Properties and applications of these nanoparticles are mainly dependent on their size and shape.[4-6] As the size of NP reduces the electron motion is confined and results in unique optical and electronic properties. Especially when the size of the gold NP is less than 2 nm, unusual atomic structures and physicochemical properties can be observed.[6-7] NPs under 2 nm size range are molecular-like with atomic monodispersity and precise number of metal atoms and ligands that can be defined as nanomolecules (NMs).[7-8] In contrast to nanoparticles with poorly defined size, shape and atomic variation of 1000 atoms, these highly stable NMs have discrete chemical formula such as $Au_{25}(SR)_{18}$, $Au_{38}(SR)_{24}$, $Au_{102}(SR)_{44}$, $Au_{137}(SR)_{56}$ and $Au_{144}(SR)_{60}$, where SR is an organo-thiolate ligand bonded to gold surface via gold-sulfur covalent bond (scheme 1.1). These NMs have their own unique optical, electronic and

physicochemical properties that are governed by the atomic structure.[9-10] Whetten's group found that the thiolate-protected gold nanoclusters had the trend to form a series of discrete sizes.[5] The mixture of clusters was separated by solvent fractionation, and each fraction was characterized by laser desorption ionization mass spectrometry (LDI-MS).

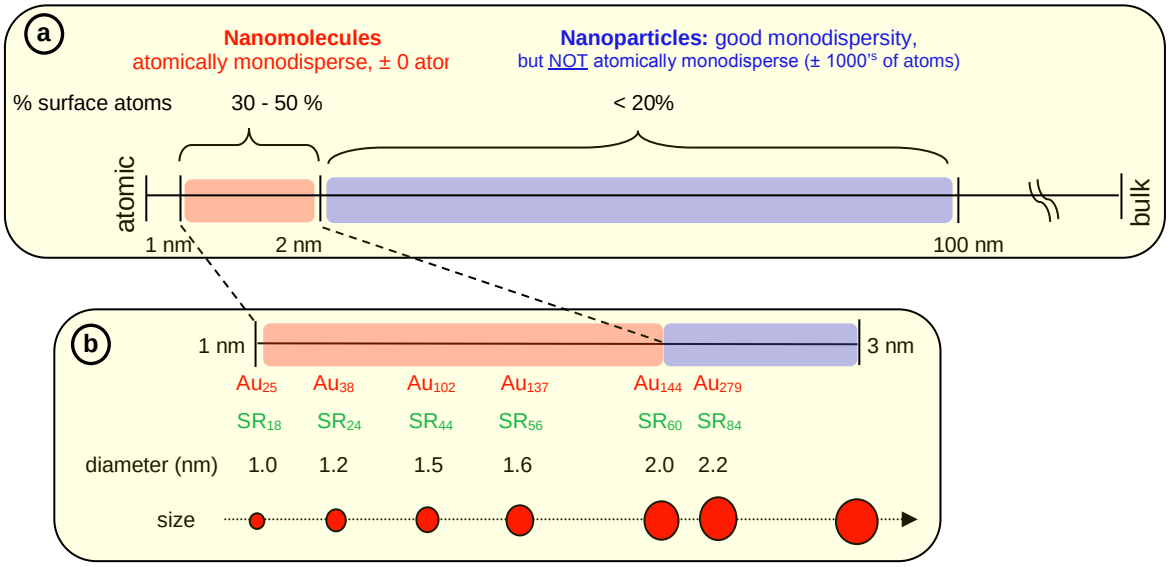

Scheme 1.1 (a) Nanoparticles with diameter of 2-00 nm range lacks atomic monodispersity, whereas nanomolecules with diameter <2 nm are molecular-like in nature and have atomic precision. (b) Series of widely studied nanomolecules with size-dependent properties. Figure reprinted with permission from ref. 53.

1.2 Thiolate Protected Gold Nanomolecules

Organo-thiols are extensively used in the synthesis of gold NMs due to extra stability of the Au-S covalent bond[11] compared to Au-P bond in phosphine-protected nanoclusters.[12-14] In addition to stability and surface properties, rest of the hydrocarbon chain of the thiolate ligand provides barriers such as electrostatic and steric repulsions between particles to prevent them from aggregation into a precipitate.[10] Hydrocarbon chain can also be modified to have specifically and selectively designed certain functions based on their applications such as controlling solubility and

delivering therapeutic agents to targeted cancer cells in bio-nanotechnology.[15-16] In addition to thiolates, different types of organic compounds have been used as capping ligands to protect gold NPs, such as phosphine, selenolate, carbonyl, alkyne, DNA, protein cages, and so on.

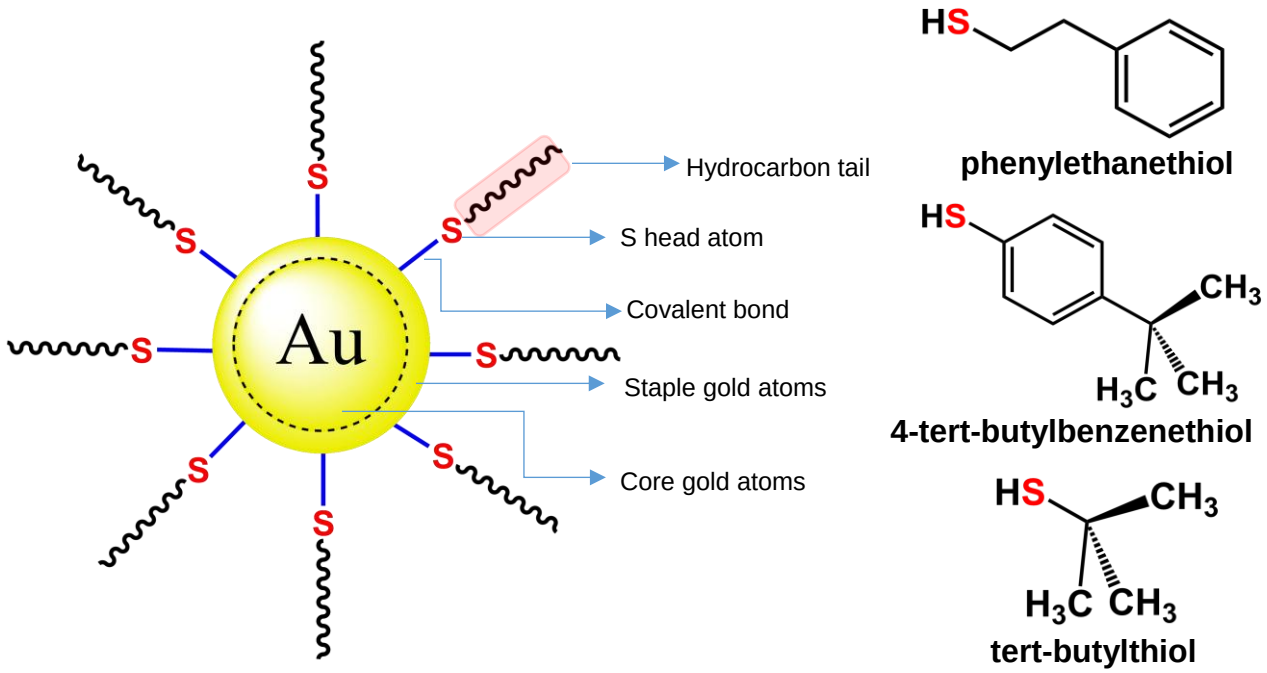

Figure 1.1. Illustration of composition of thiolate protected gold nanomolecules. Most widely studied three ligand structures are shown on the right, namely phenylethanethiol, 4-tert-butylbenzenthiol and tert-butylthiol.

Thiolate protected AuNMs and AuNPs are comprised of three main structural components: inner metallic-core, metal-thiolate interfaces composed of staple motifs and outermost thiolate surfaces that governs characteristics such as solubility. The surface of these AuNMs is surrounded by a variety of staple motifs. The staple gold atoms are the outer most layer of the core gold atoms or the metal-thiol interface that governs surface characteristics unique to the NM. The surface is

typically composed of staple motifs[10, 17] such as bridging units[18] (Au-SR) monomeric staples (SR-Au-SR), dimeric staples[19] (SR-Au-SR-Au-SR) and trimeric staples[20] (SR-Au-SR-Au-SR-Au-SR). The innermost layer is composed of one or more Au core shell.[21]

1.3 Alloy Nanomolecules

Properties of gold thiolate NMs can be greatly extended and enhanced by incorporating other metals into the structure.[22-24] The stability, chemical and physical properties of gold-alloy NMs can be achieved by tuning the atomic structure and composition by doping with elements such as Cu, Ag, Pt, Pd.[24-29] Alloys often display properties that are distinct from monometallic nanoparticles. Surface and structural properties of bimetallic nanoalloys can be quite different from their pure monometallic NMs of the same size and can give rise to interesting catalytic and optical properties.[28]

1.4 Experimental approach

Tailoring the size and shape of NPs has been explored for decades. The development of smaller, more precise, thiolate protected gold NMs was brought about by the Brust and Schriffin method and modified variation of this method.[30] This method allows to achieve the most important criterion; high monodispersity and high stability. This has enabled the field of ultra-small nanomolecules to evolve allowing researchers to have an ultimate control over NPs to obtain atomically precise nanomolecules and manipulate the material.[21, 31-32] These ultra-small (1-2 nm) Au NMs have several interesting properties such as their stability, dispersion in solution, ability to remain stable in a dried powder state for years, and unique optical properties that are highly applicable in catalysis and medical technology. Thiolate-protected gold nanoparticles have evolved from polydisperse NPs to monodisperse and finally to atomically precise nanomolecules.[31, 33]

1.4.1 Synthesis of Thiolate Protected Gold Nanomolecules

In contrast to the unstable NPs obtained from gas phase synthesis the nanoclusters synthesized from solution phase have relatively higher stability due to the surface passivation by protecting ligands. The two-phase Brust-Schiffrin method that utilized water and organic (toluene) solvents and modified one-phase methods utilizing an organic phase (toluene, tetrahydrofuran) are most commonly employed for the synthesis of thiolate protected Au NMs due to their simplicity and versatility. The core size, structure and the composition of NMs can be manipulated by tuning the reaction conditions, such as the gold to thiol ratio, relative strength of the reducing agent, type of solvent, reaction temperature, and most importantly type of the thiolate ligand.

In general, two-phase Brust-Schiffrin experimental approach involves initially dissolving gold salt (tetra-chlorauric acid, $HAuCl_4 \bullet 3H_2O$) in distilled water (reaction 1.1) and phase transferring into organic toluene phase using tetraocylactylammonium bromide (TOABr).[30, 34]

$$HAuCl_4(aq) \longrightarrow H^+(aq) + [AuC1_4]^-(aq) \qquad (1.1)$$

$$[AuC1_4]^-(aq) + [N(C_8H_{17})_4]^+ (tol) \longrightarrow [N(C_8H_{17})_4]^+[AuC1_4]^-(tol) \qquad (1.2)$$

Initially, Au^{3+} is reduced to Au^{1+} in the presence of the thiol (RSH) through the following reaction (1.3) and forms the $-(AuSR)_n-$ polymer.[30, 35-36]

$$[AuC1_4]^-(tol) + 3\,[HSR]\,(tol) \longrightarrow -(AuSR)_n-\,(tol) + RS\text{-}SR(tol) + 4Cl^-(aq) \qquad (1.3)$$

Toluene organic phase at this stage thus consisted of TOABr, dialkyl disulfide (RS-SR), $-(AuSR)n-$ polymer, and unreacted $[N(C_8H_{17})_4]^+[AuC1_4]^-$ and excess RSH. Finally, upon addition of sodium borohydride the reduction of Au^{3+} and Au^{1+} to Au^0 takes place by BH_4^- and is considered to occur through the following reactions (1.4 and 1.5).[35-36]

$$-(AuSR)_n\text{-}(tol) + RS\text{-}SR(tol) + HSR\ (tol) + BH_4^-(aq) \longrightarrow Au_x(SR)_y(tol) + B(OH)_3(aq) + H_2(g) \quad (1.4)$$

$$[N(C_8H_{17})_4]^+[AuC1_4]^-(tol) + RS\text{-}SR(tol) + HSR\ (tol) + BH_4^-(aq) \longrightarrow Au_x(SR)_y(tol) + B(OH)_3(aq) + H_2(g)\ [N(C_8H_{17})_4]^+(tol) + 4HCl^-(aq) \quad (1.5)$$

The two-phase Brust-Schiffrin method has also been modified to one-phase where polar solvents, such as tetrahydrofuran (THF)[33, 37] and methanol, are usually used for preparing gold NPs excluding the necessity of phase transfer agent TOABr. In both methods, once a synthesis is complete the product is dried, washed to remove excess thiol and extracted with a suitable solvent. Extracted product can be dispersed in various solvents such as: THF, toluene, and dichloromethane (DCM) and typically NPs have a long shelf life.

The as-obtained product is polydisperse in size and limits its' application as a nanomaterial. In 1999, Prof. Whetten introduced a thermochemical treatment procedure, also well known as "etching" to narrow down the polydispersity.[34] In short, initially obtained polydisperse NP mixture is etched in the presence of excess thiol at elevated temperature (scheme 1.2). This method is widely employed to obtain most robust and thermodynamically highly stable NMs.[38-40]

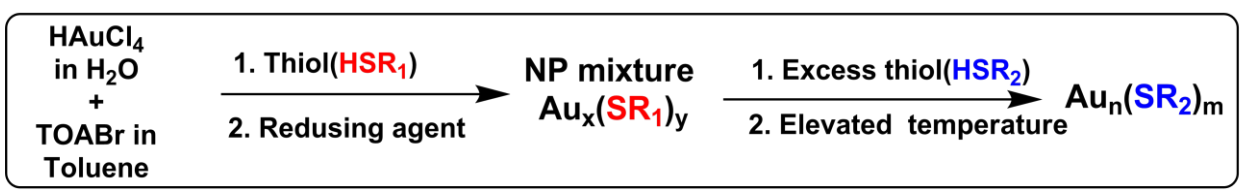

Scheme 1.2. Simplified general synthetic protocol for the synthesis of thiolate protected gold nanomolecules. HSR_1 and HSR_2 represent physicochemically two different thiol ligands. The scheme illustrates the first step to obtain $Au_x(SR_1)_y$ kinetically controlled mixture followed by second etching step to obtain thermodynamically highly stable $Au_n(SR_2)_m$ mixture.

1.4.2 Isolation techniques

Synthesis of atomically precise NPs is of paramount importance for understanding the fundamental science of NPs. Over the past decade, gold nanomolecule synthetic protocols have significantly improved to obtain highly monodisperse, atomically precise NMs. Combined separation techniques, such as etching, solvent fractionation, size exclusion chromatography(SEC) are being widely employed to separate a polydisperse mixture to obtain highly monodisperse atomically precise NMs.[41]

Etching reactions are used to obtain ultra-stable and highly monodisperse robust NMs. Initially synthesized product is reacted with excess desired thiol ligand at elevated temperature

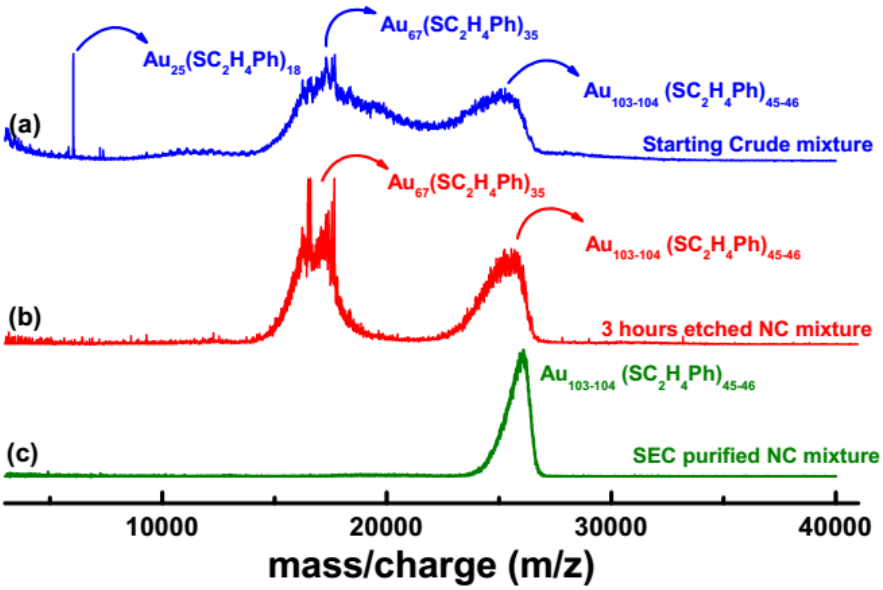

Figure 1.2. MALDI mass spectrum of the (a) starting crude mixture (blue) containing $Au_{25}(SCH_2CH_2Ph)_{18}$, $Au_{67}(SCH_2CH_2Ph)_{35}$ and $Au_{\sim103\text{-}104}(SCH_2CH_2Ph)_{\sim45\text{-}46}$ mixture. (b) This crude was etched with $HSCH_2CH_2Ph$ at 60°C for 3 hours to give the product with the mass spectrum shown in red. The purpose of this 3 hours etch was to obtain a flat baseline between $Au_{\sim67}$ and $Au_{\sim103\text{-}105}$ peaks, so a clean SEC separation can be achieved as shown in the green spectrum. (c) completely separated $Au_{\sim103\text{-}105}$ fraction via SEC.

(scheme 1.2, figure 1.2). Typically, this can be done with solvent or without solvent (neat etching). In this reaction, inherently stable NMs survive the etching reaction and unstable NMs decompose and/or core-size convert to thermodynamically most stable NMs and newly formed ultra-stable NMs remain in as the final product.[38, 42] Figure 1.2 illustrates core-size conversion of a kinetically controlled synthetic mixture of NMs namely, $Au_{25}(SCH_2CH_2Ph)_{18}$, $Au_{67}(SCH_2CH_2Ph)_{35}$, $Au_{103-104}(SCH_2CH_2Ph)_{45-46}$ and unstable NMs in the size range from Au_{67} to $Au_{103-104}$. After the etching process only $Au_{67}(SCH_2CH_2Ph)_{35}$ and $Au_{103-104}(SCH_2CH_2Ph)_{45-46}$ remain in the product. The as-synthesized NMs can be separated using appropriate separation techniques described below.

Solvent fractionation involves utilizing selectivity of certain NMs to dissolve in specific solvents. For instance, $Au_{25}(SCH_2CH_2Ph)_{18}$ is soluble in acetonitrile while other nanomolecules such as $Au_{38}(SCH_2CH_2Ph)_{24}$ and $Au_{144}(SCH_2CH_2Ph)_{60}$ are not soluble in acetonitrile, but soluble in THF and toluene. This difference in solubility can be used to separate Au_{25} from a mixture containing Au_{38} and Au_{144}.

Size exclusion chromatography is the most efficient post-synthetic separation technique available to date. Separation is achieved based on the different sizes of nanoparticles present in the mixture. Styrene divinylbenzene beads (Bio Rad SX1) are used as the stationary phase along with the mobile phase THF stabilized with butylated hydroxytoluene (BHT). The beads in the stationary phase have micro-channels which allow smaller NMs to pass through them where as larger NMs pass around the beads. In this manner, smaller NMs take longer pathlength and take more time to elute while larger NMs elute faster. Thereby earlier fractions from the SEC separation would have relatively high molecular weight NMs and later fractions would have low molecular weight NMs. This method can be further repeated until NMs of interest are completely separated (figure 1.2c

green spectrum). In terms of effectiveness and efficiency of separation, proper loading techniques, loading amount and length of the column are crucial.[38, 43]

In addition to above post-synthetic separation techniques, separation methods such as high-performance liquid chromatography (HPLC), and polyacrylamide gel electrophoresis (PAGE) can be successfully applied for the separation of gold NMs. The separation is mainly based on the difference in solubility, size, and charge state of the NMs.

1.4.3 Characterization techniques

Laser desorption ionization mass spectrometry (LDI-MS) was a revolutionary tool that Prof. Whetten[34] used to analyze the gold nanoclusters. Since then various types of MS techniques have become the general and a paramount tool in determination of metal cluster composition. Later Dass et al.[44] demonstrated that use of trans-2-[3-(4-tert-butylphenyl)-2-methyl-2-propenylidene] malononitrile (abbreviated as DCTB) as the matrix assisted in determining composition almost with no fragmentation of Au nanoclusters in MALDI-TOF mass spectra of $Au_{25}(SCH_2CH_2Ph)_{18}$ clusters. To date many well established, characterization tools are available for the gold NMs and among these tools compositional and structural characterization are utmost important and a must for any newly found NM. For instance, in addition to MALDI-MS molecular composition can be determined from mass spectrometry (electrospray ionization mass spectrometry, ESI-MS),[33, 45-46] whereas structural characterization can be achieved from UV-vis-NIR spectroscopy, fourier transform infrared (FTIR) spectroscopy,[47] and nuclear magnetic resonance (NMR) spectroscopy.[48-49] Ultimately single-crystal X-ray crystallography can be used to determine the total structure of NMs.[10, 18, 20, 50-51] In addition to these methods high resolution transmission electron microscopy (HRTEM)[52-53] is also used in determination of size distribution of NPs. These

molecular characterization tools lead to fundamental understanding of the physical and chemical properties of atomically precise nanoclusters.

1.4.3.1 Mass spectrometry

MALDI-MS is the most convenient and an essential tool in determining the composition of the synthesized NPs. The spectrum is obtained as an ion abundance versus mass to charge (m/z) ratio plot (figure 1.3b). In this method the analyte is detected regardless of the its charge state (positive, negative or neutral) at high laser fluence and provides a quantitative estimation (from peak area) of each analyte in a mixture. In general, Au NP analyte is mixed with the DCTB matrix in a ratio of 1:1000 parts and spotted on the MALDI plate for co-crystallization. Appropriate laser fluence is used to obtain a compositional analysis of the sample. For Au NMs, above the threshold laser fluence induce fragmentation of ligands and Au atoms. Due to this inherent fragmentation

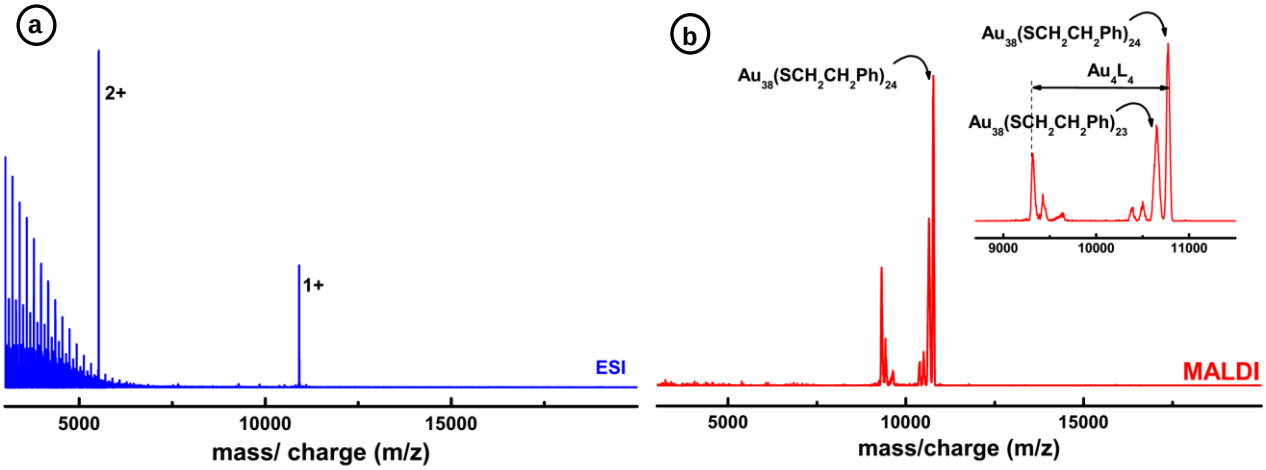

Figure 1.3. (a) Positive ESI mass spectrum from 4,000 to 20,000 m/z mas range showing $Au_{38}(SCH_2CH_2Ph)_{24}$ peaks in the 1+ and 2+ charges states corresponding to $[Au_{38}(SCH_2CH_2Ph)_{24}]Cs^+$ and $[Au_{38}(SCH_2CH_2Ph)_{24}]Cs_2^{2+}$ respectively. Below ~6,000 m/z $CsCH_3COO$ clusters can be observed. (b) MALDI mass spectrum of $Au_{38}(SCH_2CH_2Ph)_{24}$. Inset shows the expansion of the 9,000 to 11,000 m/z region, showing $Au_{38}(SCH_2CH_2Ph)_{24}$, all ligands intact species and fragmented NM at high laser fluence.

observed above the threshold laser fluence for a NM and poor resolution above >10,000 m/z other innovative soft-ionization tools such as ESI-MS are employed for accurate compositional determination of an analyte. This method can detect multiple charge states of a NM and allows the determination of accurate molecular weight of the NM accurately even upto 70 kDa mass range. For example, $Au_{38}(SCH_2CH_2Ph)_{24}$ can be observed in both 2+ and 1+ charge state (figure 1.3a). With recent innovative techniques, ESI-MS allows one to determine inherent charge state of the analyte along with cesium assisted experiments. In this experiment, $Cs^+CH_3COO^-$ is used to impart either positive (with Cs^+ addition) or negative (with CH_3COO^- addition) charge to NMs. In general, the principle behind the experiment is that in abundance of $Cs^+CH_3COO^-$, NM would prefer to be its natural charge state, hence allow one to determine the inherent charge of the NM by investigating the mass spectra.

1.4.3.2 UV-Vis-NIR spectrometry

Gold NMs < 2 nm show molecular-like optical absorption features whereas, NPs above this size range show surface plasmon resonance (SPR) absorption peak centering around 520 nm hence allows one to estimate the size distribution of the as-synthesized thiolate protected gold nanomaterials (figure 1.4). Gold NMs which are < 2nm, have a smaller HOMO-LUMO gap (HOMO-highest occupied molecular orbital, LUMO-lowest unoccupied molecular orbital) that gives rise to distinct UV-Vis-NIR absorption peak. Whereas larger Au NPs (>2 nm) have collective oscillation of the conduction band electrons in response to the incident radiation which gives rise to broad SPR peak.

Fine electronic transitions of Au NMs can be observed in temperature dependent optical studies. In these experiments, the sample dissolved in a suitable solvent (typically 1-methyltetrahydrofuran) is been cooled using a cryostat to liquid nitrogen temperature of 77 K. The

principle behind this method is that, at low temperature vibrational and rotational transitions are negligible and only electronic transitions due to incident radiation is being facilitated (figure 1.4a).

1.4.3.3 Single crystal x-ray crystallography

Single crystal x-ray diffraction (scXRD) studies allow the determination of overall atomic structures of AuNMs and require availability of a single crystal.[10] Typically obtaining single crystals of AuNMs is very rare and a challenging process which includes: growing crystals generally through vapor diffusion, crystal screening, data collection, refinement, and structure fitting. Figure 1.5 shows the complete crystal structure of $Au_{38}(SCH_2CH_2Ph)_{24}$ NMs and its assembly.

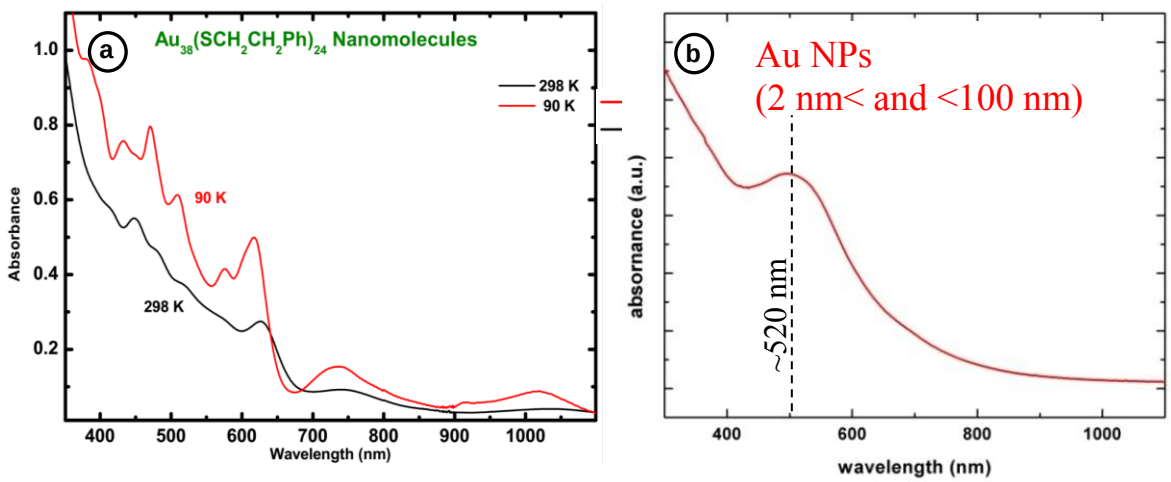

Figure 1.4. UV-vis-NIR absorption spectra of (a) $Au_{38}(SCH_2CH_2Ph)_{24}$ nanomolecules at room temperature (298 K) vs at 90 K. The absorption spectra show molecular-like multiple absorption peaks. (b) Typical UV-vis-NIR absorption spectrum of gold nanoparticles in the size range from 2–100 nm showing a broad surface plasmon resonance band centering around ~520 nm.

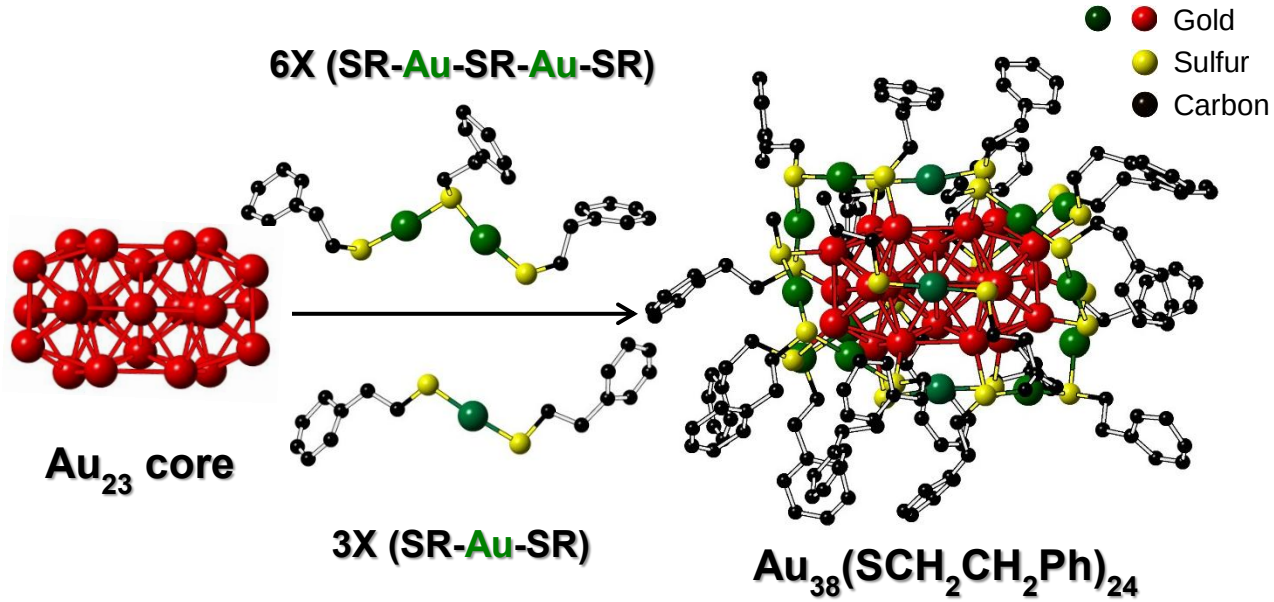

Figure 1.5. Crystallographically deduced complete crystal structure of $Au_{38}(SCH_2CH_2Ph)_{24}$ nanomolecule is shown on the right. Structural assembly includes Au_{23} bi-icosahedron core, six dimeric staples and three monomeric stables. For simplicity hydrogen atom on the ligands are avoided.

CHAPTER 2

AROMATIC THIOL-LIGAND EFFECT ON $Au_{102}(SPh)_{44}$ FORMATION

Part of the text and figures in this chapter are extracted from the following publication: Rambukwella, M.; Sementa, L.; Barcaro, G.; Fortunelli, A.; Dass, A. *J. Phys. Chem. C* **2015**, 119, 25077-25084

2.1 Abstract

Characterization of p-mercaptobenzoic acid (p-MBA) protected $Au_{102}(p\text{-}MBA)_{44}$ nanomolecules has been so far limited by its water-soluble ligand system. In this work we report the first synthesis and isolation of thiolate protected organosoluble $Au_{102}(SPh\text{-}X)_{44}$ nanomolecules via one-phase synthesis. Monodispersity of the nanomolecules was confirmed from matrix-assisted laser desorption ionization mass spectrometry (MALDI-MS), and composition was determined from high-resolution electrospray ionization mass spectrometry (ESI-MS). For the first time we report the electrochemical behavior and temperature-dependent optical spectra of $Au_{102}(SPh)_{44}$. Theoretical simulations on the titled nanomolecules fully validate experimental data and demonstrate the role of electronic conjugation on optical properties.

Author Contributions

Milan Rambukwella synthesized $Au_{102}(SPh)_{44}$ nanomolecules, conducted mass spectrometric, UV-Vis-NIR absorption, electrochemical experiments and wrote the manuscript.

Alessandro Fortunelli, Luca Sementa, and Giovanni Barcaro conducted computational studies. Amala Dass assisted in experimental design, data analysis, and structure of the manuscript. All the authors made substantial, direct and intellectual contribution to the work in the manuscript preparation.

2.2 Introduction

Gold Nanomolecules[5] are ultra-small gold nanoparticles (< 3 nm in diameter) with a distinct number of gold atoms protected by specific number of thiolate ligands. These have attracted extensive interest because of their size-dependent optical,[54] electrochemical,[6] chiral[55] and catalytic[56-57] properties. The field of research on nanomolecules expanded and grew significantly upon the discovery of the X-ray crystal structure of $Au_{102}(SC_6H_4COOH)_{44}$ followed by the structural determination of $Au_{25}(SCH_2CH_2Ph)_{18}$.[50, 58-59] The X-ray structure of $Au_{102}(SC_6H_4COOH)_{44}$ revealed the nature of the Au-S interface, which may be described as an Au_{23}(p-MBA)$_{44}$ layer protecting a central Au_{79} core. In addition to the 58 electron shell closing,[60] the gold-sulfur bonding and the interactions between p-MBA molecules were noted to account for its stability. The crystal structure of larger Au_{133}(SPh-*t*Bu)$_{52}$ has been reported.[61-62] The geometrical shapes -icosahedral,[50, 61] Marks-dehedral[58] and cuboctahedral[18, 63]- of the inner metal atom cores and the 2/3 scaling law between the number of Au atoms and the number of ligands, strongly point to geometric stability.[7] This mirrors the Euclidean surface rule, where a 2/3 scaling is observed in the surface area to volume ration in platonic solids, as incompressible objects tend to form with a minimum surface area.[64]

Despite the great interest on the 102-atom species, its synthesis and characterization have been limited to one ligand, p-MBA and have been studied exclusively by the original group of

authors of the 2007 crystal structure[58] report. This is due in part to the challenges in the water soluble nanomolecule systems,[65] as p-mecaptobenzoic acid (p-MBA) ligand was used. The synthesis,[66] purification,[67-70] and mass spectrometry of water soluble nanomolecules is challenging, even though some progress has been made, and limits the wide adoption and analysis of this species among experimental chemists.

Kornberg et. al. first reported the crystal structure,[58] followed by the synthesis, characterization,[71] and optical spectroscopy[72] of $Au_{102}(SC_6H_4COOH)_{44}$. The basis for ligand exchange on the 102-atom species was also reported.[73] However, no other research team has accomplished the synthesis of this interesting $Au_{102}(SR)_{44}$ species, either with p-MBA or any organo-soluble ligand, to date. The lack of organo-soluble $Au_{102}(SPhX)_{44}$ species has hindered the investigation of their redox behavior and low temperature optical spectroscopy.

Extensive theoretical analysis has been performed on $Au_{102}(SC_6H_4COOH)_{44}$ due the availability of the X-ray crystal structure. The stability of 102:44 species has been attributed to the 58 free electrons that are associated with a superatom electronic shell closure, with stable numbers corresponding to noble gas electronic configurations.[60] *Ab initio* studies on a homologous $Au_{102}(SCH_3)_{44}$ compound, including a comparison with $Au_{102}(SCH_3)_{42}$ and $Au_{104}(SCH_3)_{46}$ putative species, had previously been conducted by Zeng's group[74] and it was suggested that electronic shell closing of effective 58 accounts in part for the high stability of Au_{102}(p-MBA)$_{44}$. Density functional theory (DFT) calculations has being effectively used to understand properties of theses nanomolecules, such as electronic and vibrational signature illustrating structural, electronic and bonding properties.[72, 75-76] Choi and co-workers has shown that, exceptional stability of $Au_{102}(SR)_{44}$ can be attributed to three factors: effective staple-motif formation, high stability against dissociation, and a large HOMO-LUMO gap.[77] In another study the thermodynamic

stability of $Au_{102}(SR)_{44}$ was investigated as a function of the ligand group R and it was found that this quantity closely follows the strength of the Au-SR bond thus suggesting a lesser importance of shell-closure and electronic conjugation effects.[78] Other work also confirmed that local chemical bonding and surface coverage effects determine the energetics and stability of gold nanomolecule systems.[79]

The phenylethanethiol, SCH_2CH_2Ph, ligand introduced by Murray,[80] is the most commonly used ligand to prepare organosoluble nanomolecules. In a previous work, using high resolution electrospray ionization (ESI) mass spectrometry, we showed that a synthesis using phenylethanethiol resulted in the formation of $Au_{103}(SR)_{45}$, $Au_{104}(SR)_{45}$, $Au_{104}(SR)_{46}$, and $Au_{105}(SR)_{46}$ – i.e., a series of clusters, not a single molecular species.[42] Unexpectedly, $Au_{102}(SCH_2CH_2Ph)_{44}$ nanomolecules were *not found* in the synthetic mixture. Our hypothesis was that the use of non-aromatic ligands was the cause of this unexpected absence of Au_{102} species. p-MBA is aromatic, and this particular 103, 104, 105-Au atom size distribution of the series could be due to the non-aromatic ligand nature of the $–SCH_2CH_2Ph$ ligand. Use of other organo-soluble, non-aromatic ligands like $–SC_6H_{13}$, $-SC_{12}H_{25}$ also do not show Au_{102} species either, sufficiently demonstrating the generality of the lack of 102-Au atom species in the case of aliphatic and phenylethanethiolate ligands. The synthesis of $Au_{99}(SPh)_{42}$ was also reported both starting from $Au_{144}(SCH_2CH_2Ph)_{60}$ and from a direct synthesis.[81-82]

Here, we address the question whether it is possible to execute a systematically size-controlled synthesis and subsequently achieve a thorough characterization of an organo-soluble $Au_{102}(SR)_{44}$ species with high monodispersivity, using an aromatic monolayer protecting ligand. We thus successfully employed a two-step synthetic protocol to synthesize an organo-soluble $Au_{102}(SPh)_{44}$ nanomolecule. In the first step, we synthesized a precursor mixture containing the

$Au_{\sim 103\text{-}105}(SCH_2CH_2Ph)_{\sim 45,46}$ as reported earlier. This was subjected to two successive thermochemical etching steps, so core-size conversion and a complete ligand exchange occurred, thus forming for the first time, *an organo-soluble all-aromatic,* 102-Au atom species, $Au_{102}(SPh)_{44}$. The generality and reproducibility of the synthetic procedure was demonstrated by the use of a second ligand, -SPh-CH_3, to form $Au_{102}(SC_6H_4\text{-}CH_3)_{44}$. High resolution ESI-MS measurements show conclusive evidence for the formation of a single sized molecular species, $Au_{102}(SPh)_{44}$. The organo-soluble nature of the Au_{102} facilitated electrochemical and temperature dependent optical studies. For the first time, we report the electrochemical gap, the redox behavior and the optical spectrum of the Au_{102} species. Theoretical analysis of the energetics and the good agreement between measured and simulated optical spectrum confirms the experimental assignment, further demonstrating minor inter-ligand interactions (steric and/or dispersive) and a significant role of electronic conjugation effects on the optical properties.

2.3 Method

2.3.1 Materials

Sodium borohydride (Acros, 99%), thiophenol (Acros, 99%), phenylethanemercaptan, (Sigma-Aldrich), and trans-2-[3[(4-tertbutyl-phenyl)-2-methyl-2-propenylidene] malononitrile (DCTB matrix) (Fluka≥99%) were purchased and used as received. HPLC grade solvents such as tetrahydrofuran, toluene, methanol, butylated hydroxytoluene stabilized tetrahydrofuran and acetonitrile were obtained from Fisher Scientific.

2.3.2 Synthesis of $Au_{102}(SPh)_{44}$

The synthesis of $Au_{102}(SPh)_{44}$ nanomolecules was performed in three main steps (see Schemes 2.1 and 2.2) involving:[49] (i) the initial one phase synthesis of crude nanomolecule mixture

(see Fig. S1a in the Appendix A), followed by (ii) mild thermochemical etching step of the crude – containing a mixture dominated by Au_{67} and $Au_{103-105}$ – to narrow down the size distribution, to obtain a flat baseline between Au_{67} and $Au_{103-105}$ and remove other meta-stable nanomolecules (see Fig. S1b in the Appendix A). Then the $Au_{\sim 103-105}$ mixture was separated, via size exclusive chromatography, SEC (see Fig. S1c in the Appendix A). Finally, (iii) the two successive thermochemical etching were performed on $Au_{\sim 103-105}(SCH_2CH_2Ph)_{\sim 45-46}$ mixture in the presence of excess thiophenol to complete the core-size conversion and ligand exchange to form $Au_{102}(SPh)_{44}$ species (See Scheme 2.2, Fig. 2.1, Fig. S3 in the Appendix A).

Step 1; First, $HAuCl_4.3H_2O$ (0.300 g/0.762 mmol) was added to a 250 mL round bottom flask followed by the addition of the HPLC grade tetrahydrofuran, THF (20 mL). After stirring for 5 min at 500 rpm, phenylethanemercaptan (0.613 mL, 4.571 mmol) was added and continually stirred for 30 min at room temperature (gold to thiol molar ratio was set to 1:6). An aqueous solution of $NaBH_4$ (7.620 mmol, 5 mL) cooled in an ice bath, was added instantaneously to the reaction mixture under vigorous stirring. After 5 min., the reaction was ceased, and solvent was removed with rotary evaporation. The product was washed with methanol (4x) to remove the excess thiol and the residual mixture was extracted with toluene.

Step 2; The product from step 1 was dissolved in toluene (5 μL/1 mg of crude) and subjected to thermochemical treatment for 3 hours at 60 °C with excess phenylethanemercaptan (2 μL/1 mg of crude). The product was subject to SEC and $Au_{\sim 103-105}(SCH_2\ CH_2Ph)_{\sim 45-46}$ was separated (see Fig. S2 in the Appendix A).

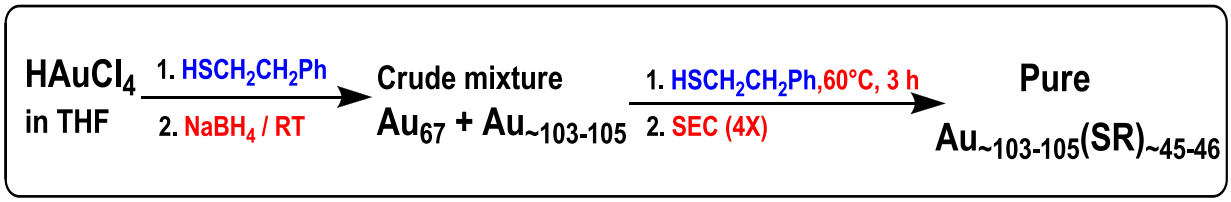

Scheme 2.1. Synthetic procedure for the precursor $Au_{\sim 103\text{-}105}(SCH_2CH_2Ph)_{\sim 45\text{-}46}$: One-phase synthetic protocol for starting nanocluster mixture containing Au_{67}, $Au_{\sim 103\text{-}105}$ and SEC separation to isolate $Au_{\sim 103\text{-}105}$ precursor.

Step 3; Finally, $Au_{103\text{-}105}$ mixture was subjected to a thermochemical etching step in the presence of excess thiophenol (HSPh) at 80°C for 15 min. The product attained after this step is then subjected to another second thermochemical treatment under the same conditions for an additional 15 mins, *vide infra*. (see Scheme 2.2, Fig. 2.1) The final product was washed with methanol several times and was extracted with toluene.

2.3.3 Characterization and Instrumentation

Matrix assisted laser desorption time-of-flight (MALDI-TOF) mass spectrometer was used to acquire mass spectra with DCTB matrix[83] on a Voyager DE PRO mass spectrometer. Compositional analysis was performed with electrospray ionization mass spectra (ESI-MS), collected from Waters Synapt HDMS with THF as the solvent and ESI-MS mass calibration was performed with $Au_{144}(SCH_2CH_2Ph)_{60}$ nanomolecules, see Fig S6. Temperature dependent UV-vis-NIR absorption measurements were collected with UV-vis-NIR Cary 5000 and JANIS VNF-100 low temperature cryostat using 1-methyltetrahydrofuran as the solvent and Lakeshore Cyotronics temperature controller was used for temperature-dependent absorption measurements. Electrochemical measurement data were recorded on CHI 620 instrument using $BTPPATBF_{20}$ as supporting electrolyte under nitrogen atmosphere.

2.4 First Synthesis of Organic Soluble $Au_{102}(SPh)_{44}$

Thiophenolate protected $Au_{102}(SPh)_{44}$ nanomolecules were prepared from phenylethanethiolate protected mixture, $Au_{\sim 103\text{-}105}(SCH_2CH_2Ph)_{\sim 45\text{-}46}$.[42] This 103-105 Au-atom crude mixture was prepared using one-phase synthesis, which forms only when using THF as solvent during synthesis, as reported earlier.[49] The first thermochemical step was carefully regulated to yield a mixture[49] dominated by Au_{67} and $Au_{\sim 103\text{-}105}$ nanomolecules (Fig. S1a in the Appendix A) and the later steps were employed to core-size convert $Au_{\sim 103\text{-}105}$ to Au_{102} and to achieve complete ligand exchange with the aromatic ligand, thiophenol (Fig. 2.1). The precursor mixture containing $Au_{103}(SCH_2CH_2Ph)_{45}$, $Au_{104}(SCH_2CH_2Ph)_{45}$, $Au_{104}(SCH_2CH_2Ph)_{46}$, $Au_{105}(SCH_2CH_2Ph)_{46}$ (abbreviated as $Au_{\sim 103\text{-}105}(SCH_2CH_2Ph)_{\sim 44\text{-}46}$, see Fig. S2 in the Appendix A) undergoes fast ligand exchange in 15 mins and core-size conversion reactions upon thermochemical treatment with excess thiophenol to form $Au_{102}(SCH_2CH_2Ph)_{44\text{-}x}(SPh)_x$, where $x_{average} = 41$, and ranges from 35 to 43, See Fig. 2.1, 15 min spectra. Complete ligand exchange is achieved upon introducing a second successive thermochemical treatment on the purified product (Scheme 2.2) to form $Au_{102}(SPh)_{44}$, see Fig. 2.1, 15min re-etch spectra. Both the etching reactions were conducted at 80 °C for 15 minutes. The etching conditions including time and temperature plays a significant role in the formation of $Au_{102}(SPh)_{44}$ and if the reaction medium is subjected to a prolonged re-etching step it would yield various sized clusters smaller than Au_{102}, but no special preference was observed for the formation of $Au_{99}(SPh)_{42}$.[82, 84] (Fig. S5). The thiophenol ligands (HSPh) leads to the solubility of $Au_{102}(SPh)_{44}$ nanomolecules in organic solvents facilitating high resolution ESI mass spectrometry, electrochemistry and temperature dependent optical spectroscopy.

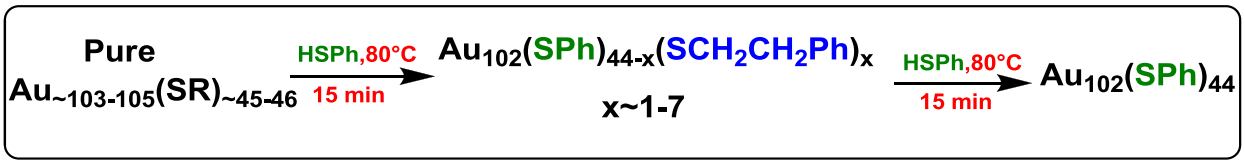

Scheme 2.2. Synthetic procedure for monodisperse $Au_{102}(SPh)_{44}$. The first thermochemical reaction yields partially exchanged $Au_{102}(SPh)_{44-x}(SCH_2CH_2Ph)_x$, where x is < 5.

2.5 Mass Spectrometry and Optical Spectroscopic Characterization

2.5.1 Mass Spectrometry

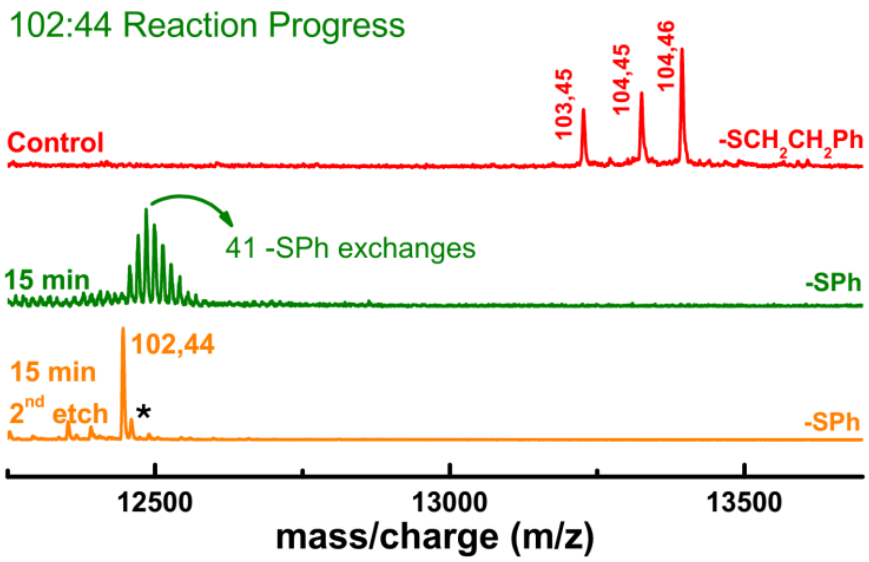

Figure 2.1. ESI mass spectra illustrating the partial and rapid ligand exchange of $Au_{\sim103-105}(SCH_2CH_2Ph)_{\sim45-46}$ in the initial thermochemical etching step followed by core-size conversion and completion of exchange to $Au_{102}(SPh)_{44}$. All species are at +2 charge states and the peak marked by asterisk depicts $Au_{102}(SPh)_{44-x}(SCH_2CH_2Ph)_x$, where x is 1.

In fig. 2.2, the MALDI mass spectrum shows signals corresponding to singly charged and doubly charged molecular ions at ~24 kDa and ~12 kDa respectively. The MALDI mass spectrum is broad due to laser induced fragmentation occurring during ionization and the lower resolution of the instrument at this mass range. But the MALDI data shows the *purity* of the sample indicating the absence of larger or smaller mass impurities. Electrospray ionization (ESI) resulting in soft ionization giving multiply charged, fragment-free, molecular ion signals with higher resolution. In the ESI mass spectrum 12,443.7 m/z and 8,295.5 m/z signals corresponds to doubly charged and triply charged ions of the $Au_{102}(SPh)_{44}$ nanomolecules respectively. Theoretical values for 2+ and 3+ ions are 12,447.5 m/z and 8,298.7 m/z with a mass error of 305 ppm and 385 ppm respectively.

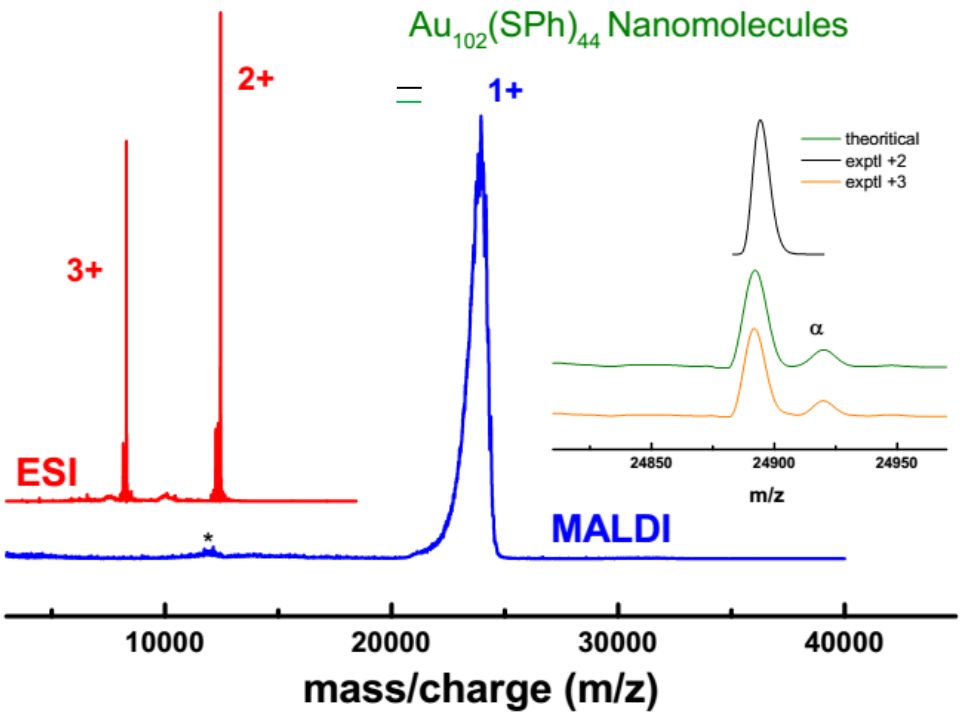

Figure 2.2. ESI mass spectra (red) and MALDI mass spectra (blue) of $Au_{102}(SPh)_{44}$ where peak marked by asterisk on the MALDI depicts +2 charge state of the analyte. Expand spectra illustrate the molecular ion of the species in comparison to the theoretically calculated molecular species where, α depicts $Au_{102}(SPh)_{43}(SC_2H_4Ph)_1$.

2.5.1.1 Determination of Composition

The synthesis of Au_{102} species was also attempted using 4-methyl thiophenol, $HSPhCH_3$. The Au_{102} species synthesized with two different ligands, thiophenol (-SPh = 109 Da) and 4-methyl thiophenol (-$SPhCH_3$ = 123 Da), highlights the reproducibility and generality of the synthesis. Figure 2.3 shows the ESI mass spectrum of Au_{102} species with the 2+ and 3+ charge states with –SPh and –$SPhCH_3$ (also see Fig S4, Fig. S7). Use of a second ligand, $HSPhCH_3$ and its mass spectrometric data, combined with that of thiophenol, HSPh facilitates the determination of the number of ligands and the compositions assignment of the formula of the type, $Au_m(SR)_n$ as shown in the figure (Fig.2.3). Calculated mass difference, Δm of the 2+ charge species is 308 Da and Δm of the 3+ species is 205 Da. The number of ligands calculated independently using these two charge state species is 44(see Fig. S7 for expanded spectra of 2+ charge state).

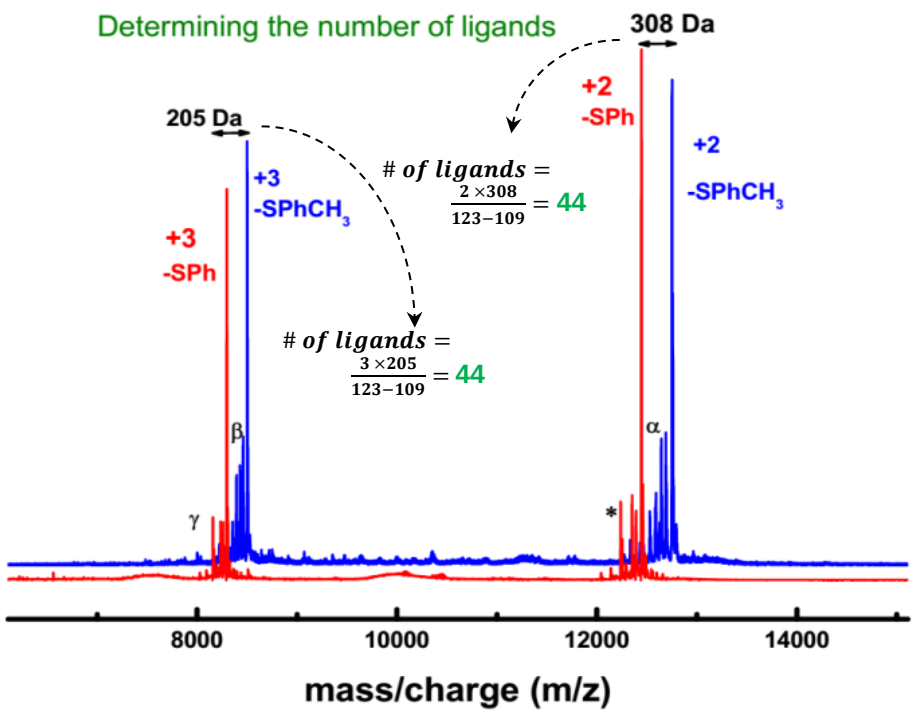

Figure 2.3. ESI mass spectra of +2 charge state of the Au_{102} species with thiophenol (red) and p-toluenethiophenol (blue) ligands. The ligand count was determined to be 44, based on the mass difference between $Au_{102}(SC_6H_4CH_3)_x$ and $Au_{102}(SPh)_y$, assuming a constant number of 102-Au atoms.

2.5.1.2 Investigation of Conversion of $Au_{\sim 103\text{-}105}(SCH_2CH_2Ph)_{\sim 45\text{-}46}$ to $Au_{102}(SPhX)_{44}$

The conversion of $Au_{\sim 103\text{-}104}$ species to $Au_{102}(SR)_{44}$ was studied at *room temperature* allowing us to monitor the ligand exchange and core-size conversion reactions with time. At room temperature, the reactions occur at a slower rate. At room temperature, the reactions occur at a slower rate. Fig. 2.4 shows that in 5 mins the 103,104-Au atom species undergoes ligand exchange with thiophenol resulting in 2 to three envelope of peaks The 2 hour sample shows both the 103-104 Au atom species and the 102-species, suggestions that a definite core-size conversion[85] occurs during this time frame. In particularly, we observed that simultaneous core-size conversion and ligand exchange of $Au_{104}(SPh)_{35}(SCH_2CH_2Ph)_{11}$ species (averaged) to $Au_{102}(SPh)_{38}(SCH_2CH_2Ph)_6$ species (averaged) is taking place in the 2 hour sample. In the 10 hour sample, all the 103-105 species has converted to the Au_{102} species.

2.5.1.3 The case of $Au_{102}(SPh)_{44}$ and the relevance to previous studies

It must be pointed out that the data presented herein is of high enough resolution to conclusively make an assignment of $Au_{102}(SPh)_{44}$; that is the possibility of other species with ±1 Au atom or ligands variation are clearly excluded. In addition, we point out the earlier report[71] though performed in a careful and meticulous manner does present a mass spectrum with high enough resolution to support an $Au_{102}(SR)_{44}$ composition. A directly comparison with the earlier

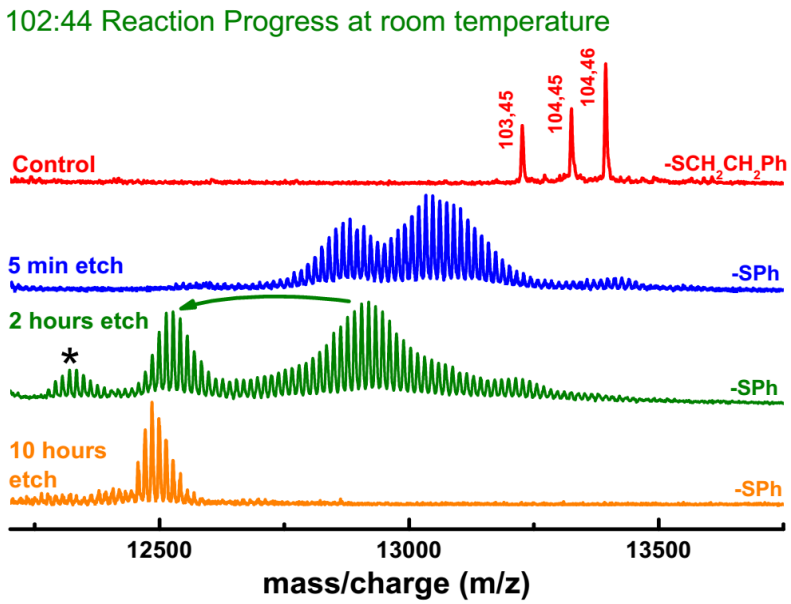

Figure 2.4. Core-size conversion of $Au_{\sim 103\text{-}104}$ to Au_{102}. Reaction progress at room temperature showing gradual core-size conversion of the $Au_{\sim 103\text{-}104}$ species to Au_{102} species (green spectra) after 2 hours of etching at room temperature with simultaneous ligand exchange and progressive ligand shell reduction from 45-46 to 44(species having 2+ charge state is shown). Peaks marked by asterisk shows metastable species that degrades as the etching progress.

enough resolution to support an $Au_{102}(SR)_{44}$ composition. A directly comparison with the earlier spectra with the data in the current manuscript in the same mass range (see Fig. S8 top and middle spectra) shows the differences in the resolution and why the data presented here is the first-time mass spectrometry evidence for the composition, $Au_{102}(SR)_{44}$. The resolution of the ESI data presented here is sufficient to clearly distinguish the variation of ±1 Au atom or ligands (see Fig. S8 bottom spectra) and all possibilities except for $Au_{102}(SR)_{44}$ are eliminated.

The structure and stability of the $Au_{102}(SPh)_{44}$ compound was investigated theoretically. Starting from the experimentally determined crystal geometry[58] of $Au_{102}(SPhCOOH)_{44}$, the COOH groups were replaced by H atoms, and AIMD simulations at 900 K were performed for a time span

of 1 psec. Then, starting from cluster coordinates averaged over this AIMD run, a local structure optimization was performed, thus producing the cluster geometry pictorially shown in Fig. S10 in the Appendix A, in which also the full cluster Cartesian coordinates are reported. The same procedure was applied to the $Au_{102}(SPhCOOH)_{44}$ parent compound and its locally optimized geometry is also shown in Appendix A, Fig. S10. Replacing the COOH substituents with H does not qualitatively alter the main structural features of these nanomolecules.

One interesting question concern rationalizing the experimentally observed formation or absence of $Au_{102}(SR)_{44}$ species as a function of the ligand group R. Previous theoretical work has shown that no peculiar thermodynamic stability is associated with the use of the R = Ph-COOH ligands. Indeed, the formation energy of $Au_{102}(SCH_3)_{44}$ species is identical to that of $Au_{102}(SPhCOOH)_{44}$ (see Figure 2 in Ref. [78]). This however might be due to a compensation between stabilizing electronic conjugation effects and geometric steric repulsion. To complement this previous analysis, we have thus quantitatively estimated the interaction among the R groups, to ascertain whether there is a significant steric hindrance or attraction, employing to this purpose a variant of a recently proposed energy decomposition method.[86] Starting from the $Au_{102}(SPh)_{44}$ optimized geometry, we have erased the Au atoms and replaced the SH groups by H atoms, whose bond distance from the phenyl groups was optimized while keeping the "crown" of Ph ligands frozen. We have then calculated the energy difference between the so-modified interacting ligands and the same ligands separated at infinite distance (frozen in their interacting geometries). This difference turned out to be negative (i.e., the ligand-ligand interaction attractive) by 0.56 eV. The negative value excludes any significant steric repulsion among the ligands. The minor attraction is simply due to a DFT/PBE π-π or T-stacking among phenyl rings,[87] as can be visually seen in Fig. S10 in the Appendix A. This figure also shows that the -SPh (or –SPhCOOH) ligands have enough

geometric space (no significant steric repulsion). The reasons for the successful formation of $Au_{102}(SR)_{44}$ compound is then probably associated with kinetic rather than thermodynamic effects.[73]

To shed further light on this issue, the effect of the ligand on Au_{102} core formation was studied by reacting the crude mixture in scheme 2.1 with similar aromatic ligands such as *para* substituted benzene thiols and bulky ligands such as cyclohexane thiol. In particular, both *para* substituted benzene thiols -tert-butyl and methoxy - formed $Au_{102}(SR)_{44}$ (data not shown). We note that when bulky aliphatic ligands, like cyclohexane thiol, was used $Au_{102}(SR)_{44}$ was not formed, but species with smaller gold core were observed.

2.5.2 Optical spectroscopy

UV-vis-NIR absorption response of $Au_{102}(SPh)_{44}$ is measured in 1-metyltetrahydrofuran at different temperatures, Fig. 2.5a. Temperature dependent optical absorption spectra of the nanomolecules shows increased intensities of the absorption with no shift of absorption maxima. Absorption intensity spectra plotted as photon energy, Fig. 2.5b, shows ~ ten distinct peaks in between 1.23 eV and 3.86 eV range and two new peaks in low energy region. Fig. 2.6 reports a detailed comparison between measured and simulated absorption spectra.

The simulated spectrum also reported in Figure 2.6 compares fairly well with the experimental one at low temperature, with both curves showing similar features (the positions of individual sub-peaks are also indicated in Fig. 2.6): a rapid increase up to 1.75 eV, a maximum at about 2.50 eV, and a decrease for higher energies beyond 3.50 eV, although in this range the theoretically predicted absorption drops less rapidly than the experimental one. Above 3.56 eV, the theoretical spectrum shows a broad band centered at about 4.24 eV which is beyond the limits

of experimental measurements. In Fig. S10 in the Appendix A, we also show a comparison of the simulated optical spectra of $Au_{102}(SPh)_{44}$ and $Au_{102}(SPhCOOH)_{44}$. It is interesting to observe that a strong similarity exists between the two spectra below 3.5 eV, with the only major difference being an increase in absorption intensity up to 7 eV which we attribute to a stronger electron delocalization and resonance due to the electron-withdrawing COOH groups, in agreement with our recent study.[88] It is also worth noting that the high-energy peak at ~7.2 eV is red-shifted to ~6.7 eV by the presence of the carboxylic residues (again an electronic conjugation effect).

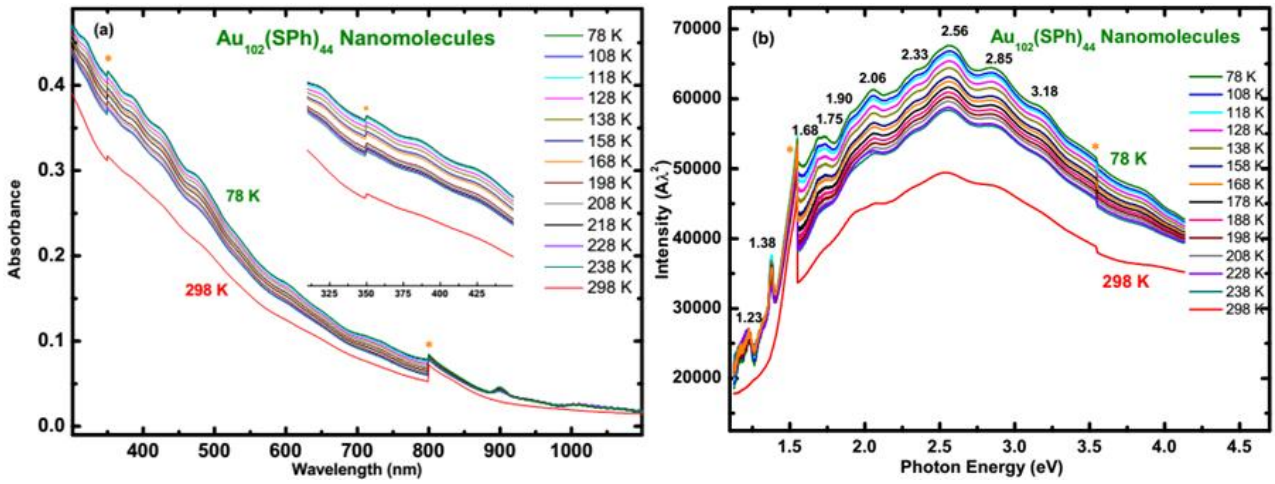

Figure 2.5. (a) Temperature-dependent UV-vis-NIR absorption spectra of $Au_{102}(SPh)_{44}$ nanomolecules in 3-methyl-tetrahydrofuran solvent. (b) Temperature-dependent UV-vis-NIR of $Au_{102}(SPh)_{44}$ nanomolecules plotted as photon energy where peaks marked by asterisk depicts an instrumental artifact.

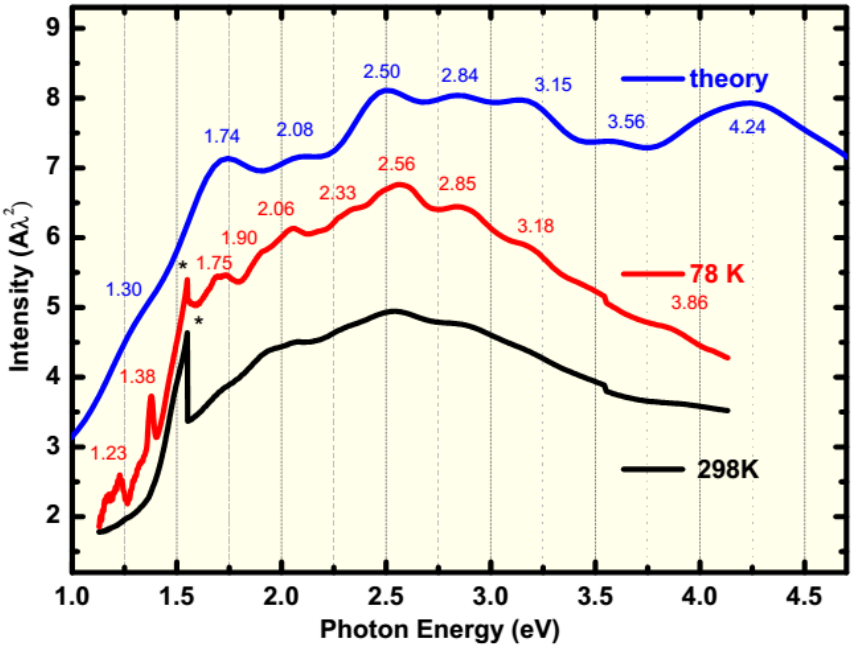

Figure 2.6. UV-vis-NIR absorption spectra of $Au_{102}(SPh)_{44}$ in 3-methyltetrahydrofuran at 298 K (black), 78 K (red) and theoretically predicted DFT spectrum (blue) where peaks marked by asterisk depicts an instrumental artifact.

2.6 Electrochemistry

For the first time, we report the electrochemical redox behavior of the organo-soluble $Au_{102}(SPh)_{44}$ nanomolecule. An electrochemical gap of 0.62 eV is observed that corresponds to the sum of the HOMO-LUMO gap and a charging energy term (fig 2.7). Additionally, twelve redox waves are observed: four reduction waves, and eight oxidation waves are observed with no indication of any trace of impurities. This electrochemical gap nicely fits the existing size-dependent trend[6] between $Au_{67}(SR)_{35}$ and $Au_{144}(SR)_{60}$, whose values are 0.74 and 0.3 eV, respectively. We believe that first reduction state is probably unstable which in turn causes the

second reduction peak to be smaller. The fourth redox state is less reversible relative to other redox states. In Fig. 2.8 we report the Projected Density of States (PDOS) around the Fermi level extracted from the DFT/PBE calculation on $Au_{102}(SPh)_{44}$ at its equilibrium geometry. The presence of an energy gap between the Highest Occupied Molecular Orbital (HOMO) and the Lowest Unoccupied Molecular Orbital (LUMO) is apparent. Since the DOS is projected onto atomic orbitals of the various elements (Au, S, C, H) it can be noticed that especially Au, but also S and C orbitals contribute to the regions both below and above the HOMO-LUMO gap. The value of the HOMO-LUMO gap is 0.44 eV, which is consistent with previous work and in good agreement with the experimental band gap.[72] In general, the present findings are in perfect agreement with previous theoretical analyses.[60, 72, 74-75, 77-78]

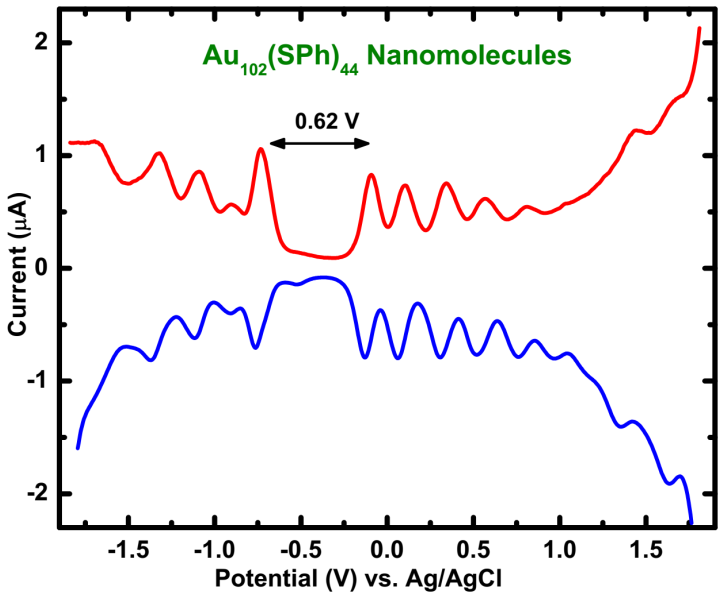

Figure 2.7. DPV response of $Au_{102}(SPh)_{44}$ nanomolecules against Ag/AgCl reference electrode.

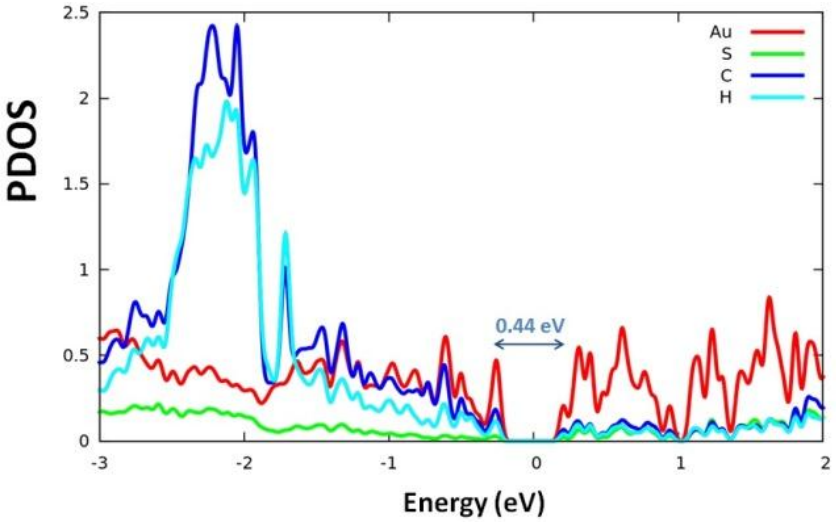

Figure 2.8. Projected Density of States (PDOS) around the Fermi level (set equal to 0) as derived from DFT/PBE calculations on $Au_{102}(SPh)_{44}$.

2.7 Conclusion

In conclusion, we present the first mass spectrometric evidence for the composition $Au_{102}(SPh)_{44}$ using high resolution electrospray mass spectrometry. This first synthesis and isolation of organo-soluble $Au_{102}(SPh)_{44}$ confirms the 102,44 composition, being the first after the first crystal structure report on Au_{102}. The organo-soluble species here achieved facilitates the study of electrochemical and temperature dependent optical characterization, which are thus presented with unprecedented resolution. Theoretical analysis confirms experimental assignments, determine that inter-ligand interactions in the coating shell have a minor influence on the stability of $Au_{102}(SR)_{44}$, and shows that electronic conjugation effects play a role in amplifying the optical response of these systems. This work opens the way to the general use of $Au_{102}(SPh\text{-}X)_{44}$ species in a variety of applications, most prominently those related to optical phenomena.

CHAPTER 3

STERIC THIOL-LIGAND EFFECT ON INTERCONVERSION OF $Au_{38}(SCH_2CH_2Ph)_{24}$ TO $Au_{30}(S\text{-}tBu)_{18}$

Part of the text and figures in this chapter are extracted from the following publication: Rambukwella, M.; Sementa, L.; Fortunelli, A.; Dass, A., *J. Phys. Chem. C* **2017**, 121, 14929-14935.

3.1 Abstract

The $Au_{38}(SCH_2CH_2Ph)_{24}$ nanomolecules upon etching with *tert*-butylthiol undergo core-size conversion to green gold, $Au_{30}(S\text{-}t\text{Bu})_{18}$ via $Au_{36}(SCH_2CH_2Ph)_{24\text{-}x}(S\text{-}t\text{Bu})_x$ intermediate. The structural transformation from Au_{38} to Au_{30} indicates a strong steric effect due to *tert*-butyl group of the exchanging ligand in contrast to electronic effect by ligands such as thiophenol, which transforms the $Au_{38}(SCH_2CH_2Ph)_{24}$ to $Au_{36}(S\text{-}t\text{Bu})_{24}$. In this work, fast reaction kinetics were observed and thermodynamically stable $Au_{30}(S\text{-}t\text{Bu})_{18}$ was obtained in molecular purity.

Author Contributions

Milan Rambukwella synthesized $Au_{38}(SCH_2CH_2Ph)_{24}$ nanomolecules, developed the experimental design, executed the core-size conversion reaction to obtain $Au_{30}(S\text{-}t\text{Bu})_{18}$ conducted mass spectrometric, UV-Vis-NIR absorption and electrochemical experiments and wrote the manuscript. Alessandro Fortunelli and Luca Sementa conducted computational studies. Amala

Dass assisted in experimental design, and data analysis. All the authors made substantial, direct and intellectual contribution to the work in the manuscript preparation.

3.2 Introduction

Gold nanomolecules[5, 89] have become a topic of great interest in chemistry due to their atomic monodispersity (± 0 atom variation), molecule-like properties[6, 90] and stability arising from geometric[7] and electronic shell[60] closings. Obtaining molecular pure product is challenging in typical synthetic protocol. In order to achieve high monodispersity, chromatographic techniques, so lvent fractionation, crystallization and core-size conversion methods are being employed.[19, 21, 81]

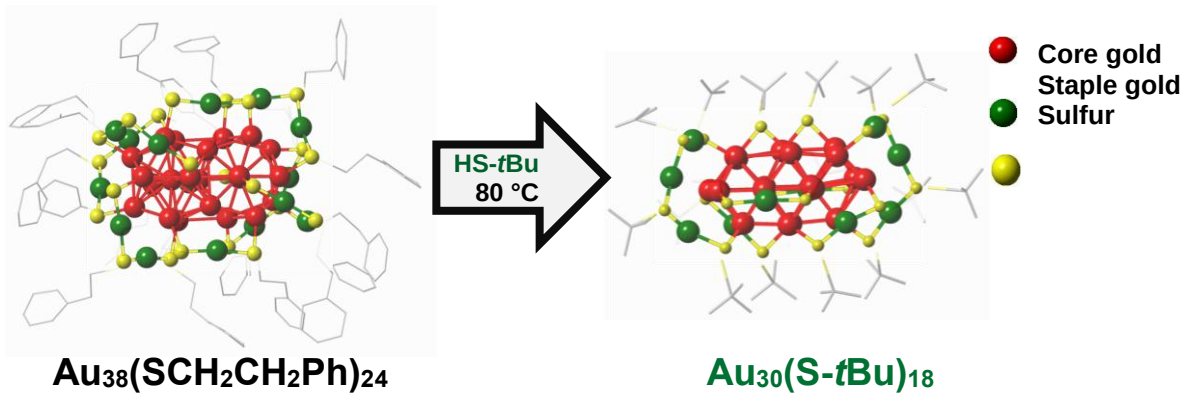

Scheme 3.1. Crystal structures of $Au_{38}(SCH_2CH_2Ph)_{24}$ and $Au_{30}(S\text{-}t\text{Bu})_{18}$ showing different ligand environments. (hydrogen atoms are avoided for clarity). The scheme illustrates tert-butylthiol ligand induced transformation of bi-icosahedron core to bi-cuboctahedron core geometry of $Au_{38}(SCH_2CH_2Ph)_{24}$ and $Au_{30}(S\text{-}t\text{Bu})_{18}$ nanomolecules, respectively.

Core-size conversion reactions are known to form a new core-size or core sizes that is different from the starting nanomolecules or nanoclusters.[38, 81] This is being achieved upon

reacting the starting nanomolecules or the nanoclusters with physicochemically different thiol. The reaction proceeds with ligand exchange, core-size conversion or both occurring simultaneously. In our previous work, we have reported the aromatic ligand induced core-size conversion of $Au_{67}(SR)_{35}$ and $Au_{103\text{-}105}(SR)_{44\text{-}46}$ nanocluster mixture to $Au_{36}(SPh)_{24}$, with its X-ray crystal structure reported subsequently[18, 91] and $Au_{38}(SCH_2CH_2Ph)_{24}$ core-size conversion to $Au_{36}(SPh)_{24}$ in the presence of thiophenol (HSPh) ligand where the aromatic nature of the -SPh ligand is inducing the core-size conversion to Au_{36}. A subsequent work by Jin and co-workers, confirmed this core-size conversion by providing evidence for the aromatic *tert*-butylbenzene thiol (TBBT) ligand induced core-size conversion of $Au_{38}(SCH_2CH_2Ph)_{24}$ starting material to $Au_{36}(TBBT)_{24}$, in the presence of TBBT, at elevated temperature (80 °C).[92] Aromatic ligand effect of TBBT was also evident by the report of core-size conversion of $Au_{144}(SCH_2CH_2Ph)_{60}$ to $Au_{133}(SPh\text{-}tBu)_{52}$.(ref[21]) It is interesting to note that TBBT ligand has a bulky *p-t*Bu group that give rise to steric effect oppose to the electronic effect that is arising from the phenyl aromatic ring. Thorough theoretical studies on this reaction reveals that core-size conversion is an electronic and kinetic effect due to aromatic nature of the new ligand, TBBT, and the purely steric effect due to *p-t*Bu is rather small.[21] Aromatic TBBT ligand introduces both aromatic and bulkiness to the ligand shell, thus it is not possible to attribute the $Au_{38}(SCH_2CH_2Ph)_{24}$ core-size conversion to $Au_{36}(TBBT)_{24}$ either electronic or steric effect. However, the report on $Au_{38}(SCH_2CH_2Ph)_{24}$ core-size conversion to $Au_{36}(SPh)_{24}$ suggests that electronic effect due to extended conjugation by -SPh ligand is sufficient to induce the core-size conversion.[91]

Green gold, $Au_{30}(S\text{-}tBu)_{18}$ was first reported in 2013 by our group followed by its crystal structure.[19-20, 93] Two other groups reported the synthesis and characterization of $Au_{30}(S\text{-}tBu)_{18}$ suggesting the reproducible nature of the synthesis.[94-95] Zhang and co-workers has successfully

synthesized $Au_{30}S(S\text{-}t\text{Bu})_{18}$ nanomolecules upon deliberately introducing NaS_2 into the reaction to incorporate S^{2-} onto the surface of the nanomolecules. Unlike the analogous nanomolecules such as $Au_{36}(SR)_{24}$ and $Au_{38}(SR)_{24}$ nanomolecules which has aromatic ligand and aliphatic-like ligand effect on core stability respectively, $Au_{30}(S\text{-}t\text{Bu})_{18}$ nanomolecules has a sterically crowded thiolate ligand shell. Also, other core-sizes Au_{21}, Au_{23}, and Au_{30} are been reported with bulky thiolate ligands. Existing method of $Au_{30}(S\text{-}t\text{Bu})_{18}$ synthesis involves chromatographic purification of the final product. [19-20] Workentin and co-workers has utilized *tert*-butylthiol in one step to synthesize $Au_{23}(S\text{-}t\text{Bu})_{16}$ nanomolecules and was able to extract with selective solvent extraction procedures with acetonitrile and dichloromethane.[94] They have successfully measured optical and electrochemical HOMO-LUMO gap for the two fractions and the difference was attributed to possible variation of ligand orientation or structural distortion in each structures of $Au_{23}(S\text{-}t\text{Bu})_{16}$ nanomolecules.

Here, we show that ligand exchange on $Au_{38}(SCH_2CH_2Ph)_{24}$ with *tert*-butylthiol results in core-size reduction to green gold, $Au_{30}(S\text{-}t\text{Bu})_{18}$ with high monodispersity (Scheme 3.1(a)). Interestingly $Au_{36}(SR)_{24}$ was observed in ESI mass spectrum as an intermediate core-size reduced species. $Au_{36}(SR)_{24}$ was observed as an intermediate product, where SR indicates a combination of $-SCH_2CH_2Ph$ and -S-*t*Bu ligands adding upto 24 ligand shell closing.

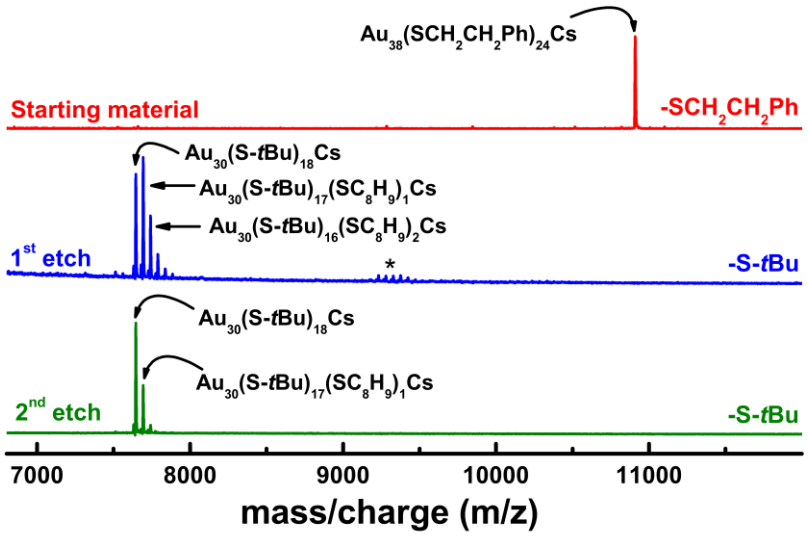

Figure 3.1. ESI mass spectra of $Au_{38}(SCH_2CH_2Ph)_{24}$ transformation to $Au_{30}(S\text{-}t\text{Bu})_{18}$ under etching with neat *tert*-butylthiol at 80 °C. First neat etching leads to $Au_{30}(SCH_2CH_2Ph)_{18\text{-}x}(S\text{-}t\text{Bu})_x$, a partial *tert*-butylthiol ligand exchange, where x_{avg} = 16. Second etching gives the complete formation of $Au_{30}(S\text{-}t\text{Bu})_{18}$. All species are observed as one Cs^+ adducts. Peaks marked by asterisk depicts the $Au_{36}(S\text{-}t\text{Bu})_{24\text{-}X}(SCH_2CH_2Ph)_X$ intermediate species, where 0< x <6.

This is the first report of structural transformation of $Au_{38}(SCH_2CH_2Ph)_{24}$ to $Au_{30}(S\text{-}t\text{Bu})_{18}$ nanomolecules. This experimental finding along with theoretical calculations allows us to understand direct steric effect of the ligand shell on gold nanomolecules. The results indicate core-size conversion mechanism undergoing via $Au_{36}(SR)_{24}$ intermediate nanomolecules.

3.3 Method

3.3.1 Materials

Hydrogen tetrachloroaurate(III) ($HAuCl_4 .3H_2O$), sodium borohydride (Acros, 99%), *tert*-butylthiol (Acros, 99%), phenyl-ethanemercaptan, (Sigma-Aldrich), cesium acetate (Acros, 99%),

anhydrous ethyl alcohol (Acros, 99.5%), glutathione (Sigma-Aldrich, 98%), and trans-2-[3[(4-tertbutyl- phenyl)-2-methyl-2-propenylidene]malononitrile (DCTB matrix) (Fluka≥99%) were purchased from Aldrich. HPLC grade solvents such as tetrahydrofuran, toluene, methanol, butylated hydroxytoluene stabilized tetrahydrofuran and acetonitrile were obtained from Fisher Scientific.

3.3.2 Synthesis

$Au_{38}(SCH_2CH_2Ph)_{24}$, was synthesized according to a modified previously reported procedure.[96] Complete aromatic ligand exchange on $Au_{38}(PET)_{24}$ nanomolecules to form $Au_{30}(S\text{-}t\text{Bu})_{18}$ without core-size conversion was performed in two main steps involving: (i) a first ligand exchange with neat etching with excess *tert*-butylthiol at 80 °C under harsh conditions gives partially exchanged intermediate and (ii) a second neat etching under identical conditions to achieve complete ligand exchange to form $Au_{30}(S\text{-}t\text{Bu})_{18}$.

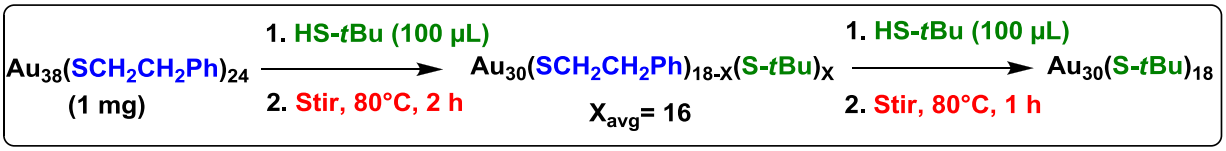

Scheme 3.2. Synthetic procedure for monodispersed $Au_{30}(S\text{-}t\text{Bu})_{18}$. In the first step, the reaction with HS-*t*Bu yields partially exchanged $Au_{30}(SCH_2CH_2Ph)_{18\text{-}x}(S\text{-}t\text{Bu})_x$, where x_{avg} is 16. Successive second step yields completely exchanged $Au_{30}(S\text{-}t\text{Bu})_{18}$.

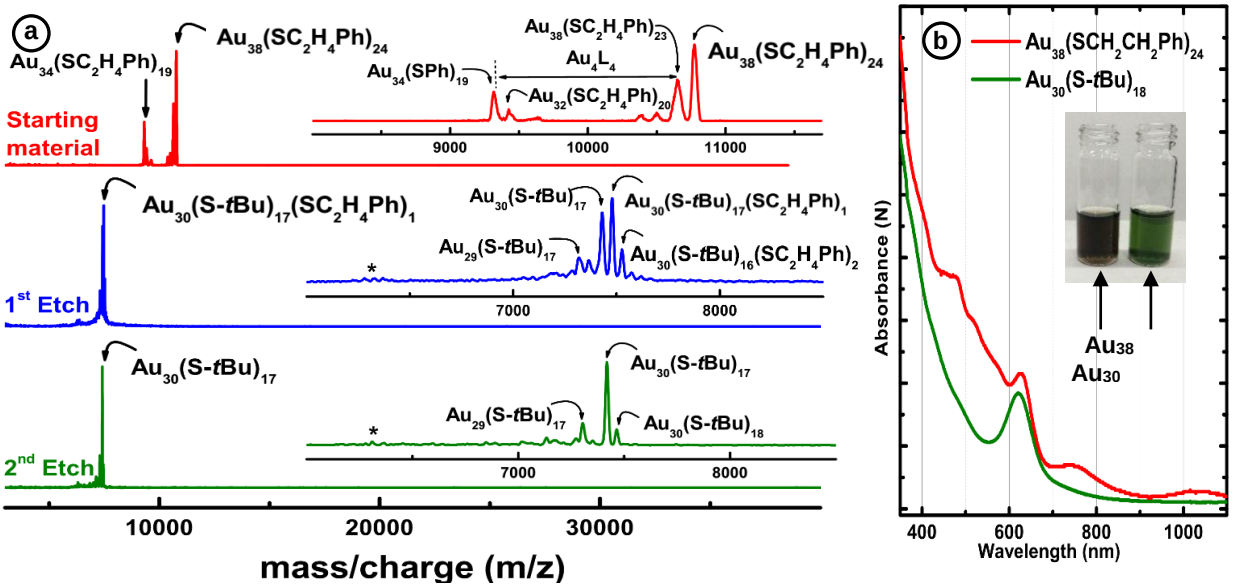

Figure 3.2. Ligand induced transformation of $Au_{38}(SCH_2CH_2Ph)_{24}$ starting nanomolecules to $Au_{30}(S\text{-}t\text{Bu})_{18}$. (a) MALDI-TOF mass spectra of starting material, products after first and second etch respectively. Expansion of the each spectra are shown as an inset and $Au_{38}(SCH_2CH_2Ph)_{24}$ spectra is intentionally fragmented to illustrate $Au_4(SR)_4$ fragmentation, common to this particular size regime. (b) Comparison of UV-Vis-NIR optical spectra of $Au_{30}(S\text{-}t\text{Bu})_{18}$ and $Au_{38}(SCH_2CH_2Ph)_{24}$ at room temperature.

First, $Au_{38}(SCH_2CH_2Ph)_{24}$ was reacted with excess *tert*-butylthiol (100 µL/ 1mg) at 80 °C for 2 hours. The product was then washed with methanol and subjected to a successive chemical treatment under same conditions for 1 hour. (see Scheme 3.1 and Fig. 3.1) The final product was washed with methanol several times and extracted with toluene.

3.3.3 Instrumentation

A Voyager DE mass spectrometer was used to acquire MALDI-TOF mass spectra using DCTB[83] matrix. Compositional analysis was performed with Electrospray Ionization mass spectra

(ESI-MS), collected from Waters Synapt HDMS with THF as the solvent and cesium acetate was added to facilitate ionization via. cesium adducts formation of the analyte. UV-Vis-NIR spectra were collected using Shimdzu UV-1601 spectrophotometer.

3.3.4 Computational Approach

Local geometry relaxations or Ab Initio Molecular Dynamics (AIMD) runs were performed using the CP2K code[97] whose DFT algorithms are based on a hybrid Gaussian/Plane-Wave scheme (GPW).[98] Pseudopotentials derived by Goedecker, Teter and Hutter [99] were chosen to describe the core electrons of all atoms and DZVP basis sets[100] to represent the DFT Kohn–Sham orbitals. Calculations were performed spin-restricted and at the Gamma point only. The semi-empirical Grimme-D3 correction[101] was added to Perdew–Burke–Ernzerhof (PBE)[102] exchange and correlation (xc-) functional to take into account dispersion interactions. The cut-off for the auxiliary plane wave representation of the density was 300 Ry. AIMD runs used a time step of 1.0 fs and the temperature was controlled by Nosé–Hoover chain thermostats.[103] The equilibrium structure of $Au_{38}(SCH_2CH_2Ph)_{24}$ and $Au_{30}(S\text{-}t\text{Bu})_{18}$ nanomolecules was obtained via fully relaxed local geometry optimizations starting from configurations derived from X-ray measurements in Refs. [51] and [20], respectively, after completing the missing atoms of $Au_{38}(SCH_2CH_2Ph)_{24}$ as needed. Other species appearing in the experiment are $Au_{36}(SR)_{24}$ nanomolecule among which $Au_{36}(S\text{-}t\text{Bu})_{22}(SCH_2CH_2Ph)_2$, which for simplicity and to make analysis of energetics more transparent we approximately model with the fully substituted $Au_{36}(S\text{-}t\text{Bu})_{24}$ nanomolecule. No crystallographic data are available for $Au_{36}(S\text{-}t\text{Bu})_{24}$, either, thus the equilibrium structure of this species was obtained by taking the coordinates of the $Au_{36}(SC)_{24}$ skeleton from X-ray measurements on $Au_{36}(SPh)_{24}$ in Ref.[18], adding C and H atoms as needed, subjecting the system to an initial full geometry optimization, followed by three sequential AIMD

runs lasting : (a) 2 psec at 300 K, (b) 2 psec at 900 K (only in this AIMD run the coordinates of the Au atoms were left frozen to the initial geometry), (c) 2 psec at 300 K, and finally leading to a sequential full geometry optimization. This long procedure was deemed necessary to minimize the significant steric hindrance in $Au_{36}(S\text{-}t\text{Bu})_{24}$, and indeed its total energy after final geometry optimization was 1.5 eV lower than the energy after initial geometry optimization. The Cartesian coordinates of the resulting $Au_{38}(SCH_2CH_2Ph)_{24}$, $Au_{30}(S\text{-}t\text{Bu})_{18}$ and $Au_{36}(S\text{-}t\text{Bu})_{24}$ species are provided in the Appendix B.

3.4 Core-size Conversion from $Au_{38}(SCH_2CH_2Ph)_{24}$ to $Au_{30}(S\text{-}tBu)_{18}$

Molecular structures the of $Au_{38}(SCH_2CH_2Ph)_{24}$ and $Au_{30}(S\text{-}t\text{Bu})_{18}$ nanomolecules has been deduced via single crystal X-ray analysis.[20, 51] The crystal structure of these nanomolecules reveals that core-size is governed by the thiolate ligand shell. Au_{23} core of $Au_{38}(SR)_{24}$ is only stable with aliphatic and alipahtic-like ligands such as hexanethiol and phenylethanethiol respectively (Scheme 3.1(a), Table 3.1). In contrast Au_{20} core of $Au_{30}(SR)_{18}$ is found to be stable with bulky ligands such as *tert*-butylthiol. The core geometry and Au-thiol staple arrangement is exclusive to each nanomolecules (Table 3.1) to minimize steric repulsions. $Au_{38}(SCH_2CH_2Ph)_{24}$ nanomolecules were synthesized using a modified protocol reported in literature.[96] The starting material $Au_{38}(SCH_2CH_2Ph)_{24}$ nanomolecules was reacted with neat *tert*-butylthiol (HS-*t*Bu) ligand at 80 °C (Scheme 3.2) in two stages to obtain $Au_{30}(S\text{-}t\text{Bu})_{18}$: (i) In the first stage a rapid core-size conversion, induced by the -S-*t*Bu ligand exchange with the $-SCH_2CH_2Ph$ was observed. Under these conditions, after 2 hours average of 16 ligand exchanges can be achieved. Fast reaction kinetics was observed during this step and brown color of the starting material changes to green within first 5 minutes of the reaction (Fig. S3 in the Appendix B). It is important to note that, after

the first etching step, dominated species is $Au_{30}(S\text{-}t\text{Bu})_{18}$ and residue species of starting material was not observed as evident by mass spectrometry and optical spectroscopy (Fig. 3.1 and Fig.

3.2(a)); (ii) In the second step, methanol washed purified product was subjected to successive

ligand exchange under

identical conditions (Fig. 3.1, Fig. 3.2). Complete ligand exchange after the second etching step was confirmed with the MALDI-TOF-MS analysis (Fig. 3.2(a)).

Ligand exchange and simultaneous core-size conversion reaction of $Au_{38}(SCH_2CH_2Ph)_{24}$ nanomolecules was monitored with ESI and MALDI mass spectrometry. The Fig. 3. 1,

Table 3.1. Comparison of $Au_{30}S_{18}$ and $Au_{38}S_{24}$ nanomolecule geometry.

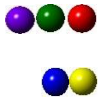 **Gold** **Sulfur**	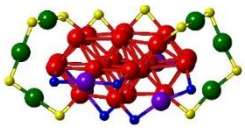	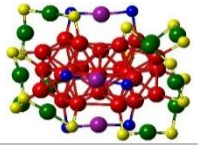
	$Au_{30}(S\text{-}t\text{Bu})_{18}$	**$Au_{38}(SCH_2CH_2Ph)_{24}$**
Ligand Type	**Bulky**	**Aliphatic-like**
Core	**20**	**23**
Geometry	**bi-cuboctahedron**	**bi-icosahedron**
Monomeric staples [SR-Au-SR]	**4**	**3**
Dimeric staples [SR-Au-SR-Au-SR]	**0**	**6**
Trimeric staples [SR-Au-SR-Au-SR-Au-SR]	**2**	**0**
Bridging thiols [SR]	**2**	**0**

illustrates ESI mass spectra of the transformation where starting material is core-size converted to $Au_{30}(S\text{-}t\text{Bu})_{18}$. Red spectrum shows the 10,911 m/z peak of starting material with one cesium ion (Cs^+) followed by mass spectra of the first etched product and second etched product. Each species was observed as Cs^+ adduct as cesium acetate was added intentionally to facilitate ionization. Fast reaction kinetics were observed as brown color of the starting material changes to green within first 5 minutes of the reaction, which indicates immediate core size-conversion of the starting

material to green gold. A detail study on the core-size conversion was carried out at 80 °C to understand the mechanism of the transformation. It was observed the reaction pathway follows via kinetic intermediate $Au_{36}(S\text{-}t\text{Bu})_{24\text{-}X}(SCH_2CH_2Ph)_x$ where, average X is equals to 2. In addition to that, ESI-MS analysis reveals four other unstable kinetic intermediate species having core-size between Au_{38} to Au_{30} (Appendix B, Fig. S4.). Similarly, Zheng and co-workers were able to report manganese (Mn) kinetic intermediate clusters Mn_{10}, Mn_{12} and Mn_{14} via high resolution ESI-MS in the hierarchical formation process of Mn_{19} disc from manganese.[104] It should be noted that although signal for $Au_{30}(S\text{-}t\text{Bu})_{18}$ species was dominating in the ESI-MS of the 5 minute sample, transformation of the $Au_{38}(SCH_2CH_2Ph)_{24}$ starting material is not complete. It was observed with MALDI mass spectrometry approximately 2 hours for etching is required to achieve significant transformation of the starting material to $Au_{30}(S\text{-}t\text{Bu})_{18}$. The transformation was concurrently monitored with MALDI mass spectrometry as shown in the Fig. 3.2a. and mass spectra illustrate the molecular purity of the starting material and the final product. Insets show the expansion of the mass range of interest and the complete transformation of the starting material, $Au_{38}(SCH_2CH_2Ph)_{24}$ to $Au_{30}(S\text{-}t\text{Bu})_{18}$. It should be noted that $Au_{38}(SCH_2CH_2Ph)_{24}$ analyte was intentionally fragmented to show the $Au_4(SCH_2CH_2Ph)_4$ fragmentation and the intact molecular peak of $Au_{30}(S\text{-}t\text{Bu})_{18}$ analyte was not the dominant peak in the MALDI mass spectra, but $Au_{30}(S\text{-}t\text{Bu})_{17}$ was observed. The latter could be due to the labile nature of the ligand that was also observed for aromatic ligand shell closed nanomolecules.

UV-Vis-NIR absorption features (Fig. 3.2(b)) of the starting material $Au_{38}(SCH_2CH_2Ph)_{24}$ is directly compared against end product $Au_{30}(S\text{-}t\text{Bu})_{18}$. Starting material has characteristic absorption peaks at 935 nm, 600 nm and 475 nm as reported earlier. Structural transformation of

the starting material is evident with the evolution of the peak at 621 nm corresponding to Au_{30}(S-*t*Bu)$_{18}$ nanomolecules.

3.5 Quantitative Determination of Transformation from $Au_{38}(SCH_2CH_2Ph)_{24}$ to Au_{30}(S-tBu)$_{18}$

To provide theoretical information on the transformation processes here investigated, we focus on a comparison of the thermodynamic stability of $Au_{38}(SCH_2CH_2Ph)_{24}$, Au_{30}(S-*t*Bu)$_{18}$ and Au_{36}(S-*t*Bu)$_{24}$ nanomolecules – the last species as a model of the $Au_{36}(SR)_{24}$ intermediate observed in the experiment. The energetics of these species were investigated and compared using analysis tools proposed in previous work [21,79,78,86], in particular energy fragment decomposition [86] and system comparison [78,21] procedures. As a starting comment, we note that the ligands here considered are both aliphatic thiols, and we should expect that their covalent interaction with gold clusters is similar. Indeed, the strength of the S-H bond in H-S-*t*Bu and H-SCH_2CH_2Ph i.e., the reaction energy of the process: HSR $\rightarrow$ SR + H, is nearly identical: 4.86 eV and 4.87 eV, respectively, so that any difference in chemical behavior cannot be attributed to differences in Au-S covalent interactions,[78] but rather in geometric or electronic effects brought about by the larger steric hindrance of S-*t*Bu with respect to SCH_2CH_2Ph. Moreover, since the nanomolecules here considered have a different stoichiometry, we need to define a normalization factor to be able to compare their energetics on the same ground. We choose to normalize to the number of ligands, M, and hereafter all quantities will be intended as per ligand (absolute energy values are reported in Appendix B, Table S1).

We dissect the formation energy of a $Au_N(SR)_M$ nanomolecule in three pieces [86]: (1) cluster fragmentation, (2) metal atomization, (3) ligand separation (energy differences are also reported in Table S2 in the Appendix B, for ease of visualization).

The first piece is the *cluster fragmentation* reaction into a metal cluster and a "crown" of ligands (normalized to the number of ligands, M):

$Au_{38}(SCH_2CH_2Ph)_{24} \rightarrow Au_{38} + (SCH_2CH_2Ph)_{24}^{crown}$ $\Delta E^{fragm}/M = 3.44$ eV (3.1)

$Au_{36}(S\text{-}t\text{Bu})_{24} \rightarrow Au_{36} + (S\text{-}t\text{Bu})_{24}^{crown}$ $\Delta E^{fragm}/M = 3.36$ eV (3.2)

$Au_{30}(S\text{-}t\text{Bu})_{18} \rightarrow Au_{30} + (S\text{-}t\text{Bu})_{18}^{crown}$ $\Delta E^{fragm}/M = 3.53$ eV (3.3)

where the coordinates of the Au_{38}, Au_{36}, Au_{30}, $(SR)_{24}^{crown}$ and $(SR)_{18}^{crown}$ fragments in the right-hand-side of the equations are frozen in their interacting configurations, ΔE is the reaction energy and is reported per ligand (ΔE/M). Clearly, *$Au_{36}(S\text{-}t\text{Bu})_{24}$ has the smallest (least stable) fragmentation energy* from Eqs.(3.1-3.3). This can be easily explained in terms of increase in the dispersion of Au-S bonds forced by steric hindrance. The average Au-S distance is nearly identical in the three compounds (i.e., 2.39 Å), but in $Au_{30}(S\text{-}t\text{Bu})_{18}$ the Au-S bond length range within 2.35-2.44 Å, this range increases in $Au_{38}(SCH_2CH_2Ph)_{24}$ to 2.33-2.49 Å, and reaches a maximum of 2.33-2.53 Å in $Au_{36}(S\text{-}t\text{Bu})_{24}$.

The second piece is the *atomization energy* of the resulting metal cluster:

Au_{38} [from $Au_{38}(SCH_2CH_2Ph)_{24}$] $\rightarrow$ 38Au $\Delta E^{atmz}/M = 3.26$ eV (3.4)

Au_{36} [from$Au_{36}(S\text{-}t\text{Bu})_{24}$] $\rightarrow$ 36 Au $\Delta E^{atmz}/M = 2.99$ eV (3.5)

Au_{30} [from$Au_{30}(S\text{-}t\text{Bu})_{18}$] $\rightarrow$ 30 Au $\Delta E^{atmz}/M = 3.44$ eV (3.6)

Again, *$Au_{36}(S\text{-}t\text{Bu})_{24}$ turns out to be the least stable compound* from Eqs.(3.4-3.6). This is also a consequence of steric hindrance, which causes that some of the staples are forced into nearly detached configurations in $Au_{36}(S\text{-}t\text{Bu})_{24}$ with respect to the more compact $Au_{30}(S\text{-}t\text{Bu})_{18}$ and $Au_{38}(SCH_2CH_2Ph)_{24}$, as illustrated in Figure S6 of the Appendix B. The latter two compounds are

apparently more similar in this respect, but a more detailed analysis shows a preferential stability of $Au_{30}(S\text{-}t\text{Bu})_{18}$ with respect to $Au_{38}(SCH_2CH_2Ph)_{24}$. It is in fact true that if we normalize the atomization energies ΔE^{atmz} of these two species per Au atom instead of per ligand we get a similar value of 2.064 eV for Au_{30} fragmentation in $Au_{30}(S\text{-}t\text{Bu})_{18}$ and 2.057 eV for Au_{38} fragmentation in $Au_{38}(SCH_2CH_2Ph)_{24}$, but Au_{38} – being larger than Au_{30} – would be expected to exhibit a monotonically increasing atomization energy, not a constant one. This is also confirmed by the values of the average Au-Au first-neighbor distance, that are 2.91 Å in $Au_{30}(S\text{-}t\text{Bu})_{18}$ and 2.95 Å in $Au_{38}(SCH_2CH_2Ph)_{24}$, i.e., larger and thus less stable in the latter compound (we define as first neighbors of a given Au atom all Au atoms within 3.2 Å, which is the inflection point in the plot of Au-Au distances).

Finally, the last piece in our analysis is the separation of the crown or shell of ligands into separated and fully relaxed thiols:

$$(SCH_2CH_2Ph)_{24}^{crown} \rightarrow 24(SCH_2CH_2Ph)_{relax} \qquad \Delta E^{ligsep}/M = 1.137 \text{ eV} \qquad (3.7)$$

$$(S\text{-}t\text{Bu})_{24}^{crown} \rightarrow 24\ (S\text{-}t\text{Bu})_{relax} \qquad \Delta E^{ligsep}/M = 0.355 \text{ eV} \qquad (3.8)$$

$$(S\text{-}t\text{Bu})_{18}^{crown} \rightarrow 18\ (S\text{-}t\text{Bu})_{relax} \qquad \Delta E^{ligsep}/M = 0.179 \text{ eV} \qquad (3.9)$$

Here interestingly we find the reasons of the stability of $Au_{38}(SCH_2CH_2Ph)_{24}$. Ligand-ligand interactions in fact slightly increase the formation energy of $Au_{36}(S\text{-}t\text{Bu})_{24}$, but not to a degree sufficient to compensate the energy cost of deforming and lengthening Au-Au and Au-S distances as discussed above. What is striking instead is the huge value of $\Delta E^{ligsep}/M$ for $Au_{38}(SCH_2CH_2Ph)_{24}$. This separation energy contains two terms: residual S-S binding (some of the sulfur atoms of thiols in the interacting configuration are not far from binding distance) and dispersion/repulsion interactions between the organic residues. We have estimated the former term

by comparison with hydrogenated ligands and found it negligible (of the order of 1-3 hundredths of an eV per ligand), so that $\Delta E^{ligsep}/M$ for $Au_{38}(SCH_2CH_2Ph)_{24}$ is found to be dominated by dispersion interactions between the organic residues, including – but not exclusively – π-π and T-stackings among phenyl rings.[21] Clearly, as discussed in Ref. [86], this type of stabilization will be strongly dependent on the medium in which the nanomolecules are immersed, and a subtle interplay involving also entropic factors (configurational entropy) that are here neglected will play a role. In any case, we can qualitatively expect that in more "wetting" (more strongly interacting) solvents, such as e.g. benzene as opposed to chloroform, $Au_{38}(SCH_2CH_2Ph)_{24}$ will adopt a "brush" rather than a "mushroom" conformation[105] possibly leading to lesser relative stability in such media.

The energy decomposition analysis described so far can be interpreted as a Born-Haber cycle, as illustrated in Figure S5 of the Appendix B. To provide further insight into the thermodynamic comparison between $Au_{30}(S\text{-}t\text{Bu})_{18}$ and $Au_{38}(SCH_2CH_2Ph)_{24}$, which is less obvious than for the $Au_{36}(S\text{-}t\text{Bu})_{24}$ species, we consider the substitution reaction:

$$Au_{30}(S\text{-}t\text{Bu})_{18} + 8\ Au + 24\ (SCH_2CH_2Ph) \rightarrow Au_{38}(SCH_2CH_2Ph)_{24} + 18\ (S\text{-}t\text{Bu}) \qquad (3.10)$$

which – in addition to total energies from QM simulations – require an estimate of the chemical potential of an Au atom, μ(Au), and the chemical potential of the ligand thiols, $\mu(HCH_2CH_2Ph)$ and μ(HS-*t*Bu). This reaction can in fact be decomposed as follows:

$$(3.10) = [\ (3.3) - (3.1) + (3.9) - (3.7) + 18\ \mu(S\text{-}t\text{Bu}) - 24\ \mu\ (SCH_2CH_2Ph)\ ] + [\ (3.6) - (3.4) - 8\ \mu(Au)\ ] \qquad (3.11)$$

Now the contribution within the first square bracket depends on the fragmentation (3.1,3.3) and separation (3.7,3.9) energies, and on the chemical potential of the ligand radical thiyls, μ(HSPhH) and μ(HS-*t*Bu), whereas the contribution within the second square bracket depends on the atomization energies (3.4,3.6), and on the chemical potential of Au, μ(Au). Normalizing to the number of ligands, and assuming a zero chemical potential of Au and equal concentrations of HS-*t*Bu and HSPhH thiols (exploiting the fact that the difference in the strength of H-S-*t*Bu and H-SPhH bonds is zero), we see that this contribution equals 0.93 eV, and is basically dominated by the strength of ligand/ligand interactions in $Au_{38}(SCH_2CH_2Ph)_{24}$. This contribution is sizeable. However, working under the experimental conditions of: (1) excess of HS-*t*Bu, (2) "wetting" solvent as discussed above that compensate for the loss of ligand/ligand interactions in Au_{30}(S-*t*Bu)$_{18}$, and (3.3) scarcity of Au, there will be a thermodynamic driving force for the transformation from $Au_{38}(SCH_2CH_2Ph)_{24}$, to Au_{30}(S-*t*Bu)$_{18}$, as experimentally reported here. Note that other reference states for the chemical potentials of Au and thiols have been proposed in the past, such as bulk Au metal and organic disulfides RS-SR – all choices of reference states are of course ultimately equivalent.

Finally, as a reference we also report the adiabatic or vertical ionization potential (IP) and electron affinity (EA) of the three clusters here investigated, i.e., the energy lost to extract or gained to add an electron to the cluster, respectively, by keeping the geometry frozen at the one optimized for the neutral species. The ionization potentials of Au_{30}(S-*t*Bu)$_{18}$, Au_{36}(S-*t*Bu)$_{24}$, and $Au_{38}(SCH_2CH_2Ph)_{24}$ nanomolecules are: 5.06 eV, 5.03 eV, 4.72 eV, respectively, while the electron affinities are: 1.75 eV, 1.90 eV, 2.29 eV, respectively. Interestingly, chemical hardness [(IP-EA)/2] and Mulliken electronegativity [(IP+EA)/2] follow an opposite order, i.e., for hardness: 1.655 eV [Au_{30}(S-*t*Bu)$_{18}$] > 1.565 eV [Au_{36}(S-*t*Bu)$_{24}$] > 1.215 eV [$Au_{38}(SCH_2CH_2Ph)_{24}$],

whereas for Mulliken electronegativity: 3.405 eV [Au_{30}(S-*t*Bu)$_{18}$] < 3.465 eV [Au_{36}(S-*t*Bu)$_{24}$] < 3.505 eV [$Au_{38}(SCH_2CH_2Ph)_{24}$], confirming that Au_{30}(S-*t*Bu)$_{18}$ is in fact the hardest and – from the purely electronic point of view – the most stable species, whereas $Au_{38}(SCH_2CH_2Ph)_{24}$ most easily exchanges (yielding or receiving) an electron with the environment.

3.6 Conclusion

The picture emerging from the above thermodynamic (total energy) analysis seems consistent with and provide further insight into experiment, and can be summarized in terms of two main conclusions;(i) not unexpectedly, Au_{36}(S-*t*Bu)$_{24}$ is the least stable species: steric hindrance brought about by bulky S-*t*Bu ligands is not compatible with a (N,M)=(36,24) stoichiometry and – depending on the conditions – this compound is predicted either to disproportionate to Au_{30}(S-*t*Bu)$_{18}$ and $Au_{38}(SCH_2CH_2Ph)_{24}$ or to transform selectively into one of these nanomolecules; (ii) the stability of Au_{30}(S-*t*Bu)$_{18}$ and $Au_{38}(SCH_2CH_2Ph)_{24}$ may be rather different depending on the conditions, as it stems from different sources: if ligand-ligand interactions are not considered Au_{30}(S-*t*Bu)$_{18}$ is actually more stable than $Au_{38}(SCH_2CH_2Ph)_{24}$, but huge ligand-ligand dispersive interaction terms can make this species much more robust in "non-wetting" solvents via a "self-solvation" mechanism (i.e., adopting "mushroom" conformations. [105] Clearly, we must point out that those proposed so far are purely thermodynamic (enthalpy) considerations, which certainly provide a basis for understanding and rationalization, but should be complemented with an analysis of kinetic effects which have also been shown to play an important role in some cases.[21]

CHAPTER 4

LIGAND EFFECT ON FORMATION OF $Au_{38}(SCH_2CH_2Ph)_{24}$, $Au_{36}(SPh\text{-}tBu)_{24}$ and $Au_{30}(S\text{-}tBu)_{18}$

Part of the text and figures in this chapter are extracted from the following publication: Rambukwella, M.; Dass, A., *Langmuir* **2017**, 33, 10958-10964.

4.1 Abstract

Phenylethanethiol protected nanomolecules such as Au_{25}, Au_{38} and Au_{144} are widely studied by a broad range of scientists in the community owing primarily to the availability of simple synthetic protocols. However, synthetic methods are not available for other ligands, such as aromatic thiol and bulky ligands, impeding progress. Here we report, the facile synthesis of three distinct nanomolecules, $Au_{38}(SCH_2CH_2Ph)_{24}$, $Au_{36}(SPh\text{-}t\text{Bu})_{24}$ and $Au_{30}(S\text{-}t\text{Bu})_{18}$, exclusively, starting from a common Au_n(glutathione)$_m$ (where n and m are number of gold atoms and glutathiolate ligands) starting material upon reaction with $HSCH_2CH_2Ph$, HSPh-tBu and HStBu respectively. The systematic synthetic approach involves two steps: (i) synthesis of kinetically controlled Au_n(glutathione)$_m$ crude nanocluster mixture with 1:4 gold to thiol molar ratio and (ii) thermochemical treatment of the purified nanocluster mixture with excess thiols to obtain thermodynamically stable nanomolecules. Thermochemical reactions with physicochemically different ligands formed highly monodispersed, exclusively three different core-size nanomolecules, suggesting a ligand induced core-size conversion and structural

transformation. The purpose of this work is to make available a facile, and simple synthetic method for the preparation of $Au_{38}(SCH_2CH_2Ph)_{24}$, $Au_{36}(SPh\text{-}tBu)_{24}$ and $Au_{30}(S\text{-}tBu)_{18}$, to non-specialists and the broader scientific community. The central idea of simple synthetic method was demonstrated with other ligand systems such as, cyclopentanethiol (HSC_5H_9), cyclohexanethiol(HSC_6H_{11}), *para*-methylbenzenethiol(pMBT), 1-pentanethiol(HSC_6H_{11}), 1-hexanethiol(HSC_6H_{13}) where, $Au_{36}(SC_5H_9)_{24}$, $Au_{36}(SC_6H_{11})_{24}$, $Au_{36}(pMBT)_{24}$, $Au_{38}(SC_5H_{11})_{24}$, and $Au_{38}(SC_6H_{13})_{24}$, was obtained, respectively.

Author Contributions

Milan Rambukwella developed the synthetic protocol to synthesize $Au_{38}(SCH_2CH_2Ph)_{24}$, $Au_{36}(SPh\text{-}tBu)_{24}$, $Au_{30}(S\text{-}tBu)_{18}$ nanomolecules conducted mass spectrometric, UV-Vis-NIR absorption, electrochemical experiments and wrote the manuscript. Amala Dass assisted in experimental design, data analysis, and edited the manuscript. Both authors made substantial, direct and intellectual contribution to the work in the manuscript preparation.

4.2 Introduction

The availability of robust, facile synthetic protocols for atomically precise gold nanomolecules[4-5] has expanded their utilization in catalysis,[27, 56, 106] biological sensing,[107-108] supramolecular chemistry,[109] and as therapeutic agents[15] due to the unique optical,[55, 110-111] electrochemical,[6, 112] and chemical properties.[56, 113] In contrast, bi-metal alloy nanoparticles[22-24] with unique optical and enhanced catalytic activity has become a widely discussed topic of interest.[114] Although the potential for applications is significant, one of the challenges and a key factor that limits the application of nanomolecules is the lack of simplified, high yield,

monodispersed synthetic protocols and stable products with high shelf life.[32] Gold nanomolecules differ from gold nanoparticles, having characteristics attribute to their atomic monodispersity (± 0 atom variation), molecule-like properties[6] and stability arising from geometric[7] and electronic shell[60] closings, and the staple motif.[17] These ultra-small (<2 nm diameter) gold nanomolecules have precise number of gold atoms protected by a precise number of ligands. A series of atomically precise, gold nanomolecules with different thiols have been synthesized.[53]

Generally, obtaining molecular purity in nanochemistry is a challenging and complicated procedure. A typical synthetic protocol yields a polydisperse mixture containing different sizes of nanoclusters. Significant optimization and tuning of the synthesis, in addition to subsequent separation and purification is required to obtain monodispersed gold nanomolecules. Among various synthetic protocols, the two-phase Brust method[30] is known to produce smaller core-size nanomolecules. One can obtain different size-dependent gold nanomolecules by tuning the gold to thiol ratio, the type of thiol, solvent, temperature, and reducing conditions of the synthetic protocol. Wu et al. has demonstrated the effect of reducing agent and formation of $Au_{19}(SC_2H_4Ph)_{13}$ by replacing $NaBH_4$ (a strong reducing agent) with a weaker one (borane tert-butylamine complex), that reduces the kinetics of the synthetic step.[115] Post synthetic steps[66, 116] and separation [41, 117-118] are also implemented to narrow down polydispersity and obtain highly monodispersed product. Similar post synthetic steps are widely used by researchers to synthesize other metallic silver clusters[119-121] as well as alloy clusters,[122] in addition to been implemented in core-size conversion of bulk $Au_n(SR)_m$ crude mixture to corresponding nanomolecules or series of nanomolecules. This systematic synthetic approach involves two steps:(i) synthesis of kinetically controlled $Au_n(SR)_m$ crude nanocluster mixture with precise control of gold to thiol molar ratio

and (ii) post thermochemical treatment of the purified mixture with excess thiols to obtain thermodynamically stable highly monodispersed nanomolecules.

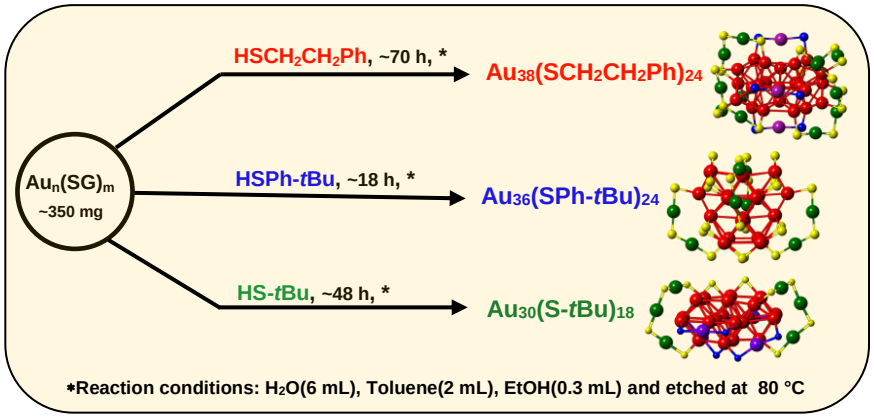

Scheme 4.1. Three synthetic strategies used to obtain three distinct nanomolecules, $Au_{38}(SCH_2CH_2Ph)_{24}$, $Au_{36}(SPh\text{-}tBu)_{24}$ and $Au_{30}(S\text{-}tBu)_{18}$ starting from the same starting kinetic nanoclusters, $Au_n(SG)_m$. Corresponding molecular structures are shown. Note that carbon and hydrogen atoms on the ligands are excluded for clarity (red- core Au, green- dimeric staple Au, purple- monomeric staple Au, yellow- dimeric, trimeric staple and bridging S, blue- monomeric staple S).

The physicochemical nature of the protecting ligands dictate the structure and properties of the gold nanomolecules.[94-95, 123-127] Recently, Tlahuice reported a density functional theory (DFT) based finding on photoluminescent $Au_{18}(SR)_{14}$ clusters where, 6 physicochemically different ligands were studied.[127] It was found that presence of different chemical groups, such as phenyl rings, nitro groups or alkyl group, that can interact with each other plays a key role in ligand effect. The study reported, ligands induce major structural distortions with para-mercaptobenzoic acid and para-nitrobenzenethiol whereas, with SCH_3, 4-*tert*-butylbenzenethiol (HSPh-tBu), thiophenol and cyclohexanethiol ligands similar core structure and ligand orientation was

observed. Similarly, Tlahuice et al. reported ligand induced structural distortions in $Au_{25}(SR)_{18}$ clusters and the effect on electronic optical properties.[124] It was found that among studied set of 11 ligands, para-thiophenolate ligands with electron-withdrawing groups induced, major structural distortions in $Au_{25}S_{18}$ framework. Therefore, different core-size structures with unique chemical properties could be synthesized with physicochemically different ligands such as aromatic, bulky and aliphatic thiols. For instance, in our previous work, we have shown that with aromatic ligands $Au_{144}(SCH_2CH_2Ph)_{60}$ core-size converts to $Au_{133}(SPh\text{-}t\text{Bu})_{52}$ due to aromatic ligand effect of *tert*-butylbenzene thiol.[21] In the presence of the incoming ligand having aromatic and a bulky *para-tertiary* butyl group, electronic and steric effects of the ligand dictates the structure of the gold nanomolecules.

Only a selected few researchers experienced in this field have synthesized $Au_{38}(SR)_{24}$, $Au_{36}(SR)_{24}$ and $Au_{30}(SR)_{18}$, because of tailored synthetic steps that are unique to each ligand.[19-20, 32, 91-93, 95-96, 128-131] Although, individual procedures for synthesis of $Au_{38}(SR)_{24}$, $Au_{36}(SR)_{24}$ and $Au_{30}(SR)_{18}$ have been reported in the literature, $Au_{36}(SR)_{24}$ and $Au_{30}(SR)_{18}$ Au NMs lack a simple synthetic technique. A majority of the previous reports for Au_{36} used Au_{38} as a starting material, which includes additional synthetic steps. Current methods for Au_{38}, Au_{36}, Au_{30} synthesis involve different procedures which are time consuming and not accessible to non-specialists interested in various sizes. The goal here is to prepare various sizes using one synthetic method, by simply changing the ligand. The focus of this work is not to prepare a new sized nanomolecule, but to report a reproducible and robust procedure to prepare these from a common and readily available precursor in good yields. In this report, we have exploited the physicochemical properties of the ligands and provided a simple procedure to circumvent the need for any demanding purification techniques. We used a common $Au_n(SG)_m$ crude mixture with glutathione (HSG) ligands and

systematically core-size convert it to three different monodispersed, good yield, three distinct nanomolecules (Scheme 4.1). In the first step, several different sizes of kinetically stable nanoclusters are formed upon $NaBH_4$ reduction of the Au(I)-SG polymer. A majority of these clusters are meta-stable which undergoes core-size conversion or decomposition upon the successive thermochemical treatment (etching step) with excess of thiol. This second step gives rise to exclusively thermodynamically stable nanomolecules (scheme 4.1). This systematic approach has proven to expand the synthetic protocols of other series of nanomolecules in high monodispersity.

It is reported by Jin and co-workers, isomeric ligand effect of (*o*-, *m*-, & *p*-) methylbenzenethiols[132] yielding three different nanomolecules from an identical synthetic protocol following Brust two phase[30] synthesis and etching.[133] A summary[134] of *tert*-butylbenzene thiol induced core-size conversion of pure Au_{25}, Au_{38} and Au_{144} phenylethanethiol protected nanomolecules[63, 92, 135] to respective Au_{28}, Au_{36} and Au_{133} nanomolecules, have been reported by Jin and co-workers. Au_{36} and Au_{30} have been reported before and its' structure elucidated, but currently there is no easily reproducible synthetic methods available to prepare these. There is only a small group of researchers who can make Au_{36} and Au_{30}. This list includes Professor Jins' group[92, 117, 134, 136] (and his former postdocs), our group,[32, 91,48] Nangfeng Zheng, and Mark Workentin.[94] The work reported herein is solely focuses on providing a facile synthesis for three distinct thermodynamically stable nanomolecules from a common readily available precursor. Lack of such simple protocol for these stable nanomolecules severely impedes the application development.

4.3 Method

4.3.1 Materials

Hydrogen tetrachloroaurate(III) ($HAuCl_4 .3H_2O$), sodium borohydride (Acros, 99%), phenyl-ethanethiol, (Sigma-Aldrich, 99%), *tert*-butylbenzenethiol (Acros, 99%), *tert*-butylthiol (Acros, 99%), cesium acetate (Acros, 99%), anhydrous ethyl alcohol (Acros, 99.5%), glutathione (Sigma-Aldrich, 98%), and trans-2-[3[(4-tertbutyl- phenyl)-2-methyl-2-propenylidene]malononitrile (DCTB matrix) (Fluka≥99%) were purchased from Aldrich. HPLC grade solvents such as tetrahydrofuran, toluene, methanol, butylated hydroxytoluene stabilized tetrahydrofuran and acetonitrile were obtained from Fisher Scientific.

4.3.2. Instrumentation

A Voyager DE mass spectrometer was used to acquire MALDI-TOF mass spectra using DCTB[83] matrix. Compositional analysis was performed with electrospray ionization mass spectra (ESI-MS), collected from Waters Synapt HDMS with THF as the solvent and cesium acetate was added to facilitate ionization via. cesium adduct formation of the analyte. UV-Vis-NIR spectra were collected using Shimdzu UV-1601 spectrophotometer.

4.3.3 Synthesis

The synthesis involves two main steps: (i) the first step to obtain the $Au_n(SG)_m$ kinetic nanocluster mixture using a procedure reported in literature[96] and (ii) the second etching step of

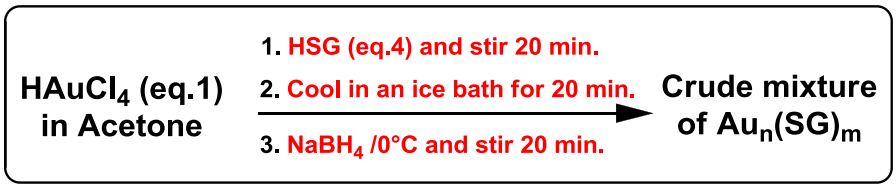

Scheme 4.2. Synthetic procedure for $Au_n(SG)_m$ nanoclusters synthesis.

$Au_n(SG)_m$ mixture with excess thiol at 80 °C to obtain corresponding nanomolecules in good yield and high monodispersity(scheme 4.2).

4.3.3.1 Synthesis of $Au_n(SG)_m$ mixture

$Au_n(SG)_m$ was synthesized using a procedure reported in literature.[96] In a typical synthesis, 1 mmol of $HAuCl_4 .3H_2O$ was dissolved in 40 mL of acetone in a round bottom flask and stirred for 20 minutes with 4 mmol of glutathione. This mixture was cooled and stirred in an ice bath for 20 minutes, followed by rapid addition of 10 mmol of $NaBH_4$ dissolved in 12 mL of ice-cold distilled water. The reaction was continued for 20 min and black sticky $Au_n(SG)_m$ product was observed stuck to the wall of the flask. After 20 mins, the solution was decanted, and the product was washed with 10 mL of methanol (3 times). This product can be dried and stored or directly dissolved in distilled water to be used for thermochemical treatment (Figure S1 in the Appendix C).

4.3.3.2 Synthesis of $Au_{38}(SCH_2CH_2Ph)_{24}$ nanomolecules

$Au_{38}(SCH_2CH_2Ph)_{24}$was synthesized using a procedure reported in literature.[96] In a typical synthesis 200-300 mg of $Au_n(SG)_m$ product was dissolved in 6 mL of distilled water in round bottom flask. To this 2 mL of toluene, 0.3 mL of ethanol and 2 mL of phenylethane thiol was added and etched at 80 °C for about 70 hours. Ethanol facilitates the phase transfer of $Au_n(SG)_m$. After the core-size conversion is completed, the organic phase was separated and dried to remove solvent, followed by thorough washing with methanol (20 mL, 5 times). Finally, the product was extracted with toluene.

4.3.3.3 Synthesis of $Au_{36}(SPh\text{-}tBu)_{24}$ nanomolecules

Similar experimental conditions as for the synthesis of $Au_{38}(SCH_2CH_2Ph)_{24}$ were used. The crude reaction mixture was etched with 2 mL of *tert*-butylbenzenethiol for 18 hours at 80 °C.

In each of the initial two washing steps 10 mL of water and 10 mL of methanol was used to precipitate the nanomolecules and facilitate the washing step. Finally, the product was extracted with toluene.

4.3.3.4 Synthesis of $Au_{30}(S\text{-}tBu)_{18}$ nanomolecules

Similar experimental conditions as for the synthesis of $Au_{38}(SCH_2CH_2Ph)_{24}$ was used. The reaction mixture was etched with 2 mL of tert-butylthiol for about 48 hours at 80 °C. Organic phase was separated, dried to remove solvent and washed with methanol to remove excess thiol. The final product $Au_{30}(S\text{-}tBu)_{18}$, was extracted with toluene.

4.4 Core-size conversion to $Au_{38}(SCH_2CH_2Ph)_{24}$, $Au_{36}(SPh\text{-}tBu)_{24}$ and $Au_{30}(S\text{-}tBu)_{18}$

4.4.1 Background on $Au_n(SG)_m$ and Core-Size Conversion

Core-size conversion reactions, originally reported as etching, [133] and more recently referred to by a new name, size-focusing[116], is a post synthetic step that reduce the polydispersity of the initial synthetic material. In our previous work, we have shown that $Au_n(SR)_m$ organo-soluble nanoclusters core-size converts to monodispersed $Au_{36}(SPh)_{24}$ nanomolecules upon etching with excess thiophenol.[91] The core-size conversion is due to the difference in chemistry of ligands used for the core-size conversion reactions. In this work, we report synthesis of three distinct nanomolecules using the same water-soluble nanocluster mixture precursor, $Au_n(SG)_m$. It is significant to note that this simplified methodology can produce highly monodispersed end product with a good yield, which is a key to facilitate the use of these nanomolecules in applications in related disciplines and including the non-specialists / the broader chemical community. In order to obtain good yield and monodispersity of the end product, the gold to thiol molar ratio of the first synthesis step is found to be crucial.[91, 96] The composition of as synthesized water soluble $Au_n(SG)_m$ clusters were determined by Tsukuda and co-workers.[137] In their work,

they have used polyacrylamide gel electrophoresis and isolated different size clusters and determined by ESI-MS. Other important parameters are the reaction time and temperature. At elevated temperatures, fast kinetics is observed in ligand induced core-size conversion reactions. In general, a direct synthetic methodology produces a polydispersed mixture of nanomolecules. Ligand exchange reactions involving core-size conversions have been employed extensively to

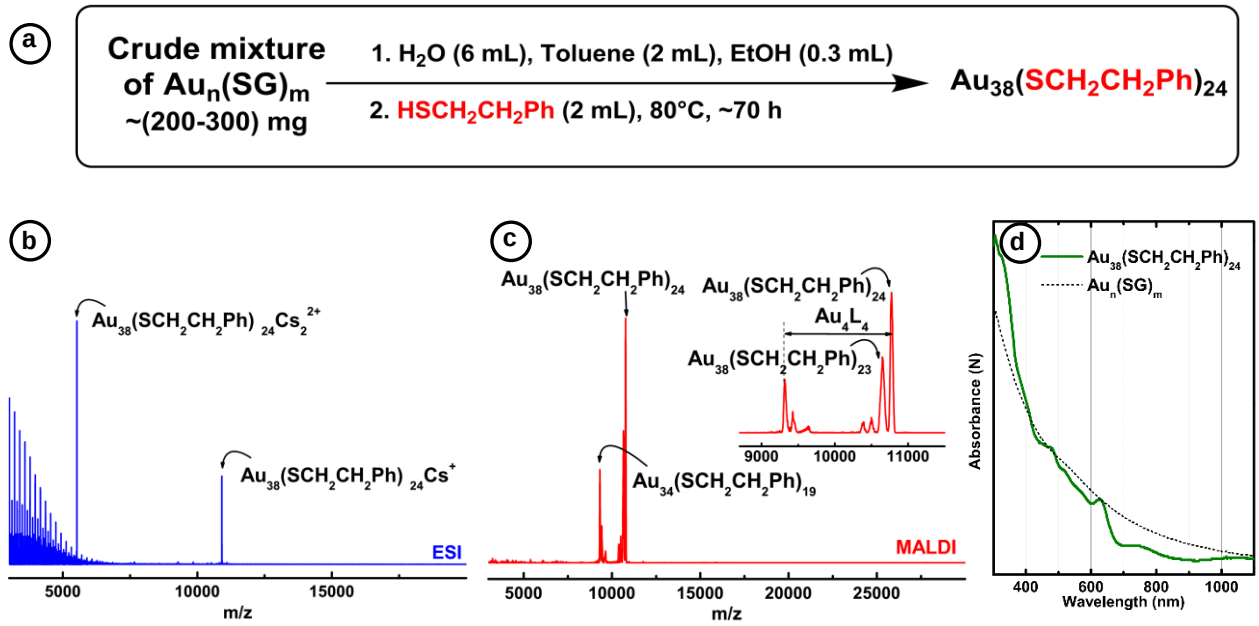

Figure 4.1. Synthesis and characterization of $Au_{38}(SCH_2CH_2Ph)_{24}$ nanomolecules. (a) The protocol for the synthesis of $Au_{38}(SCH_2CH_2Ph)_{24}$ nanomolecules. (b) ESI-MS compositional assignment of the analyte nanomolecule. $Cs(CH_3COO)$ clustering can be observed below 5000 m/z as $Cs(CH_3COO)$ was intentionally added to the sample to impart charge and analyte with one and two Cs^+ ion additions can be observed. (c) MALDI-MS shows high monodispersity of $Au_{38}(SCH_2CH_2Ph)_{24}$ and was intentionally fragmented analyte to show $Au_4(SCH_2CH_2Ph)_4$ loss. (c) UV-Vis-NIR absorption spectra illustrate the 1100 nm signature absorbance peak unique to the analyte.

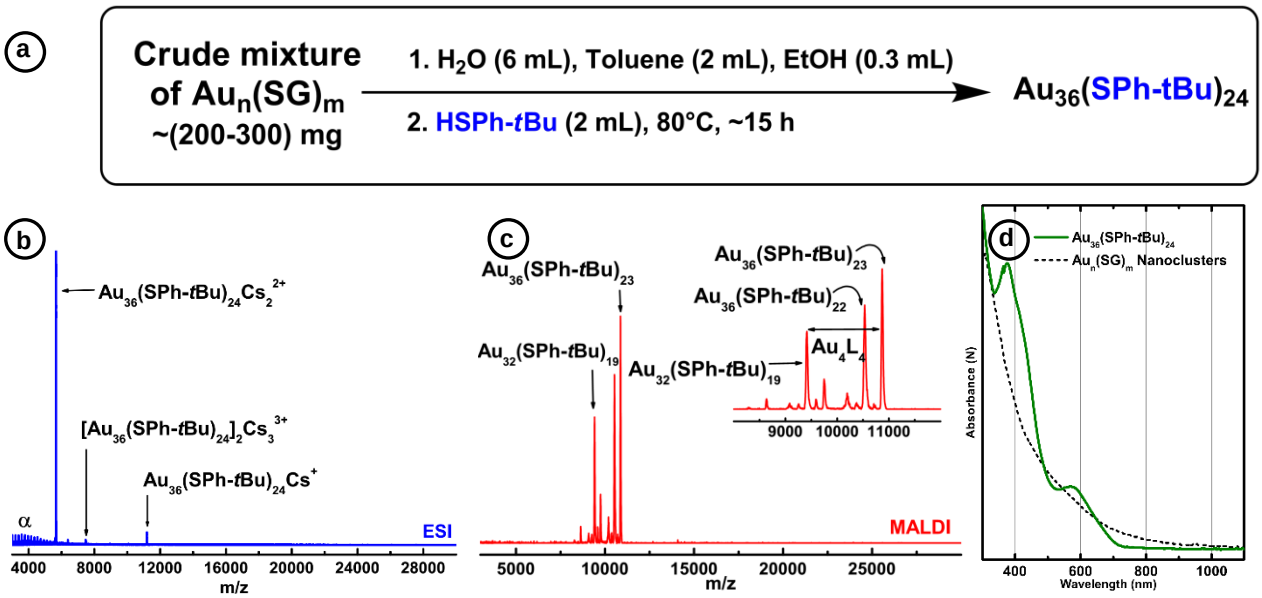

Figure 4.2. Synthesis and characterization of $Au_{36}(SPh\text{-}tBu)_{24}$ nanomolecules. (a) The protocol for the synthesis of $Au_{36}(SPh\text{-}tBu)_{24}$ nanomolecules. (b) ESI-MS compositional assignment of the analyte nanomolecule. $Cs(CH_3COO)$ clustering can be observed (peak marked by α) below 5000 m/z as $Cs(CH_3COO)$ was intentionally added to the sample to impart charge and analyte with one and two Cs^+ ion additions can be observed. Dimer of the analyte molecules was observed as a 3+ cesium adduct. (c) MALDI-MS shows purity of the sample and $Au_{36}(SPh\text{-}tBu)_{24}$ was intentionally fragmented to show $Au_4(SPh\text{-}tBu)_4$ loss. (d) UV-Vis-NIR absorption spectra illustrate the signature absorbance peaks at 375 and 570 nm unique to the $Au_{36}(SPh\text{-}tBu)_{24}$ analyte in contrast to the $Au_n(SR)_m$ nanoclusters formed in the initial stage of the reaction.

narrow down the polydispersity and synthesize new highly monodispersed nanomolecules. Qian and co-workers has developed a method to obtain a monodispersed $Au_{38}(SCH_2CH_2Ph)_{24}$ nanomolecules in large scale starting from $Au_n(SG)_m$ nanoclusters.[96] We have further studied and

developed this method to obtain other thermodynamically stable nanomolecules and the modified synthetic methodology is as referred in the experimental section. In addition, we have investigated and extended the central idea of simple synthetic protocol to explore and investigate other ligand systems as well. (Figure S2-S6 in the Appendix C).

4.4.2 Core-Size Conversion of $Au_{38}(SCH_2CH_2Ph)_{24}$

In a typical reaction, when the thermochemical treatment on the $Au_n(SG)_m$ begins, we observed an initial phase transfer within first 20 minutes and black gold nanoclusters transfer from aqueous to organic phase. Immediately after the phase transfer, we observe a mixture of nanoclusters and not one single species that is evidenced from the exponentially decaying featureless optical spectra (Fig. 4.1b-black curve). Typically, this mixture is composed of $Au_{144}(SR)_{60}$, $Au_{102\text{-}105}(SR)_{43\text{-}46}$, $Au_{67}(SR)_{35}$, $Au_{38}(SR)_{24}$ and $Au_{25}(SR)_{18}$ and other metastable nanoclusters.[42, 85] In the case of $Au_{38}(SCH_2CH_2Ph)_{24}$, continuous etching at 80 °C for about 70 hours result in decomposition or complete core-size conversion of the meta stable clusters to thermodynamically stable $Au_{38}(SCH_2CH_2Ph)_{24}$ nanomolecules, with a synthetic yield of ~21 % (Au atom basis). Mass spectrometric characterization of the product reveals the purity and the composition (Fig. 4.1). Both MALDI-MS and UV-Vis-NIR characterization reflects the high purity of the product $Au_{38}(SCH_2CH_2Ph)_{24}$ nanomolecules. It should be noted that product shows the peak for $Au_{38}(SCH_2CH_2Ph)_{24}$, in addition to its primary fragment, $Au_{34}(SCH_2CH_2Ph)_{19,}$ due to loss of $Au_4(SCH_2CH_2Ph)_4$.

4.4.2 Core-Size Conversion of $Au_{36}(SPh\text{-}tBu)_{24}$

In contrast to synthesis of $Au_{38}(SCH_2CH_2Ph)_{24}$, etching reaction of $Au_n(SG)_m$ crude with *tert*-butylbenzenethiol is rapid and fast kinetics were observed as the reaction was completed and monodispersed $Au_{36}(SPh\text{-}tBu)_{24}$ nanomolecules were formed after 18 hours of etching at 80 °C.

Fast kinetics could be due to higher acidity of the HSPh-*t*Bu ligand compared to PET (pKa = 6.6 and pKa ≈ 10 respectively). Due to aromatic nature of the *tert*-butylbenzenethiol ligand, $Au_n(SG)_m$ nanoclusters core-size convert to thermodynamically most stable $Au_{36}(SPh\text{-}tBu)_{24}$ nanomolecules upon thermochemical treatment, with significantly high yield of ~25 % (Au atom basis). The composition of the core-size conversion reaction was confirmed by ESI-MS and high monodispersity was confirmed by the MALDI-MS and UV-Vis-NIR characterization. Figure 4.1a illustrates MALDI mass spectrum of $Au_{36}(SPh\text{-}tBu)_{24}$ analyte nanomolecules and it should be noted that molecular peak is not observed, as shown in literature before,[63, 91-92, 138] due to labile nature of the aromatic ligand. Prominent optical absorbance feature at 600 nm and 400 nm matching the literature spectra[91] confirms the monodispersity of the as-synthesized $Au_{36}(SPh\text{-}tBu)_{24}$ nanomolecules without further purification. We note that all existing literature method for preparation of $Au_{36}(SPh\text{-}tBu)_{24}$ involves either expensive starting material, $Au_{38}(SCH_2CH_2Ph)_{24}$, (ref [92]) or extensive purification[117] or suffers from low yield and poor shelf-life.[91]

4.4.3 Core-Size Conversion of $Au_{30}(S\text{-}tBu)_{18}$

We systematically investigated the core-size conversion reaction of the starting material, $Au_n(SG)_m$ with bulky thiol ligands such as tert-butylthiol. It is interesting to note that, unlike the PET and thiophenol, tert-butylthiol induced core-size conversion is governed by steric effect of the ligand rather than electronic effect and results in formation of $Au_{30}(S\text{-}tBu)_{18}$ nanomolecules. Due to bulkiness, the ligand exchange and core-size conversion reaction progress rather slowly. After, 48 hours of thermochemical treatment high monodisperse product, $Au_{30}(S\text{-}tBu)_{18}$ nanomolecules were formed with a synthetic yield of ~10 % (Au atom basis) and confirmed by the MALDI-MS and optical spectroscopy (Fig. 4.1b). ESI-MS of the final product confirms the

composition of the as synthesized analyte nanomolecules as $Au_{30}(S\text{-}t\text{Bu})_{18}$. We note that the existing synthesis methods for $Au_{30}(S\text{-}t\text{Bu})_{18}$ involves SEC separation.[19-20]

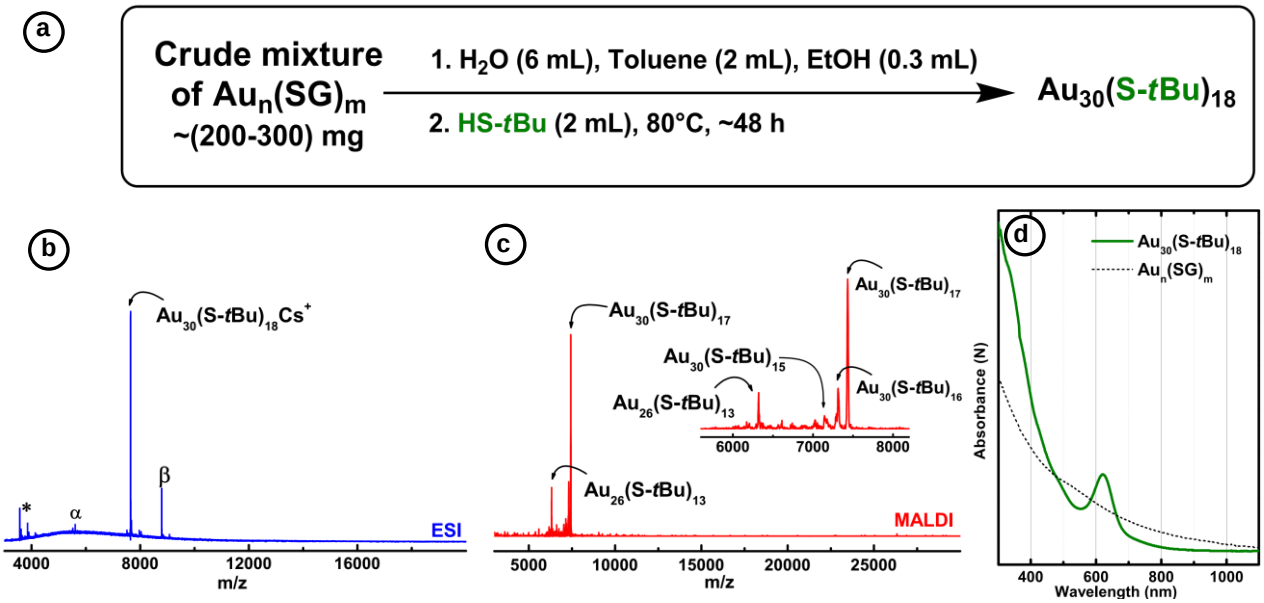

Figure 4.3. Synthesis and characterization of $Au_{30}(S\text{-}t\text{Bu})_{18}$ nanomolecules. (a) The protocol for the synthesis of $Au_{30}(S\text{-}t\text{Bu})_{18}$ nanomolecules. (b) ESI-MS compositional assignment of the analyte nanomolecule. $Cs(CH_3COO)$ was intentionally added to the sample to impart charge and analyte with one Cs^+ ion additions can be observed as $Au_{30}(S\text{-}t\text{Bu})_{18}Cs^+$. *,α and β indicates trace amount of impurities present in the sample. It is important to note that these species were not observed in MALDI-MS. (c) MALDI-MS of $Au_{30}(S\text{-}t\text{Bu})_{18}$ analyte and intentionally fragmented to show $Au_4(S\text{-}t\text{Bu})_4$ loss and purity of the sample. (d) UV-Vis-NIR absorption spectra illustrate the 620 nm signature absorbance peak unique to the analyte.

4.5 Conclusion

In summary, we have demonstrated effective facile synthetic protocols for three uniquely different gold nanomolecules, $Au_{38}(SCH_2CH_2Ph)_{24}$, $Au_{36}(SPh\text{-}t\text{Bu})_{24}$ and $Au_{30}(S\text{-}t\text{Bu})_{18}$, with high

monodispersity and good yield. The focus of the work is not to prepare new sized nanomolecules, but to report a simple, reproducible, robust synthetic protocol for $Au_{38}(SCH_2CH_2Ph)_{24}$, $Au_{36}(SPh\text{-}t\text{Bu})_{24}$ and $Au_{30}(S\text{-}t\text{Bu})_{18}$ starting from a common precursor. The two-step synthetic methodology is exclusive as the same starting $Au_n(SG)_m$ nanoclusters produces thermodynamically stable three distinct nanomolecules. Overall, the key advance of the synthetic methodology is the lack of sophisticated purification techniques, making it a universal protocol accessible for wide range of researchers, which is a key factor in improving the utility of these nanomolecules in various applications.

CHAPTER 5

AROMATIC THIOLATE PROTECTED $Au_{38}(SPh)_{24}$

Part of the text and figures in this chapter are extracted from the following publication: Rambukwella, M.; Burrage, S.; Neubrander, M.; Baseggio, O.; Aprà, E.; Stener, M.; Fortunelli, A.; Dass, A., *J. Phys. Chem. Lett.* **2017**, 8, 1530-1537.

5.1 Abstract

$Au_{38}(SR)_{24}$ is one of the most extensively investigated gold nanomolecules along with $Au_{25}(SR)_{18}$ and $Au_{144}(SR)_{60}$. However, so far it has only been prepared using aliphatic-like ligands, where R = $–SC_6H_{13}$, $-SC_{12}H_{25}$ and $–SCH_2CH_2Ph$. $Au_{38}(SCH_2CH_2Ph)_{24}$ when reacted with HSPh undergoes core-size conversion to $Au_{36}(SPh)_{24}$, and existing literature suggest that $Au_{38}(SPh)_{24}$ cannot be synthesized. Here, contrary to prevailing knowledge, we demonstrate that *$Au_{38}(SPh)_{24}$ can be prepared* if the ligand exchanged conditions are optimized, under delicate conditions, without any formation of $Au_{36}(SPh)_{24}$. Conclusive evidence is presented in the form of MALDI-MS, ESI-MS characterization, and optical spectra of $Au_{38}(SPh)_{24}$ in a solid glass form showing distinct differences from that of Au_{38}(S-aliphatic)$_{24}$. Theoretical analysis confirms experimental assignment of the optical spectrum and shows that the stability of $Au_{38}(SPh)_{24}$ is comparable to that of its aliphatic analogues, but results from different physical origins, with a significant component of ligand-ligand attractive interactions.

Author Contributions

Milan Rambukwella developed the ligand exchange experimental design to obtain $Au_{38}(SPh)_{24}$ nanomolecules, conducted the experiments, mass spectrometric, UV-Vis-NIR absorption and electrochemical experiments. Shayna Burrage, Marie Neubrander conducted conducted experiments to test reproducibility of the experimental design and synthesized $Au_{38}(SPh)_{24}$ for characterization. Oscar Baseggio, Edoardo Apra, Mauro Stener and Alessandro Fortunelli conducted computational studies. Amala Dass assisted in experimental design, structure of the manuscript and data analysis. All the authors made substantial, direct and intellectual contribution to the work in the manuscript preparation.

5.2 Introduction

Gold nanomolecules[5, 139] are ultra-small gold nanoparticles <2 nm in size with a precise number of gold atoms protected by a specific number of thiolate ligands with distinct physical and chemical properties. They have become a topic of great interest in chemistry due to their atomic monodispersity (± 0 atom variation), molecule-like properties[6] and stability arising from geometric[7] and electronic shell[60] closings. These nanomolecules can be used in a wide variety of applications and can be made reproducibly and characterized by commonly available mass spectrometric, spectroscopic and electrochemical methods.[6, 55, 58, 112, 140-144]

In previous work, we have published the *first report* of aromatic ligand induced core-size conversion of $Au_{67}(SR)_{35}$ and $Au_{103\text{-}105}(SR)_{44\text{-}46}$ nanocluster mixture to $Au_{36}(SPh)_{24}$, with its X-ray crystal structure reported subsequently.[18, 91] This reaction was shown to proceed via a Au_{38} core as an intermediate in this reaction pathway. When–SCH_2CH_2Ph ligand was replaced by the –SPh ligand, the nanomolecule underwent an $Au_{38} \rightarrow Au_{36}$ core size conversion. This is believed to have

been caused by the exchange of the aliphatic for the aromatic ligand, which being aromatic, bulkier and rigid, would distort the Au_{38} structure. $Au_{38}(SR)_{24}$ core-size conversion to $Au_{36}(SR)_{24}$ has been reported, under harsh etching conditions (Scheme 5.1(b)). It was observed after an aromatic thiophenol ligand exchange of 10, the Au_{38} intermediate converts to Au_{36} core. [91] Another subsequent report verified this conversion using Au_{38} as a starting material, and studying ligand induced core-size conversion of Au_{38} to Au_{36} in detail, in the presence of tertbutylbenzene thiophenol (TBBT) at elevated temperature (80 °C).[92] The reaction proceeds via a disproportionation mechanism with formation of a reaction intermediate, $Au_{40}(SR)_{26}$. We have reported the thiophenol induced core-size conversion of $Au_{144}(SR)_{44}$ to $Au_{99}(SPh)_{42}$ and a $Au_{103-104}(SR)_{44-45}$ mixture to $Au_{102}(SPh)_{44}$, which shows evidence for the aromatic ligand induced core-size conversion of a multiple species to one core-size, Au_{102}.(Ref.[38, 81]) Also the aromatic ligand effect was evident by the core-size conversion of $Au_{144}(SR)_{60}$ to $Au_{133}(S\text{-}tBuPh)_{52}$ with aromatic ligand tert-butylbenzenethiol(HS-tBuPh).(Ref.[21])

Several questions however remain: can we execute a systematic ligand exchange protocol to obtain all aromatic thiol protected $Au_{38}(SR)_{24}$ nanomolecules? What is the mechanism of the reaction and would we observe a stable intermediate formation in the mechanism? How would extended conjugation with aromatic ligands modify electronic effects in the nanomolecule and how significant would it influence the band gap energy? How would aromaticity affect overall electronic excitation?

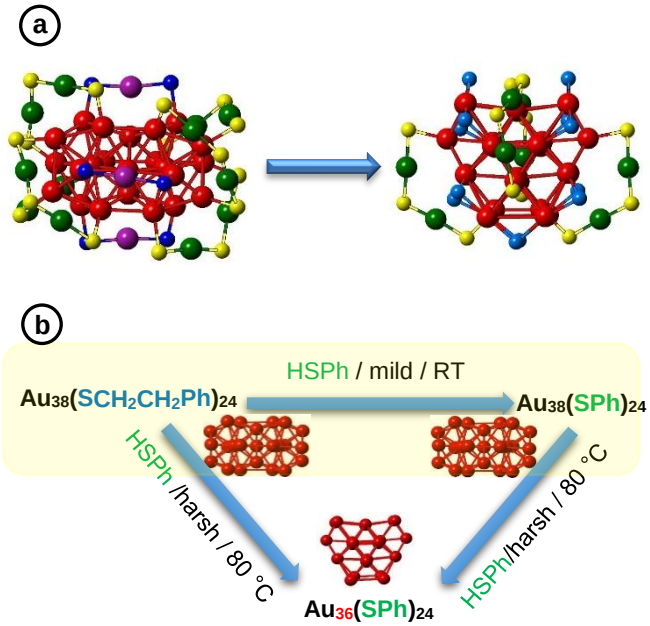

Scheme 5.1. $Au_{38}(SPh)_{24}$ nanomolecules: (a) Crystal structures of $Au_{38}(SCH_2CH_2Ph)_{24}$ and $Au_{36}(SPh)_{24}$ (red - core Au, green-dimeric staple Au, purple - monomeric staple Au, yellow-dimeric staple S, dark blue-monomeric staple S, light blue - bridging S). (b) $Au_{38}(SCH_2CH_2Ph)_{24}$ leading to form of either $Au_{38}(SPh)_{24}$ or $Au_{36}(SPh)_{24}$ based on reaction conditions.

$Au_{38}(SR)_{24}$ readily forms when aliphatic-like ligands are used in direct synthesis[145-146] or etching,[85, 147] whereas in the presence of aromatic ligands the Au_{38} core is found to be unstable, converting to Au_{36}.(Ref.[91-92]) Thus existing literature suggests that all-aromatic $Au_{38}(SPh\text{-}X)_{24}$ nanomolecules cannot be synthesized.

To provide answers to these questions, here we study the ligand exchange and core-size conversion mechanism involved and the role of a particular ligand by executing a synthetic protocol on $Au_{38}(SR)_{24}$ nanomolecules, and we report the first synthesis of $Au_{38}(SPh)_{24}$ using a systematic two-step ligand exchange process on $Au_{38}(SCH_2CH_2Ph)_{24}$ under *mild* reaction conditions. The reaction method was executed to synthesize monodisperse all aromatic ligand

protected $Au_{38}(SPh)_{24}$ species. Mass spectrometry and spectroscopic methods were utilized to verify the product. The product was then subject to low-temperature spectroscopic studies to obtain more insight into the electronic structure. These data are accompanied by a systematic theoretical study of the nanomolecule and its energetics, justifying the thermodynamic stability of aromatic $Au_{38}(SR)_{24}$ species and rationalizing the reasons for its larger sensitivity to environmental conditions.

5.3 Method

5.3.1 Synthesis

$Au_{38}(SCH_2CH_2Ph)_{24}$, was synthesized according to a previously reported procedure.[96] Complete aromatic ligand exchange on $Au_{38}(PET)_{24}$ nanomolecules to form $Au_{38}(SPh)_{24}$ without core-size conversion was performed in two main steps involving: (i) a first ligand exchange with neat etching with excess thiophenol under mild conditions gives partially exchanged intermediate and (ii) a second neat etching to achieve complete ligand exchange to form $Au_{38}(SPh)_{24}$. First, $Au_{38}(SCH_2CH_2Ph)_{24}$ was reacted with excess thiophenol (HSPh, 100 μL/ 1mg) at room temperature for 1.5 hours. The product was then washed with methanol and subjected to a successive chemical treatment under same conditions for 2 hours. (see Scheme 5.2 and Fig. 5.1) The final product was washed with methanol several times and extracted with toluene.

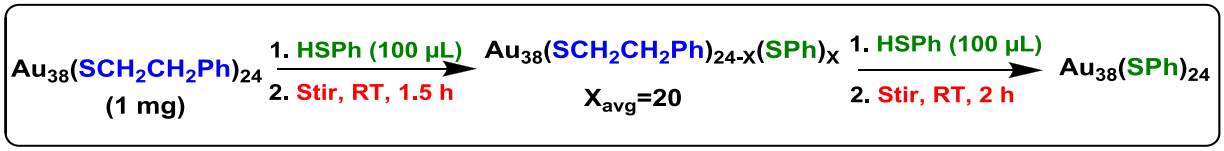

Scheme. 5.2. Synthetic procedure for monodispersed $Au_{38}(SPh)_{24}$. In the first step, the reaction with HSPh yields partially exchanged $Au_{38}(SCH_2CH_2Ph)_{24-x}(SPh)_x$, where x_{avg} is 20. Successive second step yields completely exchanged $Au_{38}(SPh)_{24}$.

5.3.2 Instrumentation

A Voyager DE PRO mass spectrometer was used to acquire MALDI-TOF mass spectra using DCTB[83] matrix. Compositional analysis was performed with Electrospray Ionization mass spectra (ESI-MS), collected from Waters Synapt HDMS with THF as the solvent and cesium acetate was added to facilitate ionization via. cesium adduct formation of the analyte. Temperature-dependent UV−Vis−NIR absorption data were measured with an UV−Vis−NIR Cary 5000 and JANIS VNF-100 low-temperature cryostat using cyclohexane/cyclopentane 1:1 (v/v)as the solvent, and a Lakeshore Cyotronics temperature controller was used for temperature-dependent absorption measurements.

5.3.3 Computational Approach

Geometry optimizations were performed using the Quantum Espresso code [148] and ultrasoft pseudopotentials[149]. A semiempirical correction[101] was added to the Perdew-Burke-Ernzerhof (PBE)[150] exchange and correlation (xc-) functional to take into account the dispersion interaction between organic residues. The cutoff for the plane-wave representation of the wave function and the density were set to 40 Ry and 400 Ry, respectively. In the local geometry optimizations, some of the atoms were kept frozen into configurations derived from X-ray measurements. In detail: in $Au_{38}(SPh)_{24}$ the Au_{23} core was taken from the $Au_{38}(SCH_2CH_2Ph)_{24}$ geometry reported in Ref. [51] (the rationale for this choice is that the PBE xc-functional describes reasonably well the Au-S, S-C, and C-H bonding but is known to overestimate Au-Au distances). This experimental $Au_{38}(SCH_2CH_2Ph)_{24}$ geometry was also used to input the coordinates of all Au and S atoms in the relaxation of $Au_{38}(SCH_2CH_2Ph)_{24}$. From the relaxed geometry thus derived, a model $Au_{38}(SCH_3)_{24}$ system was obtained by replacing $-CH_2CH_2Ph$ with $-CH_3$ residues, and then relaxing only the atomic coordinates of the methyl groups.

Optical spectra were simulated at the TDDFT level, employing the recently developed complex polarizability algorithm, [151]implemented in a modified local version of the ADF code[152]. Such algorithm is more suited with respect to the conventional Casida scheme to calculate the spectrum for large systems to high energy, since does not suffer of the limitations connected with the Davidson diagonalization. The algorithm extracts the spectrum from the imaginary part of the complex dynamical polarizability, calculated point by point at the values of the light frequency. A Slater Type Orbitals (STO) basis set of Triple Zeta plus Polarization (TZP) quality has been employed. The asymptotically correct LB94 exchange-correlation potential[153] has been employed for the resolution of the Kohn-Sham equations. The exchange-correlation kernel in the TDDFT equations is approximated by ALDA[154] taking the derivative of the VWN LDA xc-potential[155]. The calculated spectra are smoothed by adding a small imaginary part (0.075 eV) to the real part of the frequency, corresponding to a lorentzian broadening with the same HWHM. All the calculations have been performed at scalar relativistic level with Zero Order Relativistic Approximation (ZORA).[156]

5.4 Mass Spectrometry and Optical Spectroscopic Characterization

In previous work, extensive theoretical and experimental studies have been reported on $Au_{38}(SR)_{24}$ and $Au_{36}(SR)_{24}$ nanomolecules. Single crystal X-ray diffraction studies have revealed their corresponding total structure (Scheme 5.1(a), Table 5.1). $Au_{38}(SR)_{24}$ nanomolecules have a fused bi-icosahedral Au_{23} inner core protected with three $Au(SR)_2$ monomeric staples and six $Au_2(SR)_3$ dimeric staples.[51] In contrast $Au_{36}(SR)_{24}$ nanomolecules possess a Au_{28} core with four interpenetrated cuboctahedrons, protected with four dimeric staples, and twelve bridging sulfur that can also be viewed as another set of four dimeric staples (SPh-tBu[63], SPh).

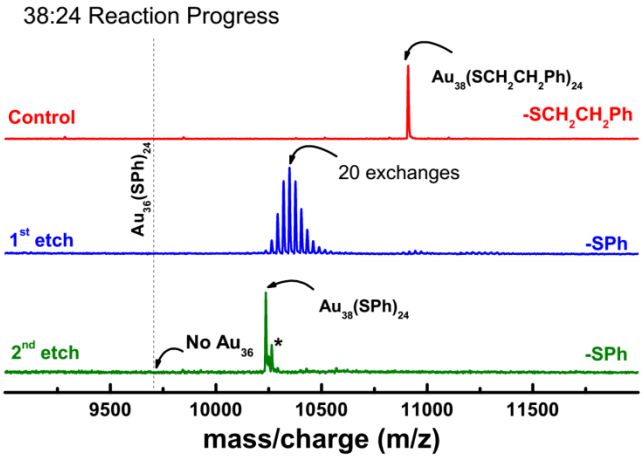

Figure 5.1. ESI mass spectra of the reaction between $Au_{38}(SCH_2CH_2Ph)_{24}$ and HSPh under *optimized mild* conditions to form $Au_{38}(SPh)_{24}$. First neat etching leads to $Au_{38}(SCH_2CH_2Ph)_{24-x}(SPh)_x$, a partial thiophenol ligand exchange, where $x_{avg} = 20$. Second etching gives the complete formation of $Au_{38}(SPh)_{24}$. All species are observed as Cs^+ adducts. No signal was observed for $Au_{36}(SPh)_{24}$. The peak marked by the asterisk depicts trace amount of $Au_{38}(SPh)_{23}(SCH_2CH_2Ph)_1$.

Table 5.1. Comparison of $Au_{38}(SCH_2CH_2Ph)_{24}$ and $Au_{36}(SPh)_{24}$ nanomolecules.

Gold Sulfur	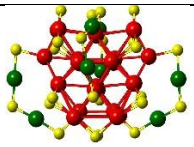	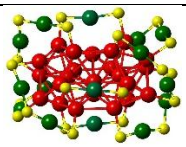
	$Au_{36}(SPh)_{24}$	**$Au_{38}(SCH_2CH_2Ph)_{24}$**
Symmetry	D_{2d}	D_3
Ligand Type	Aromatic	Aliphatic
Core	28	23
Geometry	Cuboctahedron	bi-icosahedron
Monomeric staples [SR-Au-SR]	0	3
Dimeric staples [SR-Au-SR-Au-SR]	4	6
Bridging thiols [SR]	12	0

Thiophenol protected $Au_{38}(SPh)_{24}$ nanomolecules were synthesized via ligand exchange on precursor $Au_{38}(SCH_2CH_2Ph)_{24}$ (Appendix D Scheme S1). The precursor $Au_{38}(SCH_2CH_2Ph)_{24}$ nanomolecules was reacted with neat thiophenol ligand at room temperature (Scheme 5.2) in two stages: (1) In the first stage a rapid ligand exchange with the $-SCH_2CH_2Ph$ was observed. Under these conditions, after 1.5 hours average of 20 ligand exchanges can be achieved with no core-size conversion of $Au_{38}(SR)_{24}$ to $Au_{36}(SR)_{24}$. Note that, if the reaction is carried out for more than 1.5 hours it would result in core-size conversion of the starting material Au_{38} to $Au_{36}(SR)_{24}$. (2) In the second step, a second successive ligand exchange under identical conditions was carried out after purification of the product from first etch (Scheme 5.2, Fig. 5.1). No $Au_{36}(SR)_{24}$ species was observed. An all -aromatic $Au_{38}(SPh)_{24}$ was observed after 2 hours as evidenced by mass spectrometry shown in Fig. 5.2.

In Fig. 5.2a, the ESI mass spectrum of the product from step 2 upon addition of cesium acetate to facilitate ionization shows singly charged $[Au_{38}(SPh)_{24} \bullet Cs]^{+}$ and doubly charged, $[Au_{38}(SPh)_{24} \bullet 2Cs]^{2+}$ species at 10,238 and 5,186 m/z respectively. The inset shows the comparison of the experimental and theoretical peaks for the 2+ species. The inset shows the theoretically calculated +1 peak against the experimental data. The Fig. 5.2b. shows the MALDI mass spectra illustrating the molecular purity of the analyte, $Au_{38}(SPh)_{24}$. In the product, $Au_{36}(SPh)_{24}$ was not observed in this analysis, instead one ligand fragmented $Au_{38}(SPh)_{23}$ species was observed as noted before.[91] The inset illustrates the minor fragmentation at low laser due to labile nature of the thiophenol ligand.

MALDI-MS obtained at high laser fluence is a good indication of purity of nanomolecules. The characteristic fragmentation signature having $Au_4(SR)_4$ is prominently observed in small nanomolecules such as $Au_{25}(SR)_{18}$, $Au_{36}(SR)_{24}$ and $Au_{38}(SR)_{24}$ and can be used as an identification

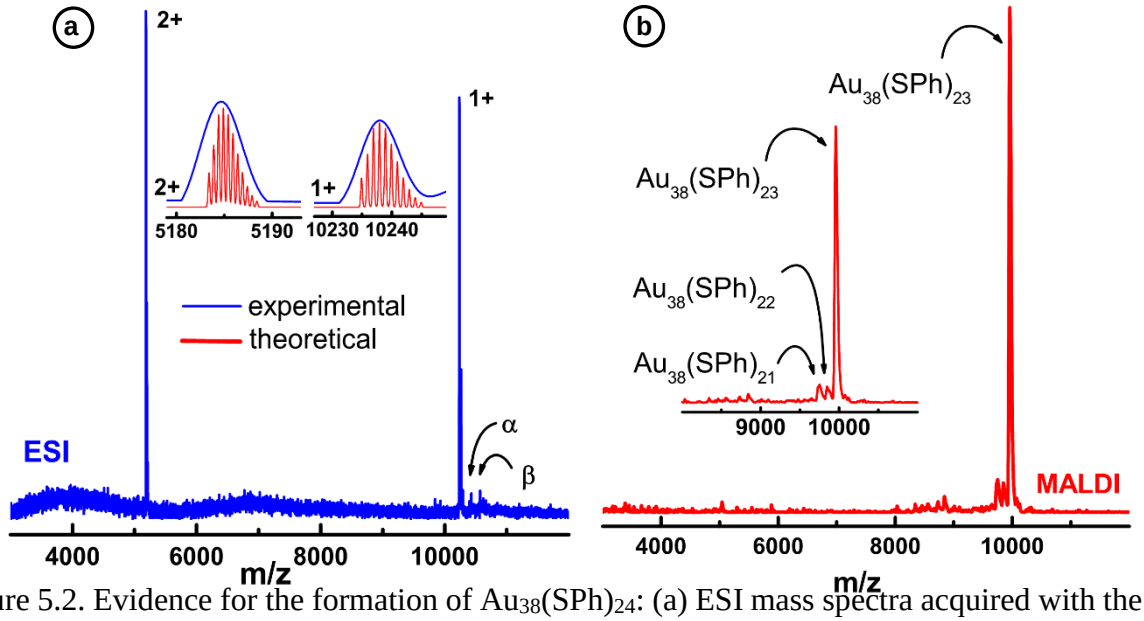

Figure 5.2. Evidence for the formation of $Au_{38}(SPh)_{24}$: (a) ESI mass spectra acquired with the addition of cesium acetate (blue), and inset shows the comparison of experimental and theoretical peaks for the 2+ species where peaks marked by α and β represents successive $CsCH_3COO$ addition on to the molecular peak; (b) MALDI mass spectra (red) and expansion of the fragmentation pattern.

method of these nanomolecules, especially in a mixture, because the fragment peak is more prominent at higher laser fluence.[157-158] Figure 5.3a,b illustrate a detailed comparison of starting material $Au_{38}(SR)_{24}$ against a pure $Au_{36}(SR)_{24}$ 'control' sample showing evidence of exclusive formation of $Au_{38}(SPh)_{24}$ and absence of $Au_{36}(SR)_{24}$ in the final product. Pure samples of $Au_{38}(SCH_2CH_2Ph)_{24}$, ligand exchanged $Au_{38}(SPh)_{24}$ and $Au_{36}(SPh)_{24}$ nanomolecules were intentionally fragmented to observe the characteristic fragmentation (Fig. 5.3a and 5.3b). In the final ligand exchanged $Au_{38}(SPh)_{24}$ product, we did not observe $Au_{36}(SPh)_{23}$ or $Au_{32}(SPh)_{19}$ species which indicates absence of $Au_{36}(SPh)_{24}$. Also, UV-Vis-NIR absorption profile of the product further illustrates absence of well-defined optical features characteristic to $Au_{36}(SPh)_{24}$ and $Au_{38}(SCH_2CH_2Ph)_{24}$ nanomolecules (Fig. 5.3c). Optical spectra of $Au_{38}(SPh)_{24}$ shows 3

distinct features from 425 to 725 nm; peak at 470 nm, 560 nm and 655 nm, where $Au_{38}(SCH_2CH_2Ph)_{24}$ shows 2 distinct absorption peaks at 445 nm and 620 nm. In contrast latter two nanomolecules, $Au_{36}(SPh)_{24}$ shows a single absorption peak at 575 nm.

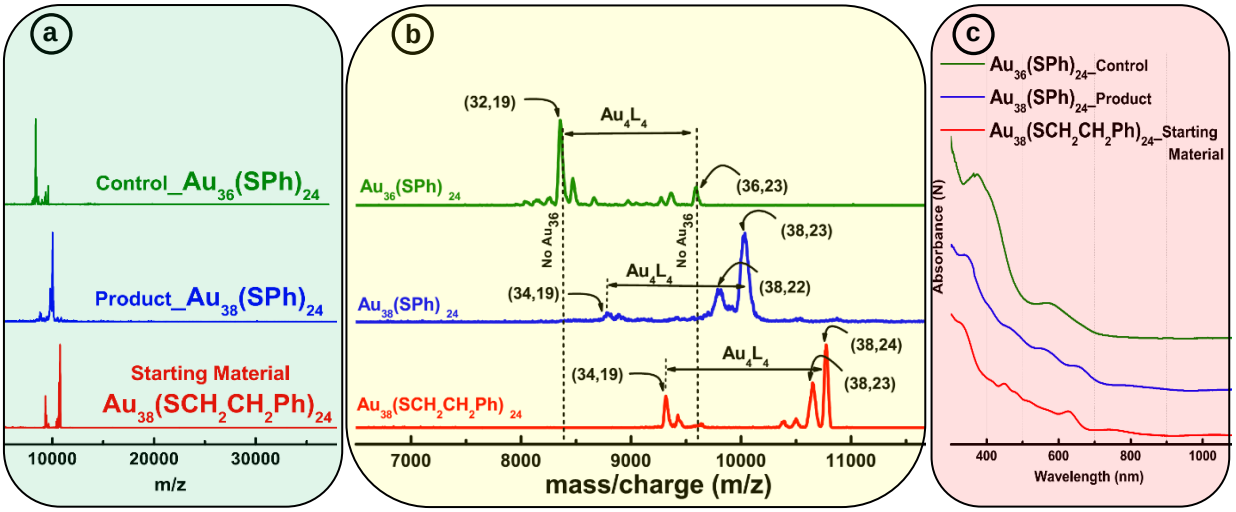

Figure 5.3. Evidence of the formation of $Au_{38}(SPh)_{24}$ and absence of $Au_{36}(SPh)_{24}$. (a) MALDI-TOF mass spectrum of the starting material, $Au_{38}(SCH_2CH_2Ph)_{24}$, and the final product, $Au_{38}(SPh)_{24}$, compared with a control sample, $Au_{36}(SPh)_{24}$. The data shows that only $Au_{38}(SPh)_{24}$ was synthesized. (b) MADLI-TOF mass spectrum showing the fragmentation patterns of three nanomolecules. (c) comparison of UV-Vis-NIR absorption spectrum features of $Au_{38}(SCH_2CH_2Ph)_{24}$, $Au_{38}(SPh)_{24}$, and $Au_{36}(SPh)_{24}$.

Temperature dependent UV-Vis-NIR absorption spectra were measured in a solvent mixture of cyclohexane/cyclopentane 1:1 (v/v). Spectra shows increased intensities with a significant bathochromic shift in absorption maxima (red shift) at 78 K compared to room temperature, 298 K (Fig. 5.4). Absorption intensity spectra plotted as the photon energy shows well resolved 11 distinct peaks and interestingly the peak at 1.7 eV was resolved into two new peaks. The temperature dependent optical features of $Au_{38}(SCH_2CH_2Ph)_{24}$ shows that upon reducing the temperature the band gap increases.[159] In contrast, $Au_{38}(SPh)_{24}$ nanomolecules have

an extended conjugation due to presence of the aromatic ring adjacent to the Au-S bridge. This results in a bathochromic shift and thereby reducing the band gap energy of the nanomolecule.

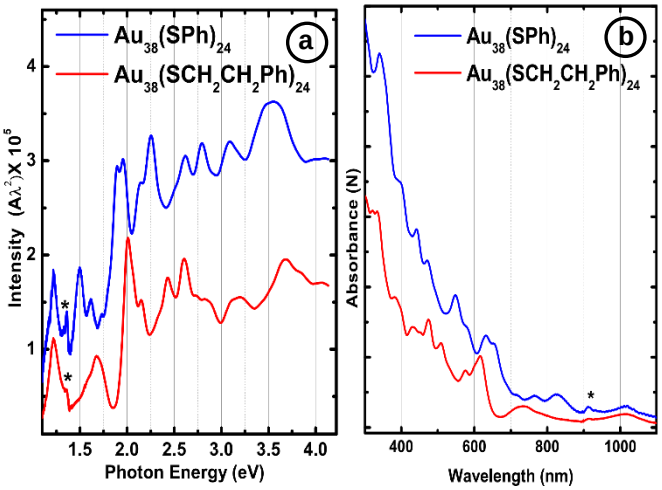

Figure 5.4. UV-Vis-NIR optical spectrum of $Au_{38}(SPh)_{24}$ and $Au_{38}(SCH_2CH_2Ph)_{24}$ at 78K(a) energy plot (b) absorption spectra. Peaks marked by asterisk depicts instrumental artifact.

5.5 Stabilization $Au_{38}(SPh)_{24}$ of by aromatic thiolate ligands

The structure and stability of $Au_{38}(SPh)_{24}$ were investigated theoretically. Starting from the experimentally determined crystal geometry of $Au_{38}(SCH_2CH_2Ph)_{24}$,[51] and after replacing the CH_2CH_2Ph with Ph residues, a local geometry optimization produced a geometry that was then used for property prediction and energy analysis (the full cluster Cartesian coordinates are reported in the Appendix D). A relaxed geometry of $Au_{38}(SCH_2CH_2Ph)_{24}$ was also derived, as well as that of a $Au_{38}(SCH_3)_{24}$ cluster obtained from the relaxed geometry of $Au_{38}(SCH_2CH_2Ph)_{24}$ by replacing CH_2CH_2Ph with CH_3 residues and then optimizing their coordinates (keeping Au and S atoms frozen). Structure optimization does not bring about major changes in the $Au_{38}(SPh)_{24}$ cluster configuration, although some of the Au atoms in the –S-Au-S-Au-S– staples move slightly away

from the Au core, as shown in Figure S6 of the Appendix D. Here we assume that the replacement of aliphatic with aromatic ligands does not change the basic structure of the cluster, although we cannot exclude reconstructions [such as in Au_{28} (Ref.[160])].

An important question concerning $Au_{38}(SPh)_{24}$ is whether there are energetic reasons, e.g., connected with electronic conjugation effects, which destabilize this gold nanomolecule with aromatic ligands. To assess the effects of electronic conjugation on energetics, we use energy decomposition and system comparison procedures proposed in previous work.[21, 38, 74, 78-79, 86] As a system to compare with, we use the aliphatic $Au_{38}(SCH_3)_{24}$ cluster derived from $Au_{38}(SCH_2CH_2Ph)_{24}$ as described above.

We first consider fragmentation reactions[86] for both the original and system-compared[21] clusters:

$$Au_{38}(SPh)_{24} \rightarrow Au_{38}[\text{fromPh}] + (SPh)_{24} \quad \Delta E = 82.5 \text{ eV} \qquad (5.1)$$

$$Au_{38}(SCH_3)_{24} \rightarrow Au_{38}[\text{fromMet}] + (SCH_3)_{24} \quad \Delta E = 81.8 \text{ eV} \qquad (5.2)$$

where the coordinates of the Au_{38} and $(SR)_{24}$ fragments in the right-hand-side of the equations are frozen in their interacting configurations. Fragmentation energies are sizeable, but with only a minor ≈1% difference between them. This occurs despite the fact that the atomization energies of the metal fragments are quite different:

$$Au_{38}[\text{fromPh}] \rightarrow 38\ Au \quad \Delta E = 89.3 \text{ eV} \qquad (5.3)$$

$$Au_{38}[\text{fromMet}] \rightarrow 38\ Au \quad \Delta E = 93.3 \text{ eV} \qquad (5.4)$$

due to the detachment of Au atoms in the staples from the metal core in $Au_{38}(SPh)_{24}$ (Figure S6) which destabilizes the Au_{38} fragment. However, the loss of Au-Au binding is compensated by the strengthening of S-Au bonds[74, 78], finally resulting in an overall similar energy balance.

Next we consider the fragmentation of the crown or shell of ligands[86]:

$$(SPh)_{24} \rightarrow 24 \times SPh \quad \Delta E = 3.46 \text{ eV} \tag{5.5}$$

$$(SCH_3)_{24} \rightarrow 24 \times SCH_3 \quad \Delta E = 2.98 \text{ eV} \tag{5.6}$$

where the 24 SR thiols are still frozen internally but are separated at infinite distance in the processes of Eqs. (5.5, 5.6). This fragmentation energy contains two terms: residual S-S binding (the sulfur atoms of thiols in the interacting configuration of the MPC are at binding distance) and dispersion/repulsion interactions between the organic residues. The latter contribution is negligible for $(SCH_3)_{24}$, but it can substantial for $(SPh)_{24}$: we evaluate it by transforming the SPh ligands into HPh (i.e., thiols into benzene molecules) and calculating the fragmentation energy of the so-obtained benzene crown [21, 38]:

$$(HPh)_{24} \rightarrow 24 \times HPh \quad \Delta E = 2.42 \text{ eV} \tag{5.7}$$

The sizeable value of 2.42 eV for this process proves that part of the energetic stability of $Au_{38}(SPh)_{24}$ – which makes it similar to its aliphatic $Au_{38}(SCH_3)_{24}$ analogue in terms of formation energy from Eqs. (5.1, 5.2) – is due to ligand-ligand attractive interactions such as π-π and T-stackings among phenyl rings[21] which overcome repulsive steric interactions (that are expected to be minor for this cluster as in $Au_{102}(SPh)_{44}$ [38]). These stabilizing terms compensate for a decrease in residual S-S binding, associated with the weakening of S-S bonds due to conjugation effects – the counterpart of the noted strengthening of S-Au bonds[74, 78]. It can be noted the weakening of S-S bonds is not due to a variation of S-S distances which indeed do not change be minor for this cluster as in $Au_{102}(SPh)_{44}$ [38]). These stabilizing terms compensate for a decrease in residual S-S binding, associated with the weakening of S-S bonds due to conjugation effects – the counterpart of the noted strengthening of S-Au bonds[74, 78]. It can be noted the weakening of S-S bonds is not

due to a variation of S-S distances which indeed do not change much: the energy of a crown of thio-methyls obtained by transforming the phenyl residues of $(SPh)_{24}$ into methyls is similar to that of the analogue $(SCH_3)_{24}$ crown from $Au_{38}(SCH_3)_{24}$ (the energy difference is 0.54 eV in favor of the former).

In synthesis, ligand replacement [38, 74, 78], between aliphatic and aromatic ligands does not bring about qualitative changes in the system energetics. However, this results from a cancellation of contributions changing in opposite sense. Notably, a significant component of the energetic stability of the aromatic $Au_{38}(SPh)_{24}$ is determined by ligand-ligand interactions, especially attractive dispersive interactions among the phenyl rings.[21] The fact that these interactions are expected to be sensitive to temperature and solvent effects is in keeping with experimental observations summarized in Scheme 5.1. Note that our analysis is purely thermodynamic and we do not investigate here possible contributions of kinetic effects to the cluster stability such as e.g. found for $Au_{133}(SPh\text{-}tBu)_{52}$ due to dynamic fluctuation phenomena. [21]

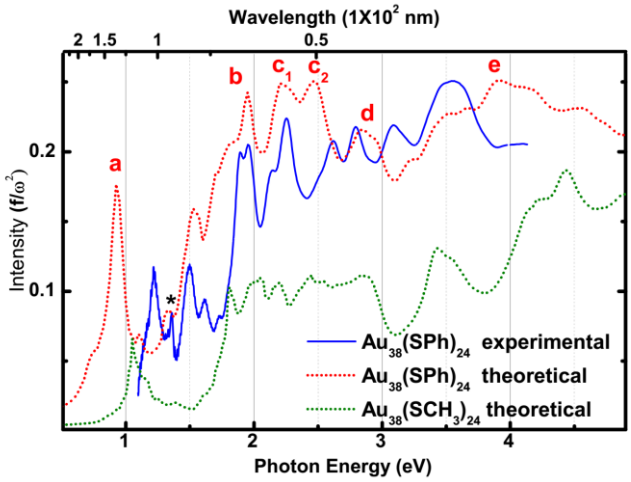

Figure 5.5. Comparison of experimental and simulated optical spectra of $Au_{38}(SPh)_{24}$ and simulated optical spectrum of $Au_{38}(SCH_3)_{24}$. Asterisk depicts an instrumental artifact.

Switching now to optical properties, Figure 5.5 reports a comparison between simulated and experimental photo-absorption spectra of $Au_{38}(SPh)_{24}$. The fair agreement between simulated and measured spectra, including a bathochromic shift of the peaks with respect to the aliphatic counterpart, confirms the experimental assignment. Apart from this bathochromic shift, the overall

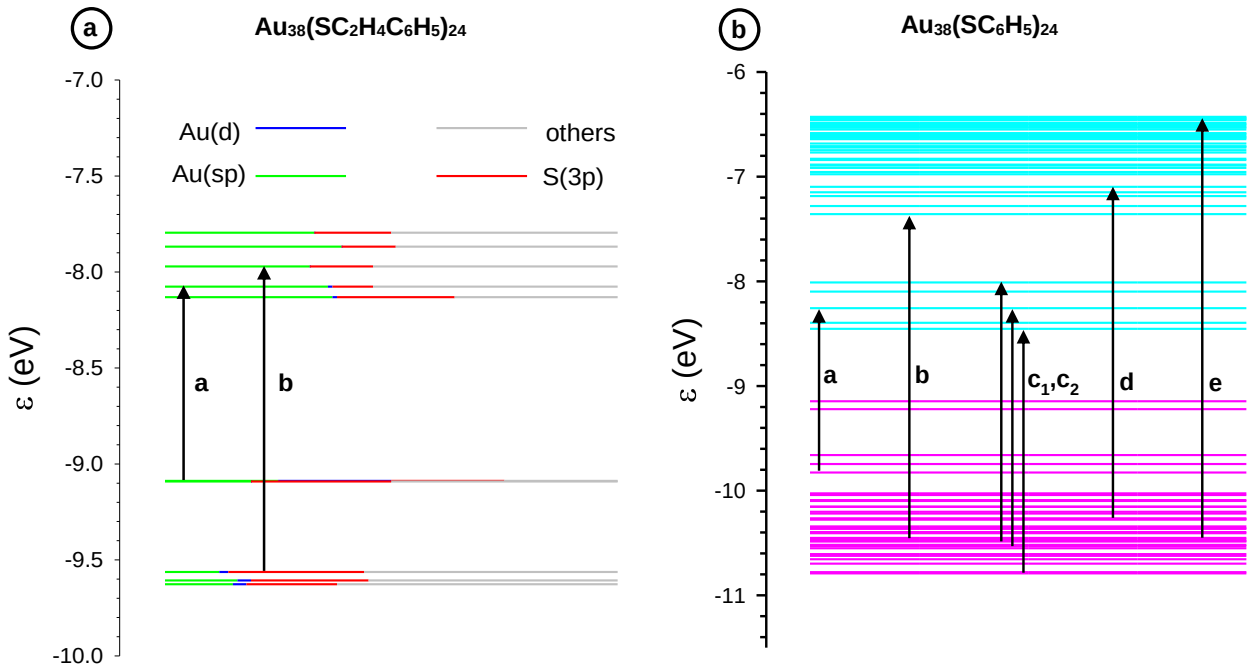

Figure 5.6. (a) Molecular Orbital (MO) energies of $Au_{38}(SCH_2CH_2Ph)_{24}$ relevant for the analysis of its TDDFT photo-absorption spectrum. MO are represented as horizontal lines colored in green, blue, red, and grey segments whose length is proportional to the Mulliken contribution in the projection of the corresponding MO onto Au(6s6p), Au(3d), S(3s) and other atomic orbitals, respectively. Black arrows denoted by (a) and (b) visualize transitions relative to the spectral features at 0.95 and 1.75 eV respectively. (b) MO energies of $Au_{38}(SPh)_{24}$ relevant for the analysis of its TDDFT photo-absorption spectrum. MO are represented as horizontal lines colored in pink and cyan for occupied and virtual orbitals, respectively. Black arrows denoted by (a), (b), (c1), (c2) (d), and (e) visualize transitions relative to the spectral features at 0.95, 1.95, 2.22, 2.48, 2.85, and 3.95 eV respectively.

similarity in appearance of the spectra may induce to think that $Au_{38}(SPh)_{24}$ is not qualitatively different in terms of optical properties from its aliphatic analogues such as $Au_{38}(SCH_2CH_2Ph)_{24}$.(Ref.[159, 161]) However, a more punctual analysis produces a qualitatively different picture. As shown in Figure 5.6a, in fact, an analysis of the electronic excitations determining the optical spectrum of $Au_{38}(SPh)_{24}$ in terms of atomic components[162] clearly shows that the transitions in the aliphatic compound are easily expressed as separate single-particle excitations, with the lowest-energy peak associated with HOMO-LUMO or HOMO-LUMO(+1) excitations. In $Au_{38}(SPh)_{24}$, instead, as partially shown in Figure 5.6b, electronic transitions are composed of many more single-particle excitations (see especially the c-peak at 2.40 eV) and with a strong presence of orbitals localized on the organic residues. Moreover, the lowest-energy transition is no more associated with HOMO-LUMO or close excitations but corresponds mostly to a HOMO (-4)-LUMO (+2) one. A major difference also concerns the *intensity* of the spectrum, a quantity less easily determined at the experimental level. Electronic conjugation in fact leads to an integrated intensity in the optical region roughly doubled in $Au_{38}(SPh)_{24}$ with respect to $Au_{38}(SCH_2CH_2Ph)_{24}$, despite the larger size (number of atoms) of the latter. In synthesis, in agreement with previous studies and proposals,[124, 163-164] we find that electronic conjugation between organic residues and the (Au-S) system produces large effects in aromatic $Au_{38}(SPh)_{24}$.

5.6 Conclusion

In conclusion, we present here the first synthesis and thorough experimental and theoretical characterization of $Au_{38}(SR)_{24}$ nanomolecule containing purely aromatic ligands: R = Ph. Conclusive evidence of this achievement comes from MALDI-MS, ESI-MS characterization, and optical spectra of $Au_{38}(SPh)_{24}$ in a solid glass and accompanying theoretical analysis. $Au_{38}(SPh)_{24}$

has a non-negligible interval of stability that is comparable to that of its aliphatic analogues, however resulting from different physical origins, with a significant component connected with ligand-ligand attractive interactions, thus making it more sensitive to environmental conditions.

CHAPTER 6

LIGAND STRUCTURE DETERMINES NANOPARTICLES' ATOMIC STRUCTURE, METAL-LIGAND INTERFACE AND PROPERTIES

Part of the text and figures in this chapter are extracted from the following publication: Rambukwella, M.; Sakthivel, N.A.; Delcamp, J.H.; Sementa, L.; Fortunelli, A.; Dass, A., Frontiers in Chemistry **2018**, 6, 2296-2646.

6.1 Abstract

The nature of the ligands dictates the composition, molecular formulae, atomic structure and the physical properties of thiolate protected gold nanomolecules, $Au_n(SR)_y$. In this review, we describe the ligand effect for three classes of thiols namely, aliphatic, AL or aliphatic-like, aromatic, AR, or bulky, BU thiol ligands. The ligand effect is demonstrated using three experimental setups namely: (1) The nanomolecule series obtained by direct synthesis using AL, AR, and BU ligands; (2) Molecular conversion and interconversion between $Au_{38}(S\text{-}AL)_{24}$, $Au_{36}(S\text{-}AR)_{24}$, and $Au_{30}(S\text{-}BU)_{18}$ nanomolecules such as $Au_{38}(S\text{-}AL)_{24}$, $Au_{36}(S\text{-}AR)_{24}$, and $Au_{30}(S\text{-}BU)_{18}$; and (3) Synthesis of Au_{38}, Au_{36}, and Au_{30} nanomolecules from one precursor $Au_n(S\text{-glutathione})_m$ upon reacting with AL, AR and BU ligands. These nanomolecules possess unique geometric core structure, metal-ligand staple interface, optical and electrochemical properties. The results unequivocally demonstrate that the ligand structure determines the nanomolecules' atomic structure, metal-ligand interface and properties. The direct synthesis

approach reveals that AL, AR, and BU ligands form nanomolecules with unique atomic structure and composition. Similarly, the nature of the ligand plays a pivotal role and has a significant impact on the passivated systems such as metal nanoparticles, quantum dots, magnetic nanoparticles and self-assembled monolayers (SAMs). Computational analysis demonstrates and predicts the thermodynamic stability of gold nanomolecules and the importance of ligand-ligand interactions that clearly stands out as a determining factor, especially for species with AL ligands such as $Au_{38}(S\text{-}AL)_{24}$.

Author Contributions

Milan Rambukwella contributed the experimental approach to ligand effect understanding on NMs in three aspects and wrote the manuscript. Naga Sakthivel contributed the nano-scaling law for three series of AuNMs. Jared Delcamp contributed the physicochemical insights of the ligands. Luca Sementa and Alessandro Fortunelli contributed to the computational section of this work. Aamala Dass formed the concept, structure of the manuscript and supervised the manuscript preparation. All the authors made substantial, direct and intellectual contribution to the work in the manuscript preparation.

6.2 Introduction

The effect of the nature of ligand on passivated nanoparticles (NPs) is not well understood. A variety of nanoparticles that are monodispersed in size [55-56, 110-111, 165] are available, through the advancement in synthetic protocols. This is important since lack of atomic monodispersity can, limit the use of NPs in their applications. Recently, a wide variety of atomically precise gold nanomolecules (AuNMs) [4-5, 109] and NPs, with unique-structures and properties have been synthesized using robust synthetic protocols [31-32, 37, 96, 122, 166]. These are used in a wide range of

applications, such as catalysis, [27, 56, 106] biosensing, [107-108] supra molecular chemistry [109, 167] and therapeutic agents [15]. In contrast to AuNPs (diameter 3-100 nm) with surface plasmon resonance

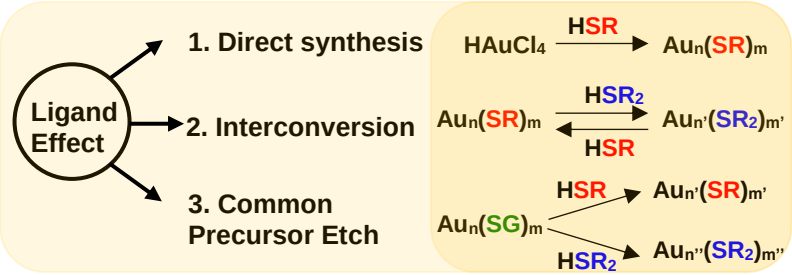

Scheme 6.1. Ligand effect demonstrated by three experimental setups namely; via 1. direct synthesis of NMs, 2. interconversion of NMs and, 3. etching of a common precursor ($Au_n(SG)_m$) with different thiols (HSR and HSR_2).

and high degree of polydispersity in size (scheme 6.2b), AuNMs (diameter <2 nm) have characteristics attributed to their atomic monodispersity (± 0 atom) and size-dependent molecule-like properties [6]. Among the highly investigated AuNMs, crystallographically characterized, examples includes $Au_{25}(SR)_{18}$, $Au_{30}(SR)_{18}$, $Au_{36}(SR)_{24}$, $Au_{38}(SR)_{24}$, $Au_{102}(SR)_{44}$, $Au_{130}(SR)_{50}$, $Au_{133}(SR)_{52}$ and $Au_{279}(SR)_{84}$ [10, 18, 50-51, 63, 93, 162, 164, 168-169] where, SR represents physicochemically different thiolate ligands.

Typically, thiolate ligands are implemented as self-assembling monolayer (SAM), [170-172] that govern the atomic structure, stability, electrochemical properties and functionality of the as-synthesized nanoparticles. Thiolate protected AuNMs and AuNPs are comprised of three main structural components: inner metallic-core, metal-thiolate interfaces composed of staple motifs and outermost thiolate surfaces that governs characteristics such as solubility. The surface of these AuNMs is surrounded by a variety of staple motifs [17]. For instance, a combination of directly linked gold-thiolate motifs, [17, 172], monomeric staples (RS-Au-SR), dimeric staples (RS-Au-SR-Au-SR) and trimeric staples (RS-Au-SR-Au-SR-Au-SR) have been identified for AuNMs with

physicochemically different ligands (Fig. S1 in the in the Appendix E) [10, 18, 20, 50-51]. The bridge between the surface structure assembly and how it relates to surface chemistry of the metal-thiolate of nanocomposites and their structural stability and selectivity remains unclear to date [63].

Density functional theory (DFT) based investigation on photoluminescent $Au_{18}(SR)_{14}$ clusters, was reported by Tlahuice-Flores, where, they study the effect of 6 physicochemically different ligands [127]. They found that presence of different functional groups, such as phenyl rings, nitro groups or alkyl group, plays a key role on the structure and properties of $Au_{18}(SR)_{14}$. Major structural distortions in $Au_{18}(SR)_{14}$ clusters were observed with para-mercaptobenzoic acid and para-nitrobenzenethiol whereas, with $-SCH_3$, 4-tert-butylbenzenethiol (TBBT, HSPh-*t*Bu), thiophenol and cyclohexanethiol ligands, similar structure and ligand orientation were observed. Another study by Tlahuice-Flores et al. reported ligand induced structural distortions in $Au_{25}(SR)_{18}$ clusters, [124] where they investigated set of 11 ligands. From these ligands, they found that para-substituted thiophenolate ligands with electron-withdrawing groups induced, major structural distortions in $Au_{25}S_{18}$ framework resulting in less symmetric structures. Interestingly, the thiolate ligands with low polarity such as $-SH$, $-SCH_3$, and $-SC_6H_{13}$ as well as the $-S(CH_2)_2Ph$ (phenylethane thiol) retain the C_i symmetry of the total crystal structure. As a result, a decrease in the HOMO-LUMO gap was found to be more evident in the case of electron withdrawing ligand protected $Au_{25}(SR)_{18}$. Thus, ligand effect is not necessarily due to only ligands' bulkiness but also due to the aromaticity and electronic nature of the ligand structure. Experimentally, we have shown that in the presence of aromatic TBBT ligand $Au_{144}(SCH_2CH_2Ph)_{60}$ transform to a new core-size to give $Au_{133}(SPh\text{-}tBu)_{52}$ [21]. We hypothesize the effect by aromatic phenyl rings contribute a favorable inter-ligand interaction while para-tertiary groups create steric repulsion and trigger the core-size conversion to $Au_{133}(SPh\text{-}tBu)_{52}$. In the presence of only aromatic ligands (without drastic

sterically crowding substitutes, -tBu) such as thiophenol, it was observed that the $Au_{144}(SCH_2CH_2Ph)_{60}$ NMs transforms to $Au_{99}(SPh)_{42}$ [81] which suggest that the bulk *tert*-butyl group of TBBT plays a key role in determining the atomic structure by changing ligand-ligand interactions. Recent reports on $Au_{38}(SCH_2CH_2Ph)_{24}$ NMs revealed that ligands can induce core-size conversions on relatively small NMs as well. In presence of TBBT ligands $Au_{38}(SCH_2CH_2Ph)_{24}$ is core size converted to give $Au_{36}(SPh\text{-}t\text{Bu})_{24}$ NMs [92] and in the presence of bulky tert-butylthiol ligands to give $Au_{30}(S\text{-tBu})_{18}$ NMs [173]. Furthermore, recently we have demonstrated ligand induced molecular interconversion [174] between $Au_{36}(SPh\text{-}X)_{24}$ (where X= -H or -tBu,) and $Au_{30}(S\text{-tBu})_{18}$ NMs. These reports demonstrated that by controlling the ligand-ligand interaction by means of steric bulk and aromaticity of the thiolate ligand, it is possible to interconvert between similar size physicochemically different AuNMs. Therefore, physicochemically different thiolate ligands have been widely used to control the atomic structures and ligand environments of AuNMs and tune unique properties in nanoparticles.

Maran et al. have reported the effect of alkyl ligand length on electron transfer reactions in $Au_{25}(SC_nH_{2n+1})_{18}$ NMs with n = 2, 4, 6, 8, 10, 12, 14, 16, 18[175]. The results show difference in electron transfer rates between short ligands and long ligands. Cirri et al. have also showed that chain length of the ligands has a direct control over electronic properties of AuNMs and the degree of charge transfer can be controlled by the difference between the dielectric constant of the solvent and the surface ligand of the AuNMs[176]. Another study carried out on $[Au_{25}(SCH_2CH_2Ph)_{18}]^0$ NMs by Agrachev et al. showed that magnetism can be controlled from paramagnetic to superparamagnetic to ferromagnetic as a function of the aggregation state of the clusters[177]. Recently, we have demonstrated that in contrast to AL ligands, AR ligands induces a bathochromic shift in $Au_{38}(SR)_{24}$ absorption spectra and reduces the electrochemical band gap[178].

Interestingly, Wang et al. demonstrated the importance of halides in the formation of large bimetallic $Au_{80}Ag_{30}$ NMs [179]. In their study, a total of 9 chloride atoms were found coordinated to the third shell and each chloride atom was found bridged to two Ag atoms. In contrast to larger NMs, Zhu et al. reported a comparison of aliphatic ligand against aromatic ligand protected small $Au_{15}Ag_3$ NMs, where different structural, electronic and optical properties were observed with structurally different thiolate ligands [180]. Recently, it has been shown that TBBT thiol protected Au_{28}(SPh-*t*Bu)$_{20}$ can be interconverted to cyclohexyl thiol protected $Au_{28}(SR)_{20}$ [160] and $Au_{24}L_{20}$ (L- ligand) with phenylethane thiol and selenophenol ligand [181] can be synthesized, but the atomic structure and properties of those NMs were found to be different. Han et al. theoretically investigated aromatic and aliphatic thiol ligand effect on Au_{25}, Au_{38}, and Au_{102} NMs and they reported aliphatic thiols stabilizes the NMs more than the aromatic ligands both thermodynamically and electrochemically [78]. The authors also reported that the stabilization energy of NMs varies depending on ligand structure regardless of inter-ligand interaction, system size and shape. Similarly, it was reported that subtle changes in the structure of the surface ligand would trigger formation of NMs [169, 182] with completely different atomic structures and properties. However, the underlying fundamental aspects of the ligand structure dependence on NMs' atomic structure remains to be not well established.

A major advancement of NMs' research took place with the pioneering work by Kornberg et al. in the discovery of the crystal structure of para-mercaptobenzoic acid (p-MBA) protected Au_{102}(p-MBA)$_{44}$ NMs. The stability of the Au_{102} system has been attributed to the "superatom chemistry" of the nanomolecule [10]. The reasoning behind the superatom electronic configuration is analogous to the inert electronic shell closing observed and attained by gas-phase atoms and molecules. It is assumed that each gold atom contributes one valence electron to the molecular

orbitals and each thiolate ligand localize one electron thus, Au_{102}(p-MBA)$_{44}$ NMs possess 58 electrons (102-44=58) with superatom electronic configuration (2, 8, 20, 40, 58, 84). While well studied AuNMs systems such as $Au_{10}(SR)_{10}$, $Au_{15}(SR)_{13}$, $Au_{25}(SR)_{18}^{-}$, $Au_{144}(SR)_{60}$ obeys superatom theory, stability of other AuNMs such as Au_{30}, Au_{36}, Au_{38} and Au_{133} does not fit in the superatom magic electron shell closing trend. Superior stability associated with AuNMs that deviate from the electronic structural integrity governed by superatom theory, entails the right perspective of AuNMs structural selectivity and stability being governed by the ligand structure and geometry.

In this review we have investigated the bulkiness and electronic nature of surface ligands on the formation of AuNMs and their influence on physicochemical properties using three experimental setups approaches namely: (1) The nanomolecule series obtained by direct synthesis of AuNMs employing AL, AR, BU ligands; (2) Molecular conversion and interconversion between Au_{38}(S-AL)$_{24}$, Au_{36}(S-AR)$_{24}$, and Au_{30}(S-BU)$_{18}$ nanomolecules; and (3) Synthesis of Au_{38}, Au_{36}, and Au_{30} nanomolecules from a common precursor Au_n(S-glutathione)$_m$ upon reacting with AL, AR and BU ligands (scheme 6.1). These experimental approaches demonstrate the fundamental aspects between surface ligand structure and atomic structure of AuNMs and their physicochemical properties. This review emphasizes the consideration of ligand effect in the design and synthesis of novel NMs.

6.3 Ligand Effect Demonstrated by Direct Synthesis

The two-phase Brust method [30] and methods derived from Brust synthesis have been widely implemented to synthesize a wide range of AuNMs (scheme 6.2b). The strong Au-S covalent bond [183] between thiolate ligands and surface gold atoms makes synthetic protocols highly

robust for thiolate protected AuNMs. The surface orientations of each thiol vary and for instance when the steric requirements of the ligand preclude the ordering found for the aliphatic thiolate structures, other ordering are found in SAMs [165]. In contrast to aliphatic thiols, aromatic thiols such as *p*-biphenylthiols, *p*-terphenylthiols, and oligo (phenylene ethynylene) thiols are found to have a slightly less bent orientation on Au (111) surface. Most importantly, a wide variety of AuNMs has been reported mainly by altering the structure of thiolate ligands. Various size-dependent properties are found in these AuNMs protected by different thiolate ligands. Interestingly, based on the physicochemical nature of the thiol, we have observed that certain class of thiolate ligands exclusively forms a unique series of AuNMs. Based on these experimental observations, thiolate ligands can be categorized into three main classes, namely; aliphatic, aromatic and bulky (scheme 6.2d and Fig. S1 in the Appendix E) thiolate ligands, where they differ from each other at the sulfur-carbon bond. For instance, aliphatic ligands possess a primary carbon atom immediately bond to the sulfur atom, aromatic ligands have carbon atom in aromatic ring bond to the sulfur atom and bulky thiols have a tertiary carbon atom immediately bond to the sulfur atom.

Among the AL ligands, phenylethane thiol ($HSCH_2CH_2Ph$, PET) is the most widely used and studied ligand by Murray and co-workers, followed by others. To date, a series of highly robust and thermodynamically stable NMs (scheme 6.2c) such as $Au_{25}(SCH_2CH_2Ph)_{18}$, $Au_{38}(SCH_2CH_2Ph)_{24}$ and $Au_{144}(SCH_2CH_2Ph)_{60}$ have been reported with PET ligand [51, 96, 162, 184] and other physicochemically similar ligands such as ethanethiol, [185] hexanethiol [186-187] octanethiol [187] and dodecanethiol [128, 187-188]. Interestingly, we have observed that NMs such as $Au_{21}(SR)_{15}$, $Au_{30}(SR)_{18}$, $Au_{36}(SR)_{24}$, $Au_{133}(SR)_{52}$ etc. are not formed or not been reported with AL ligands. Thus, AL and aliphatic-like ligands govern the exclusive formation of a unique series of NMs (scheme 6.2c and table 6.1).

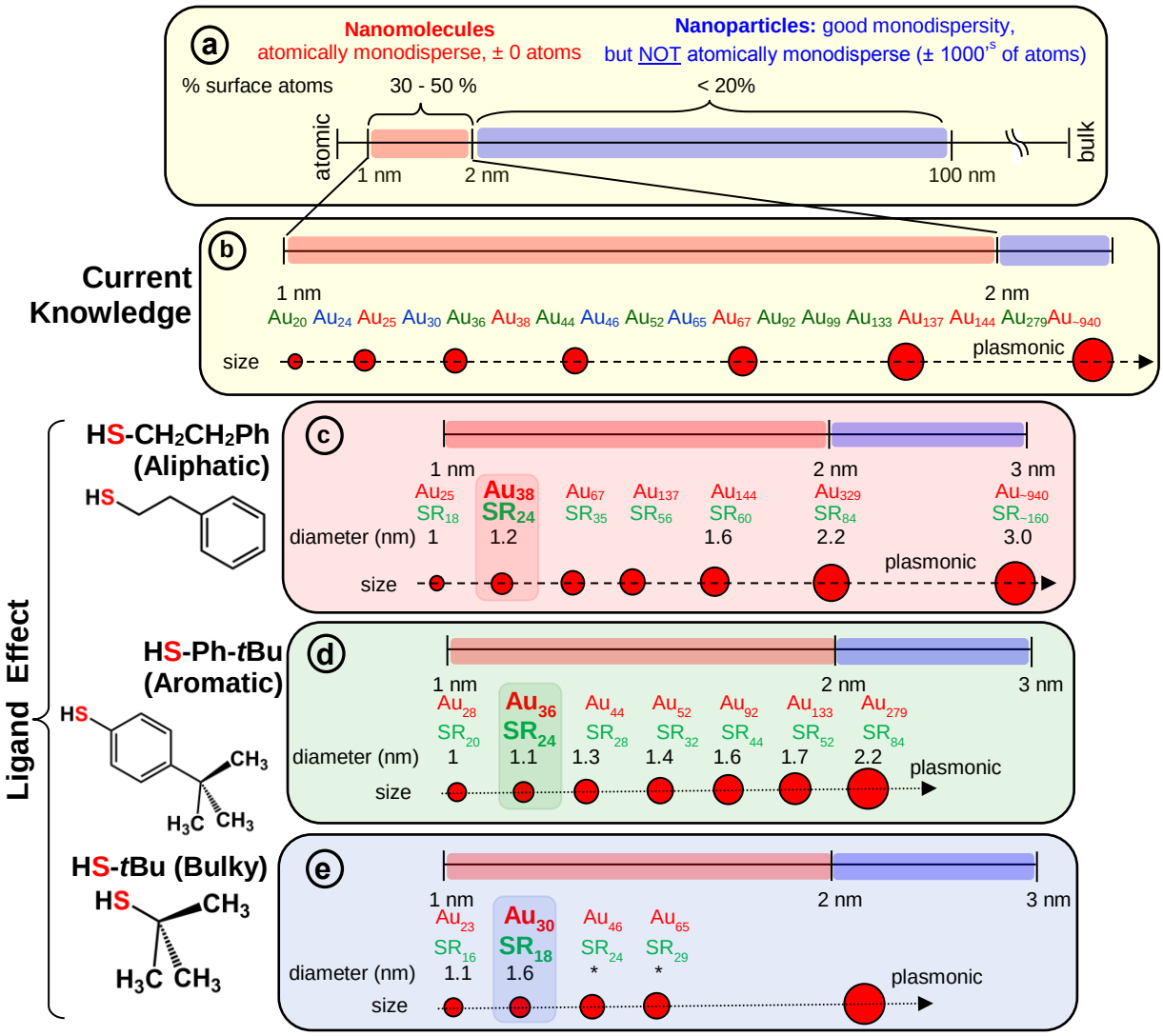

Scheme 6.2. (a) The scheme shows the 1 - 100 nm size regime with atomically precise NMs in the 1-2 nm region, and NPs in the 2-100 nm regime (where, very good monodispersity in size has been achieved, but atomic composition can vary by ± 1000's of atoms). Examples of widely investigated NMs with three classes of thiolate ligand are given under each series. (b) Widely investigated thiolate protected gold NM systems in each series. NMs with; (c) aliphatic and aliphatic-like ligand, $HSCH_2CH_2Ph$, (d) aromatic ligand, HSPh-*t*Bu, and (e) bulky ligand, HS-*t*Bu are illustrated under each scheme. Most stable NM in aliphatic, aromatic, and bulky series namely, $Au_{38}(SCH_2CH_2Ph)_{24}$, $Au_{36}(SPh\text{-}tBu)_{24}$ and $Au_{30}(S\text{-}tBu)_{18}$ NMs respectively are highlighted. Asterix indicates unknown diameter of the NMs due to lack of crystal structure.

Table 6.1. Three physicochemically different series of NMs observed with class of aliphatic, aromatic and bulky thiolate ligands.

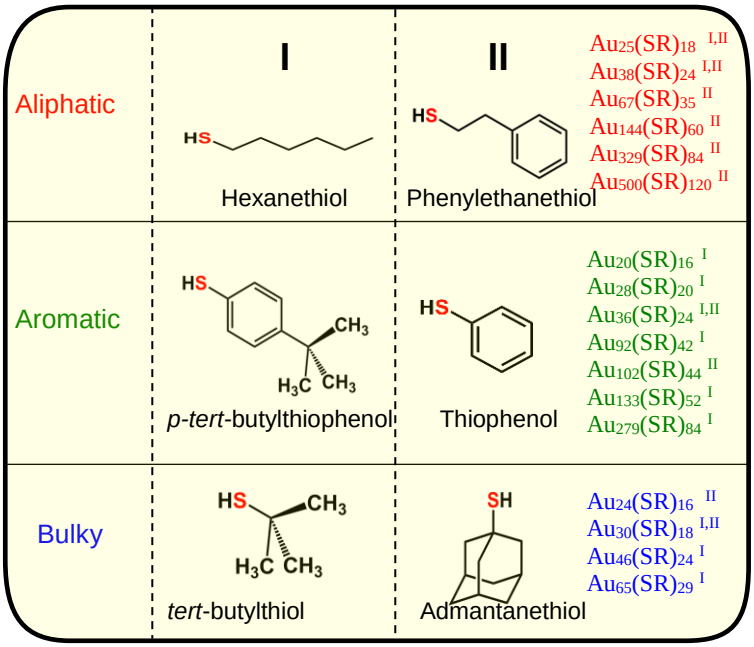

Size	Citations
-SCH_2CH_2Ph (Aliphatic)	
$Au_{25}(SR)_{18}$	*J. Am. Chem. Soc.*, 2007, 16209
$Au_{38}(SR)_{24}$	*J. Am. Chem. Soc.*, 2004, 6193
$Au_{67}(SR)_{35}$	*J. Phys. Chem. A*, 2013, 504
$Au_{137}(SR)_{56}$	*Chem. Commun.*, 2014, 9895
$Au_{144}(SR)_{60}$	*J. Phys. Chem. C*, 2009, 5035
$Au_{329}(SR)_{84}$	*Anal. Chem.*, 2014, 4227
$Au_{\sim 940}(SR)_{\sim 160}$	*ACS Nano*, 2014, 6431
-S-Ph-*t*Bu (Aromatic)	
$Au_{28}(SR)_{20}$	*J. Am. Chem. Soc.*, 2013, 10011
$Au_{36}(SR)_{24}$	*J. Am. Chem. Soc.*, 2011, 9175
$Au_{44}(SR)_{28}$	*J. Am. Chem. Soc.*, 2005, 13750
$Au_{52}(SR)_{32}$	*Nanoscale*, 2016, 1299
$Au_{92}(SR)_{44}$	*J. Am. Chem. Soc.*, 2016, 8710
$Au_{102}(SR)_{44}$*	*Chemtracts*, 2007, 308
$Au_{133}(SR)_{52}$	*J. Am. Chem. Soc.*, 2015, 4610
$Au_{279}(SR)_{84}$	*J. Am. Chem. Soc.*, 2017, 15450
-S-*t*Bu (Bulky)	
$Au_{24}(SR)_{16}$	*J. Am. Chem. Soc.*, 2014, 14933
$Au_{30}(SR)_{18}$	*J. Am. Chem. Soc.*, 2014, 5000
$Au_{46}(SR)_{24}$	*J. Phys. Chem. C*, 2018
$Au_{65}(SR)_{29}$	*J. Phys. Chem. C*, 2018

We have investigated the effect of physicochemically different ligands on AuNMs by comparing an aliphatic-like thiol ligand (-$S(CH_2)_2Ph$), a BU thiol ligand (*tert*-butyl thiol), and an AR thiol (TBBT). Multiple factors have been examined including: (1) sterics based on ligand size, (2) ligand electron donor strength as evaluated by pKa values, and (3) π-π ligand interactions. These ligands were selected for comparison in AuNM core-size control since each of these ligands have at least one property examined which is similar to one of the ligands and vastly different to the other (Figure 6.1). The potentially similar interactions are highlighted for each ligand in the overlapping circle areas in Figure 6.1. Specifically, the AL and AL-like thiol, -$S(CH_2)_2Ph$, has a very similar pKa to BU tert-butyl thiol (both at ~17 in DMSO) [189]. However, the pKa of the

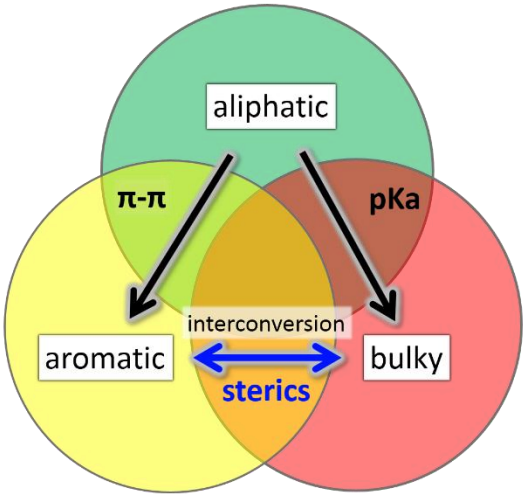

Figure 6.1. Illustration of overlapping characteristics (π-π interactions, pka values, steric bulk) of the primary, aromatic and tertiary ligands in this work. Arrows show the direction of conversion for Au NMs using these ligand classes.

aromatic ligand, TBBT, is ~10 in DMSO. This represents a 10^7 more stabilized anion for the TBBT ligand upon deprotonation. Given the tremendously large ability of the aromatic ligand to stabilize the sulfur lone electron pairs through resonance, a vastly diminished (by 7 orders of magnitude) sulfur electron donation strength is expected when compared with either of the alkyl ligands in organic solvent. This allows for the influence of the sulfur electron density to be probed with respect to AuNMs structure. Thermodynamically, the AL and BU tertiary alkyl thiols would be predicted from first principles to form stronger Au-S bonds than aromatic thiols since aromatic thiols have competing π* orbitals to accept electron density from the sulfur atom while alkyl thiols do not. The relatively larger amount of electron density at the sulfur atom of the alkyl thiols should promote stronger bonding to Au atoms. In support of this prediction, normalized cluster

fragmentation energies of the AL, AR and BU AuNMs are calculated as discussed below with reference to equations 6.1, 6.2 and 6.3, respectively. Also, average bond lengths for alkyl thiol Au-S bonds measured by x-ray crystallography are shorter than that of aromatic thiols by 0.008 Å (see discussion below). It is noteworthy that this bond length value does have some uncertainty associated with it based on the resolution for the three structures. This suggests a potentially thermodynamically more stable Au-S bond from the alkyl thiols. Providing aromatic thiols have weaker bonds, AuNMs based on AR thiols should be most easily converted to other AuNM core sizes. Importantly, the two ligands with similar pKas are vastly different in size and the TBBT ligand cannot have π-interactions, which allows for the probing of electron donor strength on the AuNM core-size primarily.

Concerning sterics, while A-values must be used with caution in assigning steric bulk, they do provide a general guideline for assigning steric influence of the ligand at the sulfur atom for our ligands. It should be noted that A-values apply best to cyclohexane systems, where diaxial conformation interactions are being quantified. A-values show the largest influence near the point where the group being analyzed is bound. When comparing the A-values of the groups (-$(CH_2)_2$Ph, TBBT and *tert*-butyl thiol) attached to the sulfur atom, it is important to remember that the atoms near the S atom will have the largest influence sterically according to the A-value scale. As an example, A-values decrease dramatically far from the attachment point (e.g. -Me is 1.70 and -Et is 1.75 despite a doubling of carbon atoms). With this in mind, the AL thiol would be predicted to have an A-value of 1.75 as the smallest ligand. Both the BU thiol (A-value of 4.5) and the AR thiol (A-value of 3.0) are considerably larger in terms of sterics. Given that the sulfur atom itself has an A-value of ~1.0, the primary group adds relatively little additional sterics. The other AR and BU tertiary alkyl thiol ligands provide significantly increased steric bulk beyond the size of the sulfur.

Notably, the two largest ligands have vastly different pKas (AR versus BU) and both cannot have π-π interactions (BU doesn't have an aryl group). Thus, this comparison allows for probing the steric influence with minimal input from other parameters.

Finally, concerning potential π-π interactions, two of the ligands utilize aryl groups, while BU *tert*-butyl thiol does not have an aryl group which precludes the influence of π-π ligand interactions. Importantly, the ligands which can have π-π interactions are vastly different in size and pKa values, which allows for the probing of π-interactions primarily on AuNM core-size with a minimization of the other properties. Through these analyses, each of the commonly discussed parameters (sterics, π-π system interactions, and sulfur donation strength) can be independently examined with lesser contributions from the other effects.

Interestingly, the AL alkyl thiol protected AuNMs can be converted to other AuNMs through the use of either AR thiol or BU *tert*-butyl thiol ligands. While both of these ligands do give different core sizes, the ready conversion of the primary alkyl thiol protected AuNMs by these ligands suggests pKa and π-π interaction are not as strong in stabilizing the AuNMs as compared to ligand sterics. Importantly, the conversion of the AuNMs core-size occurs despite analyzing ligands that could also π-stack or that have similar pKa values. This conversion suggests that these factors alone do not control AuNMs' core size and sterics plays a significant role. The critical experiments of attempting to convert AR and BU *tert*-butyl thiol protected AuNMs core-sizes back to that of the AL alkyl thiol show that the stabilization which occurs through the use of large ligands changing Au core-sizes cannot be readily reversed [173]. Thus, sterics are a dominant factor in predicting the AuNMs cores size based on ligand selection.

In our previous report, we have investigated the steric ligand effect on Au_{38} system and subsequent core-size conversion to Au_{30} system indicating a clear bulky ligand effect[173]. Compared

to aliphatic ligands, in the class of bulky ligands, steric effect dominates over aromatic effect, thereby physicochemically different series of AuNMs are observed where sterics governs the stability of the AuNMs. The *tert*-butylthiol is a classic example of a bulky ligand (scheme 6.2e and Fig. S1 in the Appendix E) where, head S atom is directly bond to a tertiary carbon atom. Most widely investigated robust and thermodynamically most stable NM series with this ligand comprise of Au_{23}(S-*t*Bu)$_{16}$, [94] and Au_{30}(S-*t*Bu)$_{18}$ [19-20, 95, 190]. Similarly, bulky adamantanethiol (S-Adm) ligand has shown to form Au_{24}(S-Adm)$_{16}$, [86] Au_{30}(S-Adm)$_{18}$ [136] as well as Au_{21}(S-Adm)$_{15}$ [191-192] NMs governed by the steric ligand effect. Interestingly to date larger sizes (Au atoms > 100) of BU thiol protected NMs have not been reported. This could be due to the BU ligands hindering the growth of the AuNMs as it blocks metal atom transportation to the core as the size increases. Therefore, we believe that tuning of the synthetic protocol may be required for the synthesize of larger BU thiolate-protected AuNMs. It has been shown by Krommenhoek et. al that use of BU thiols such as adamantanethiol and cyclohexanethiol (SCy) results in smaller core sizes and narrows down the size distribution.[125] In their synthesis they discovered Au_{30}(S-Adm)$_{18}$, Au_{39}(S-Adm)$_{23}$, Au_{65}(SCy)$_{30}$ and Au_{67}(SCy)$_{30}$ NMs. Interestingly for BU thiolate ligand protected NMs, more Au atoms per thiolate ligand were observed due to steric crowding at the thiolate monolayer. Also, Chen et al. have demonstrated the effect of steric hindrance on the formation of Au_{130}(p-MBT)$_{50}$, Au_{104}(m-MBT)$_{41}$ and Au_{40}(o-MBT)$_{24}$ NMs using isomeric para, meta, and ortho substituted methylbenzene thiols (MBT), respectively [182]. The authors synthesized three different NMs from the one stating precursor mixture and the results were attributed to sterics governed by the methyl group of the ligand, where, closer the methyl group to the sulfur atom in the thiol, the more structural hindrance would be. Due to the steric crowding by the bulky thiolate ligands such as *tert*-butylthiol and adamantanethiol, NMs such as Au_{25}(S-AL)$_{18}$, Au_{36}(S-AR)$_{24}$, Au_{38}(S-AL)$_{24}$,

$Au_{144}(S\text{-}AL)_{60}$, or $Au_{279}(S\text{-}AR)_{84}$ cannot be synthesized, instead of only a series of AuNMs governed by steric effect is being formed (scheme 6.2e and table 6.1).

In contrast to AL and BU ligands, the class of aromatic thiolate ligands have a direct aromatic effect due to the presence of phenyl aromatic ring immediately bond to the head S atom (Fig.S1 in the Appendix E). Due to presence of aromatic rings, π electrons contribute to favorable ligand-ligand attractions which results in stabilizing the ligand shell rather than a repulsive steric effect. In contrast to the AL and BU thiolate-protected NMs, the electronic conjugation due to aromatic ligands result in bathochromic shift in optical features and thereby reduce the band gap energy of the AuNMs [178]. Also, it has been discovered that contribution from phenyl ring is very critical in manifestation of metallic properties in the form of surface plasmons for Au_{279} [193]. Thiophenol is a classic example of aromatic thiol. TBBT thiol is found to have similar aromatic ligand effect with minimal variation of the end product except for instance reported case where, $Au_{133}(SR)_{52}$ [21] is reported with TBBT, but not with thiophenol. This is expected as the surface availability of the nanomolecule decreases as the size increases steric effect by *para*-tert-butyl groups becomes significant compared to smaller core-size $Au_{36}(SR)_{24}$. Similarly, it was found that physicochemical differences between thiophenol, 4-methoxybenzene thiol, 4-methylbenzene thiol, and 4-bromobenzene thiol are subtle and results in same composition of AuNMs [31, 38, 81, 182]. Although, $Au_{36}(SR)_{24}$ NMs system was reported [138] with bulky cyclopentane thiol, exclusive formation of $Au_{36}(SR)_{24}$ is dominated by electronic effect by aromatic nature of the ligand rather than steric effect. Thus, in terms of competing electronic and steric effect in the same ligand, thermodynamically stable and final composition of the product would be determined by the overall dominating factor; electronic or steric [182]. It should be noted that, in our previous work, we have shown that kinetic product $Au_{38}(SPh)_{24}$ NMs can be synthesized and isolated under controlled

ligand exchange reaction conditions while core-size converts to $Au_{36}(SPh)_{24}$ if subjected to prolonged reaction [178]. BU or AL thiol-protected NMs such as $Au_{21}(S\text{-}BU)_{15}$, $Au_{25}(S\text{-}AL)_{18}$, $Au_{30}(S\text{-}BU)_{18}$, $Au_{38}(S\text{-}AL)_{24}$, or $Au_{144}(S\text{-}AL)_{60}$ cannot be synthesized with aromatic thiolate ligands (scheme 6.2d and table 6.1).

6.4 Ligand Effect Demonstrated by Molecular Conversion and Interconversion

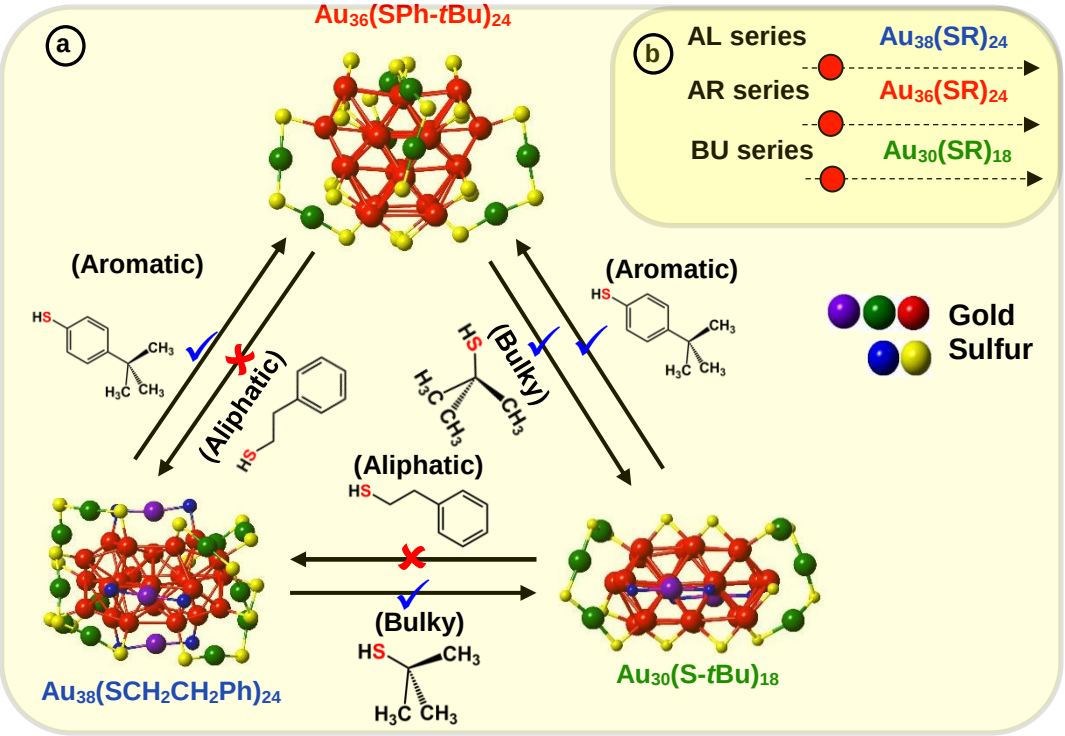

Scheme 6.3. (a) Molecular interconversion between $Au_{38}(SCH_2CH_2Ph)_{24}$, $Au_{36}(SPh\text{-}tBu)_{24}$ and $Au_{30}(S\text{-}tBu)_{18}$ NMs. Red (✗) indicates interconversion that is restricted or not observed whereas blue (✓) indicates possible and observed interconversions. (b) Three series of aliphatic (AL), aromatic (AR), and, bulky (BU) NMs illustrating most stable NMs in each series, $Au_{38}(SCH_2CH_2Ph)_{24}$, $Au_{36}(SPh\text{-}tBu)_{24}$ and $Au_{30}(S\text{-}tBu)_{18}$ respectively.

Ligand exchange protocols on AuNMs are a highly versatile strategy that is employed to tune the synthesis to obtain new nanomolecules that are difficult to obtain via direct Brust method [30, 194]. Ligand exchange reactions on molecular pure AuNMs allows us to investigate the influence of thiolate ligand on AuNMs' structure and to understand the fundamental aspects of ligand effect on structural selectivity [11, 136, 172, 195]. It has been demonstrated by many, that a distinct AuNMs can be converted to a new one via ligand exchange in the presence of a physicochemically different ligand [21, 85, 92, 173, 196-197].

For the first time, we have demonstrated the ligand induced interconversion between Au_{30}(S-tBu)$_{18}$ and Au_{36}(SPhX)$_{24}$ NMs (where, X=-H, -tBu, scheme 6.3)[174]. The two AuNMs, Au_{30}(S-tBu)$_{18}$ and Au_{36}(SPhX)$_{24}$ have interpenetrating-cuboctahedral Au_{20} and Au_{28} core structures, respectively and completely different staple motifs (scheme 6.3). This discovery leads to *a valuable insight into the inherent nature of ligand structure dependency on atomic structure* of thiolate protected AuNMs. The experiment was carried out on molecular pure starting materials, Au_{30}(S-tBu)$_{18}$ and Au_{36}(SPh-X)$_{24}$ NMs, which were reacted with TBBT and *tert*-butyl thiol at elevated temperature, respectively (scheme 6.3). The results demonstrated that when Au_{30}(S-tBu)$_{18}$ is treated with aromatic thiophenol or TBBT, the core converts to the preferred Au_{36}(SPhX)$_{24}$ structure, as dictated by the exchanging ligand. Likewise, when Au_{36}(SPhX)$_{24}$ is treated with the bulky *tert*-butyl thiol, it converts to the preferred and most stable structure Au_{30}(S-tBu)$_{18}$ NMs. It should be underlined that the interconversion of each AuNMs completes with the respective thiolate ligand retaining its original physicochemical properties, i.e. Au_{36} and Au_{30} formed upon interconversion reaction possess their intrinsic properties unaltered. Au_{38}(SCH_2CH_2Ph)$_{24}$, a similar core sized AuNM was reported to undergo transformation to Au_{30}(S-tBu)$_{18}$ [173] and Au_{36}(SPh-tBu)$_{24}$ [92] NMs when etched with *tert*-butyl thiol and TBBT,

respectively. Interestingly, when the products were etched with AL ligand it was found that Au_{30} or Au_{36} was not completely converted back to Au_{38} system retaining its original physicochemical properties. Instead a mixture of NMs composing $Au_{38}(SCH_2CH_2Ph)_{24}$, $Au_{38}(SCH_2CH_2Ph)_{26}$ and other small NMs was observed. This could be due to the difference in core structures, where Au_{38} has an icosahedron core and Au_{36} and Au_{30} has cuboctahedron core structures. Also, it could be attributed to the description on scheme 6.3 revealing the interconversion being allowed between bulky and aromatic thiolate protected AuNMs and not with the primary alkyl thiolate ligands. Therefore, complete atomic rearrangement is "*forbidden*" in the case of converting Au_{30} or Au_{36} to large Au_{38} system. Thus, these results demonstrate that atomic structure and metal-ligand interface of NMs can be tuned with AL, AR and BU ligands.

To provide theoretical information on the thermodynamic stability of $Au_{38}(SCH_2CH_2Ph)_{24}$, $Au_{36}(SPh)_{24}$, and $Au_{30}(StBu)_{18}$ nanomolecules, we compared their energetics using analysis tools proposed in previous work [21, 78-79, 86], in particular:

(1) energy decomposition (fragmentation) [86], and (2) system comparison [21, 78] procedures.

6.4.1 Energy Decomposition Analysis

The first point to be noted when comparing the $Au_{38}(SCH_2CH_2Ph)_{24}$, $Au_{36}(SPh)_{24}$, and $Au_{30}(StBu)_{18}$ series is that the strength of S-Au bonds is different in aliphatic vs. aromatic thiols, and, as previously pointed out in the literature [78], it parallels the strength of S-H bonds. Specifically, if we compare the bond strength given by the process: HSR → H + SR, we find that the reaction energy is nearly the same for H-StBu and H-SCH_2CH_2Ph: 4.86 eV and 4.87 eV, respectively, which should correspond to a similar covalent bonding of these ligands to gold, whereas it is different in H-SPh: 4.50 eV, i.e., smaller by 0.36-0.37 eV. As we discuss below, the different strength of the Au-S bond is one important factor determining the differences in chemical

behavior of aliphatic vs. aromatic ligands, other important factors being steric effects associated with the larger hindrance of -StBu with respect to $-SCH_2CH_2Ph$ or electronic effects such as conjugation and resonance associated with thiols exhibiting aromatic rings directly bound to sulfur such as -SPh-R.

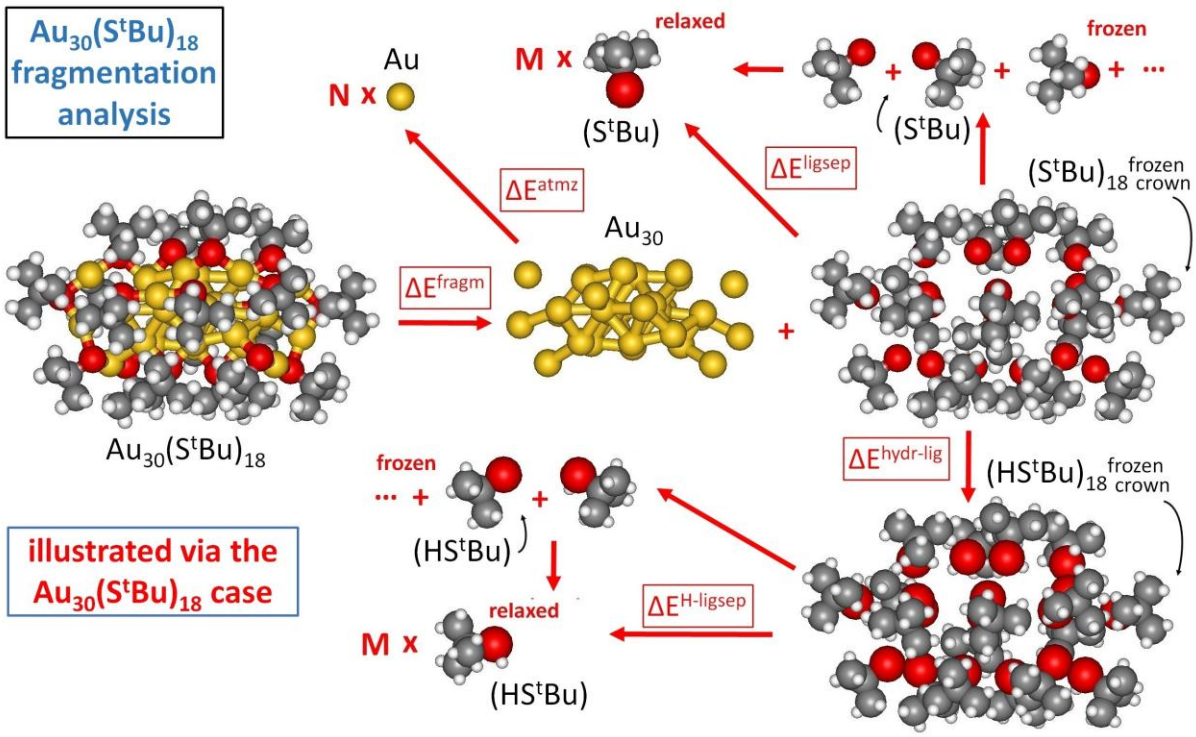

Figure 6.2. Fragmentation analysis of the energy of Au nanomolecules, illustrated for definitiveness in the case of $Au_{30}(S\text{-}tBu)_{18}$.

A second point is the question of how to compare nanomolecules with a different stoichiometry – $Au_N(SR)_M$. Clearly, their energetics must be properly normalized for such a comparison to be meaningful. Here we use the number of ligands, M, as a normalization factor, so that all quantities here reported should be intended as per ligand (absolute energy values used to calculate fragmentation and charging energies are reported in Table S1 of the Appendix E).

We dissect In our approach, the formation energy of a $Au_N(SR)_M$ nanomolecule is partitioned into three components [86], as schematically illustrated in Fig. 6.1:

(1) cluster fragmentation – ΔE_{fragm}

(2) metal atomization – ΔE_{atmz}

(3) ligand separation – ΔE_{ligsep}

so that the formation energy of a $Au_N(SR)_M$ cluster from N, Au atoms and M, SR thiyl radicals – E_{form} (at T = 0 K and neglecting vibrational and entropic contributions) can be expressed as: $E_{form} = \Delta E_{fragm} + \Delta E_{atmz} + \Delta E_{ligsep}$.

The first component corresponds to fragmentation of the nanomolecule into a metal cluster and a "crown" of ligands, with the reaction energy normalized to the number of ligands, M, as anticipated above:

$$Au_{38}(SCH_2CH_2Ph)_{24} \rightarrow Au_{38} + (SCH_2CH_2Ph)_{24}^{crown} \qquad \Delta E_{fragm/M} = 3.440 \text{ eV} \qquad (6.1)$$

$$Au_{36}(SPh)_{24} \rightarrow Au_{36} + (SPh)_{24}^{crown} \qquad \Delta E_{fragm/M} = 3.095 \text{ eV} \qquad (6.2)$$

$$Au_{30}(StBu)_{18} \rightarrow Au_{30} + (StBu)_{18}^{crown} \qquad \Delta E_{fragm/M} = 3.532 \text{ eV} \qquad (6.3)$$

where the coordinates of the Au_{38}, Au_{36}, Au_{30}, $(SR)_{24}^{crown}$ and $(SR)_{18}^{crown}$ fragments in the right-hand-side of the equations are frozen in their interacting configurations, ΔE_{fragm} is the reaction energy and is reported per ligand ($\Delta E_{fragm/M}$). Without entering into a finer analysis considering the difference between ligand detachment from monomeric, dimeric, and trimeric staples (see Fig. 6.3a, table S1, and Fig. S2 in the Appendix E), it can be noted from Eqs.(6.1-6.3) that $Au_{36}(SPh)_{24}$ has the smallest fragmentation energy, due to its aromatic nature discussed above [78, 86]: the difference in $\Delta E_{fragm/M}$ between (6.1) and (6.2) is indeed close to 0.36-0.37 eV, while the larger value of $\Delta E_{fragm/M}$ for $Au_{30}(StBu)_{18}$ can be explained by its sparser ligand density at the surface which increases the strength of Au-S bonds.

The second component is the atomization energy of the metal cluster:

Au_{38} [from $Au_{38}(SCH_2CH_2Ph)_{24}$] → 38 Au $\Delta E_{atmz/M}$ = 3.257 eV (6.4)

Au_{36} [from$Au_{36}(SPh)_{24}$] → 36 Au $\Delta E_{atmz/M}$ = 3.087 eV (6.5)

Au_{30} [from$Au_{30}(StBu)_{18}$] → 30 Au $\Delta E_{atmz/M}$ = 3.440 eV (6.6)

In this case it is worthwhile reporting also the atomization energies normalized by the number of Au atoms: $\Delta E_{atmz/N}[Au_{38}]$ = 2.057 eV, $\Delta E_{atmz/N}[Au_{36}]$ = 2.058 eV, $\Delta E_{atmz/N}[Au_{30}]$ = 2.064 eV. By comparing the resulting energy values, we find again that $Au_{30}(StBu)_{18}$ seems to be more stable than $Au_{38}(SCH_2CH_2Ph)_{24}$, because $\Delta E_{atmz/N}[Au_{30}]$ is larger than $\Delta E_{atmz/N}[Au_{38}]$ in absolute value, which indication is even stronger considering that Au_{38} is larger than Au_{30} and should thus exhibit a larger atomization energy (usually increasing with increasing size). By defining as first neighbors of a given Au atom all Au atoms within 3.2 Å, which is the inflection point in the plot of Au-Au distances, we can monitor Au-Au first-neighbor distances, finding that $Au_{38}(SCH_2CH_2Ph)_{24}$ exhibits an average Au-Au first-neighbor distance of 2.95 Å, that is larger than in $Au_{30}(StBu)_{18}$, where it amount to 2.91 Å, thus explaining the lesser stability of the Au_{38} metal cluster.

The last component of our energy fragmentation analysis corresponds to the decomposition of the crown or shell of ligands into separated thiyl radicals (we allow the radicals to fully relax in this analysis):

$(SCH_2CH_2Ph)_{24}^{crown}$ → 24 $(SCH_2CH_2Ph)_{relax}$ $\Delta E_{ligsep/M}$ = 1.137 eV (6.7)

$(SPh)_{24}^{crown}$ → 24 $(SPh)_{relax}$ $\Delta E_{ligsep/M}$ = 0.158 eV (6.8)

$(StBu)_{18}^{crown}$ → 24 $(StBu)_{relax}$ $\Delta E_{ligsep/M}$ = 0.179 eV (6.9)

The similar values for $(StBu)_{18}^{crown}$ and $(SPh)_{24}^{crown}$ can be noted, despite their different origin in π-π and T-stackings interactions among phenyl rings [21] in the aromatic case with respect

to CH/CH dispersion interactions [198] in the bulky aliphatic case. However, the most dramatic difference is associated with the huge value of $\Delta E_{ligsep/M}$ for $Au_{38}(SCH_2CH_2Ph)_{24}$. To single out the physical origin of this striking difference we need to make a further analysis and distinguish two terms in the ΔE_{ligsep} separation energy: the energy of the S-S bonds among the under-coordinated sulfur atoms of the thiyls (some of the sulfur atoms in the interacting configuration are at close distance) and dispersion/repulsion interactions among the organic residues. To separately estimate these contributions, we first hydrogenate the sulfur atoms of the thiyl radicals in the ligand crown, relaxing the geometry of the added H atoms while keeping all other atoms frozen ($\Delta E^{hyrd\text{-}lig}$), and then calculate the separation energy of the thus formed thiol ligand shell into relaxed and separated thiols ($\Delta E^{H\text{-}ligsep}$), as pictorially illustrated in Fig. 6.1:

$$(SCH_2CH_2Ph)_{24}\text{crown} + 24\ H \rightarrow (HSCH_2CH_2Ph)^{crown} \quad \Delta E_{hyrd\text{-}lig/M} = 4.847\ eV \qquad (6.10)$$

$$(SPh)_{24}^{crown} + 24\ H \rightarrow (HSPh)_{24}^{crown} \quad \Delta E_{hyrd\text{-}lig/M} = 4.597\ eV \qquad (6.11)$$

$$(StBu)_{18}^{crown} + 18\ H \rightarrow (HStBu)_{18}^{crown} \quad \Delta E_{hyrd\text{-}lig/M} = 4.861\ eV \qquad (6.12)$$

and

$$(HSCH_2CH_2Ph)_{24}^{crown} \rightarrow 24\ (HSCH_2CH_2Ph)_{relax} \quad \Delta E_{H\text{-}ligsep/M} = 1.109\ eV \qquad (6.13)$$

$$(HSPh)_{24}^{crown} \rightarrow 24\ (HSPh)_{relax} \quad \Delta E_{H\text{-}ligsep/M} = 0.253\ eV \qquad (6.14)$$

$$(HStBu)_{18}^{crown} \rightarrow 18\ (HStBu)_{relax} \quad \Delta E_{H\text{-}ligsep/M} = 0.178\ eV \qquad (6.15)$$

$\Delta E_{hyrd\text{-}lig/M}$ can be compared with the strength of the S-H bond that is 4.875 eV in H-SCH_2CH_2Ph, 4.503 eV in H-SPh, and 4.863 eV in H-StBu, respectively: for $(StBu)_{18}$ it is nearly identical, whereas for $(SPh)_{24}$ and $(SCH_2CH_2Ph)_{24}$ it differs by 0.094 and 0.028 eV, respectively. Analogously, the separation energy of hydrogenated ligands for $Au_{30}(StBu)_{18}$ is nearly identical to that of the thiyl radical shell, this quantity is also close for $Au_{38}(SCH_2CH_2Ph)_{24}$ (1.109 vs. 1.137

eV), whereas for $Au_{36}(SPh)_{24}$ the value of 0.253 eV is somewhat larger than 0.159 eV for thiyl radicals, due to the fact that residual S-S bonds are weakened by conjugation. Notably, this proves that ligand-ligand interactions between phenyl rings [21], in which the major role is played by dispersion interactions among the organic residues, especially π-π and T-stackings interactions, account for the huge value of $\Delta E_{ligsep/M}$ in $Au_{38}(SCH_2CH_2Ph)_{24}$, and should thus be kept in mind when rationalizing the reasons of the experimentally observed thermodynamic stability of this compound. In particular, as discussed in Ref. [86], this stabilization will depend in a decisive way on the cluster environment, i.e., the solvent or the crystal, and will also depend on effects of configurational entropy, important for such floppy systems (but here provisionally neglected). Considering solvated species for example, we can expect that $Au_{38}(SCH_2CH_2Ph)_{24}$ will adopt a "brush" conformation in more "wetting" (more strongly interacting) solvents, such as e.g. benzene, and a "mushroom" conformation in less "wetting" solvents such as chloroform [105], possibly leading to its lesser stability in such media.

Finally, we note that for specific compounds here investigated we do not need to distinguish dispersion and repulsion interactions among the organic residues, i.e., attractive dispersion interactions from steric repulsion, due to the fact that steric repulsion is small in these species. It is however possible to make this distinction approximately quantitative as discussed in Ref. [38] via a system comparison approach of the type reviewed in the next sub-section, i.e., by transforming into and comparing with non-sterically hindered species via ligand exchange and matching the resulting energetics.

6.4.2 System Comparison Analysis and Chemical Potentials

To shed further light on interconversion processes experimentally investigated, it is useful to calculate direct energy balances among different mono-layer protected cluster species. In a

previous analysis [86] we analyzed the energetics of processes such as incremental formation or addition:

$Au_N(SR)_M + Au \rightarrow Au_{N+1}(SR)_M$ metal addition (6.16)

$Au_N(SR)_M + HSR \rightarrow Au_N(SR)_{M+1} + ½ H_2$ ligand addition (6.17)

$Au_N(SR)_M + e^- \rightarrow Au_N(SR)_M^-$ electron affinity (6.18)

In this analysis one needs values for the chemical potentials of an Au atom, μ(Au), a ligand thiol, μ (HSR), and an electron, μ (e^-), in addition to QM total energies. In the present context we won't use the electron chemical potential (6.18) as all species here considered are neutral, and for an easier read we will replace (6.16, 6.17) with a ligand exchange and cluster inter-conversion processes:

$Au_{N'}(SR')_{M'} + M'(HSR) \rightarrow Au_{N'}(SR)_{M'} + M'(HSR')$ ligand exchange (6.19)

$N\,Au_{N'}(SR)_{M'} + MN'(SR) \rightarrow N'\,Au_N(SR)_M + NM'(SR)$ cluster interconversion (6.20)

where we denote the reaction energy of the ligand exchange process (6.19) as $\Delta E_{lig\text{-}exch}$, and that of the cluster interconversion process (6.20) as $\Delta E_{int\text{-}conv}$. It should be noted that, while $Au_{N'}(SR')_{M'}$ and $Au_N(SR)_M$ are experimentally determined compounds, $Au_{N'}(SR)_{M'}$ intermediate species are not necessarily so, and their energetics have here been derived via simulations as described in the computational details.

Without analyzing all possible interconversion processes, let us focus on the most salient information that can be derived using Eqs. (6.19, 6.20) in addition to that already singled out in the previous sub-section.

First, it is instructive to system-compare via ligand exchange $Au_{38}(SCH_2CH_2Ph)_{24}$ and $Au_{38}(SCH_3)_{24}$. In detail, the reaction energy for ligand exchange ΔElig-exch for

"$Au_{38}(SCH_2CH_2Ph)_{24}$ → $Au_{38}(SCH_3)_{24}$" amounts to 24.285 eV, and is perfectly matched by the difference in ligand separation energy, ΔE_{ligsep}, between $(SCH_2CH_2Ph)_{24}^{crown}$[from-$Au_{38}(SCH_2CH_2Ph)_{24}$] and $(SCH_3)_{24}^{crown}$[from-$Au_{38}(SCH_3)_{24}$] = 24.276 eV. Not surprisingly, the energy difference between these two chemically similar species is *exclusively due to ligand-ligand interactions*.

Less obvious is that the ligand exchange reaction energy $\Delta E_{lig\text{-}exch}$ for "$Au_{38}(SCH_2CH_2Ph)_{24}$ → $Au_{38}(SPh)_{24}$" amounts to 16.498 eV and is partially albeit largely matched by the difference in ligand separation energy, ΔE_{ligsep}, between $(SCH_2CH_2Ph)_{24}^{crown}$[from-$Au_{38}(SCH_2CH_2Ph)_{24}$] and $(SPh)_{24}^{crown}$[from-$Au_{38}(SPh)_{24}$] = 15.809 eV. In other words, it turns out that the ligand exchange process "$Au_{38}(SCH_2CH_2Ph)_{24}$ → $Au_{38}(SPh)_{24}$" is also dominated by ligand-ligand interactions plus an additional stabilization of ≈0.7 eV. This is in tune with the fact that $Au_{38}(SPh)_{24}$ can indeed be synthesized under appropriate experimental conditions [173]: a stabilization of ≈0.7 eV can in fact be overcome by playing with the chemical potentials $\mu(HSCH_2CH_2Ph)$ and $\mu(HSPh)$ (i.e., changing temperature and reactant concentrations).

In contrast, the ligand exchange reaction energy $\Delta E_{lig\text{-}exch}$ for "$Au_{30}(SPh)_{18}$ → $Au_{30}(StBu)_{18}$" amounts to 1.185 eV and is over-matched by the difference in ligand separation energy, ΔE_{ligsep}, between $(SPh)_{18}^{crown}$[from-$Au_{30}(SPh)_{18}$] and $(StBu)_{18}^{crown}$[from-$Au_{30}(StBu)_{18}$] = 2.162 eV. In other words, $Au_{30}(SR)_{18}$ prefers to be in the bulky form, $Au_{30}(StBu)_{18}$ with respect to the aromatic form $Au_{30}(SPh)_{18}$ by ≈1.0 eV (neglecting ligand-ligand interaction effects). This suggests that $Au_{30}(SPh)_{18}$ could also be synthesized under carefully controlled conditions by playing with the chemical potentials $\mu(HSPh)$ and $\mu(HStBu)$.

As an example of cluster inter-conversion process, we take "$Au_{38}(SPh)_{24}$ → $Au_{36}(SPh)_{24}$":

$$36Au_{38}(SR)_{24} + 24x38(SPh) \rightarrow 38Au_{24}(SPh)_{24} + 24x36\ (SPh) \qquad (6.21)$$

or, equivalently,

$$36/24\ Au_{38}(SR)_{24} + 2\ (SPh) \rightarrow 38/24\ Au_{24}(SPh)_{24} \qquad (6.22)$$

The corresponding energy $\Delta E_{int\text{-}conv/M}$ normalized to the number of ligands (M=24) amounts to 2.983 eV. To further quantify this value, we need the chemical potential of SPh, μ(SPh), which we roughly estimate as the energy of the reaction:

$$HSPh \rightarrow \tfrac{1}{2}\ H_2 + SR \quad \Delta E = 1.320\ eV \qquad (6.23)$$

Thus, obtaining a total contribution due to μ(SPh) = 2 ΔE = 2.640 eV, 0.343 eV smaller than $\Delta E_{int\text{-}conv/M}$. In other words, $Au_{36}(SPh)_{24}$ turns out to be more stable than $Au_{38}(SPh)_{24}$ by 0.343 eV, but not quite enough as to recover the extra stabilization of $Au_{38}(SCH_2CH_2Ph)_{24}$, which we evaluated above as ≈0.7 eV. This can be interpreted in the sense that the structure of $Au_{38}(SCH_2CH_2Ph)_{24}$ is indeed particularly apt to favor SCH_2CH_2Ph-SCH_2CH_2Ph interactions.

The picture drawn from this total energy analysis seems in tune with experiment and able to provide further insight. What we believe is most important is the foundation of a quantitative basis to dissect and predict the thermodynamic stability of mono-layer protected clusters. From this analysis the importance of ligand-ligand interactions clearly stands out as a determining factor, especially for species with complex ligands such as $Au_{38}(SCH_2CH_2Ph)_{24}$ which, according to our analysis, due to substantial part of their stability to dispersive interactions, so that they may be expected to adopt "mushroom" conformations [105] in "non-wetting" solvents and thus be more stable in such media due to a "self-solvation" mechanism.

Clearly, we must point out that we focused here on electronic energies at equilibrium and zero temperature, i.e., we have here neglected vibrational and entropic contributions and kinetic

effects. However such effects have been shown to produce important effects for some nanomolecules [21], and will therefore be the subject of future studies.

Finally, to make connections with electrochemical applications of these systems [199] and also to extract useful quantities such as Mulliken electronegativity [200] and chemical hardness [201] which are commonly utilized to make semi-quantutative predictions of chemical propensity, we report vertical ionization potential (IP) and electron affinity (EA) of the nanomolecules here investigated. IP is the energy needed to extract an electron from the cluster, while EA is the energy gained in add an electron to the cluster, respectively, while keeping the geometry frozen at that optimized for the neutral species. The ionization potentials of $Au_{38}(SCH_2CH_2Ph)_{24}$, $Au_{36}(SPh)_{24}$, and $Au_{30}(StBu)_{18}$ nanomolecules are: 4.72 eV, 5.44 eV, 5.06 eV, respectively, while the electron affinities are: 2.29 eV, 2.17 eV, 1.75 eV, respectively. Interestingly, the chemical hardness [(IP-EA)/2] follow the order: 1.655 eV [$Au_{30}(StBu)_{18}$] ≈ 1.635 eV [$Au_{36}(SPh)_{24}$] > 1.215 eV [$Au_{38}(SCH_2CH_2Ph)_{24}$], whereas for the Mulliken electronegativity [(IP+EA)/2] the order is: 3.805 eV [$Au_{36}(SPh)_{24}$] > 3.505 eV [$Au_{38}(SCH_2CH_2Ph)_{24}$] > 3.405 eV [$Au_{30}(StBu)_{18}$], indicating that $Au_{36}(SPh)_{24}$] most easily receives an electron from the environment (because of delocalization on phenyl rings), whereas $Au_{38}(SCH_2CH_2Ph)_{24}$ is thermodynamically (although probably not kinetically) and chemically the most reactive species.

We have shown that with aromatic ligands $Au_{144}(SCH_2CH_2Ph)_{60}$ core-size converts to $Au_{133}(SPh\text{-}t\text{Bu})_{52}$ [21] and our hypothesis is that similar interconverting cycle of NMs (scheme 6.4) should exist at this size regime (1.6-1.7 nm). To date NM with bulky thiolate ligand in this size regime was not reported and potentially bulky thiolate ligand-induced core-size conversion on $Au_{144}(SCH_2CH_2Ph)_{60}$ NMs can be used to explore this area.

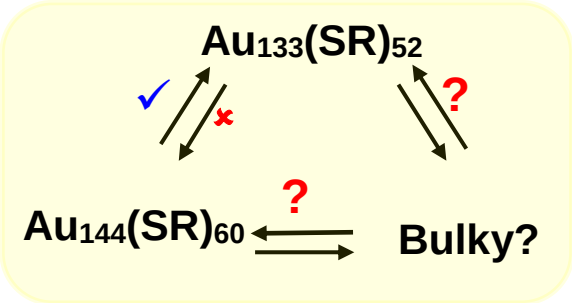

Scheme 6.4. Potential molecular interconversion cycle between similar core-size $Au_{144}(SCH_2CH_2Ph)_{60}$, $Au_{133}(SPh\text{-}t Bu)_{52}$ and bulky $Au_n(S\text{-}t Bu)_y$ NMs. Red (✗) indicates conversion that is restricted or not observed whereas blue (✓) indicates observed conversion and red (?) indicates possible or to be explored conversions.

6.5 Ligand Effect Demonstrated by Etching of a Common Precursor with Different Thiols

Core-size conversion reactions, initially reported as etching, [34] and more recently referred as , size-focusing [116], is a widely implemented post synthetic step that reduces the polydispersity of the initial product. It has been shown that $Au_n(SR)_m$ organo-soluble nanoclusters core-size converts to monodisperse $Au_{36}(SPh)_{24}$ NMs upon etching with thiophenol [91]. In our recent report, motivated by ligand induced core-size conversion reactions, we have devised a new synthetic protocol to demonstrate the ligand effect of the three class of thiolate ligands (AL, AR, and BU) using a common precursor based experimental setup. Core-size conversion of the common precursor Au_x(glutathiolate)$_y$ nanoclusters (SG-glutathiolate) is induced by the physicochemical difference in the exchanging ligand (Fig. 6.3a). Thus, the difference in steric and electronic effect between the two exchanging ligands plays a crucial role in determining the structure and properties of the NMs being synthesized, $Au_{38}(SCH_2CH_2Ph)_{24}$, $Au_{36}(SPh\text{-}tBu)_{24}$, and $Au_{30}(S\text{-}tBu)_{18}$. In the

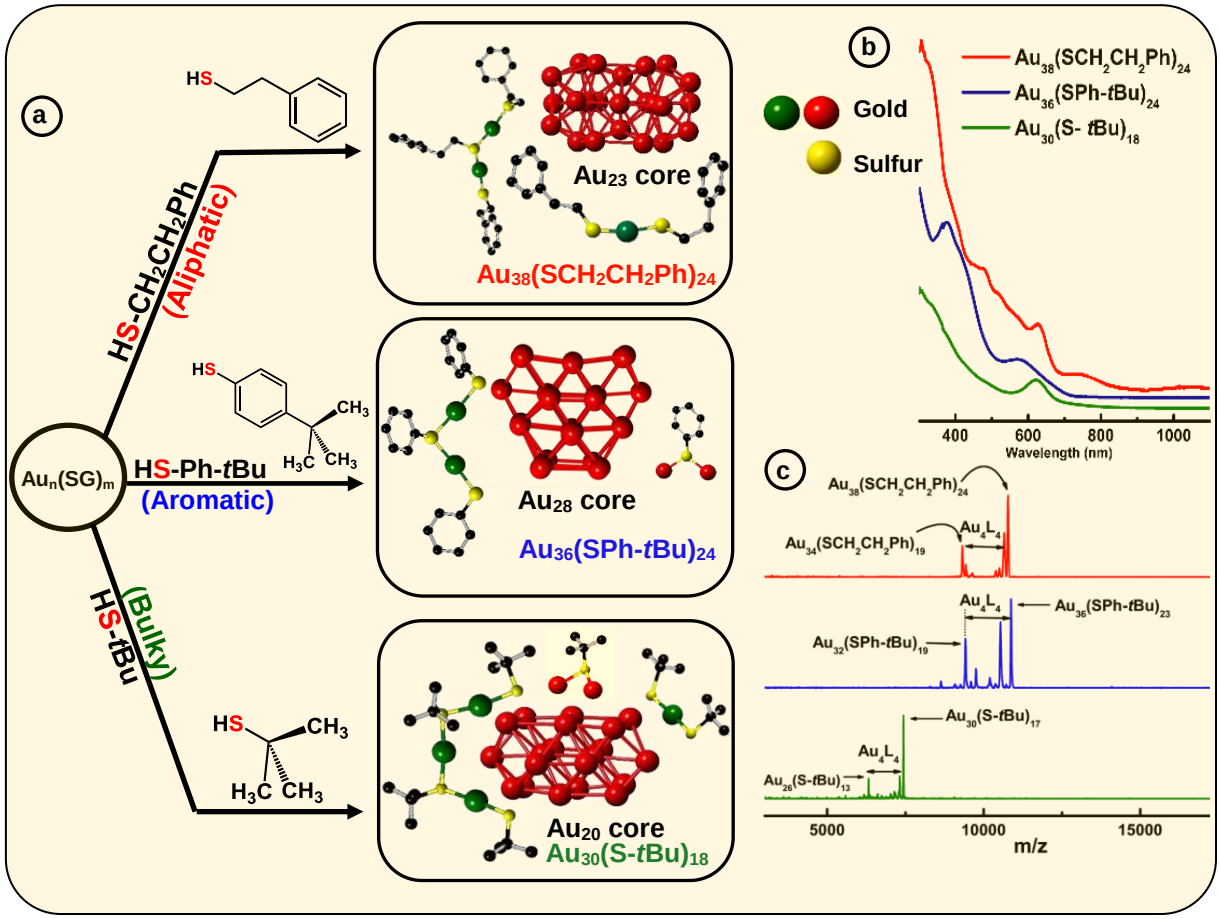

Figure 6.3. Ligand effect on the common $Au_n(SG)_m$ crude nanocluster mixture. (a) Upon thermochemical treatment on $Au_n(SG)_m$ kinetic product, with aliphatic ligand $HSCH_2CH_2Ph$, aromatic ligand HSPh-*t*Bu and bulky ligand HS-*t*Bu produce, monodisperse $Au_{38}(SCH_2CH_2Ph)_{24}$, $Au_{36}(SPh\text{-}tBu)_{24}$ and $Au_{30}(S\text{-}tBu)_{18}$ NMs, respectively. Corresponding assembly of crystal structures are shown to illustrate different core geometry and ligand environments (red - core Au, green-dimeric staple Au and monomeric staple Au, yellow--staple S and bridging S). (b) Corresponding UV-Vis-NIR absorption spectra illustrate the signature absorbance features unique to each individual NMs. (c) MALDI-MS of the core-size converted final products namely, $Au_{38}(SCH_2CH_2Ph)_{24}$, $Au_{36}(SPh\text{-}tBu)_{24}$ and $Au_{30}(S\text{-}tBu)_{18}$ NMs. Analytes were intentionally fragmented to demonstrate $Au_4(SR)_4$ loss, that is prominent in all three NMs.

case of $Au_{38}(SCH_2CH_2Ph)_{24}$, continuous prolonged etching at 80 °C for about 70 hours results in core-size conversion of the higher clusters to thermodynamically stable $Au_{38}(SCH_2CH_2Ph)_{24}$ NMs in the AL series. In PET, aliphatic C_2 chain $-CH_2CH_2-$ links between the sulfur head and phenyl ring hinders the extended conjugation of π electron. Therefore, electronic effect of the phenyl ring is minimum and primarily the structure of the nanomolecule is governed by the aliphatic-like nature of the PET ligand. During this core-size conversion all other meta-stable nanoclusters transform to most stable $Au_{38}(SCH_2CH_2Ph)_{24}$ or undergoes decomposition (Fig. 6.3c).

In contrast to the synthesis of $Au_{38}(SCH_2CH_2Ph)_{24}$, etching reaction with TBBT is rapid and fast kinetics were observed as monodisperse thermodynamically most stable $Au_{36}(SPh\text{-}tBu)_{24}$ NMs were formed after 18 hours of etching the $Au_n(SG)_m$ crude mixture at 80 °C. Fast reaction kinetics was observed possibly due to relatively higher acidity of the HSPh-*t*Bu ligand compared to PET (pKa = 6.6 and pKa ≈ 10 respectively). In contrast to AL and BU ligands, the TBBT (HSPh-

Table 6.2. Comparison of bond distance and bond angles of the $Au_{38}(SCH_2CH_2Ph)_{24}$, $Au_{36}(SPh\text{-}tBu)_{24}$ and $Au_{30}(S\text{-}tBu)_{18}$ NMs.

Parameter	$Au_{30}(S\text{-}tBu)_{18}$	$Au_{36}(SPh\text{-}tBu)_{24}$	$Au_{38}(SCH_2CH_2Ph)_{24}$
d(S-C)	**(1.848 ± 0.044) Å**	**(1.757 ± 0.032) Å**	**(1.842 ± 0.044) Å**
d(Au-S)	(2.325 ± 0.024) Å	(2.333 ± 0.016) Å	(2.325 ± 0.016) Å
a(Au-S-Au) monomeric staples	95.08°	-	93.53°
a(Au-S-Au) dimeric staples	-	94.28°	97.73°
a(Au-S-Au) trimeric staples	91.04°	-	-
Maximum a(Au-S-Au) higher	**94.57°**	**103.42°**	**101.08°**

Note: Average bond length and angle are indicated by *d* and *a*, respectively. Average bond distances and bond angle values of the three NMs having drastic difference are bolded.

*t*Bu) ligands have a direct electronic effect due to the presence of phenyl aromatic ring attached to head S atom. The π electron conjugation is extended to the gold atomic core results in electronic effect. This is evidence by the reduction of S-C bond length in Au_{36}(SPh-*t*Bu)$_{24}$ NMs in contrast to $Au_{38}(SCH_2CH_2Ph)_{24}$ and Au_{30}(S-*t*Bu)$_{18}$ NMs (table 6.2). In Au_{36}(SPh-*t*Bu)$_{24}$ NMs, overall 4.8% reduction in S-C average bond length can be seen with reference to aliphatic and bulky ligands. It is worth noting that, in our previous work we have observed that geometric stability arising form π-π or T-stacking of the phenyl ring are also somewhat important for the stability of aromatic thiolate shell protected NMs [38]. This ligand-ligand interaction favors the stability of ligand shell by electronic interactions and minimizes the steric repulsions. In fact, bond strain is reflected in higher order staples in corresponding crystal structures. Au_{30}(S-*t*Bu)$_{18}$, has relatively more strained Au-S-Au bond angles mainly due to bulky nature of the ligands. TBBT ligands being not as bulky as tert-butyl ligands the interpenetrating cuboctahedral geometry of the Au_{36}(SPh-*t*Bu)$_{24}$ core results in less strained bonds relative to $Au_{38}(SCH_2CH_2Ph)_{24}$, where $-CH_2CH_2-$ bridging of PET ligands may eliminate the requirement of having π-π or T-stacking among phenyl rings. Therefore,the core-size transformation of the $Au_n(SG)_m$ nanocluster mixture to Au_{36}(SPh-*t*Bu)$_{24}$ is induced by the combined effect of sterics and aromaticity of the TBBT ligand.

Tailoring the structure of metal nanoparticles is of paramount importance to utilize them effectively in related applications. Lammerhofer et al. have reported a size independent but ligand chain length dependent ligand density phenomenon. They have observed that ligand density increases from 4.3 to 6.3 molecules nm^{-2} upon decreasing the ligand chain length from 3.52 to .068 nm. Recent reports show that ligand density and ligand environment affect cell targeting efficacy and cellular uptake in biomedicine. Figure 6.3a illustrates that, three physicochemically different ligands investigated in this study results in different metallic core structures with unique surface

staple environments and optical properties. The three classes of thiols (AL, AR and BU) investigated in this study forms unique combination of surface staple arrangement unique to each nanomolecule. Among them, the bulky tert-butyl thiol is the only thiol to form two trimeric staples ($Au_3(SR)_4$). In addition, the surface occupies two dimeric ($Au_2(SR)_3$) and six bridging (AuSR) staples that surrounds Au_{22} bi-cuboctahedral gold core of the $Au_{30}(StBu)_{18}$ NMs. This could be a result of the bulkiness of the ligand inducing the metal core to be more elongated and to accommodate long trimeric staples minimizing the steric repulsions among ligands. In contrast, aromatic TBBT forms a four fused cuboctahedral Au_{28} gold core with a surface ligand shell of twelve bridging and four dimeric staples in $Au_{36}(SPh\text{-}t\text{Bu})_{24}$ NMs, whereas PET ligand forms an Au_{23} bi-icosahedral gold core with three monomeric ($Au(SR)_2$) and six dimeric surface staples in corresponding $Au_{38}(SCH_2CH_2Ph)_{24}$ NMs. Therefore, ligand structure is directly correlated to the structure and properties of the AuNMs and similarly it should be possible to tune atomic structure, metal-ligand interface and overall properties of the nanoparticle in higher size regime and quantum dots, simply by modifying the structure of the ligand.

6.6 Nano-scaling Law for Physicochemically Different Thiolate Protected Series of AuNMs

The common three-dimensional geometric objects such as sphere, cube, cuboctahedra etc., have been known to follow a simple Euclidean surface rule with a scaling factor of 2/3 corresponding to the surface area/volume ratio of the object. The allometric power fit of the surface area and volume of those objects provides the slope and y-intercept which relates to the scaling factor and compactness of the object. Likewise, allometric power fit of the number of gold atoms and thiolate ligands in a log-log plot has been empirically shown to provide similar insights on the AuNMs geometry and surface coverage [7]. The ligand dictates the AuNMs core atomic structure,

overall geometry and surface coverage. Distinct ligands form unique series of AuNMs and their scaling-law varies accordingly. Here we study the nano-scaling-law for three physicochemically different thiolate ligands, namely, aliphatic (PET), aromatic (TBBT) and bulky (S-*t*Bu) to determine the variability in scaling factor and compactness. Figure 6.4 reveal the nano-scaling for the three distinct series and Table S2 in the Appendix E lists the standard values and errors associated with the fit. It is very interesting that all three ligand types have a very similar scaling factor of ~0.6 which is very close to the 2/3 scaling factor for regular geometric objects. However, the compactness varies evidently for each series. The compactness index for aliphatic, aromatic

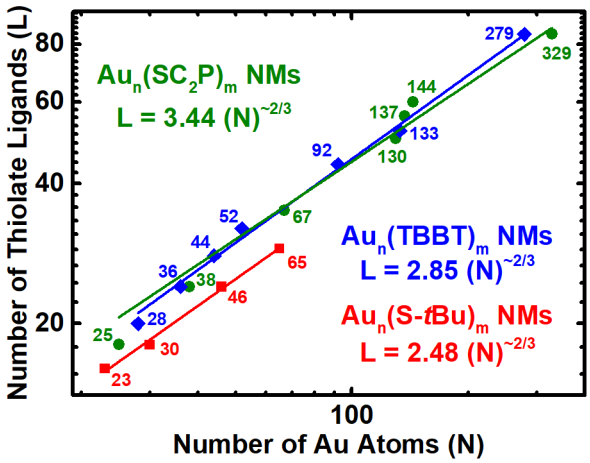

Figure 6.4. Nano-Scaling law for aliphatic, aromatic and bulky thiolated AuNMs series obtained by allometric powerfit of Log-Log plot of number of gold atoms (N) vs thiolate ligands (L). $Au_n(SCH_2CH_2Ph)_m$ - olive – spheres; $Au_n(TBBT)_m$ - blue – rhombus; Au_n(S-*t*Bu)$_m$ - Red – squares. The standard errors for aliphatic, aromatic and bulky thiolated AuNMs series are slope = 0.56±0.04, 0.60±0.01, and 0.59±0.02, respectively, and intercept = 3.44±0.68, 2.85±0.20, and 2.48±0.23, respectively. Reduced χ^2=11.48, 1.49, and 0.17, respectively; Adjusted R^2=0.9781, 0.9970, and 0.9953, respectively. Table S2 in Appendix E lists the standard errors and associated values.

and bulky ligand protected AuNMs are 3.44, 2.85, and 2.48, respectively. It is intriguing that all three series are compact than the most compact regular geometric shape, sphere, whose compactness index is 4.8. On the outlook, the bulky ligand protected AuNMs are more compact than aromatic and aliphatic ligands. Although the comparison between four sizes of bulky thiolated AuNMs and a large population of aliphatic and aromatic ligated AuNMs is not linear, it has to be realized that the slope trend is similar in all three AuNM series and compactness index of the bulky thiolated AuNMs might vary as the larger sizes are discovered. Overall, AuNMs follow a 2/3 scaling factor independent of the type of ligand and their compactness alone varies based on the respective ligand type.

6.7 Conclusions

In summary, the three experimental setups demonstrated here shows that physicochemically different thiolate ligands dictates the structure, metal-ligand staple interface and induces various optical and electrochemical properties unique to individual AuNMs. The effect of the thiolate ligand can be electronic due to aromaticity or steric or both and plays a key role in determining the thermodynamically stable structure. Attractive and steric ligand-ligand interactions are significant factors of AL, AR and BU thiolate ligands and overall dominating effect of these two factors determines the stability of the structure and properties of the AuNMs. Understanding the ligand structure dependence on atomic structure allows one to design and synthesize novel NMs. These understanding will improve the predictability of the designed synthetic protocols.

From this analysis, the importance of ligand-ligand interactions clearly stands out as a determining factor, especially for species with complex ligands such as $Au_{38}(SCH_2CH_2Ph)_{24}$

which, according to our computational analysis, dispersive interaction energy components make robust in “non-wetting” solvents via a “self-solvation” mechanism.

When aromatic thiol protected AuNMs are treated with BU *tert*-butyl thiol (which have the most similar sterics of the ligands examined), a core-size change was observed. Significantly, the observation of the reverse reaction (*tert*-butyl thiol protected Au NMs convert back with the introduction of aromatic thiol ligands) proves that thiol electronics and π-π interactions does not significantly influences the conversion as pKa values of these ligands are very different and the BU *tert*-butyl thiol does not have an aryl group. Potentially, the relative steric balance struck with these ligands allows for AuNMs core-size interconversions through simple excess ligand addition driving the AuNM core-size interconversion equilibrium to a single size.

It should be noted that while these experiments do suggest that sterics is a key factor in determining AuNM core-size with large ligands giving a more stabilized Au NM structure, this does not mean that π-π interaction and electron density at the sulfur atom do not have important effects on Au NM core-size selection. However, this does predict that for these weaker effects to become evident, sterics must first be balanced between the systems being compared. This observation is in line with literature precedent, when sulfur electron density was shown to control core-size selection, the steric component was held near constant.

BIBLIOGRAPHY

1. Edwards, P. P.; Thomas, J. M., Gold in a Metallic Divided State—From Faraday to Present-Day Nanoscience. *Angew. Chem. Int. Ed.* **2007,** *46* (29), 5480-5486.
2. Faraday, M., The Bakerian Lecture: Experimental Relations of Gold (and Other Metals) to Light. *Philosophical Transactions of the Royal Society of London* **1857,** *147*, 145-181.
3. Graham, T., Liquid diffusion applied to analysis. *Philosophical Transactions of the Royal Society of London* **1861** *151*, 183-224.
4. Tsukuda, T.; Häkkinen, H., *Protected Metal Clusters;From Fundamentals to Applications*. Elsevier: Amsterdam, 2015; Vol. 9.
5. Whetten, R. L.; Khoury, J. T.; Alvarez, M. M.; Murthy, S.; Vezmar, I.; Wang, Z. L.; Stephens, P. W.; Cleveland, C. L.; Luedtke, W. D.; Landman, U., Nanocrystal gold molecules. *Adv. Mater.* **1996,** *8* (5), 428-433.
6. Murray, R. W., Nanoelectrochemistry: Metal nanoparticles, nanoelectrodes, and nanopores. *Chem. Rev.* **2008,** *108* (7), 2688-2720.
7. Dass, A., Nano-scaling law: geometric foundation of thiolated gold nanomolecules. *Nanoscale* **2012,** *4* (7), 2260-2263.
8. Walter, M.; Akola, J.; Lopez-Acevedo, O.; Jadzinsky, P. D.; Calero, G.; Ackerson, C. J.; Whetten, R. L.; Grönbeck, H.; Häkkinen, H., A unified view of ligand-protected gold clusters as superatom complexes. *Proceedings of the National Academy of Sciences* **2008,** *105* (27), 9157-9162.
9. Bai, C.; Liu, M., From Chemistry to Nanoscience: Not Just a Matter of Size. *Angew. Chem. Int. Ed.* **2013,** *52* (10), 2678-2683.
10. Jadzinsky, P. D.; Calero, G.; Ackerson, C. J.; Bushnell, D. A.; Kornberg, R. D., Structure of a Thiol Monolayer-Protected Gold Nanoparticle at 1.1 Å Resolution. *Science* **2007,** *318* (5849), 430-433.
11. Kurashige, W.; Yamaguchi, M.; Nobusada, K.; Negishi, Y., Ligand-Induced Stability of Gold Nanoclusters: Thiolate versus Selenolate. *J. Phys. Chem. Lett.* **2012,** *3* (18), 2649-2652.
12. McPartlin, M.; Mason, R.; Malatesta, L., Novel cluster complexes of gold(0)-gold(I). *Journal of the Chemical Society D: Chemical Communications* **1969,** (7), 334-334.

13. Pettibone, J. M.; Hudgens, J. W., Gold Cluster Formation with Phosphine Ligands: Etching as a Size-Selective Synthetic Pathway for Small Clusters? *ACS Nano* **2011,** *5* (4), 2989-3002.

14. Yang, H.; Wang, Y.; Lei, J.; Shi, L.; Wu, X.; Mäkinen, V.; Lin, S.; Tang, Z.; He, J.; Häkkinen, H.; Zheng, L.; Zheng, N., Ligand-Stabilized Au13Cux (x = 2, 4, 8) Bimetallic Nanoclusters: Ligand Engineering to Control the Exposure of Metal Sites. *J. Am. Chem. Soc.* **2013,** *135* (26), 9568-9571.

15. Thakor, A. S.; Jokerst, J.; Zavaleta, C.; Massoud, T. F.; Gambhir, S. S., Gold Nanoparticles: A Revival in Precious Metal Administration to Patients. *Nano Lett.* **2011,** *11* (10), 4029-4036.

16. Li, T.; Li, F.; Xiang, W.; Yi, Y.; Chen, Y.; Cheng, L.; Liu, Z.; Xu, H., Selenium-Containing Amphiphiles Reduced and Stabilized Gold Nanoparticles: Kill Cancer Cells via Reactive Oxygen Species. *ACS Applied Materials & Interfaces* **2016,** *8* (34), 22106-22112.

17. Jiang, D.-e.; Tiago, M. L.; Luo, W.; Dai, S., The "Staple" Motif: A Key to Stability of Thiolate-Protected Gold Nanoclusters. *J. Am. Chem. Soc.* **2008,** *130* (9), 2777-2779.

18. Nimmala, P. R.; Knoppe, S.; Jupally, V. R.; Delcamp, J. H.; Aikens, C. M.; Dass, A., $Au_{36}(SPh)_{24}$ Nanomolecules: X-ray Crystal Structure, Optical Spectroscopy, Electrochemistry, and Theoretical Analysis. *J. Phys. Chem. B* **2014,** *118* (49), 14157-14167.

19. Crasto, D.; Dass, A., Green Gold: $Au_{30}(S\text{-}t\text{-}C_4H_9)_{18}$ Molecules. *J. Phys. Chem. C* **2013,** *117* (42), 22094-22097.

20. Dass, A.; Jones, T.; Rambukwella, M.; Crasto, D.; Gagnon, K. J.; Sementa, L.; De Vetta, M.; Baseggio, O.; Aprà, E.; Stener, M.; Fortunelli, A., Crystal Structure and Theoretical Analysis of Green Gold $Au_{30}(S\text{-}tBu)_{18}$ Nanomolecules and Their Relation to $Au_{30}S(S\text{-}tBu)_{18}$. *J. Phys. Chem. C* **2016,** *120* (11), 6256-6261.

21. Nimmala, P. R.; Theivendran, S.; Barcaro, G.; Sementa, L.; Kumara, C.; Jupally, V. R.; Apra, E.; Stener, M.; Fortunelli, A.; Dass, A., Transformation of $Au_{144}(SCH_2CH_2Ph)_{60}$ to $Au_{133}(SPh\text{-}tBu)_{52}$ Nanomolecules: Theoretical and Experimental Study. *J. Phys. Chem. Lett.* **2015,** *6* (11), 2134-2139.

22. Yan, N.; Liao, L.; Yuan, J.; Lin, Y.-j.; Weng, L.-h.; Yang, J.; Wu, Z., Bimetal Doping in Nanoclusters: Synergistic or Counteractive? *Chem. Mater.* **2016,** *28* (22), 8240-8247.

23. Wang, S.; Song, Y.; Jin, S.; Liu, X.; Zhang, J.; Pei, Y.; Meng, X.; Chen, M.; Li, P.; Zhu, M., Metal Exchange Method Using Au25 Nanoclusters as Templates for Alloy Nanoclusters with Atomic Precision. *J. Am. Chem. Soc.* **2015,** *137* (12), 4018-4021.

24. Kumara, C.; Gagnon, K. J.; Dass, A., X-ray Crystal Structure of $Au_{38-x}Ag_x(SCH_2CH_2Ph)_{24}$ Alloy Nanomolecules. *J. Phys. Chem. Lett.* **2015,** *6* (7), 1223-1228.

25. Dharmaratne, A. C.; Dass, A., $Au_{144-x}Cu_x(SC_6H_{13})_{60}$ nanomolecules: effect of Cu incorporation on composition and plasmon-like peak emergence in optical spectra. *Chem. Commun.* **2014,** *50* (14), 1722-1724.

26. Jupally, V. R.; Dass, A., Synthesis of $Au_{130}(SR)_{50}$ and $Au_{130-x}Ag_x(SR)_{50}$ nanomolecules through core size conversion of larger metal clusters. *PCCP* **2014,** *16* (22), 10473-10479.

27. Kwak, K.; Choi, W.; Tang, Q.; Kim, M.; Lee, Y.; Jiang, D.-e.; Lee, D., A molecule-like $PtAu_{24}(SC_6H_{13})_{18}$ nanocluster as an electrocatalyst for hydrogen production. *Nat. Commun.* **2017,** *8*, 14723.

28. Peiris, S.; Sarina, S.; Han, C.; Xiao, Q.; Zhu, H.-Y., Silver and palladium alloy nanoparticle catalysts: reductive coupling of nitrobenzene through light irradiation. *Dalton Transactions* **2017,** *46* (32), 10665-10672.

29. Jiang, T.; Jia, C.; Zhang, L.; He, S.; Sang, Y.; Li, H.; Li, Y.; Xu, X.; Liu, H., Gold and gold-palladium alloy nanoparticles on heterostructured TiO_2 nanobelts as plasmonic photocatalysts for benzyl alcohol oxidation. *Nanoscale* **2015,** *7* (1), 209-217.

30. Brust, M.; Walker, M.; Bethell, D.; Schiffrin, D. J.; Whyman, R., Synthesis of thiol-derivatised gold nanoparticles in a two-phase Liquid-Liquid system. *J. Chem. Soc., Chem. Commun.* **1994,** (7), 801-802.

31. Rambukwella, M.; Dass, A., Synthesis of $Au_{38}(SCH_2CH_2Ph)_{24}$, $Au_{36}(SPh\text{-}tBu)_{24}$, and $Au_{30}(S\text{-}tBu)_{18}$ Nanomolecules from a Common Precursor Mixture. *Langmuir* **2017,** *33* (41), 10958-10964.

32. Theivendran, S.; Dass, A., Synthesis of Aromatic Thiolate-Protected Gold Nanomolecules by Core Conversion: The Case of $Au_{36}(SPh\text{-}tBu)_{24}$. *Langmuir* **2017,** *33* (30), 7446-7451.

33. Dharmaratne, A. C.; Krick, T.; Dass, A., Nanocluster Size Evolution Studied by Mass Spectrometry in Room Temperature $Au_{25}(SR)_{18}$ Synthesis. *J. Am. Chem. Soc.* **2009,** *131* (38), 13604-13605.

34. Schaaff, T. G.; Whetten, R. L., Controlled Etching of Au:SR Cluster Compounds. *J. Phys. Chem. B* **1999,** *103* (44), 9394-9396.

35. Shon, Y.-S.; Mazzitelli, C.; Murray, R. W., Unsymmetrical Disulfides and Thiol Mixtures Produce Different Mixed Monolayer-Protected Gold Clusters. *Langmuir* **2001,** *17* (25), 7735-7741.

36. Chen, S.; Templeton, A. C.; Murray, R. W., Monolayer-Protected Cluster Growth Dynamics. *Langmuir* **2000,** *16* (7), 3543-3548.

37. Wu, Z.; Suhan, J.; Jin, R., One-pot synthesis of atomically monodisperse, thiol-functionalized Au_{25} nanoclusters. *J. Mater. Chem.* **2009,** *19* (5), 622-626.

38. Rambukwella, M.; Sementa, L.; Barcaro, G.; Fortunelli, A.; Dass, A., Organosoluble $Au_{102}(SPh)_{44}$ Nanomolecules: Synthesis, Isolation, Compositional Assignment, Core Conversion, Optical Spectroscopy, Electrochemistry, and Theoretical Analysis. *J. Phys. Chem. C* **2015,** *119* (44), 25077-25084.

39. Dass, A., Faradaurate Nanomolecules: A Superstable Plasmonic 76.3 kDa Cluster. *J. Am. Chem. Soc.* **2011,** *133* (48), 19259-19261.

40. Negishi, Y.; Sakamoto, C.; Ohyama, T.; Tsukuda, T., Synthesis and the Origin of the Stability of Thiolate-Protected Au_{130} and Au_{187} Clusters. *J. Phys. Chem. Lett.* **2012,** *3* (12), 1624-1628.

41. Knoppe, S.; Boudon, J.; Dolamic, I.; Dass, A.; Bürgi, T., Size Exclusion Chromatography for Semipreparative Scale Separation of $Au_{38}(SR)_{24}$ and $Au_{40}(SR)_{24}$ and Larger Clusters. *Anal. Chem.* **2011,** *83* (13), 5056-5061.

42. Dass, A.; Nimmala, P. R.; Jupally, V. R.; Kothalawala, N., $Au_{103}(SR)_{45}$, $Au_{104}(SR)_{45}$, $Au_{104}(SR)_{46}$ and $Au_{105}(SR)_{46}$ nanoclusters. *Nanoscale* **2013,** *5* (24), 12082-12085.

43. Jupally, V. R.; Dharmaratne, A. C.; Crasto, D.; Huckaba, A. J.; Kumara, C.; Nimmala, P. R.; Kothalawala, N.; Delcamp, J. H.; Dass, A., $Au_{137}(SR)_{56}$ nanomolecules: composition, optical

spectroscopy, electrochemistry and electrocatalytic reduction of CO_2. *Chem. Commun.* **2014,** *50* (69), 9895-9898.

44. Dass, A.; Stevenson, A.; Dubay, G. R.; Tracy, J. B.; Murray, R. W., Nanoparticle MALDI-TOF Mass Spectrometry without Fragmentation: $Au_{25}(SCH_2CH_2Ph)_{18}$ and Mixed Monolayer $Au_{25}(SCH_2CH_2Ph)_{18-x}(L)_x$. *J. Am. Chem. Soc.* **2008,** *130* (18), 5940-5946.
45. Tracy, J. B.; Crowe, M. C.; Parker, J. F.; Hampe, O.; Fields-Zinna, C. A.; Dass, A.; Murray, R. W., Electrospray Ionization Mass Spectrometry of Uniform and Mixed Monolayer Nanoparticles: $Au_{25}[S(CH_2)_2Ph]_{18}$ and $Au_{25}[S(CH_2)_2Ph]_{18}^{-}x(SR)x$. *J. Am. Chem. Soc.* **2007,** *129* (51), 16209-16215.
46. Qian, H.; Zhu, M.; Wu, Z.; Jin, R., Quantum Sized Gold Nanoclusters with Atomic Precision. *Acc. Chem. Res.* **2012,** *45* (9), 1470-1479.
47. Qian, H.; Zhu, Y.; Jin, R., Atomically precise gold nanocrystal molecules with surface plasmon resonance. *Proceedings of the National Academy of Sciences* **2012,** *109* (3), 696-700.
48. Wu, Z.; Gayathri, C.; Gil, R. R.; Jin, R., Probing the Structure and Charge State of Glutathione-Capped $Au_{25}(SG)_{18}$ Clusters by NMR and Mass Spectrometry. *J. Am. Chem. Soc.* **2009,** *131* (18), 6535-6542.
49. Nimmala, P. R.; Yoon, B.; Whetten, R. L.; Landman, U.; Dass, A., $Au_{67}(SR)_{35}$ Nanomolecules: Characteristic Size-Specific Optical, Electrochemical, Structural Properties and First-Principles Theoretical Analysis. *J. Phys. Chem. A* **2013,** *117* (2), 504-517.
50. Heaven, M. W.; Dass, A.; White, P. S.; Holt, K. M.; Murray, R. W., Crystal structure of the gold nanoparticle $[N(C_8H_{17})_4][Au_{25}(SCH_2CH_2Ph)_{18}]$. *J. Am. Chem. Soc.* **2008,** *130* (12), 3754-3755.
51. Qian, H.; Eckenhoff, W. T.; Zhu, Y.; Pintauer, T.; Jin, R., Total Structure Determination of Thiolate-Protected Au_{38} Nanoparticles. *J. Am. Chem. Soc.* **2010,** *132* (24), 8280-8281.
52. Kumara, C.; Zuo, X.; Ilavsky, J.; Cullen, D.; Dass, A., Atomic Structure of $Au_{329}(SR)_{84}$ Faradaurate Plasmonic Nanomolecules. *J. Phys. Chem. C* **2015,** *119* (20), 11260-11266.

53. Kumara, C.; Zuo, X.; Ilavsky, J.; Chapman, K. W.; Cullen, D. A.; Dass, A., Super-Stable, Highly Monodisperse Plasmonic Faradaurate-500 Nanocrystals with 500 Gold Atoms: $Au_{\sim 500}(SR)_{\sim 120}$. *J. Am. Chem. Soc.* **2014,** *136* (20), 7410-7417.

54. Alvarez, M. M.; Khoury, J. T.; Schaaff, T. G.; Shafigullin, M. N.; Vezmar, I.; Whetten, R. L., Optical absorption spectra of nanocrystal gold molecules. *J. Phys. Chem. B* **1997,** *101* (19), 3706-3712.

55. Knoppe, S.; Bürgi, T., Chirality in Thiolate-Protected Gold Clusters. *Acc. Chem. Res.* **2014,** *47* (4), 1318-1326.

56. Li, G.; Jin, R., Atomically Precise Gold Nanoclusters as New Model Catalysts. *Acc. Chem. Res.* **2013,** *46* (8), 1749-1758.

57. Yamazoe, S.; Koyasu, K.; Tsukuda, T., Nonscalable Oxidation Catalysis of Gold Clusters. *Acc. Chem. Res.* **2013,** *47* (3), 816-824.

58. Jadzinsky, P. D.; Calero, G.; Ackerson, C. J.; Bushnell, D. A.; Kornberg, R. D., Structure of a thiol monolayer-protected gold nanoparticle at 1.1 angstrom resolution. *Science* **2007,** *318*, 430-433.

59. Qian, H.; Zhu, M.; Wu, Z.; Jin, R., Quantum Sized Gold Nanoclusters with Atomic Precision. *Acc. Chem. Res.* **2012,** *45* (9), 1470-79.

60. Walter, M.; Akola, J.; Lopez-Acevedo, O.; Jadzinsky, P. D.; Calero, G.; Ackerson, C. J.; Whetten, R. L.; Gronbeck, H.; Hakkinen, H., A unified view of ligand-protected gold clusters as superatom complexes. *Proc. Natl. Acad. Sci. U.S.A.* **2008,** *105* (27), 9157-9162.

61. Dass, A.; Theivendran, S.; Nimmalla, P.; Kumara, C.; Jupally, V.; Fortunelli, A.; Sementa, L.; Barcaro, G.; Zuo, X.; Noll, B. C., $Au_{133}(SR)_{52}$ Nanomolecules: X-ray Crystallography, Optical, Electrochemical, and Theoretical Analysis. *J. Am. Chem. Soc.* **2015**, DOI: 10.1021/ja51312h.

62. Zeng, C.; Chen, Y.; Kirschbaum, K.; Appavoo, K.; Sfeir, M. Y.; Jin, R., *Structural patterns at all scales in a nonmetallic chiral $Au_{133}(SR)_{52}$ nanoparticle*. 2015; Vol. 1.

63. Zeng, C.; Qian, H.; Li, T.; Li, G.; Rosi, N. L.; Yoon, B.; Barnett, R. N.; Whetten, R. L.; Landman, U.; Jin, R., Total Structure and Electronic Properties of the Gold Nanocrystal Au36(SR)24. *Angew. Chem. Int. Ed.* **2012,** *51* (52), 13114-13118.

64. Williams, R., *The Geometrical Foundation of Natural Structure: a Source Book of Design*. Dover Publications, Inc. : New York, 1979.

65. Ackerson, C. J.; Jadzinsky, P. D.; Kornberg, R. D., Thiolate ligands for synthesis of water-soluble gold clusters. *J. Am. Chem. Soc.* **2005,** *127* (18), 6550-6551.

66. Tvedte, L. M.; Ackerson, C. J., Size-Focusing Synthesis of Gold Nanoclusters with p-Mercaptobenzoic Acid. *J. Phys. Chem. A* **2014,** *118* (37), 8124-8128.

67. Negishi, Y.; Nobusada, K.; Tsukuda, T., Glutathione-protected gold clusters revisited: Bridging the gap between gold(I)-thiolate complexes and thiolate-protected gold nanocrystals. *J. Am. Chem. Soc.* **2005,** *127* (14), 5261-5270.

68. Kimura, K.; Sugimoto, N.; Sato, S.; Yao, H.; Negishi, Y.; Tsukuda, T., Size Determination of Gold Clusters by Polyacrylamide Gel Electrophoresis in a Large Cluster Region. *J. Phys. Chem. C.* **2009,** *113* (32), 14076-14082.

69. Kothalawala, N.; Lee West Iv, J.; Dass, A., Size-dependent molecule-like to plasmonic transition in water-soluble glutathione stabilized gold nanomolecules. *Nanoscale* **2014,** *6* (2), 683-687.

70. Desireddy, A.; Kumar, S.; Guo, J.; Bolan, M. D.; Griffith, W. P.; Bigioni, T. P., Temporal stability of magic-number metal clusters: beyond the shell closing model. *Nanoscale* **2013,** *5* (5), 2036-2044.

71. Levi-Kalisman, Y.; Jadzinsky, P. D.; Kalisman, N.; Tsunoyama, H.; Tsukuda, T.; Bushnell, D. A.; Kornberg, R. D., Synthesis and Characterization of Au_{102}(p-MBA)$_{44}$ Nanoparticles. *J. Am. Chem. Soc.* **2011,** *133* (9), 2976-2982.

72. Hulkko, E.; Lopez-Acevedo, O.; Koivisto, J.; Levi-Kalisman, Y.; Kornberg, R. D.; Pettersson, M.; Häkkinen, H., Electronic and Vibrational Signatures of the Au_{102}(p-MBA)$_{44}$ Cluster. *J. Am. Chem. Soc.* **2011,** *133* (11), 3752-3755.

73. Heinecke, C. L.; Ni, T. W.; Malola, S.; Mäkinen, V.; Wong, O. A.; Häkkinen, H.; Ackerson, C. J., Structural and Theoretical Basis for Ligand Exchange on Thiolate Monolayer Protected Gold Nanoclusters. *J. Am. Chem. Soc.* **2012,** *134* (32), 13316-13322.

74. Gao, Y.; Shao, N.; Zeng, X. C., Ab initio study of thiolate-protected Au_{102} nanocluster. *ACS Nano* **2008,** *2* (7), 1497-1503.

75. Li, Y.; Galli, G.; Gygi, F. o., Electronic Structure of Thiolate-Covered Gold Nanoparticles: $Au_{102}(MBA)_{44}$. *Acs Nano* **2008,** *2* (9), 1896-1902.

76. Mednikov, E. G.; Dahl, L. E., Crystallographically proven nanometer-sized gold thiolate cluster $Au_{102}(SR)_{44}$: Its unexpected molecular anatomy and resulting stereochemical and bonding consequences. *Small* **2008,** *4* (5), 534-537.

77. Han, Y.-K.; Kim, H.; Jung, J.; Choi, Y. C., Understanding the Magic Nature of Ligand-Protected Gold Nanoparticle $Au_{102}(MBA)_{44}$. *J. Phys. Chem. C.* **2010,** *114* (17), 7548-7552.

78. Jung, J.; Kang, S.; Han, Y.-K., Ligand effects on the stability of thiol-stabilized gold nanoclusters: $Au_{25}(SR)_{18}^{-}$, $Au_{38}(SR)_{24}$, and $Au_{102}(SR)_{44}$. *Nanoscale* **2012,** *4* (14), 4206-4210.

79. Reimers, J. R.; Wang, Y.; Cankurtaran, B. O.; Ford, M. J., Chemical Analysis of the Superatom Model for Sulfur-Stabilized Gold Nanoparticles. *J. Am. Chem. Soc.* **2010,** *132* (24), 8378-8384.

80. Chen, S. W.; Murray, R. W., Arenethiolate monolayer-protected gold clusters. *Langmuir* **1999,** *15* (3), 682-689.

81. Nimmala, P. R.; Dass, A., $Au_{99}(SPh)_{42}$ Nanomolecules: Aromatic Thiolate Ligand Induced Conversion of $Au_{144}(SCH_2CH_2Ph)_{60}$. *J. Am. Chem. Soc.* **2014,** *136* (49), 17016-17023.

82. Li, G.; Zeng, C.; Jin, R., Thermally Robust $Au_{99}(SPh)_{42}$ Nanoclusters for Chemoselective Hydrogenation of Nitrobenzaldehyde Derivatives in Water. *J. Am. Chem. Soc.* **2014,** *136* (9), 3673-3679.

83. Dass, A.; Stevenson, A.; Dubay, G. R.; Tracy, J. B.; Murray, R. W., Nanoparticle MALDI-TOF mass spectrometry without fragmentation: $Au_{25}(SCH_2CH_2Ph)_{18}$ and mixed monolayer $Au_{25}(SCH_2CH_2Ph)_{18-x}(L)_x$. *J. Am. Chem. Soc.* **2008,** *130* (18), 5940-5946.

84. Nimmala, P. R.; Dass, A., $Au_{99}(SPh)_{42}$ Nanomolecules: Aromatic Thiolate Ligand Induced Conversion of $Au_{144}(SCH_2CH_2Ph)_{60}$. *J. Am. Chem. Soc.* **2014**.

85. Nimmala, P. R.; Jupally, V. R.; Dass, A., Core Size Conversion: Route for Exclusive Synthesis of Au_{38} or Au_{40} Nanomolecules. *Langmuir* **2014,** *30* (9), 2490-2497.

86. Crasto, D.; Barcaro, G.; Stener, M.; Sementa, L.; Fortunelli, A.; Dass, A., $Au_{24}(SAdm)_{16}$ Nanomolecules: X-ray Crystal Structure, Theoretical Analysis, Adaptability of Adamantane Ligands to Form $Au_{23}(SAdm)_{16}$ and $Au_{25}(SAdm)_{16}$, and Its Relation to $Au_{25}(SR)_{18}$. *J. Am. Chem. Soc.* **2014,** *136* (42), 14933-14940.

87. Sinnokrot, M. O.; Sherrill, C. D., Highly Accurate Coupled Cluster Potential Energy Curves for the Benzene Dimer: Sandwich, T-Shaped, and Parallel-Displaced Configurations. *J. Phys. Chem. A.* **2004,** *108* (46), 10200-10207.

88. Sementa, L.; Barcaro, G.; Dass, A.; Stener, M.; Fortunelli, A., Designing ligand-enhanced optical absorption of thiolated gold nanoclusters. *Chem. Commun.* **2015**, 10.1039/C5CC01951F.

89. Maity, P.; Xie, S.; Yamauchi, M.; Tsukuda, T., Stabilized gold clusters: from isolation toward controlled synthesis. *Nanoscale* **2012,** *4* (14), 4027-4037.

90. Wang, L.-M.; Wang, L.-S., Probing the electronic properties and structural evolution of anionic gold clusters in the gas phase. *Nanoscale* **2012,** *4* (14), 4038-4053.

91. Nimmala, P. R.; Dass, A., $Au_{36}(SPh)_{23}$ Nanomolecules. *J. Am. Chem. Soc.* **2011,** *133* (24), 9175-9177.

92. Zeng, C.; Liu, C.; Pei, Y.; Jin, R., Thiol Ligand-Induced Transformation of $Au_{38}(SC_2H_4Ph)_{24}$ to $Au_{36}(SPh\text{-}t\text{-}Bu)_{24}$. *ACS Nano* **2013,** *7* (7), 6138-6145.

93. Crasto, D.; Malola, S.; Brosofsky, G.; Dass, A.; Häkkinen, H., Single Crystal XRD Structure and Theoretical Analysis of the Chiral $Au_{30}S(S\text{-}t\text{-}Bu)_{18}$ Cluster. *J. Am. Chem. Soc.* **2014,** *136* (13), 5000-5005.

94. Hesari, M.; Workentin, M. S., Facile synthesis of $Au_{23}(SC(CH_3)_3)_{16}$ clusters. *J. Mater. Chem. C* **2014,** *2* (18), 3631-3638.

95. Yang, H.; Wang, Y.; Edwards, A. J.; Yan, J.; Zheng, N., High-yield synthesis and crystal structure of a green Au_{30} cluster co-capped by thiolate and sulfide. *Chem. Commun.* **2014,** *50* (92), 14325-14327.

96. Qian, H.; Zhu, Y.; Jin, R., Size-Focusing Synthesis, Optical and Electrochemical Properties of Monodisperse $Au_{38}(SC_2H_4Ph)_{24}$ Nanoclusters. *ACS Nano* **2009,** *3* (11), 3795-3803.

97. Hutter, J.; Iannuzzi, M.; Schiffmann, F.; VandeVondele, J., cp2k: atomistic simulations of condensed matter systems. *Wiley Interdisciplinary Reviews: Computational Molecular Science* **2014,** *4* (1), 15-25.

98. Lippert, G.; Hutter, J.; Parrinello, M., The Gaussian and augmented-plane-wave density functional method for ab initio molecular dynamics simulations. *Theor. Chem. Acc.* **1999,** *103* (2), 124-140.

99. Goedecker, S.; Teter, M.; Hutter, J., Separable dual-space Gaussian pseudopotentials. *Physical Review B* **1996,** *54* (3), 1703-1710.

100. VandeVondele, J.; Hutter, J., Gaussian basis sets for accurate calculations on molecular systems in gas and condensed phases. *J. Chem. Phys.* **2007,** *127* (11), 114105.

101. Grimme, S.; Antony, J.; Ehrlich, S.; Krieg, H., A consistent and accurate ab initio parametrization of density functional dispersion correction (DFT-D) for the 94 elements H-Pu. *J. Chem. Phys.* **2010,** *132* (15), 154104.

102. Perdew, J. P.; Burke, K.; Ernzerhof, M., Generalized Gradient Approximation Made Simple. *Phys. Rev. Lett.* **1996,** *77* (18), 3865-3868.

103. Martyna, G. J.; Klein, M. L.; Tuckerman, M., Nosé–Hoover chains: The canonical ensemble via continuous dynamics. *J. Chem. Phys.* **1992,** *97* (4), 2635-2643.

104. Deng, Y.-K.; Su, H.-F.; Xu, J.-H.; Wang, W.-G.; Kurmoo, M.; Lin, S.-C.; Tan, Y.-Z.; Jia, J.; Sun, D.; Zheng, L.-S., Hierarchical Assembly of a {MnII15MnIII4} Brucite Disc: Step-by-Step Formation and Ferrimagnetism. *J. Am. Chem. Soc.* **2016,** *138* (4), 1328-1334.

105. de Gennes, P. G., Conformations of Polymers Attached to an Interface. *Macromolecules* **1980,** *13* (5), 1069-1075.

106. Qian, H.; Jiang, D.-e.; Li, G.; Gayathri, C.; Das, A.; Gil, R. R.; Jin, R., Monoplatinum Doping of Gold Nanoclusters and Catalytic Application. *J. Am. Chem. Soc.* **2012,** *134* (39), 16159-16162.

107. Saha, K.; Agasti, S. S.; Kim, C.; Li, X.; Rotello, V. M., Gold Nanoparticles in Chemical and Biological Sensing. *Chem. Rev.* **2012,** *112* (5), 2739-2779.

108. Kwak, K.; Kumar, S. S.; Pyo, K.; Lee, D., Ionic Liquid of a Gold Nanocluster: A Versatile Matrix for Electrochemical Biosensors. *ACS Nano* **2014,** *8* (1), 671-679.

109. Daniel, M.-C.; Astruc, D., Gold Nanoparticles: Assembly, Supramolecular Chemistry, Quantum-Size-Related Properties, and Applications toward Biology, Catalysis, and Nanotechnology. *Chem. Rev.* **2004,** *104* (1), 293-346.

110. Alvarez, M. M.; Khoury, J. T.; Schaaff, T. G.; Shafigullin, M. N.; Vezmar, I.; Whetten, R. L., Optical Absorption Spectra of Nanocrystal Gold Molecules. *J. Phys. Chem. B* **1997,** *101* (19), 3706-3712.

111. Weissker, H. C.; Escobar, H. B.; Thanthirige, V. D.; Kwak, K.; Lee, D.; Ramakrishna, G.; Whetten, R. L.; López-Lozano, X., Information on quantum states pervades the visible spectrum of the ubiquitous Au144(SR)60 gold nanocluster. *Nature Communications* **2014,** *5*, 3785.

112. Antonello, S.; Perera, N. V.; Ruzzi, M.; Gascón, J. A.; Maran, F., Interplay of Charge State, Lability, and Magnetism in the Molecule-like Au25(SR)18 Cluster. *J. Am. Chem. Soc.* **2013,** *135* (41), 15585-15594.

113. Yamazoe, S.; Koyasu, K.; Tsukuda, T., Nonscalable Oxidation Catalysis of Gold Clusters. *Acc. Chem. Res.* **2014,** *47* (3), 816-824.

114. Wang, S.; Jin, S.; Yang, S.; Chen, S.; Song, Y.; Zhang, J.; Zhu, M., Total structure determination of surface doping $[Ag_6Au_{24}(SR)_{32}](BPh_4)_2$ nanocluster and its structure-related catalytic property. *Science Advances* **2015,** *1* (7).

115. Wu, Z.; MacDonald, M. A.; Chen, J.; Zhang, P.; Jin, R., Kinetic Control and Thermodynamic Selection in the Synthesis of Atomically Precise Gold Nanoclusters. *J. Am. Chem. Soc.* **2011,** *133* (25), 9670-9673.

116. Jin, R.; Qian, H.; Wu, Z.; Zhu, Y.; Zhu, M.; Mohanty, A.; Garg, N., Size Focusing: A Methodology for Synthesizing Atomically Precise Gold Nanoclusters. *J. Phys. Chem. Lett.* **2010,** *1* (19), 2903-2910.

117. Liao, L.; Yao, C.; Wang, C.; Tian, S.; Chen, J.; Li, M.-B.; Xia, N.; Yan, N.; Wu, Z., Quantitatively Monitoring the Size-Focusing of Au Nanoclusters and Revealing What Promotes the Size Transformation from $Au_{44}(TBBT)_{28}$ to $Au_{36}(TBBT)_{24}$. *Anal. Chem.* **2016,** *88* (23), 11297-11301.

118. Black, D. M.; Bach, S. B. H.; Whetten, R. L., Capillary Liquid Chromatography Mass Spectrometry Analysis of Intact Monolayer-Protected Gold Clusters in Complex Mixtures. *Anal. Chem.* **2016,** *88* (11), 5631-5636.

119. Desireddy, A.; Conn, B. E.; Guo, J.; Yoon, B.; Barnett, R. N.; Monahan, B. M.; Kirschbaum, K.; Griffith, W. P.; Whetten, R. L.; Landman, U.; Bigioni, T. P., Ultrastable silver nanoparticles. *Nature* **2013,** *501* (7467), 399-402.

120. AbdulHalim, L. G.; Ashraf, S.; Katsiev, K.; Kirmani, A. R.; Kothalawala, N.; Anjum, D. H.; Abbas, S.; Amassian, A.; Stellacci, F.; Dass, A.; Hussain, I.; Bakr, O. M., A scalable synthesis of highly stable and water dispersible $Ag_{44}(SR)_{30}$ nanoclusters. *J. Mat. Chem. A* **2013,** *1* (35), 10148-10154.

121. Yang, H.; Wang, Y.; Huang, H.; Gell, L.; Lehtovaara, L.; Malola, S.; Häkkinen, H.; Zheng, N., All-thiol-stabilized Ag_{44} and $Au_{12}Ag_{32}$ nanoparticles with single-crystal structures. *Nat. Commun.* **2013,** *4*, 2422.

122. Udayabhaskararao, T.; Pradeep, T., New Protocols for the Synthesis of Stable Ag and Au Nanocluster Molecules. *J. Phys. Chem. Lett.* **2013,** *4* (9), 1553-1564.

123. Tlahuice-Flores, A., New insight into the structure of thiolated gold clusters: a structural prediction of the $Au_{187}(SR)_{68}$ cluster. *PCCP* **2015,** *17* (8), 5551-5555.

124. Tlahuice-Flores, A.; Whetten, R. L.; Jose-Yacaman, M., Ligand Effects on the Structure and the Electronic Optical Properties of Anionic $Au_{25}(SR)_{18}$ Clusters. *J. Phys. Chem. C* **2013,** *117* (40), 20867-20875.

125. Krommenhoek, P. J.; Wang, J.; Hentz, N.; Johnston-Peck, A. C.; Kozek, K. A.; Kalyuzhny, G.; Tracy, J. B., Bulky Adamantanethiolate and Cyclohexanethiolate Ligands Favor Smaller Gold Nanoparticles with Altered Discrete Sizes. *ACS Nano* **2012,** *6* (6), 4903-4911.

126. Nishigaki, J.-i.; Tsunoyama, R.; Tsunoyama, H.; Ichikuni, N.; Yamazoe, S.; Negishi, Y.; Ito, M.; Matsuo, T.; Tamao, K.; Tsukuda, T., A New Binding Motif of Sterically Demanding Thiolates on a Gold Cluster. *J. Am. Chem. Soc.* **2012,** *134* (35), 14295-14297.

127. Tlahuice-Flores, A., Ligand effects on the structure and vibrational properties of the thiolated Au18 cluster. *Progress in Natural Science: Materials International* **2016,** *26* (5), 510-515.

128. Qian, H.; Zhu, M.; Andersen, U. N.; Jin, R., Facile, Large-Scale Synthesis of Dodecanethiol-Stabilized Au_{38} Clusters. *J. Phys. Chem. A* **2009,** *113* (16), 4281-4284.

129. Kurashige, W.; Yamazoe, S.; Kanehira, K.; Tsukuda, T.; Negishi, Y., Selenolate-Protected Au_{38} Nanoclusters: Isolation and Structural Characterization. *J. Phys. Chem. Lett.* **2013,** *4* (18), 3181-3185.

130. Niihori, Y.; Hossain, S.; Sharma, S.; Kumar, B.; Kurashige, W.; Negishi, Y., Understanding and Practical Use of Ligand and Metal Exchange Reactions in Thiolate-Protected Metal Clusters to Synthesize Controlled Metal Clusters. *The Chemical Record* **2017**, n/a-n/a.

131. Xu, Q.; Wang, S.; Liu, Z.; Xu, G.; Meng, X.; Zhu, M., Synthesis of selenolate-protected $Au_{18}(SeC_6H_5)_{14}$ nanoclusters. *Nanoscale* **2013,** *5* (3), 1176-1182.

132. Chen, Y.; Zeng, C.; Kauffman, D. R.; Jin, R., Tuning the Magic Size of Atomically Precise Gold Nanoclusters Via Isomeric Methylbenzenethiols. *Nano Lett.* **2015,** *15*, 3603.

133. Schaaff, T. G.; Whetten, R. L., Controlled Etching of Au:SR Cluster Compounds. *J. Phys. Chem. B* **1999,** *103*, 9394.

134. Zeng, C.; Chen, Y.; Das, A.; Jin, R., Transformation Chemistry of Gold Nanoclusters: From One Stable Size to Another. *J. Phys. Chem. Lett.* **2015,** *6*, 2976.

135. Zeng, C.; Li, T.; Das, A.; Rosi, N. L.; Jin, R., Chiral Structure of Thiolate-Protected 28-Gold-Atom Nanocluster Determined by X-ray Crystallography. *J. Am. Chem. Soc.* **2013,** *135* (27), 10011-10013.

136. Higaki, T.; Liu, C.; Zeng, C.; Jin, R.; Chen, Y.; Rosi, N. L.; Jin, R., Controlling the Atomic Structure of Au_{30} Nanoclusters by a Ligand-Based Strategy. *Angew. Chem. Int. Ed.* **2016,** *55* (23), 6694-6697.

137. Negishi, Y.; Nobusada, K.; Tsukuda, T., Glutathione-Protected Gold Clusters Revisited: Bridging the Gap between Gold(I)−Thiolate Complexes and Thiolate-Protected Gold Nanocrystals. *J. Am. Chem. Soc.* **2005,** *127* (14), 5261-5270.

138. Das, A.; Liu, C.; Zeng, C.; Li, G.; Li, T.; Rosi, N. L.; Jin, R., Cyclopentanethiolato-Protected $Au_{36}(SC_5H_9)_{24}$ Nanocluster: Crystal Structure and Implications for the Steric and Electronic Effects of Ligand. *J. Phys. Chem. A* **2014,** *118* (37), 8264-8269.

139. Tsukuda, T.; Hakkinen, H., *Protected Metal Clusters: From Fundamental to Applications*. Elsevier: 2015.

140. Pei, Y.; Zeng, X. C., Investigating the structural evolution of thiolate protected gold clusters from first-principles. *Nanoscale* **2012,** *4* (14), 4054-4072.

141. Aikens, C. M., Electronic Structure of Ligand-Passivated Gold and Silver Nanoclusters. *J. Phys. Chem. Lett.* **2010,** *2* (2), 99-104.

142. Weissker, H. C.; Escobar, H. B.; Thanthirige, V. D.; Kwak, K.; Lee, D.; Ramakrishna, G.; Whetten, R. L.; López-Lozano, X., Information on quantum states pervades the visible spectrum of the ubiquitous $Au_{144}(SR)_{60}$ gold nanocluster. *Nat Commun* **2014,** *5*.

143. Jin, R., Atomically precise metal nanoclusters: stable sizes and optical properties. *Nanoscale* **2015,** *7* (5), 1549-1565.

144. Wong, O. A.; Heinecke, C. L.; Simone, A. R.; Whetten, R. L.; Ackerson, C. J., Ligand symmetry-equivalence on thiolate protected gold nanoclusters determined by NMR spectroscopy. *Nanoscale* **2012,** *4* (14), 4099-4102.

145. Chaki, N. K.; Negishi, Y.; Tsunoyama, H.; Shichibu, Y.; Tsukuda, T., Ubiquitous 8 and 29 kDa gold: Alkanethiolate cluster compounds: Mass-spectrometric determination of molecular formulas and structural implications. *J. Am. Chem. Soc.* **2008,** *130* (27), 8608-8610.

146. Toikkanen, O.; Ruiz, V.; Ronholm, G.; Kalkkinen, N.; Liljeroth, P.; Quinn, B. M., Synthesis and stability of monolayer-protected Au_{38} clusters. *J. Am. Chem. Soc.* **2008,** *130* (33), 11049-11055.

147. Schaaff, T. G.; Whetten, R. L., Controlled etching of Au : SR cluster compounds. *J. Phys. Chem. B* **1999,** *103* (44), 9394-9396.

148. Paolo, G.; Stefano, B.; Nicola, B.; Matteo, C.; Roberto, C.; Carlo, C.; Davide, C.; Guido, L. C.; Matteo, C.; Ismaila, D.; Andrea Dal, C.; Stefano de, G.; Stefano, F.; Guido, F.; Ralph, G.; Uwe, G.; Christos, G.; Anton, K.; Michele, L.; Layla, M.-S.; Nicola, M.; Francesco, M.; Riccardo, M.; Stefano, P.; Alfredo, P.; Lorenzo, P.; Carlo, S.; Sandro, S.; Gabriele, S.; Ari, P. S.; Alexander, S.; Paolo, U.; Renata, M. W., QUANTUM ESPRESSO: a modular and open-source software project for quantum simulations of materials. *J. Phys.: Condens. Matter* **2009,** *21* (39), 395502.

149. Vanderbilt, D., Soft self-consistent pseudopotentials in a generalized eigenvalue formalism. *Physical Review B* **1990,** *41* (11), 7892-7895.

150. Perdew, J. P.; Burke, K.; Ernzerhof, M., Generalized Gradient Approximation Made Simple [Phys. Rev. Lett. 77, 3865 (1996)]. *Phys. Rev. Lett.* **1997,** *78* (7), 1396-1396.

151. Baseggio, O.; Fronzoni, G.; Stener, M., A new time dependent density functional algorithm for large systems and plasmons in metal clusters. *J. Chem. Phys.* **2015,** *143* (2), 024106.

152. Fonseca Guerra, C.; Snijders, G. J.; te Velde, G.; Baerends, J. E., Towards an order-N DFT method. *Theor. Chem. Acc.* **1998,** *99* (6), 391-403.

153. van Leeuwen, R.; Baerends, E. J., Exchange-correlation potential with correct asymptotic behavior. *Physical Review A* **1994,** *49* (4), 2421-2431.

154. Gross, E. K. U.; Kohn, W., Time-Dependent Density-Functional Theory. In *Adv. Quantum Chem.*, Per-Olov, L., Ed. Academic Press: 1990; Vol. Volume 21, pp 255-291.

155. Vosko, S. H.; Wilk, L.; Nusair, M., Accurate spin-dependent electron liquid correlation energies for local spin density calculations: a critical analysis. *Can. J. Phys.* **1980,** *58* (8), 1200-1211.

156. van Lenthe, E.; Baerends, E. J.; Snijders, J. G., *J. Chem. Phys.* **1993,** *99*, 4597-4610.

157. Angel, L. A.; Majors, L. T.; Dharmaratne, A. C.; Dass, A., Ion Mobility Mass Spectrometry of $Au_{25}(SCH_2CH_2Ph)_{18}$ Nanoclusters. *ACS Nano* **2010,** *4* (8), 4691-4700.

158. Dass, A., Mass Spectrometric Identification of $Au_{68}(SR)_{34}$ Molecular Gold Nanoclusters with 34-Electron Shell Closing. *J. Am. Chem. Soc.* **2009,** *131* (33), 11666-11667.

159. Devadas, M. S.; Bairu, S.; Qian, H.; Sinn, E.; Jin, R.; Ramakrishna, G., Temperature-Dependent Optical Absorption Properties of Monolayer-Protected Au_{25} and Au_{38} Clusters. *J. Phys. Chem. Lett.* **2011,** *2* (21), 2752-2758.

160. Chen, Y.; Liu, C.; Tang, Q.; Zeng, C.; Higaki, T.; Das, A.; Jiang, D.-e.; Rosi, N. L.; Jin, R., Isomerism in $Au_{28}(SR)_{20}$ Nanocluster and Stable Structures. *J. Am. Chem. Soc.* **2016,** *138* (5), 1482-1485.

161. Lopez-Acevedo, O.; Tsunoyama, H.; Tsukuda, T.; Häkkinen, H.; Aikens, C. M., Chirality and Electronic Structure of the Thiolate-Protected Au38 Nanocluster. *J. Am. Chem. Soc.* **2010,** *132* (23), 8210-8218.

162. Zhu, M.; Aikens, C. M.; Hollander, F. J.; Schatz, G. C.; Jin, R., Correlating the Crystal Structure of A Thiol-Protected Au_{25} Cluster and Optical Properties. *J. Am. Chem. Soc.* **2008,** *130* (18), 5883-5885.

163. Sementa, L.; Barcaro, G.; Dass, A.; Stener, M.; Fortunelli, A., Designing ligand-enhanced optical absorption of thiolated gold nanoclusters. *Chem. Commun.* **2015,** *51* (37), 7935-7938.

164. Dass, A.; Theivendran, S.; Nimmala, P. R.; Kumara, C.; Jupally, V. R.; Fortunelli, A.; Sementa, L.; Barcaro, G.; Zuo, X.; Noll, B. C., $Au_{133}(SPh\text{-}tBu)_{52}$ Nanomolecules: X-ray Crystallography, Optical, Electrochemical, and Theoretical Analysis. *J. Am. Chem. Soc.* **2015,** *137* (14), 4610-4613.

165. Love, J. C.; Estroff, L. A.; Kriebel, J. K.; Nuzzo, R. G.; Whitesides, G. M., Self-Assembled Monolayers of Thiolates on Metals as a Form of Nanotechnology. *Chem. Rev.* **2005,** *105* (4), 1103-1170.

166. Zhang, Y.; Liu, C.; Yang, X.; Bao, M.; Huang, J.; Shen, W., Controlled synthesis of pure Au_{25}(2-Nap)$_{18}$ and Au_{36}(2-Nap)$_{24}$ nanoclusters from 2-(diphenylphosphino)pyridine protected Au nanoclusters. *RSC Advances* **2016,** *6* (107), 105166-105170.

167. Abbas, M. A.; Kim, T.-Y.; Lee, S. U.; Kang, Y. S.; Bang, J. H., Exploring Interfacial Events in Gold-Nanocluster-Sensitized Solar Cells: Insights into the Effects of the Cluster Size and Electrolyte on Solar Cell Performance. *J. Am. Chem. Soc.* **2016,** *138* (1), 390-401.

168. Sakthivel, N. A.; Theivendran, S.; Ganeshraj, V.; Oliver, A. G.; Dass, A., Crystal Structure of Faradaurate-279: Au_{279}(SPh-tBu)$_{84}$ Plasmonic Nanocrystal Molecules. *J. Am. Chem. Soc.* **2017,** *139* (43), 15450-15459.

169. Chen, Y.; Zeng, C.; Liu, C.; Kirschbaum, K.; Gayathri, C.; Gil, R. R.; Rosi, N. L.; Jin, R., Crystal Structure of Barrel-Shaped Chiral Au_{130}(p-MBT)$_{50}$ Nanocluster. *J. Am. Chem. Soc.* **2015,** *137* (32), 10076-10079.

170. Burrows, N. D.; Lin, W.; Hinman, J. G.; Dennison, J. M.; Vartanian, A. M.; Abadeer, N. S.; Grzincic, E. M.; Jacob, L. M.; Li, J.; Murphy, C. J., Surface Chemistry of Gold Nanorods. *Langmuir* **2016,** *32* (39), 9905-9921.

171. Azcárate, J. C.; Corthey, G.; Pensa, E.; Vericat, C.; Fonticelli, M. H.; Salvarezza, R. C.; Carro, P., Understanding the Surface Chemistry of Thiolate-Protected Metallic Nanoparticles. *J. Phys. Chem. Lett.* **2013,** *4* (18), 3127-3138.

172. Indrasekara, A. S. D. S.; Wadams, R. C.; Fabris, L., Ligand Exchange on Gold Nanorods: Going Back to the Future. *Particle & Particle Systems Characterization* **2014,** *31* (8), 819-838.

173. Rambukwella, M.; Sementa, L.; Fortunelli, A.; Dass, A., Core-Size Conversion of Au_{38}(SCH_2CH_2Ph)$_{24}$ to Au_{30}(S–tBu)$_{18}$ Nanomolecules. *J. Phys. Chem. C* **2017,** *121* (27), 14929-14935.

174. Dass, A.; Jones, T. C.; Theivendran, S.; Sementa, L.; Fortunelli, A., Core Size Interconversions of Au_{30}(S-tBu)$_{18}$ and Au_{36}(SPhX)$_{24}$. *J. Phys. Chem. C* **2017,** *121* (27), 14914-14919.

175. Antonello, S.; Arrigoni, G.; Dainese, T.; De Nardi, M.; Parisio, G.; Perotti, L.; René, A.; Venzo, A.; Maran, F., Electron Transfer through 3D Monolayers on Au_{25} Clusters. *ACS Nano* **2014,** *8* (3), 2788-2795.

176. Cirri, A.; Silakov, A.; Jensen, L.; Lear, B. J., Chain Length and Solvent Control over the Electronic Properties of Alkanethiolate-Protected Gold Nanoparticles at the Molecule-to-Metal Transition. *J. Am. Chem. Soc.* **2016,** *138* (49), 15987-15993.

177. Agrachev, M.; Antonello, S.; Dainese, T.; Ruzzi, M.; Zoleo, A.; Aprà, E.; Govind, N.; Fortunelli, A.; Sementa, L.; Maran, F., Magnetic Ordering in Gold Nanoclusters. *ACS Omega* **2017,** *2* (6), 2607-2617.

178. Rambukwella, M.; Burrage, S.; Neubrander, M.; Baseggio, O.; Aprà, E.; Stener, M.; Fortunelli, A.; Dass, A., $Au_{38}(SPh)_{24}$: Au_{38} Protected with Aromatic Thiolate Ligands. *J. Phys. Chem. Lett.* **2017,** *8* (7), 1530-1537.

179. Zeng, J.-L.; Guan, Z.-J.; Du, Y.; Nan, Z.-A.; Lin, Y.-M.; Wang, Q.-M., Chloride-Promoted Formation of a Bimetallic Nanocluster $Au_{80}Ag_{30}$ and the Total Structure Determination. *J. Am. Chem. Soc.* **2016,** *138* (25), 7848-7851.

180. Kang, X.; Silalai, C.; Lv, Y.; Sun, G.; Chen, S.; Yu, H.; Xu, F.; Zhu, M., $Au_{15}Ag_3(SPhMe_2)_{14}$ Nanoclusters – Crystal Structure and Insights into Ligand-Induced Variation. *Eur. J. Inorg. Chem.* **2017,** *2017* (10), 1414-1419.

181. Song, Y.; Wang, S.; Zhang, J.; Kang, X.; Chen, S.; Li, P.; Sheng, H.; Zhu, M., Crystal Structure of Selenolate-Protected $Au_{24}(SeR)_{20}$ Nanocluster. *J. Am. Chem. Soc.* **2014,** *136* (8), 2963-2965.

182. Chen, Y.; Zeng, C.; Kauffman, D. R.; Jin, R., Tuning the Magic Size of Atomically Precise Gold Nanoclusters via Isomeric Methylbenzenethiols. *Nano Lett.* **2015,** *15* (5), 3603-3609.

183. Kokkin, D. L.; Zhang, R.; Steimle, T. C.; Wyse, I. A.; Pearlman, B. W.; Varberg, T. D., Au–S Bonding Revealed from the Characterization of Diatomic Gold Sulfide, AuS. *J. Phys. Chem. A* **2015,** *119* (48), 11659-11667.

184. Qian, H.; Jin, R., Controlling Nanoparticles with Atomic Precision: The Case of $Au_{144}(SCH_2CH_2Ph)_{60}$. *Nano Lett.* **2009,** *9* (12), 4083-4087.

185. Dainese, T.; Antonello, S.; Gascón, J. A.; Pan, F.; Perera, N. V.; Ruzzi, M.; Venzo, A.; Zoleo, A.; Rissanen, K.; Maran, F., $Au_{25}(SEt)_{18}$, a Nearly Naked Thiolate-Protected Au25 Cluster: Structural Analysis by Single Crystal X-ray Crystallography and Electron Nuclear Double Resonance. *ACS Nano* **2014,** *8* (4), 3904-3912.

186. García-Raya, D.; Madueño, R.; Blázquez, M.; Pineda, T., Electrochemistry of Molecule-like Au_{25} Nanoclusters Protected by Hexanethiolate. *J. Phys. Chem. C* **2009,** *113* (20), 8756-8761.

187. Stellwagen, D.; Weber, A.; Bovenkamp, G. L.; Jin, R.; Bitter, J. H.; Kumar, C. S. S. R., Ligand control in thiol stabilized Au38 clusters. *RSC Advances* **2012,** *2* (6), 2276-2283.

188. Toikkanen, O.; Ruiz, V.; Rönnholm, G.; Kalkkinen, N.; Liljeroth, P.; Quinn, B. M., Synthesis and Stability of Monolayer-Protected Au_{38} Clusters. *J. Am. Chem. Soc.* **2008,** *130* (33), 11049-11055.

189. Bordwell, F. G., Equilibrium acidities in dimethyl sulfoxide solution. *Acc. Chem. Res.* **1988,** *21* (12), 456-463.

190. Jones, T. C.; Sumner, L.; Ramakrishna, G.; Hatshan, M. b.; Abuhagr, A.; Chakraborty, S.; Dass, A., Bulky t-Butyl Thiolated Gold Nanomolecular Series: Synthesis, Characterization, Optical Properties, and Electrocatalysis. *J. Phys. Chem. C* **2018**.

191. Chen, S.; Xiong, L.; Wang, S.; Ma, Z.; Jin, S.; Sheng, H.; Pei, Y.; Zhu, M., Total Structure Determination of Au21(S-Adm)15 and Geometrical/Electronic Structure Evolution of Thiolated Gold Nanoclusters. *J. Am. Chem. Soc.* **2016,** *138* (34), 10754-10757.

192. Jones, T. C.; Sementa, L.; Stener, M.; Gagnon, K. J.; Thanthirige, V. D.; Ramakrishna, G.; Fortunelli, A.; Dass, A., $Au_{21}S(SAdm)_{15}$: Crystal Structure, Mass Spectrometry, Optical Spectroscopy, and First-Principles Theoretical Analysis. *J. Phys. Chem. C* **2017**.

193. Sakthivel, N. A.; Stener, M.; Sementa, L.; Fortunelli, A.; Ramakrishna, G.; Dass, A., $Au_{279}(SR)_{84}$: The Smallest Gold Thiolate Nanocrystal That Is Metallic and the Birth of Plasmon. *J. Phys. Chem. Lett.* **2018,** *9* (6), 1295-1300.

194. Hostetler, M. J.; Templeton, A. C.; Murray, R. W., Dynamics of Place-Exchange Reactions on Monolayer-Protected Gold Cluster Molecules. *Langmuir* **1999,** *15* (11), 3782-3789.

195. Carducci, T. M.; Blackwell, R. E.; Murray, R. W., Charge-Transfer Effects in Ligand Exchange Reactions of Au25 Monolayer-Protected Clusters. *J. Phys. Chem. Lett.* **2015,** *6* (8), 1299-1302.

196. Kamei, Y.; Shichibu, Y.; Konishi, K., Generation of Small Gold Clusters with Unique Geometries through Cluster-to-Cluster Transformations: Octanuclear Clusters with Edge-sharing Gold Tetrahedron Motifs. *Angew. Chem. Int. Ed.* **2011,** *50* (32), 7442-7445.

197. Bootharaju, M. S.; Burlakov, V. M.; Besong, T. M. D.; Joshi, C. P.; AbdulHalim, L. G.; Black, D. M.; Whetten, R. L.; Goriely, A.; Bakr, O. M., Reversible Size Control of Silver Nanoclusters via Ligand-Exchange. *Chem. Mater.* **2015,** *27* (12), 4289-4297.

198. Fortunelli, A.; Selmi, M., Density functional calculations on hydrocarbon isodesmic reactions. *Chem. Phys. Lett.* **1994,** *223* (4), 390-396.

199. Antonello, S.; Maran, F., Molecular electrochemistry of monolayer-protected clusters. *Current Opinion in Electrochemistry* **2017,** *2* (1), 18-25.

200. Pauling, L., *The Nature of the Chemical Bond*. Cornell University Press: Ithaca, United States, 1960.

201. Pearson, R. G., Chemical hardness and density functional theory. *Journal of Chemical Sciences* **2005,** *117* (5), 369-377.

LIST OF APPENDICES

APPENDIX A: SUPPLEMENTARY INFORMATION FOR CHAPTER 2

Table S2.1. Reproducibility and yield of $Au_{102}(SPh)_{44}$ synthesis

Batch No.	Amount of $HAuCl_4$ used (g)	Crude product yield (mg)	PET etched product yield (mg)	$Au_{\sim 103\text{-}104}$ mixture yield (%)	$Au_{102}(SPh)_{44}$ yield (%)
MR2_06	0.3	224.0	160.1	26.2	NA
MR2_08	0.3	220.8	155.0	28.7	9
MR2_10_A	0.3	196.7	162.0	22.2	NA
MR2_10_B	0.3	202.4	162.1	18.3	NA
MR2_19_A	0.3	173.5	117.7	18.1	NA
MR2_19_C	0.3	220.0	146.5	18.1	10
MR2_21	0.9	603.7	*	27.9	13
MR2_29_A	0.9	624.0	513.2	18.8	NA

Note: * data is not available; NA - percent yield is not available for these reactions as these reactions were used to monitor the reaction progress, and significant sample fractions were taken out as aliquots for analysis.

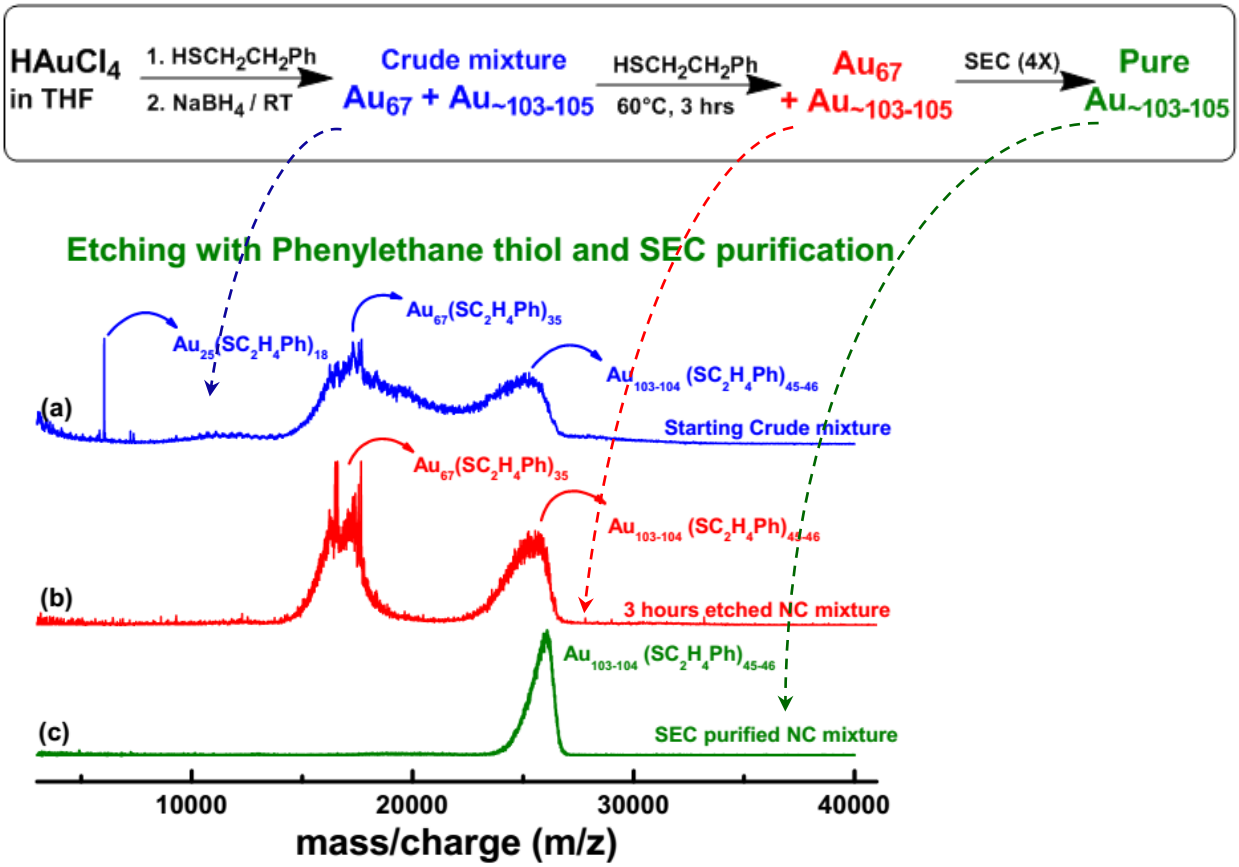

Figure S2.1. MALDI mass spectrum of the starting crude mixture (blue) containing $Au_{25}(SCH_2CH_2Ph)_{18}$, $Au_{67}(SCH_2CH_2Ph)_{35}$ and $Au_{\sim103\text{-}104}(SCH_2CH_2Ph)_{\sim45\text{-}46}$ mixture. This crude was etched with $HSCH_2CH_2Ph$ at 60°C for 3 hours to give the product with the mass spectrum shown in red. The purpose of this 3 hours etch was to obtain a flat baseline between $Au_{\sim67}$ and $Au_{\sim103\text{-}105}$ peaks, so a clean SEC separation can occur.

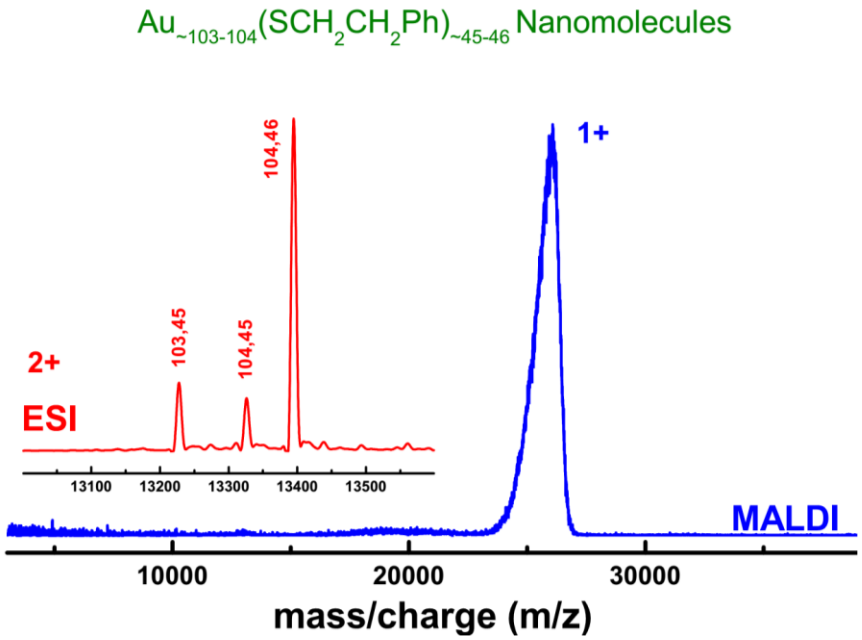

Figure S2.2. MALDI and ESI of the SEC purified fraction containing pure $Au_{\sim 103\text{-}104}$. In our earlier report[42] we showed that 103,104, and 105 atom species were present during the synthesis. In this work, another worker (M.R.) finds that the above spectra containing 103, and 104 is the *most representative spectra* obtained in his synthetic method, but occasionally all three species (103,104,105) were also observed. For this reason, we will refer to this species as $Au_{\sim 103\text{-}105}(SR)_{\sim 45\text{-}46}$ as originally reported.

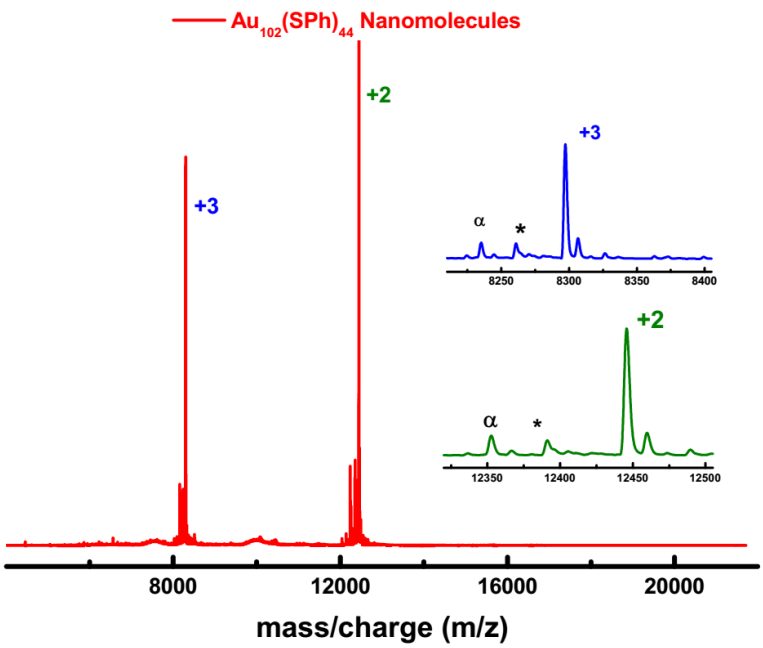

Figure S2.3. ESI mass spectrum of the $Au_{102}(SPh)_{44}$ nanomolecules. The peaks marked by asterisk and α correspond to $Au_{101}(SPh)_{44}$ and $Au_{102}(SPh)_{43}$ respectively.

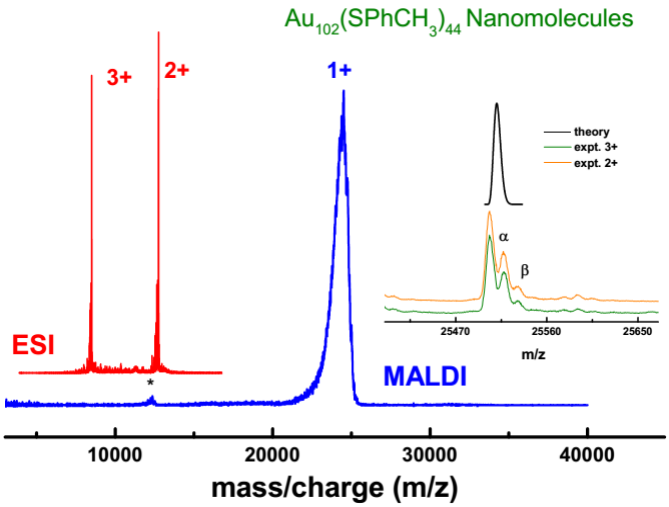

Figure S2.4. ESI mass spectra (red) and MALDI mass spectra (blue) of $Au_{102}(SPhCH_3)_{44}$ where peak marked by asterisk on the MALDI depicts +2 charge state of the analyte. Expand spectra illustrate the molecular ion of the species in comparison to the theoretically calculated molecular species where, α depicts $Au_{102}(SPhCH_3)_{43}(SCH_2CH_2Ph)_1$ and β depicts $Au_{102}(SPhCH_3)_{42}(SCH_2CH_2Ph)_2$.

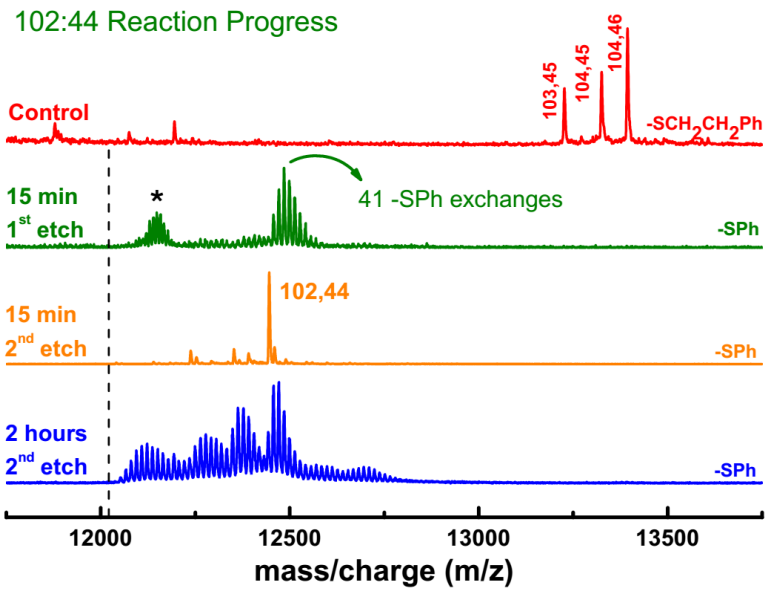

Figure S5. ESI mass spectra showing the reaction progress after prolonged second etching at 80 °C *that lasts for 2 hours*. Mass spectra of precursor nanomolecule mixture of $Au_{\sim 103\text{-}104}(SC_2H_4Ph)_{\sim 45\text{-}46}$ (red), and mass spectra of products etched with thiophenol (olive, orange and blue) are shown. After 2 hours of continuous etching with thiophenol, Au_{102} core begins starts to degrade to smaller cores (blue). The peaks marked by asterisk correspond to partially ligand exchanged nanoclusters, which are unpurified impurities. These decompose and are not found upon second etching. The dotted line at ~12040 Da indicates where theoretically +2 charge state of $Au_{99}(SPh)_{42}$ should occur.

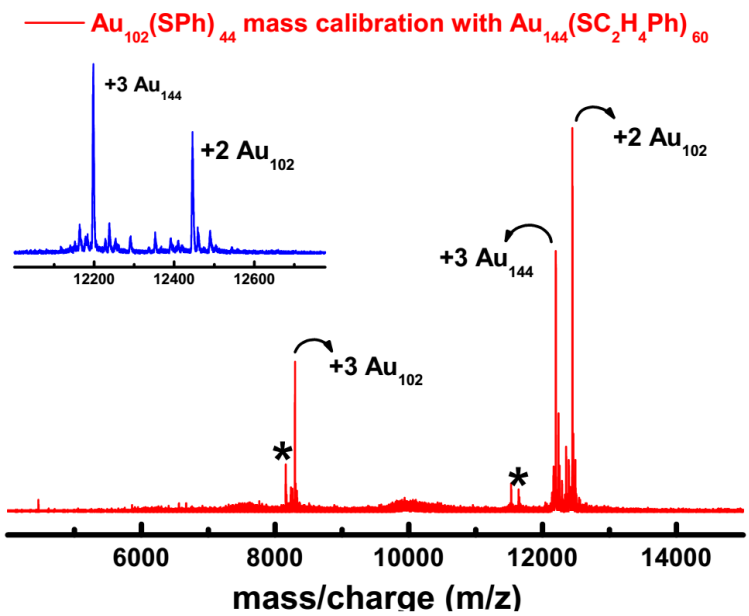

Figure S2.6. ESI MS calibration: Mass spectra of $Au_{102}(SPh)_{44}$ and intentionally added $Au_{144}(SCH_2CH_2Ph)_{60}$ as the internal standard for calibration purposes. The asterisk indicates impurities that were present in the internal standard. Inset shows the expansion of the 12,000 to 13,000 m/z region, showing the 2+ ions of $Au_{102}(SPh)_{44}$ and 3+ of $Au_{144}(S\ CH_2CH_2Ph)_{60}$.

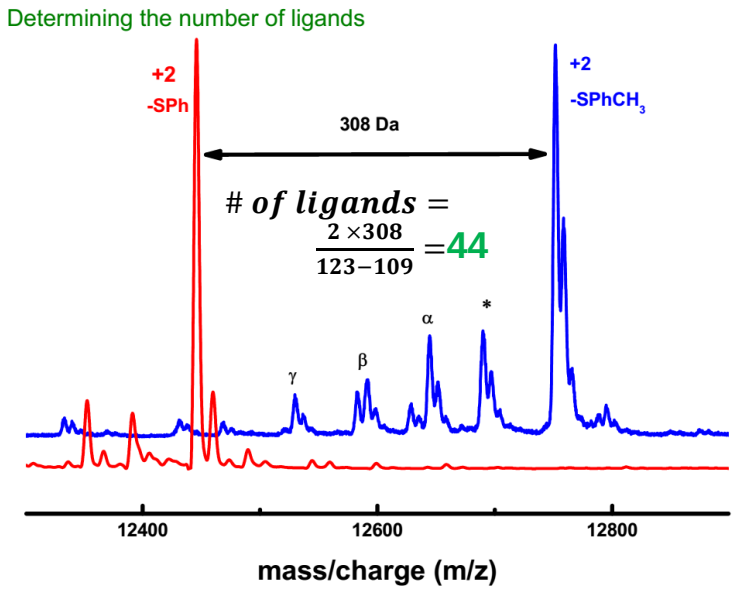

Figure S2.7. ESI mass spectrum(blue) of Au_{102} nanomolecules with -$SPhCH_3$ ligand and (red) with -SPh ligand for ligand composition assignment of $Au_{102}(SR)_x$ type nanomolecules. Peaks assigned by γ, α, β, and * represents 2+ charge state of $Au_{101}(SPhCH_3)_{42}$, $Au_{101}(SPhCH_3)_{43}$, $Au_{102}(SPhCH_3)_{42}$ and $Au_{102}(SPhCH_3)_{43}$ species respectively.

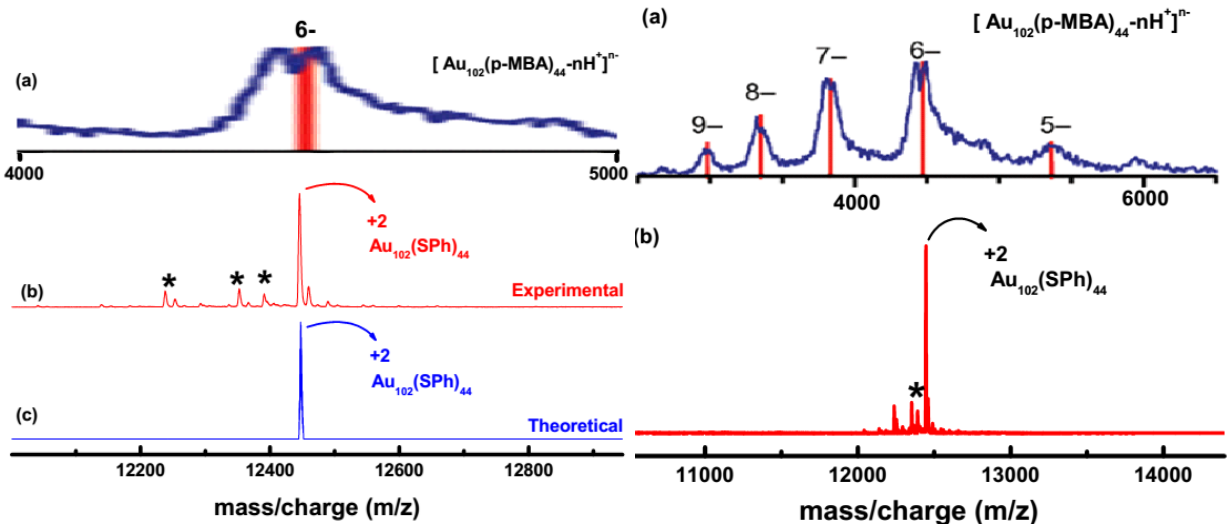

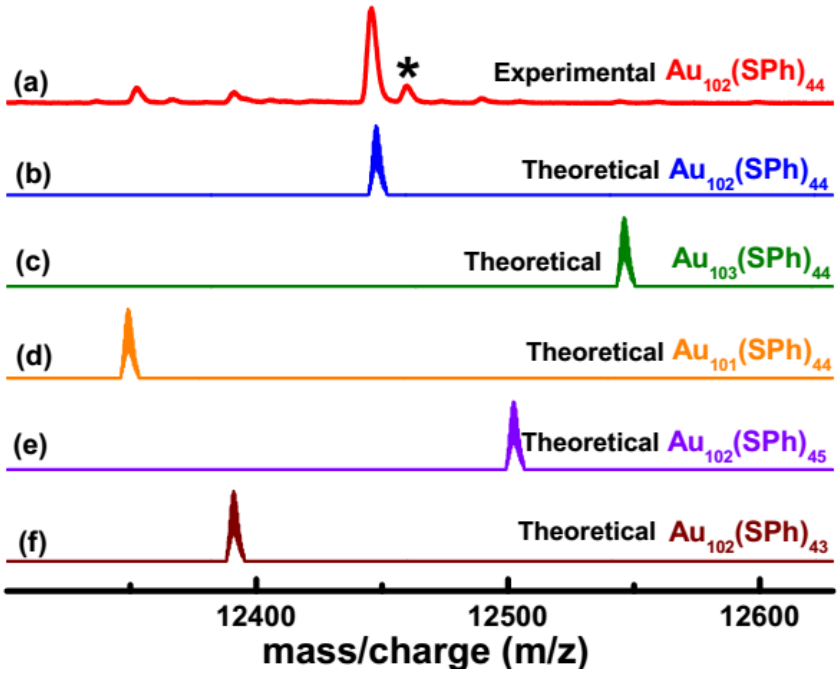

Figure S2.8. (top-left) Comparison of high resolution ESI mass spectra of 2+ charge state of $Au_{102}(SPh)_{44}$ species against Kornbergs' $[Au_{102}(p\text{-}MBA)_{44}-nH^+]^{n-}$ over 4000 m/z mass range; Fig. S2.8 (top-right) over 1000 m/z mass range and Fig. S2.8 (bottom) comparison of 2+charge state of experimental $Au_{102}(SPh)_{44}$ species against theoretical $Au_{102}(SPh)_{44}$ species and species with close composition to $Au_{102}(SPh)_{44}$.

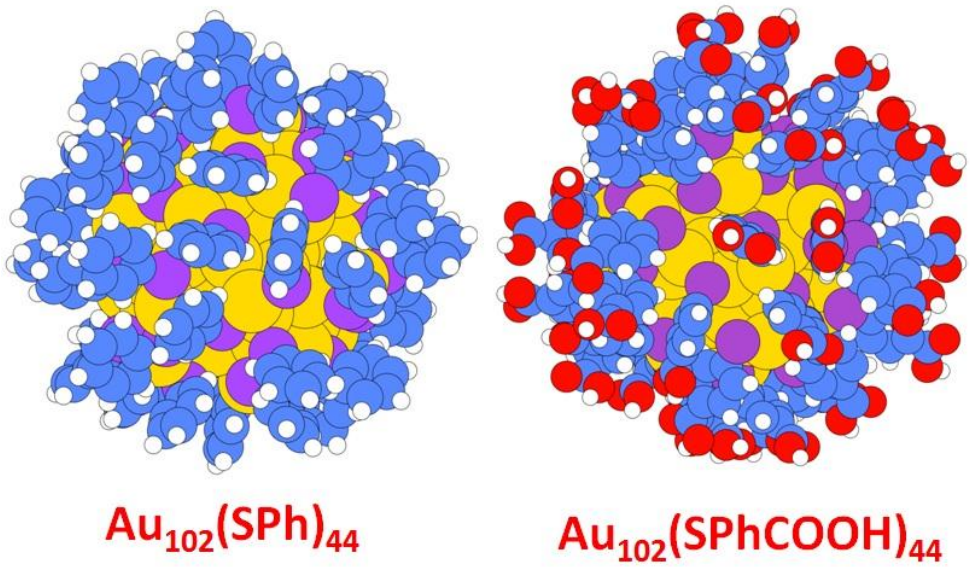

Figure S2.9. Pictorial illustration of the DFT-optimized geometries of $Au_{102}(SPh)_{44}$ and $Au_{102}(SPhCOOH)_{44}$. Au in yellow, C in blue, S in magenta, O in red, H in white.

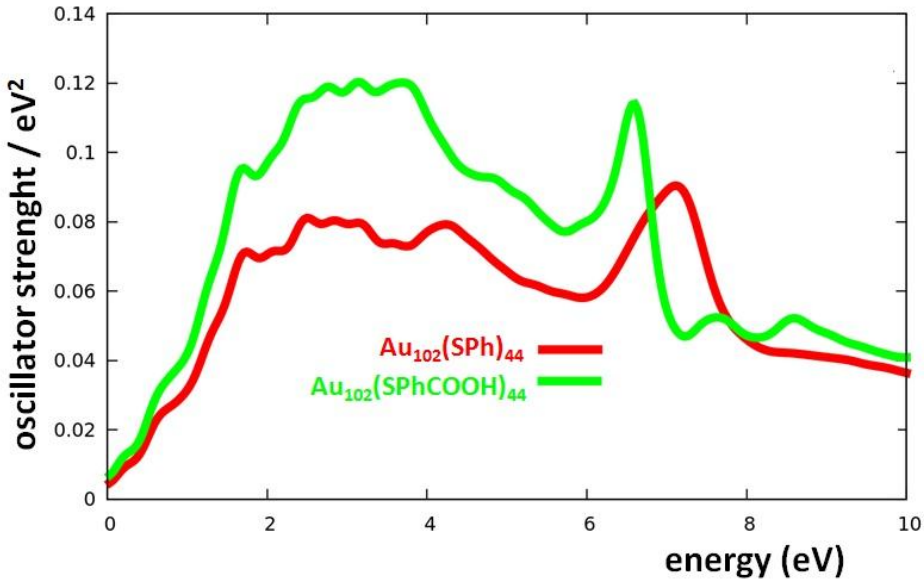

Figure S2.10. Simulated optical spectra of $Au_{102}(SPh)_{44}$ and $Au_{102}(SPhCOOH)_{44}$.

APPENDIX B: SUPPLEMENTARY INFORMATION FOR CHAPTER 3

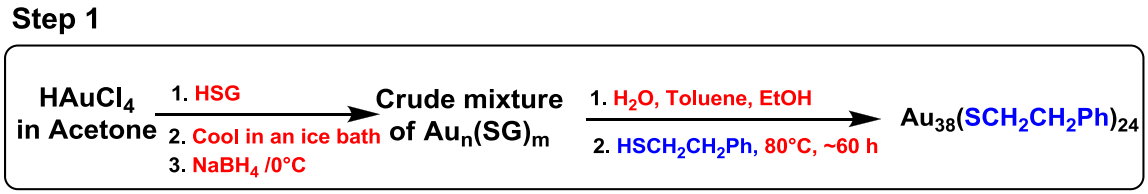

Scheme S3.1. The protocol for the synthesis of $Au_{38}(SCH_2CH_2Ph)_{24}$.

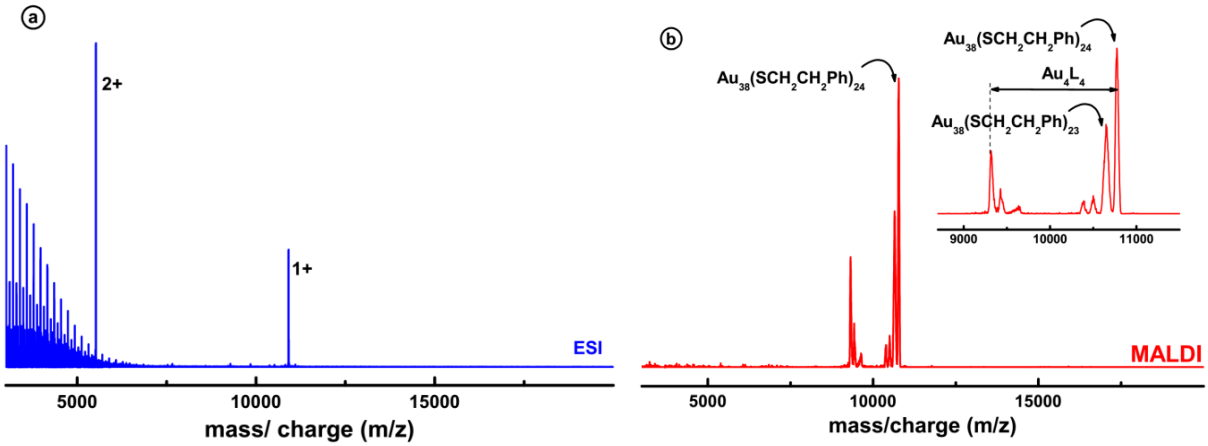

Figure S3.1. (a) ESI mass spectrum showing $Au_{38}(PET)_{24}$ peaks in the 1+ and 2+ charges states. The inset shows the expansion of the 10,900 to 10,920 m/z region, showing the $Au_{38}(PET)_{24}$ with 1+ charge state overlap with theoretical spectum. (b) MALDI mass spectrum of $Au_{38}(SCH_2CH_2Ph)_{24}$. Inset shows the expansion of the 9,000 to 11,000 m/z region, showing completely exchanged $Au_{38}(SCH_2CH_2Ph)_{24}$, a partial SCH_2CH_2Ph exchange ($Au_{38}(SCH_2CH_2Ph)_{23}$) and a fragment of m/z difference of four gold and four ligands.

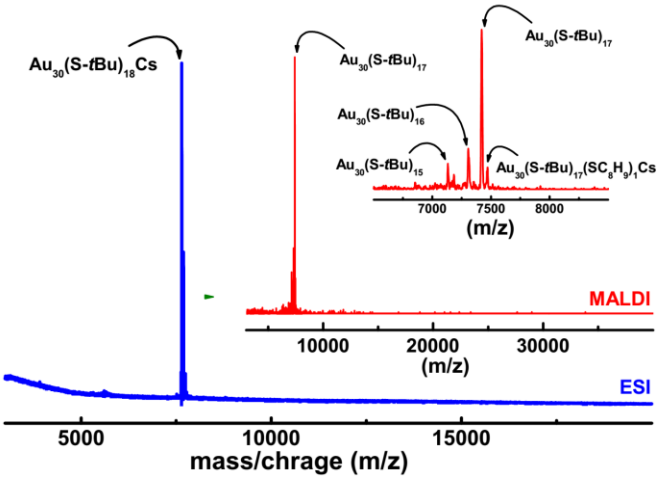

Figure S3.2. ESI and MALDI mass spectra of $Au_{30}(S\text{-}t\text{Bu})_{18}$ nanomolecules. Extend spectra shows purity of the final product the expanded MALDI spectrum in the inset (red) shows fragmentation of $Au_{30}(S\text{-}t\text{Bu})_{18}$ at low laser. It should be noted that all ligand shell intact molecular peak of $Au_{30}(S\text{-}t\text{Bu})_{18}$ was not the dominating peak in the MALDI mass spectrum and instead $Au_{30}(S\text{-}t\text{Bu})_{17}$ was the base peak.

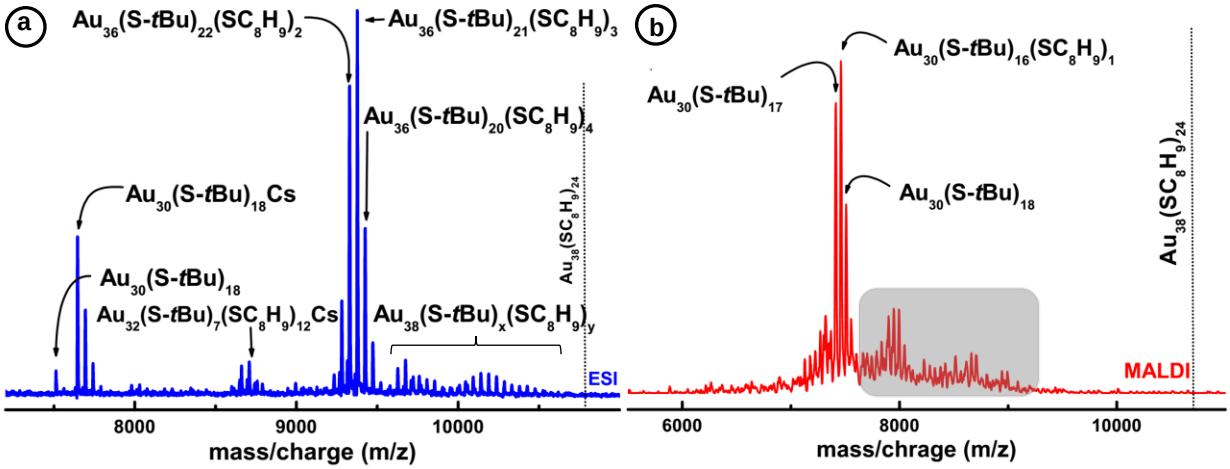

Figure S3.3. Mass spectra of the 5 min sample during the transformation of the $Au_{38}(SCH_2CH_2Ph)_{24}$ to $Au_{30}(S\text{-}t\text{Bu})_{18}$. (a) ESI-MS illustrating intermediates of the reaction. Well

know $Au_{36}(SR)_{24}$ species (where R represents combination of both phenylethanethiol and *tret*-butylthiol) was observed as an intermediate species along with other unstable clusters of species. x and y represent a combination of ligands adding upto 24. (b) MALDI-MS showing fragments of the remaining Au_{38} and Au_{36} species (the gray area) and incomplete transformation of $Au_{38}(SCH_2CH_2Ph)_{24}$ to $Au_{30}(S\text{-}t\text{Bu})_{18}$.

Table S3.1. Absolute electronic energy values for the $Au_N(SR)_M$ systems.

System : $Au_N(SR)_M$	N,M=30,18,R=tBu	N,M=36,24,R=tBu	N,M=38,24,R=EtPh
$Au_N(SR)_M$	1687.98201666	2117.67843145	2730.59465752
Au_N	996.60577862	1195.83837315	1262.35730340
$(SR)_M^{crown}$	689.039641560	918.874554633	1465.20378111
SR_relaxed	38.27338148	38.27338148	61.00837653
HSR_relaxed	38.91610700	38.91610700	61.65151849
Au_atom	33.1443376704	33.1443376704	33.1443376704
$Au_N(SR)_M$_anion-adiab	1688.04648476	2117.74821839	2730.67891792
$Au_N(SR)_M$_cation-adiab	1687.79592159	2117.49365427	2730.42134317

Note: The nomenclature is the following: $Au_N(SR)_M$ = full nanomolecule; Au_N = gold cluster in the interacting configuration; $(SR)_M$ = crown or shell of ligands in the interacting configuration; SR_relaxed = fully relaxed SR thyil; fully relaxed HSR thiol; Au_atom = isolated Au atom; $Au_N(SR)_M$_anion-adiab = total energy of $Au_N(SR)_M$ anion in the geometry of the neutral species; $Au_N(SR)_M$_cation-adiab = total energy of $Au_N(SR)_M$ anion in the geometry of the neutral species. All energies are in atomic units.

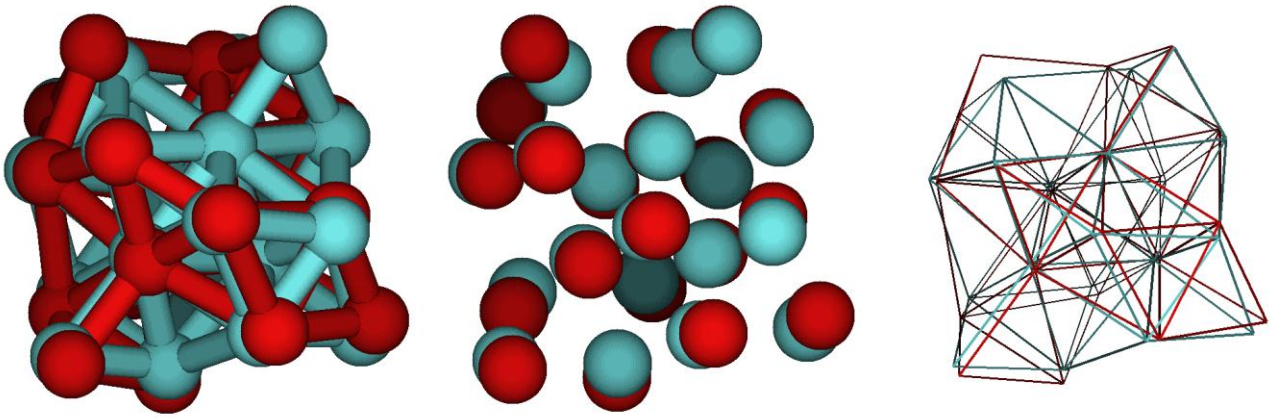

Figure S3.4. Schematic pictures according to different view formats comparing the Au_{20} core skeleton of $Au_{36}(SR)_{24}$ nanomolecules derived from the crystallographic data for $Au_{36}(SPh)_{24}$ in Ref. [18] and from simulation data for $Au_{36}(S\text{-}t\text{Bu})_{24}$ from the present simulations. See main text for more details.

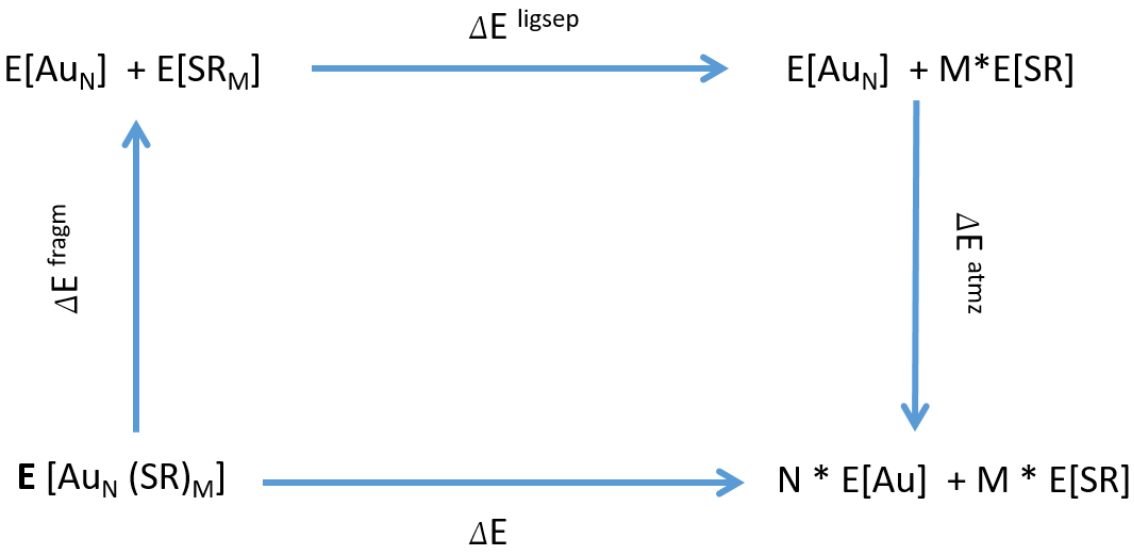

Figure S3.5. Born-Haber cycle for monolayer-protected clusters

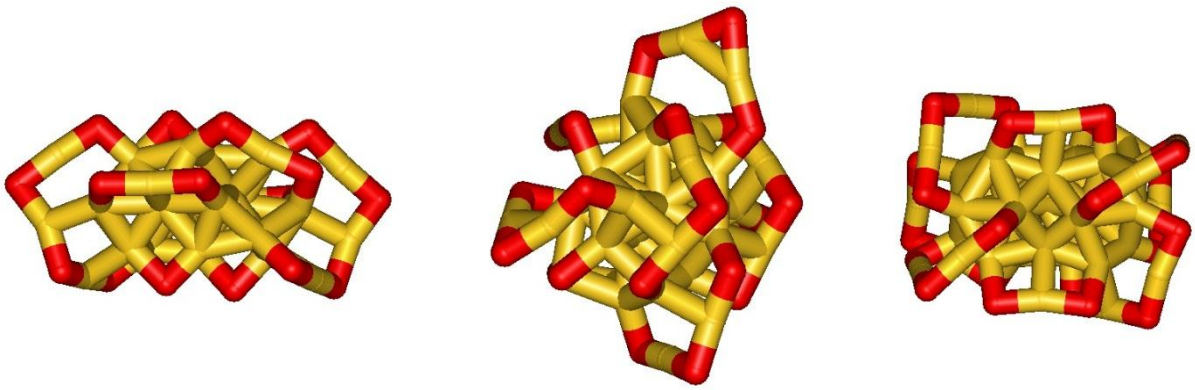

Figure S3.6. Schematic pictures of the $Au_N(S)_M$ skeletal framework of $Au_{30}(S^tBu)_{18}$, $Au_{36}(S^tBu)_{24}$ and $Au_{38}(SCH_2CH_2Ph)_{24}$, respectively, from left to right

Table S3.2. Energy differences for the reactions considered in the main text.

Au_{38}		ΔE^{frag}	ΔE^{atmz}	ΔE^{ligsep}	$\Delta E^{hyrd-lig}$	$\Delta E^{H-ligsep}$	μ_{ligand}	**IP/EA**
	$(SCH_2CH_2Ph)_{24}$	***3.440***	***3.257***	***1.137***	***4.847***	***1.109***	***1.692***	***4.72/2.29***
	$(SPh)_{24}$	***3.120***	***3.178***	***0.478***	***4.604***	***0.579***	***1.320***	
	$(SCH_3)_{24}$	***3.304***	***3.347***	***0.125***	***4.839***	***0.135***	***1.647***	
Au_{36}								
	$(SPh)_{24}$	***3.095***	***3.087***	***0.158***	***4.597***	***0.253***	***1.320***	***5.44/2.17***
Au_{30}	**$(StBu)_{18}$**	***3.532***	***3.440***	***0.179***	***4.861***	***0.178***	***1.681***	
	$(SPh)_{18}$	***3.037***	***3.522***	***0.300***	***4.613***	***0.409***	***1.320***	***5.06/1.75***

APPENDIX C: SUPPLEMENTARY INFORMATION FOR CHAPTER 4

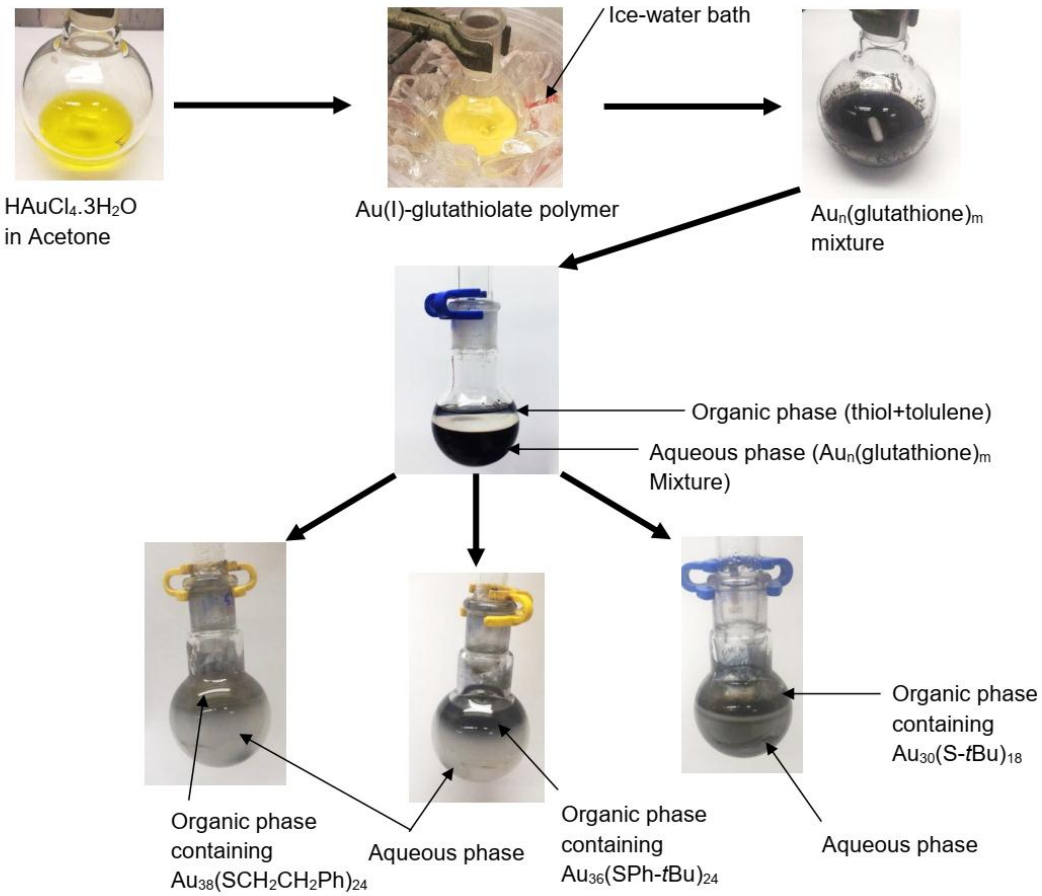

Figure S1. Photographs of the reaction vessels during the synthesis of precursor Au_n(glutathione)$_m$ mixture $Au_{38}(SCH_2CH_2Ph)_{24}$, Au_{36}(SPh-*t*Bu)$_{24}$ and Au_{30}(S-*t*Bu)$_{18}$ nanomolecules.

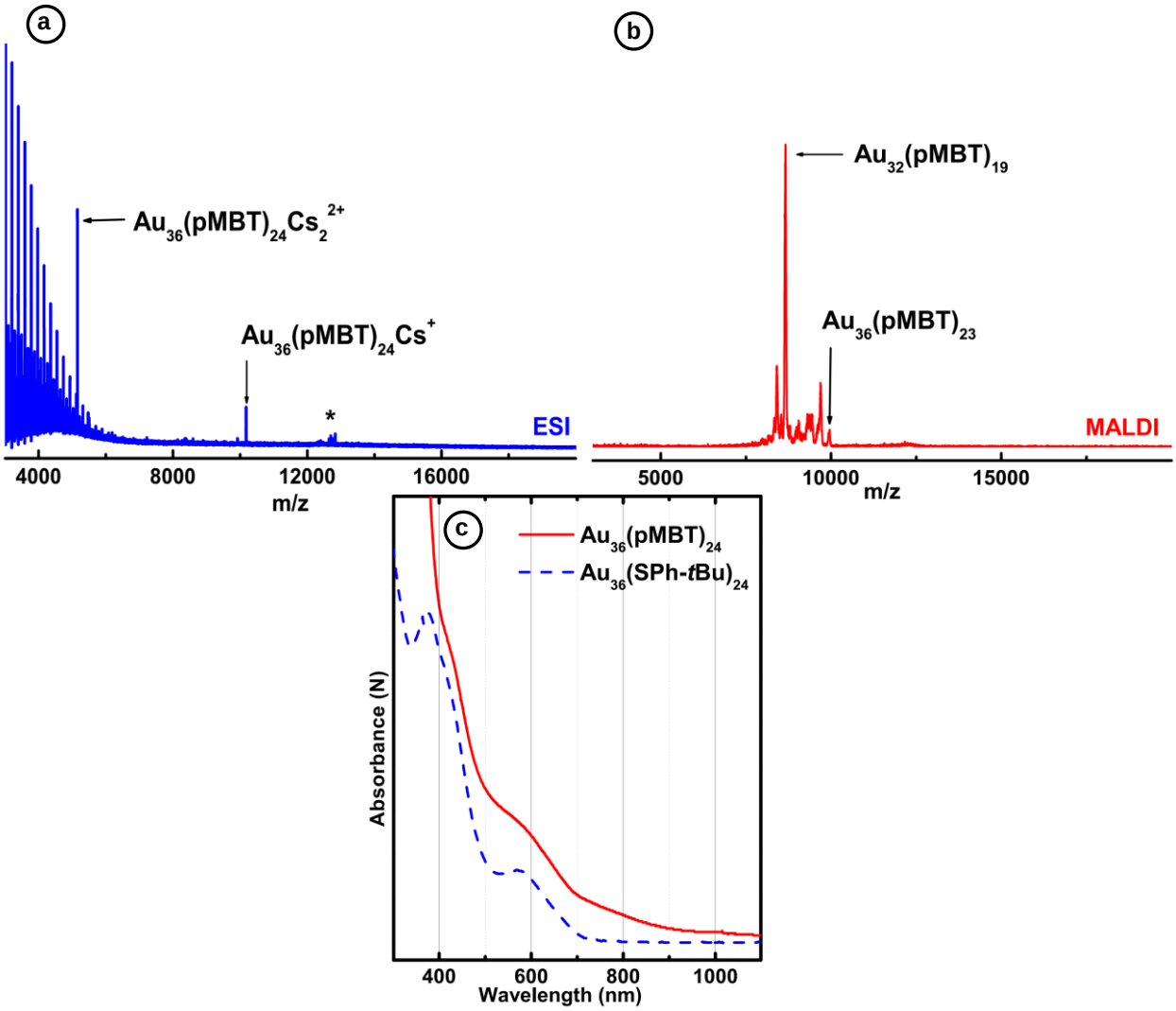

Figure S2. Characterization of $Au_{36}(pMBT)_{24}$ nanomolecules. (a) ESI-MS compositional assignment of the analyte nanomolecule. $Cs(CH_3COO)$ clustering can be observed (peak marked by α) below 5000 m/z as $Cs(CH_3COO)$ was intentionally added to the sample to impart charge and analyte with one and two Cs^+ ion additions can be observed. Peaks marked by asterisk indicates other impurities. (b) MALDI-MS shows purity of the sample and $Au_{36}(pMBT)_{24}$. (c) UV-Vis-NIR absorption spectra illustrate a comparison of the signature absorbance peaks at 375 and 570 nm unique to the $Au_{36}(SPh\text{-}t\text{Bu})_{24}$ analyte against as synthesized $Au_{36}(pMBT)_{24}$.

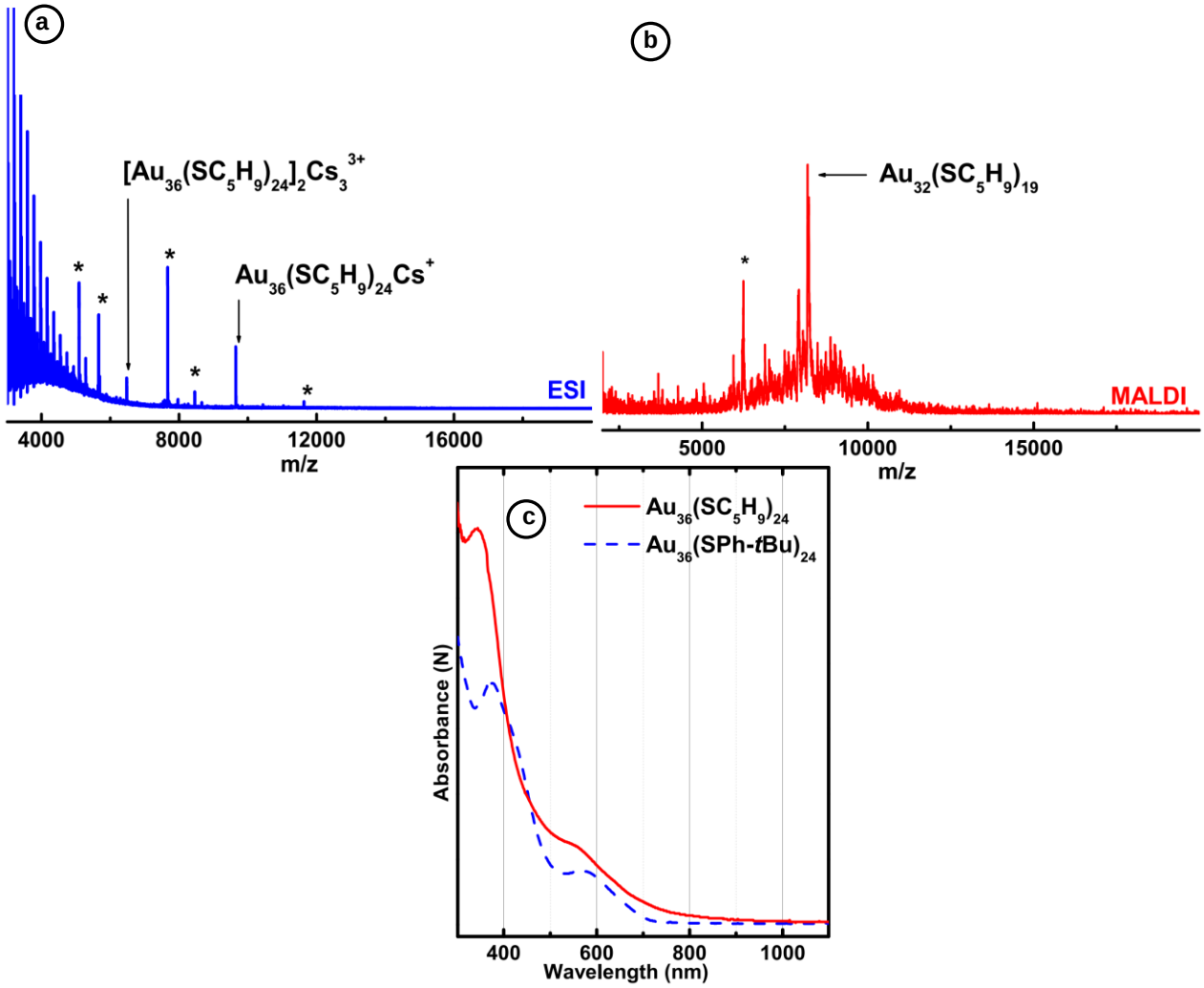

Figure S3. Characterization of $Au_{36}(SC_5H_9)_{24}$ nanomolecules. (a) ESI-MS compositional assignment of the analyte nanomolecule. $Cs(CH_3COO)$ clustering can be observed (peak marked by α) below 5000 m/z as $Cs(CH_3COO)$ was intentionally added to the sample to impart charge and analyte with one and two Cs^+ ion additions can be observed. Peaks marked by asterisk indicates other impurities. (b) MALDI-MS shows $Au_{32}(SC_5H_9)_{19}$ fragmente of $Au_{36}(SC_5H_9)_{24}$. (c) UV-Vis-NIR absorption spectra illustrate a comparison of the signature absorbance peaks at 375 and 570 nm unique to the $Au_{36}(SPh\text{-}tBu)_{24}$ analyte against as synthesized $Au_{36}(SC_5H_9)_{24}$.

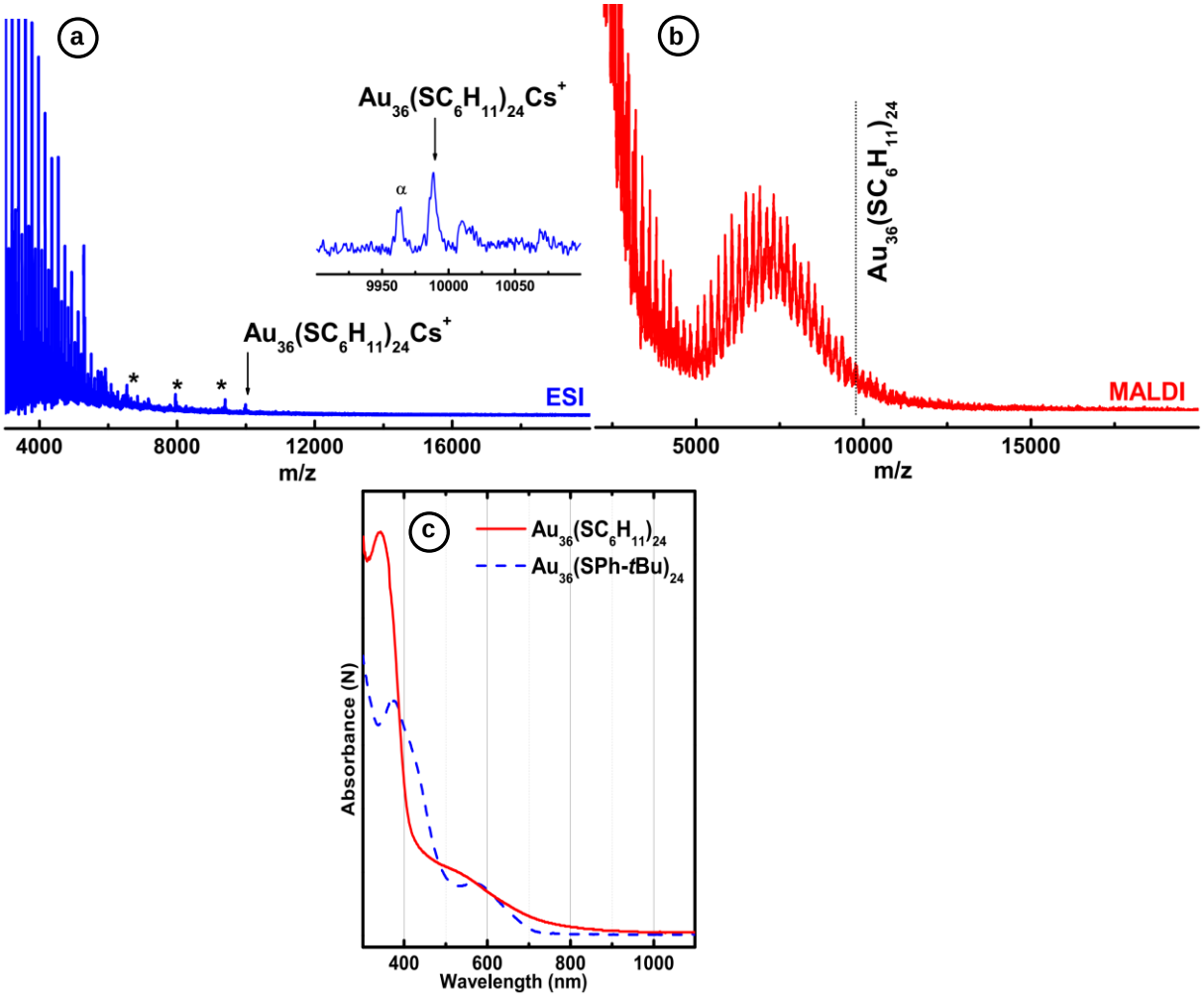

Figure S4. Characterization of $Au_{36}(SC_6H_{11})_{24}$ nanomolecules. (a) ESI-MS compositional assignment of the analyte nanomolecule. $Cs(CH_3COO)$ clustering can be observed (peak marked by α) below 5000 m/z as $Cs(CH_3COO)$ was intentionally added to the sample to impart charge and analyte with one and two Cs^+ ion additions can be observed. Peaks marked by asterisk indicates other impurities. (b) MALDI-MS shows highly fragmenting $Au_{36}(SC_6H_{11})_{24}$ and resolved peak could not be obtained due to other impurities. (c) UV-Vis-NIR absorption spectra illustrate a comparison of the signature absorbance peaks at 375 and 570 nm unique to the $Au_{36}(SPh\text{-}tBu)_{24}$ analyte against as synthesized $Au_{36}(SC_6H_{11})_{24}$.

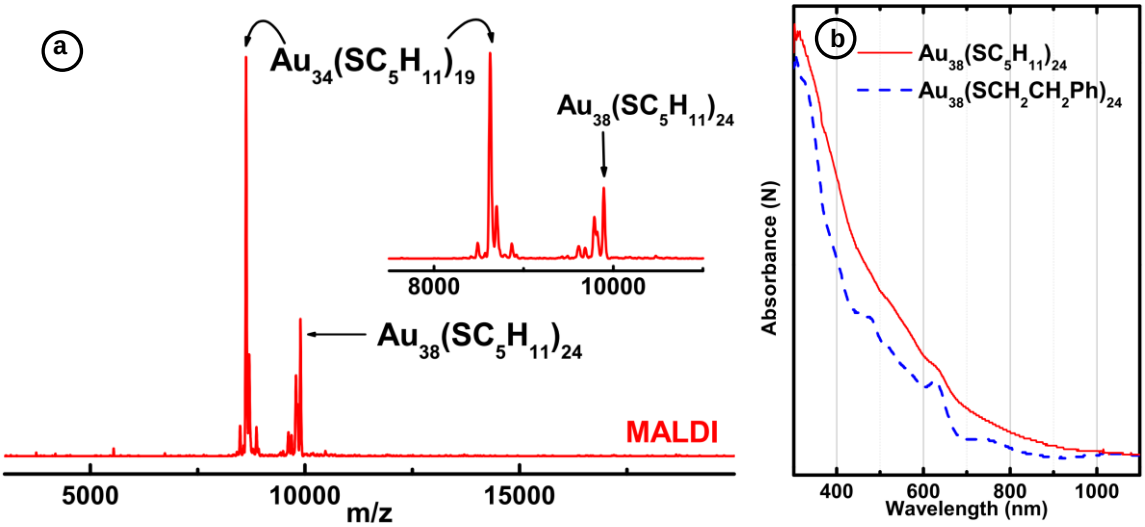

Figure S5. Characterization of $Au_{38}(SC_5H_{11})_{24}$ nanomolecules. (a) MALDI-MS shows purity of the sample $Au_{38}(SC_5H_{11})_{24}$. ESI-MS was not performed due to lack of instrumental facility during this time. (b) UV-Vis-NIR absorption spectra illustrate a comparison of the signature absorbance peaks unique to the $Au_{38}(SCH_2CH_2Ph)_{24}$ analyte against as synthesized $Au_{38}(SC_5H_{11})_{24}$. Absorption features are not well resolved due to presence of other impurities.

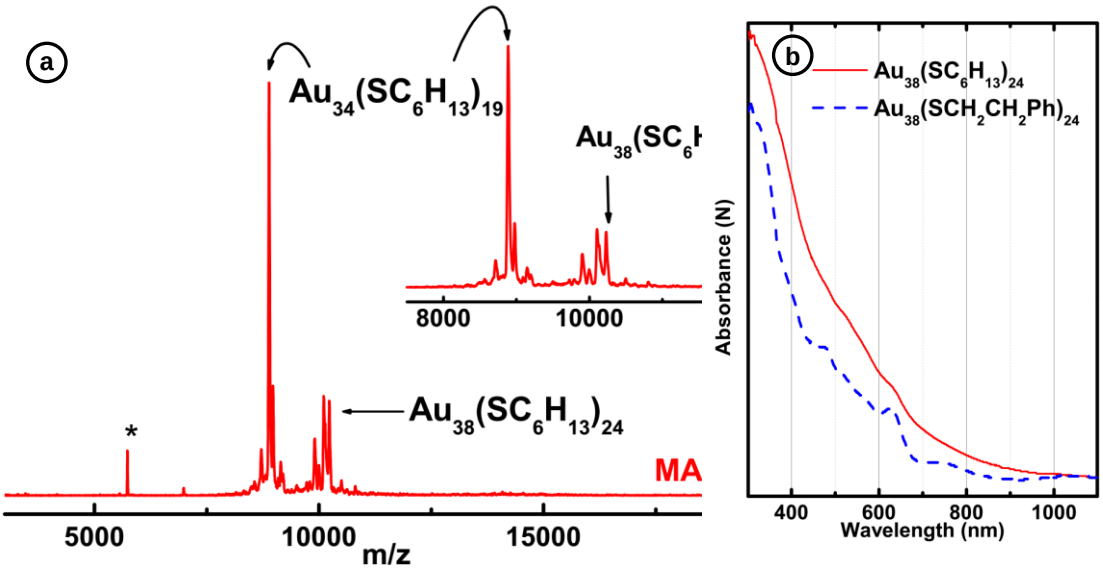

Figure S6. Characterization of $Au_{38}(SC_6H_{13})_{24}$ nanomolecules. (a) MALDI-MS shows purity of the sample $Au_{38}(SC_6H_{13})_{24}$. The peak marked by asterisk depicts $Au_{21}(SCH_2CH_2Ph)_{14}$ fragment from $Au_{25}(SCH_2CH_2Ph)_{18}$ in the sample. ESI-MS was not performed due to lack of instrumental facility during this time. (b) UV-Vis-NIR absorption spectra illustrate a comparison of the signature absorbance peaks unique to the $Au_{38}(SCH_2CH_2Ph)_{24}$ analyte against as synthesized $Au_{38}(SC_6H_{13})_{24}$. Absorption features are not well resolved due to presence of other impurities.

APPENDIX D: SUPPLEMENTARY INFORMATION FOR CHAPTER 5

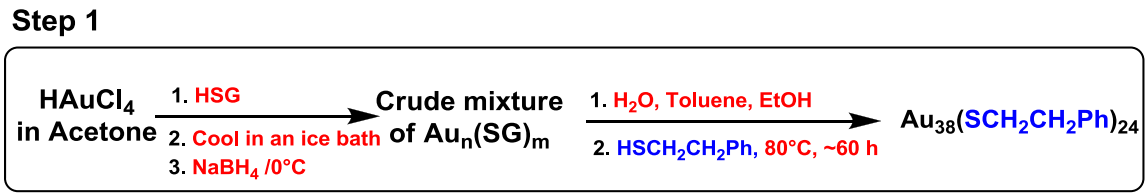

Scheme S5.1. The protocol for the synthesis of $Au_{38}(PET)_{24}$.

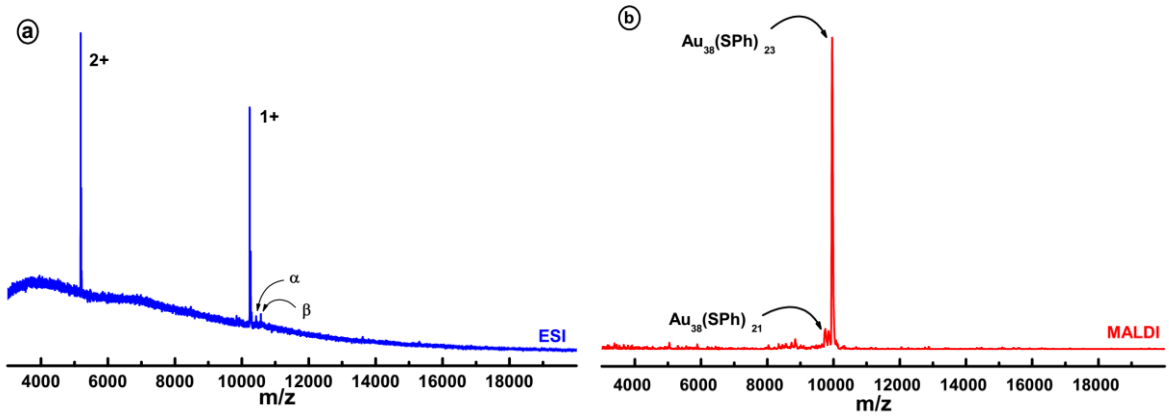

Figure S5.1. (a) ESI mass spectrum showing $Au_{38}(SPh)_{24}$ peaks in the 1+ and 2+ charges states. The peaks marked by asterisk depicts noise due to cesium acetate clustering and α depicts $CsCH_3COO$ adduct and β depicts Cs_2CH_3COO adduct on molecular ion. (b) MALDI mass spectrum of $Au_{38}(SPh)_{24}$ with no higher mass or low mass impurities.

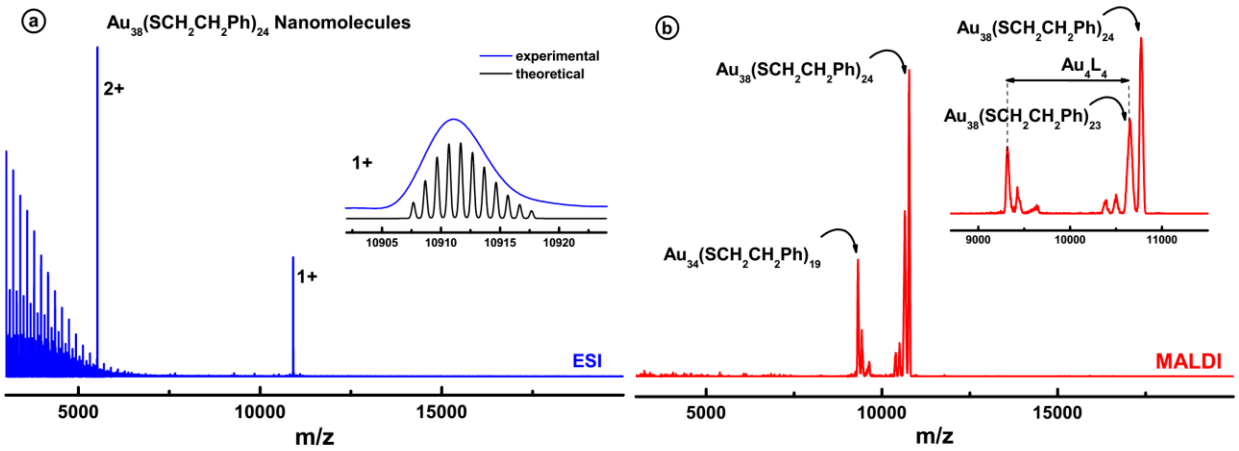

Figure S5.2. (a) ESI mass spectrum showing $Au_{38}(PET)_{24}$ peaks in the 1+ and 2+ charges states. The inset shows the expansion of the 10,900 to 10,920 m/z region, showing the $Au_{38}(PET)_{24}$ with 1+ charge state overlap with theoretical spectrum. (b) MALDI mass spectrum of $Au_{38}(SCH_2CH_2Ph)_{24}$. Inset shows the expansion of the 9,000 to 11,000 m/z region, showing completely exchanged $Au_{38}(SCH_2CH_2Ph)_{24}$, a partial SCH_2CH_2Ph exchange ($Au_{38}(SCH_2CH_2Ph)_{23}$) and a fragment of m/z difference of four gold and four ligands.

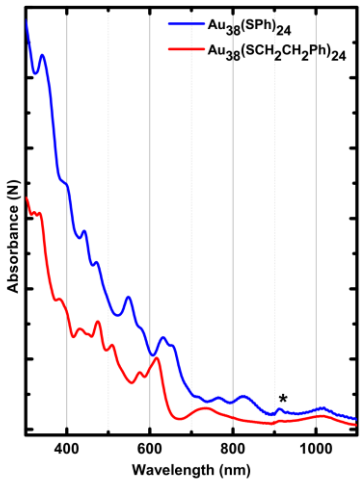

Figure S5.3. UV-vis-NIR absorption spectra of $Au_{38}(SPh)_{24}$ (blue) and $Au_{38}(SCH_2CH_2Ph)_{24}$ (red) at 78K where peak marked by asterisk depicts an instrumental artifact.

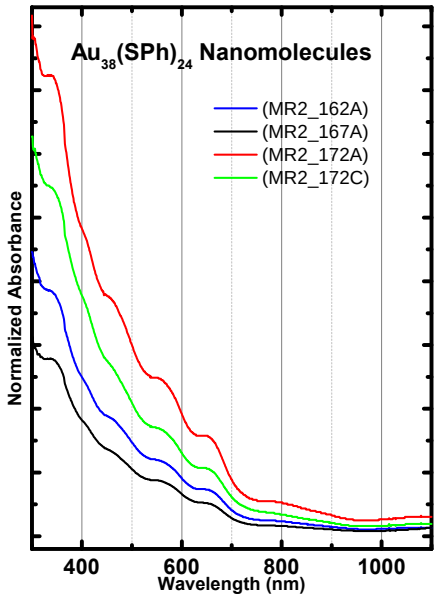

Figure S5.4. UV-vis-NIR absorption spectra of four trials of complete $Au_{38}(SPh)_{24}$ ligand exchange.

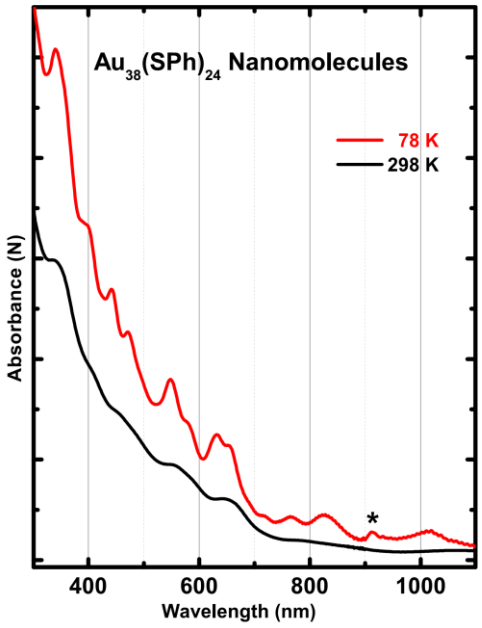

Figure S5.5. UV-vis-NIR spectra of $Au_{38}(SPh)_{24}$ at 78K (red) and 298 K (black).

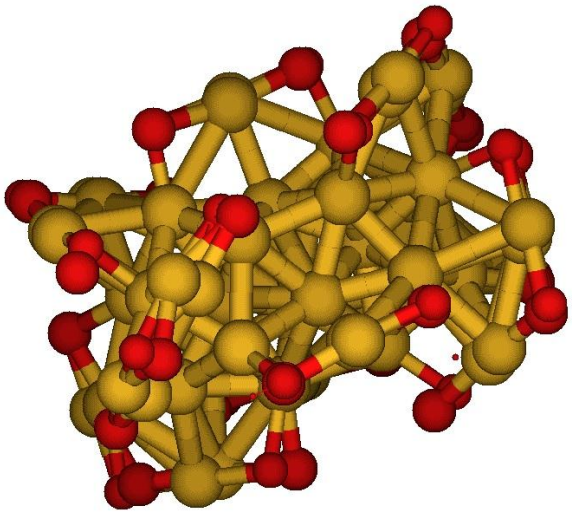

Figure S5.6. Visual comparison (superimposition) of the $Au_{38}S_{24}$ frameworks of $Au_{38}(SPh)_{24}$ and $Au_{38}(SCH_2CH_2Ph)_{24}$ predicted from QM simulations as described in the main text. Au atoms in orange, S atoms in red. The Au, S atoms of $Au_{38}(SCH_2CH_2Ph)_{24}$ are shown with slightly larger sphere radii to facilitate comparison.

APPENDIX E: SUPPLEMENTARY INFORMATION FOR CHAPTER 6

Computational details

Local geometry relaxations and Ab Initio Molecular Dynamics (AIMD) runs were performed using the CP2K code [97] whose DFT algorithms are based on a hybrid Gaussian/Plane-Wave scheme (GPW) [98]. Pseudopotentials derived by Goedecker, Teter and Hutter [99] were chosen to describe the core electrons of all atoms and DZVP basis sets [100] to represent the DFT Kohn–Sham orbitals. Calculations were performed spin-restricted and at the Gamma point only. The semi-empirical Grimme-D3 correction [101] was added to Perdew–Burke–Ernzerhof (PBE) [102] exchange and correlation (xc-) functional to take into account dispersion interactions. The cut-off for the auxiliary plane wave representation of the density was 400 Ry. AIMD runs used a time step of 1.0 fs and the temperature was controlled by Nosé–Hoover chain thermostats [103]. The geometries of $Au_{38}(SCH_2CH_2Ph)_{24}$, $Au_{36}(SPh)_{24}$, and $Au_{30}(S^tBu)_{18}$ clusters were obtained via fully relaxed local geometry optimizations starting from configurations derived from X-ray measurements in Refs. [51], [18] and [20], respectively, after completing the missing atoms of $Au_{38}(SCH_2CH_2Ph)_{24}$ as needed. The Cartesian coordinates of the resulting $Au_{38}(SCH_2CH_2Ph)_{24}$, $Au_{36}(SPh)_{24}$, and $Au_{30}(S^tBu)_{18}$ species are provided in the Supplementary Information (SI). In the system comparison analysis, we use clusters for some of which no crystal structure is available (or have not even been synthesized yet). For these systems we create initial geometries starting from the experimental structures in Refs. [51], [18] and [20], we perform local optimizations, and follow these by three sequential AIMD runs lasting : (a) 2 psec at 300 K, (b) 2 psec at 900 K (only in this AIMD run the coordinates of the Au atoms were left frozen to the initial geometry), (c) 2 psec at 300 K, leading to a final full geometry optimization. This long procedure is deemed necessary to equilibrate structure and ligand-ligand interactions especially for $Au_{38}(SPh)_{24}$, and indeed the total

energy of this system decreased by 3.7 eV after the equilibration protocol, while a smaller decrease in energy was observed for $Au_{36}(S^tBu)_{24}$ and $Au_{30}(SPh)_{18}$. (1.5 eV and 0.6 eV, respectively).

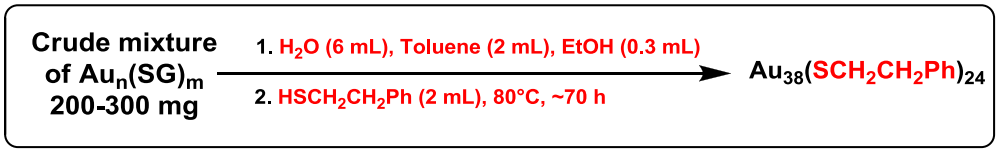

Scheme S6.1. The protocol for the synthesis of $Au_{38}(SCH_2CH_2Ph)_{24}$.

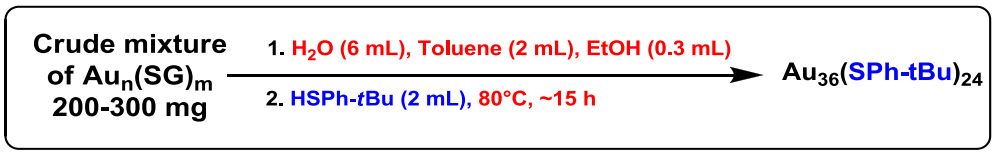

Scheme S6.2. The protocol for the synthesis of $Au_{36}(SPh\text{-}tBu)_{24}$.

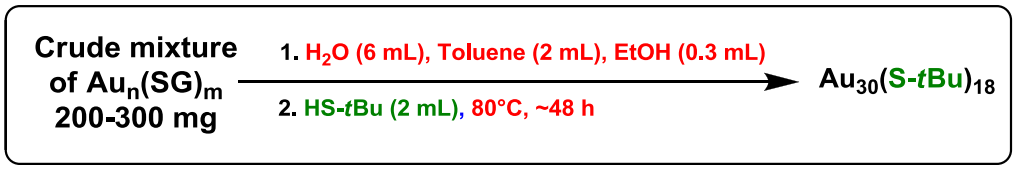

Scheme S6.3. The protocol for the synthesis of $Au_{30}(S\text{-}tBu)_{18}$.

System : $Au_N(SR)_M$	N,M=30,18,R=tBu	N,M=36,24,R=Ph	N,M=38,24,R=EtPh
$Au_N(SR)_M$	1687.98201666	2332.90823832	2730.59465752
Au_N	996.60577862	1195.91865934	1262.35730340
$(SR)_M^{crown}$	689.039641560	1134.25963456	1465.20378111
$SR_{relaxed}$	38.27338148	47.25499543	61.00837653
$HSR_{relaxed}$	38.91610700	47.88447318	61.65151849
Au_{atom}	33.1443376704	33.1443376704	33.1443376704
$Au_N(SR)_M$-anion-adiab	1688.04648476	2332.98786144	2730.67891792
$Au_N(SR)_M$-cation-adiab	1687.79592159	2332.70818507	2730.42134317

Table S6.1. Absolute electronic energy values for the $Au_N(SR)_M$ systems here considered. The nomenclature is the following: $Au_N(SR)_M$ = full nanomolecule; Au_N = gold cluster in the interacting configuration; $(SR)_M^{crown}$ = crown or shell of ligands in the interacting configuration; $SR_{relaxed}$ = fully relaxed SR thiyl radical; $HSR_{relaxed}$ = fully relaxed HSR thiol; Au_{atom} = isolated Au atom; $Au_N(SR)_M$-anion-adiab = total energy of $Au_N(SR)_M$ anion in the geometry of the neutral species; $Au_N(SR)_M$-cation-adiab = total energy of $Au_N(SR)_M$ anion in the geometry of the neutral species. All energies are in atomic units.

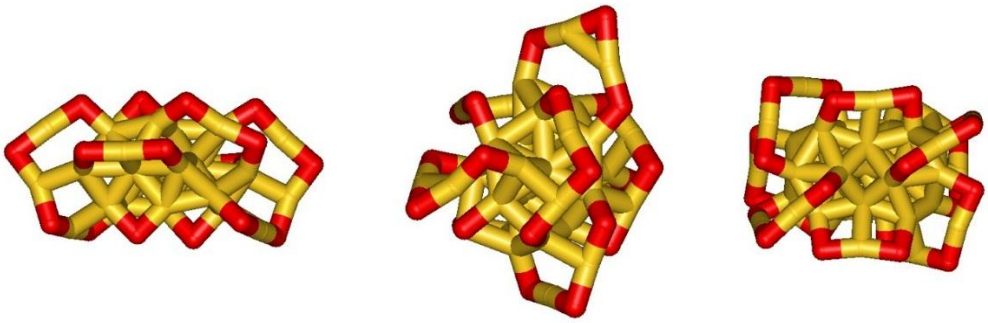

Figure S6.1. Schematic pictures of the $Au_N(S)_M$ skeletal framework of $Au_{30}(S^tBu)_{18}$, $Au_{36}(SPh)_{24}$ and $Au_{38}(SCH_2CH_2Ph)_{24}$, respectively, from left to right.

Model	Allometric1		
Equation	y = a*x^b	$Au_n(SC_2P)_m$	
Reduced Chi-Sqr	11.48284		
Adj. R-Square	0.97807		
		Value	Standard Error
B	a	3.43606	0.68056
	b	0.55675	0.03821
Model	Allometric1		
Equation	y = a*x^b	$Au_n(TBBT)_m$	
Reduced Chi-Sqr	1.49222		
Adj. R-Square	0.99697		
		Value	Standard Error
B	a	2.85048	0.19808
	b	0.60018	0.0138
Model	Allometric1		
Equation	y = a*x^b	$Au_n(StBu)_m$	
Reduced Chi-Sqr	0.16585		
Adj. R-Square	0.99525		
		Value	Standard Error
B	a	2.48161	0.23067
	b	0.5896	0.02424

Table S6.2. Standard values and errors associated with the nano-scaling law.

VITA

Milan Rambukwella

Ph.D. (Chemistry), B.Sc. Chemistry (Hons),

☎ : +94 812421517

✉ : milanrambukwella@gmail.com

🖃 : Balagolla, Kandy, Sri Lanka

Professional Skills & Key Strengths

- Ph.D. in nanotechnology and material science
- B.Sc. chemistry honors degree.
- 5+ years of experience in analytical chemistry and nano-materials.
- Excellent track record of research publications.
- Research collaborations in gold nanoparticle research.
- Expertise in material characterization techniques: MALDI-TOF-MS, ESI-MS, FTIR, TGA,
- Experience in chemical analysis techniques: HPLC, GC-MS, and UV-Vis-NIR.
- 6+ Years of university teaching and supervision experience.
- Excellent written and verbal communication skills.

Research Experience

- Gold nanoparticle synthesis; using wet chemical methods of synthesis, large scale synthesis of gold nanoclusters
- Complete characterization of gold nanoclusters using mass spectrometry, spectroscopy, microscopy and X-ray diffraction tools
- Optimization of synthetic protocols for high yield synthesis of gold nanoclusters
- Develop and design nanoengineering at atomic level to the monolayer composition of gold nanomolecules
    - Ligand exchange experiments on gold nanomolecules with several functional ligands to modify the properties of gold nanomolecules

    - Mass spectrometry tools like MALDI-TOF-MS and ESI-MS were used for these experiments
- Separation of gold nanoclusters
- Method development for size exclusion chromatography gold nanoclusters
- Microscopy of gold nanoclusters
- X-ray diffraction studies of gold nanoclusters
- Single crystal X-ray diffraction of gold nanoclusters
- Powder X-ray diffraction of gold nanoclusters to understand the structure
- Electrochemistry of gold nanoclusters
    - Cyclic voltammetry and differential pulse voltammetry of gold nanoclusters to understand the size dependent transition
- Temperature dependent UV-Vis-NIR absorption studies of gold nanomolecules

Education

Ph.D. Nanotechnology & Material Science (2014-2018)
University of Mississippi, Oxford, MS, USA
Dissertation: Aliphatic, Aromatic and Bulky thiolate Ligand Effect on Gold Nanomolecules
Advisors: Prof. Amala Dass

B.Sc. Chemistry Honours (Second Class Upper Division) **(**2007-2011)
University of Peradeniya, Peradeniya, Sri Lanka
GPA: 3.35 / 4.0, Minor Subjects: Biology, Botany
Dissertation: Dye sensitized solar cells for solar energy harvesting.
Advisor: Prof. Gamini Rajapakse

Professional Experience

- **Research Assistant** **(**2014-2018)
  University of Mississippi, Oxford, MS; Supervisor Dr. Amala Dass

    - 7 peer reviewed publications
    - Synthesis and publication of new nanomolecular structures
    - Crystal growth, atomic structure determination, and publication of new structures
    - Collaborated on 5 research projects
    - 1 National Level Oral Presentation at American Chemical Society meeting
    - 3 Oral presentations at American Chemical Society SERMACS meetings
    - 1 Poster presentation at American Chemical Society SERMACS meetings

- Experienced in several analytical techniques including: nESI-Q-TOF-MS, MALDI- TOF-MS, UV-Vis spectroscopy, low temperature UV-Vis spectroscopy, x-ray crystallography (sc-XRD), ICP-MS, HPLC-MS, SEC, chromatography, and electrochemical methods (CV and DPV)
- Fabrication of in-house emitters for the nano-ESI source
- Maintenance and general upkeep of analytical instruments

➢ **Teaching Assistant** (2014-2018)
University of Mississippi, Oxford, MS

- Worked as a teaching assistant for general chemistry labs for three semesters under supervisor Dr. John Wiginton
    - The responsibilities for these positions include mentoring the labs and assess their performance in the lab.
    - 3 semesters; 150+ students.
- Worked as teaching assistant for advanced instrumental analysis for graduate students.
    - The labs are designed based on spectroscopic and mass spectrometry techniques for the first time.
- Mentored four high school students (J.D. Olivet, Shayna Burrage, Marie Neubrander and Anish Ravishanker) as part of summer research program from high school students at University of Mississippi.
    - These students are part of research publications for his research contributions.
- Mentored three undergraduate students in our research laboratory to work on synthesis of gold nanoparticles.

➢ **Mass Spectrometry Analyst** (2014-2017)
University of Mississippi, Oxford, MS; Supervisor Dr. Amala Dass

- Analysis using ESI and MALDI mass spectrometry for publication quality determination of a wide variety of compounds for the Department of Chemistry & Biochemistry and Department of Pharmacy

➢ **Technical skills** **(**2014-2017)
University of Mississippi, Oxford, MS; Supervisor Dr. Amala Dass

- nESI-Q-TOF-MS high resolution electrospray ionization mass spectrometry
    - Analysis and identification of large and small (200-40,000Da) organic molecules

    - Mass Lynx Software utilized for ESI-MS interface for sample analysis, calibration, and isotopic modeling
    - Experience in troubleshooting, programming and repairing
    - Completed evaluation and modification of control systems of the ESI source to nano-ESI source
    - Ensured effective and continuous 24 hr. operation of all control systems
    - Diagnosed control system problems using manuals, schematics
    - Preventative maintenance and general upkeep
- MALDI-TOF-MS matrix assisted laser desorption ionization mass spectrometry
    - Analysis of large and small (200-300,000Da) organic molecules and proteins
    - Voyager Pro Software utilized for sample analysis and data processing with MALDI-MS
    - Experience in troubleshooting, programming and repairing
    - Completed evaluation and modification of control systems of the ESI source to nano-ESI source
    - Ensured effective and continuous 24 hr. operation of all control systems
    - Diagnosed control system problems using manuals, schematics and various test equipment.
    - Preventative maintenance and general upkeep
- UV-Vis-NIR spectroscopy
    - Analysis of large and small (200-300,000Da) organic molecules
    - Low temperature 77K analysis of large and small (200-300,000Da) organic molecules
    - Installation of low temperature cryostat to the UV-Vis-NIR spectrophotometer
- Single Crystal x-ray diffraction (crystallography)
    - Small and large (200-10,000 Da) complex organic molecules
    - Crystal growth of large, complex, and organic soluble nanomaterials
    - Experienced in growing, handling, mounting, and diffracting microscopic crystals
    - Experienced with various mounting techniques
    - Olex Software for crystal structure refinement
    - Bruker Apex II software used in the analysis and data processing of crystallographic data
    - Mercury Software crystallographic information file processing and modeling
    - Crystal Maker crystallographic information file processing, and modeling
- HPLC-MS (high pressure liquid chromatography)
    - Formal in-house training at University of Mississippi
    - Used in investigation of new separation and analysis techniques of gold thiolated nanomolecules
- ICP-MS

- Formal in-house training at University of Mississippi
- Analysis of trace metals from soil samples
- Processing and statistical data analysis of ICP-MS data

- Experience on Windows Office package, Origin, Olex2, Crystal maker, Endnote, ChemDraw and proficient in ACS journal guidelines, publication, and review process of manuscripts
- Instrument manager of research laboratory, 4 years

Peer Reviewed Publications

1. **Rambukwella, M**.; Sementa, L.; Barcaro, G.; Fortunelli, A.; Dass, A., Organosoluble $Au_{102}(SPh)_{44}$ Nanomolecules: Synthesis, Isolation, Compositional Assignment, Core Conversion, Optical Spectroscopy, Electrochemistry, and Theoretical Analysis. *J. Phys. Chem. C* **2015**, 119, 25077-25084.
2. Dass, A.; Jones, T.; **Rambukwella, M.**; Crasto, D.; Gagnon, K. J.; Sementa, L.; De Vetta, M.; Baseggio, O.; Aprà, E.; Stener, M.; Fortunelli, A. Crystal Structure and Theoretical Analysis of Green Gold Au30(S-Tbu)18 Nanomolecules and Their Relation to $Au_{30}S(StBu)_{18}$. *J. Phys. Chem. C* **2016**, 120, 6256-6261.
3. **Rambukwella, M.**; Dass, A., Synthesis of $Au_{38}(SCH_2CH_2Ph)_{24}$, $Au_{36}(SPhtBu)_{24}$, and $Au_{30}(StBu)_{18}$ Nanomolecules from a Common Precursor Mixture. *Langmuir* **2017**, 33, 10958-10964.
4. **Rambukwella, M.**; Burrage, S.; Neubrander, M.; Baseggio, O.; Aprà, E.; Stener, M.; Fortunelli, A.; Dass, A., $Au_{38}(SPh)_{24}$: Au_{38} Protected with Aromatic Thiolate Ligands. *J. Phys. Chem. Lett.* **2017**, 8, 1530-1537.
5. **Rambukwella, M.**; Sementa, L.; Fortunelli, A.; Dass, A., Core-Size Conversion of $Au_{38}(SCH_2CH_2Ph)_{24}$ to $Au_{30}(StBu)_{18}$ Nanomolecules. *J. Phys. Chem. C* **2017**, 121, 14929-14935.
6. **Rambukwella, M.**; Chang, L.; Ravishanker, A.; Stener, M.; Fortunelli, A.; Dass, A., $Au_{36}(SePh)_{24}$ Nanomolecules: Synthesis, Optical Spectroscopy and Theoretical Analysis. PCCP **2018**, 20, 13255-13262.
7. **Rambukwella, M.**; Sakthivel, N.A.; Delcamp, J.H.; Sementa, L.; Fortunelli, A.; Dass, A., Ligand Structure Determines Nanoparticles' Atomic Structure, Metal-Ligand Interface and Properties, Frontiers in Chemistry **2018**, 6, 2296-2646.

Presentations

1. "**Synthesis of $Au_{38}(SCH_2CH_2Ph)_{24}$, $Au_{36}(SPhtBu)_{24}$, and $Au_{30}(StBu)_{18}$ Nanomolecules & Structural Selectivity**" Mar 2018
   Oral presentation, 255th American Chemical Society National Meeting, New Orleans, LA

2. "**Core-Size Conversion of $Au_{38}(SCH_2CH_2Ph)_{24}$ to $Au_{30}(StBu)_{18}$**" Nov 2017
   Oral presentation, Southeastern Regional American Chemical Society meeting, Charlotte, NC
3. "**Organosoluble $Au_{102}(SPh)_{44}$ Nanomolecules**" Oct 2016
   Oral presentation, Southeastern Regional American Chemical Society meeting, Columbia, SC
4. "**Tuning the synthesis of $Au_{102}(SPh)_{44}$ and $Au_{38}(SPh)_{24}$ Nanomolecules**" Oral presentation, University of Mississippi Departmental Seminar, Oxford, MS Apr 2016
5. "**Organosoluble $Au_{102}(SPh)_{44}$ Nanomolecules**" Nov 2015
   Oral presentation, 2015 Southeastern Regional American Chemical Society meeting, Memphis, TN
6. "**Synthesis and Characterization of 24 kDa Gold Nanomolecules**" Oct 2014
   Poster presentation, Southeastern Regional American Chemical Society meeting, Nashville, TN
7. "**Approach on Platinum Doping of Gold-25 Nanomolecules**" May 2014
   Poster presentation, Established Program to Stimulate Competitive Research, Starkville, MS

Synergistic Activities

- Actively participated in outreach activities to set up chemistry laboratories at North Panola High School (NPHS), Sardis, MS. NPHS does not have chemistry labs for high school students. As a part of this outreach program we visit the school regularly, conduct the chemistry labs and support them with the required supplies.
- Active member of the inorganic literature club at the University of Mississippi.
- Active committee member of the Zoological Society during 2008-2009 and as the Junior Treasurer of the Peradeniya University Chemical Society during 2009-2011.
- The president of the Peradeniya University Chemical Society during 2010-2011 and conducted Science-Camp workshops and seminars in selected schools at Kandy, District.
- Member of American Chemical Society from 2016-2018.

References

- Dr. Amala Dass, Assistant Professor, Department of Chemistry, University of Mississippi, email: amal@olemiss.edu, Phone: 662-915-1826
- Prof. R. M. G. Rajapakse, Department of Chemistry, Faculty of Science, University of Peradeniya, Peradeniya, Sri Lanka
  email: rmgr@pdn.ac.lk, Phone: +9481-239-4442